LOCAL CONFORMATIONS AND EXCITED STATE DYNAMICS OF PORPHYRINS AND NUCLEIC ACIDS BY 2-DIMENSIONAL FLUORESCENCE SPECTROSCOPY

by

JULIA R. WIDOM

A DISSERTATION

Presented to the Department of Chemistry and Biochemistry
and the Graduate School of the University of Oregon
in partial fulfillment of the requirements
for the degree of
Doctor of Philosophy

December 2013

DISSERTATION APPROVAL PAGE

Student: Julia R. Widom

Title: Local Conformations and Excited State Dynamics of Porphyrins and Nucleic Acids by 2-Dimensional Fluorescence Spectroscopy

This dissertation has been accepted and approved in partial fulfillment of the requirements for the Doctor of Philosophy degree in the Department of Chemistry and Biochemistry by:

Peter von Hippel	Chairperson
Andrew Marcus	Advisor
John Hardwick	Core Member
Marina Guenza	Core Member
Michael Raymer	Institutional Representative

and

Kimberly Andrews Espy	Vice President for Research and Innovation; Dean of the Graduate School

Original approval signatures are on file with the University of Oregon Graduate School.

Degree awarded December 2013

© 2013 Julia R. Widom

DISSERTATION ABSTRACT

Julia R. Widom

Doctor of Philosophy

Department of Chemistry and Biochemistry

December 2013

Title: Local Conformations and Excited State Dynamics of Porphyrins and Nucleic Acids by 2-Dimensional Fluorescence Spectroscopy

Biological systems present many challenges to researchers attempting to study them using spectroscopy. Low specificity, low sensitivity, and broad and overlapping lineshapes limit the amount of information that can be obtained in experiments. Two-dimensional fluorescence spectroscopy (2D FS) is a highly sensitive and information-rich spectroscopic technique that was developed to study the conformations and excited state dynamics of systems exhibiting exciton coupling. In this dissertation, I describe a variety of extensions of 2D FS that further increase its utility for the study of biological systems. I describe experiments on a dimer of zinc tetraphenylporphyrin embedded in a membrane, in which the signals from two conformational subpopulations were separated in order to study the thermodynamics of their interconversion. I present proof-of-principle experiments on nucleic acids that utilize fluorescence resonance energy transfer to separate signals from different subpopulations. I also describe experiments in which 2D FS was performed using ultraviolet excitation to determine the conformation of a dinucleotide of a fluorescent analogue of the nucleic acid base adenine. I discuss experiments on porphyrin dimers in which 2D FS was used as a probe of excited state dynamics. Finally, I present model calculations for a proposed variation of 2D FS in

which entangled photons would be used as the excitation source. These calculations suggest that this approach has the potential to yield significantly narrower spectral lineshapes than conventional 2D FS. These experiments and calculations yield new insight into the systems investigated and establish a 'toolbox' of variations of 2D FS that can be used to gain as much information as possible from experiments on challenging systems such as protein-DNA complexes.

This dissertation contains previously published and unpublished co-authored material.

CURRICULUM VITAE

NAME OF AUTHOR: Julia R. Widom

GRADUATE AND UNDERGRADUATE SCHOOLS ATTENDED:

University of Oregon, Eugene
Northwestern University, Evanston, Illinois

DEGREES AWARDED:

Doctor of Philosophy, Chemistry, 2013, University of Oregon
Bachelor of Arts, Chemistry, 2009, Northwestern University

AREAS OF SPECIAL INTEREST:

Multidimensional Optical Spectroscopy
Structure and Dynamics of Nucleic Acids

PROFESSIONAL EXPERIENCE:

Graduate Teaching Assistant, Department of Chemistry, University of Oregon, Eugene, 2009-2010

Graduate Research Assistant, Department of Chemistry, University of Oregon, Eugene, 2010-2013

GRANTS, AWARDS, AND HONORS:

Mathcad Award for Physical Chemistry Coursework, Northwestern University, Evanston, 2007

R. K. Summerbell Memorial Fund Award for Chemistry Research and Coursework, Northwestern University, Evanston, 2008

Marple-Schweitzer Memorial Award for Chemistry Research and Coursework, Northwestern University, Evanston, 2009

Rosaria Haugland Chemistry Graduate Research Fellowship, University of Oregon, Eugene, 2010

Peter von Hippel Graduate Scholar Award, Institute of Molecular Biology, University of Oregon, Eugene, 2013

PUBLICATIONS:

Raymer, M. G.; Marcus, A. H.; Widom, J. R.; Vitullo, D. L. P. Entangled Photon-Pair Two-Dimensional Fluorescence Spectroscopy (EPP-2DFS). *J. Phys. Chem. B.* **2013,** DOI 10.1021/jp405829n.

Karki, K.; Torbjörnsson, M.; Widom, J. R.; Marcus, A. H.; Pullerits, T. Digital Cavities and Their Potential Applications. *J. Instrum.* **2013**, *8*, T05005-1-12.

Widom, J. R.; Lee, W.; Perdomo-Ortiz; A., Rappoport, D.; Molinski, T. F.; Aspuru-Guzik, A.; Marcus, A. H. Temperature-Dependent Conformations of a Membrane Supported 'Zinc Porphyrin Tweezer' by 2D Fluorescence Spectroscopy. *J. Phys. Chem. A.* **2013**, *117*, 6171-6184.

Widom, J. R.; Johnson, N. P.; von Hippel, P. H.; Marcus, A. H. Solution Conformation of 2-Aminopurine Dinucleotide Determined by Ultraviolet 2D Fluorescence Spectroscopy. *New J. Phys.* **2013**, *15*, 025028-1-16.

Widom, J. R.; Rappoport, D.; Perdomo-Ortiz, A.; Thomsen, H.; Johnson, N. P.; von Hippel, P. H.; Aspuru-Guzik, A.; Marcus, A. H. Electonic Transition Moments of 6-Methyl Isoxanthopterin – a Fluorescent Analogue of the Nucleic Acid Base Guanine. *Nucleic Acids Res.* **2013**, *41*, 995-1004.

Sanders, J. N.; Saikin, S. K.; Mostame, S.; Andrade, X.; Widom, J. R.; Marcus, A. H.; Aspuru-Guzik, A. Compressed Sensing for Multidimensional Spectroscopy Experiments. *J. Phys. Chem. Lett.* **2012**, *3*, 2697-2702.

Perdomo-Ortiz, A.; Widom, J. R.; Lott, G. A.; Aspuru-Guzik, A.; Marcus, A. H. Conformation and Electronic Population Transfer in Membrane-Supported Self-Assembled Porphyrin Dimers by 2D Fluorescence Spectroscopy. *J. Phys. Chem. B* **2012**, *116*, 10757-10770.

Lott, G. A.; Perdomo-Ortiz, A.; Utterback, J. K.; Widom, J. R.; Aspuru-Guzik, A.; Marcus, A. H. Conformation of Self-Assembled Porphyrin Dimers in Liposome Vesicles by Phase-Modulation 2D Fluorescence Spectroscopy. *Proc. Natl. Acad. Sci. U.S.A.* **2011**, *108*, 16521-16526.

Wang, C.; Widom, J.; Petronijevic, F.; Burnett, J. C.; Nuss, J. E.; Bavari, S.; Gussio, R.; Wipf, P. Synthesis and Biological Evaluation of Inhibitors of Botulinum Neurotoxin Metalloprotease. *Heterocycles*, **2009**, *79*, 487-520.

ACKNOWLEDGMENTS

I sincerely thank my advisor, Professor Andrew Marcus, and our close collaborator, Pete von Hippel, for the valuable research and career mentorship they have provided. Thanks largely to their guidance, I have grown not only as a scientist, but also in my belief in myself during my time at the University of Oregon.

I thank all the members of the Marcus and von Hippel labs, as well as our numerous collaborators in other labs. I thank former Marcus Lab member Geoff Lott for teaching me how to run our laser system during my first term in the lab. I thank the numerous undergraduates who have worked with me for their contributions to my research as well as for giving me the opportunity to gain experience in mentorship. I also thank Larry Scatena for his valuable contributions to the design and implementation of the optical systems that I used for my experiments, and Clifford Dax for his work designing and building custom electronics to suit our unique needs.

I thank all of the members of my family for their love and support. I thank my parents and grandparents for helping me to get excited about science at a young age and for insisting that every Christmas visit include an update about my research. I thank my friends for helping make graduate school a time of fun as well as learning.

Finally, my graduate tuition and stipend were funded largely by the Rosaria Haugland Graduate Fellowship. I thank Dr. Haugland for her contributions to science and the community, and for supporting my education through this wonderful fellowship.

This dissertation is dedicated to the memory of Jonathan Widom,
a beloved family member and admired scientist.

TABLE OF CONTENTS

Chapter Page

Chapter Page

Chapter Page

Chapter Page

LIST OF FIGURES

Figure Page

Figure Page

LIST OF TABLES

Table Page

CHAPTER I

INTRODUCTION

1. Overview

Biological systems exhibit astonishing complexity that arises out of the properties and interactions of relatively simple building blocks. Complete understanding of a 'macromolecular machine' that functions in a living organism requires experiments that target multiple different timescales and layers of complexity, from the fast fluctuations that occur in the shell of solvent surrounding a molecule[1] to the relatively slow changes that occur as a cell moves through its phases of development and replication.[2] An example of such a macromolecular machine, the bacteriophage T4 DNA replication system, is shown in Figure 1.1. This system requires many proteins such as a helicase to unwind the DNA, a primase to lay down RNA primers on the lagging strand, two polymerases to synthesize new strands of DNA that are complimentary to the leading and lagging strands, and a single-stranded DNA binding protein to protect exposed sections of ssDNA from degradation.[3] Each of these proteins has characteristic conformations and timescales governing its behavior and its interactions with DNA.

This dissertation will focus on the use of spectroscopy to determine the conformations adopted by molecules of biological interest. These systems present many challenges to researchers attempting to study them with spectroscopy. They operate at ambient temperature in condensed phases, leading to broad spectral lineshapes and congested spectra. A functional biological macromolecular machine may consist of proteins, nucleic acids, small molecules and more, and each of these components may

exist in a mixture of different binding states and conformations. The vast majority of biological molecules absorb light only below 300 nm and emit little to no fluorescence, making it difficult to detect low concentrations of them and to separate one species' signal from another's. Many of these problems can be mitigated by labeling specific molecules with fluorescent dyes, thus allowing higher specificity and more sensitive detection. Experiments can also be designed to yield greater sensitivity to the properties of interest, such as molecular conformation.

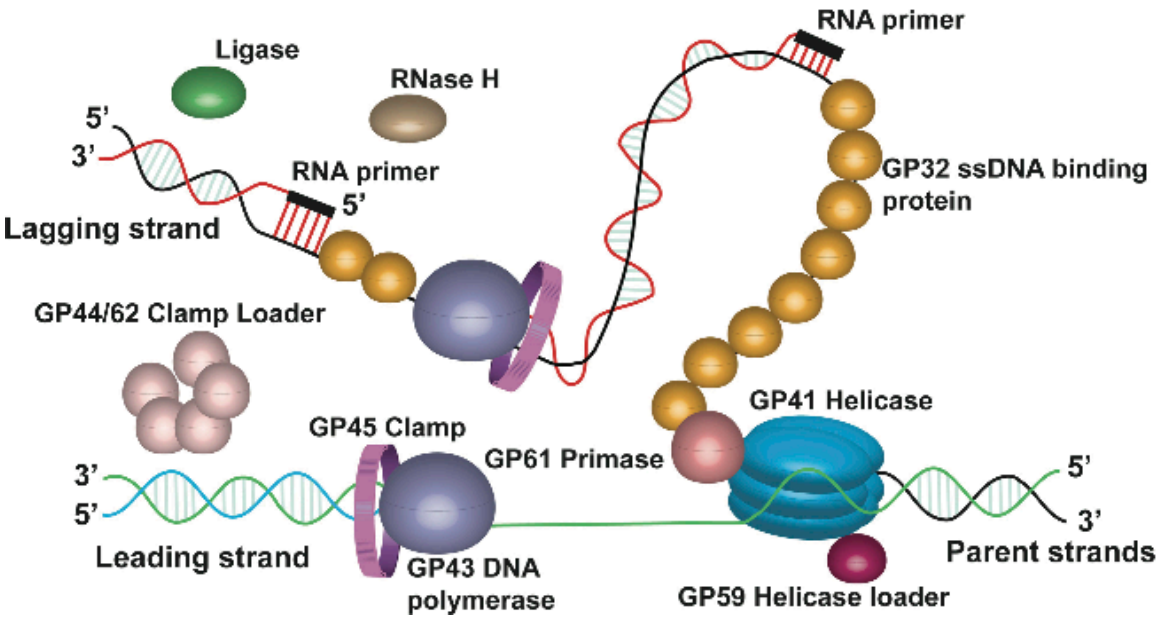

Figure 1.1. A cartoon of DNA replication by the bacteriophage T4 replisome.[3] The proteins involved include the primosome, which consists of the helicase gp41 that unwinds double-stranded DNA, the primase gp61 that synthesizes RNA primers on the lagging strand, the single-stranded DNA binding protein gp32, which protects ssDNA from degradation and the gp59 helicase loading protein. The replicase proteins include two units of the gp43 DNA polymerase, which synthesize new DNA complimentary to the leading and lagging strands, and the gp45 sliding clamp, which contributes to polymerase processivity and fidelity, as well as the gp44/62 clamp loader. Lagging strand synthesis is completed by RNase H, an exonuclease that removes RNA primers, and gp30 DNA ligase, which ligates the Okazaki fragments together into a unified strand.

2. Two-Dimensional Fluorescence Spectroscopy

To address these goals and challenges, Tekavec, Lott and Marcus developed the technique of two-dimensional fluorescence spectroscopy (2D FS),[4] a fluorescence-detected version of two-dimensional electronic spectroscopy.[5-6] Based on an earlier experiment by Tian and Warren,[7] this experiment derives high sensitivity and signal-to-noise by exciting a sample with laser pulses whose relative phases are modulated and detecting a modulated fluorescence signal. The spectra that result are highly sensitive to the conformations and excited state dynamics of systems that exhibit electronic coupling. 2D FS was originally applied to the study of electronic coherences in rubidium vapor,[4] then applied to a molecular system consisting of magnesium tetraphenylporphyrin dimers embedded in a membrane.[8] In this dissertation, I will present a number of different extensions of 2D FS that specifically address the challenges of studying biological systems, allowing new systems to be studied and additional information to be gathered in experiments. I will explain how each of these experiments addresses a common challenge in studying biological systems using spectroscopy, and how the unique features of fluorescence-detected 2D spectroscopy facilitate the advances presented.

2D FS involves exciting a sample with a series of four laser pulses and monitoring the sample's fluorescence as a function of the delays between the first two pulses (t_{21}) and between the third and fourth pulses (t_{43}). The 2-dimensional Fourier transform of these signals with respect to t_{21} and t_{43} yields a spectrum that reveals correlations between the energy gaps of the electronic coherences that are present during t_{21} and t_{43}. The delay between pulses 2 and 3 (t_{32}) is fixed for a given experiment, and represents the amount of

time over which the system is allowed to evolve between the two samplings of its coherence frequencies.

The remainder of this dissertation will focus on the technique of 2D FS and its application to the study of membranes and nucleic acids. I will present an overview of the theory of 2D FS, absorption and circular dichroism spectroscopy,[9] followed by studies on a linked dimer of zinc tetraphenylporphyrin (ZnTPP) embedded in a phospholipid membrane.[10] I will present measurements on DNA labeled with cyanine dyes that take advantage of fluorescence resonance energy transfer (FRET) to enhance the specificity of 2D FS. I will then discuss the use of fluorescent base analogues to study nucleic acids and protein-nucleic acid interactions,[11-12] and will present studies in which 2D FS was extended to the ultraviolet regime to study the conformation adopted by a dinucleotide of the fluorescent adenine analogue 2-aminopurine (2-AP).[13] I will then discuss the analysis of population time-dependent 2D spectra to study excited state relaxation pathways in porphyrin dimers.[9] Finally, I will present model calculations for a proposed experiment that uses entangled photons to perform 2D spectroscopy.[14]

3. Exciton-Coupled Molecular Dimers

The systems mentioned above have a commonality – in each case, the spectra that are measured can be interpreted in terms of an exciton-coupled dimer model. In this section, I will introduce the phenomenon of exciton coupling and discuss how it affects various spectroscopic signals. Chapter II will present a more detailed theoretical overview.

Consider two identical molecules, each with a single electronic transition with transition dipole moment $\vec{\mu}$ and energy ε_1 within the wavelength range of interest. If these molecules are brought into close proximity with each other, they will exhibit a dipolar interaction between their electronic transition dipole moments $\vec{\mu}_1$ and $\vec{\mu}_2$. In the point-dipole approximation, the energy of their interaction is given by eq 1.1,

$$V_{12} = \frac{\mu_1 \mu_2}{4\pi\varepsilon_0 R^3}\left(\hat{\mu}_1 \cdot \hat{\mu}_2 - 3\hat{\mu}_1 \cdot \hat{R}\, \hat{R} \cdot \hat{\mu}_2\right) = \frac{\mu_1 \mu_2}{4\pi\varepsilon_0 R^3}\kappa^2 \tag{1.1}$$

where μ_i is the norm of the ith momoner's electronic transition dipole moment and $\hat{\mu}_i$ is its unit vector. R is the norm of the vector connecting the centers of the two monomers and $\hat{R}$ is its unit vector. κ^2 is often called the 'orientation factor'.

This coupling adds off-diagonal terms to the site basis Hamiltonian. Diagonalization yields the exciton basis Hamiltonian, revealing the new eigenenergies and eigenstates of the coupled system. It is found that the electronic excited state of the monomer is split into two new states, $|+\rangle$ and $|-\rangle$, with

$$|\pm\rangle = \frac{1}{\sqrt{2}}\left[|e_1\rangle|g_2\rangle \pm |g_1\rangle|e_2\rangle\right] \tag{1.2}$$

The subscript indicates which state is associated with which monomer. Likewise, the energies of the transitions between the ground state and these new singly excited states are

$$\varepsilon_{\pm} = \varepsilon_1 \pm V_{12} \tag{1.3}$$

A doubly excited state, $|f\rangle = |e_1\rangle|e_2\rangle$ with energy $\varepsilon_f \approx 2\varepsilon_1$ corresponds to the concurrent excitation of both monomers. The new transition dipole moments are given by eq 1.4,

$$\bar{\mu}_{\pm} = (1/2)\left[\bar{\mu}_1 \pm \bar{\mu}_2\right] \tag{1.4}$$

Note that $\bar{\mu}_+$ and $\bar{\mu}_-$ may have different magnitudes from each other, depending on the angle δ between $\bar{\mu}_1$ and $\bar{\mu}_2$. In this exciton-coupled dimer picture, the two coupled monomers act as one chromophore, with the singly-excited states having one excitation delocalized over both monomers and the doubly excited state having two.

The conformation of the dimer has a significant impact on the quantities defined above. The distance and relative orientation between the two monomers (and therefore their transition dipole moments) as well as the vector connecting them, determine V_{12}. The relative orientation of $\bar{\mu}_1$ and $\bar{\mu}_2$ determines the relative magnitudes of $\bar{\mu}_+$ and $\bar{\mu}_-$, and therefore the intensities of the new transitions. All of the forms of spectroscopy mentioned above probe the energies and intensities of transitions between electronic states. Therefore, the changes in these quantities upon introduction of exciton coupling have a significant impact on the spectra that are measured. These impacts are summarized and shown schematically here, and discussed in more detail in Chapter II's theoretical overview.

In absorption spectra, the monomer transition is split, leading to an asymmetric broadening (Figure 1.2A). In principal, one could determine V_{12} and δ from the absorption spectrum, but in practice the spectral features are usually so broad and overlapping that this is impractical. The circular dichroism (CD) signal (that is, the difference in absorption of left- and right-handed circularly polarized light) of any achiral molecule is zero, but it is greatly enhanced by exciton coupling if the two monomers are in a chiral arrangement. If only the two degenerate monomer transitions are considered, the intensity of the CD spectrum at energy $\varepsilon_{\pm}$ is determined by the rotational strength,

$$RS^{\pm} = \pm \frac{\varepsilon_1}{4\hbar}\left[\vec{\mu}_1 \times \vec{\mu}_2 \cdot \vec{R}\right] \tag{1.5}$$

where $\vec{\mu}_1$, $\vec{\mu}_2$ and $\vec{R}$ are as defined above. This leads to a positive CD signal at either ε_+ or ε_- and a negative signal at the other. Because each of these transition consists of a broad band that largely overlaps with the other, much of the rotational strength is cancelled out once the width of the transitions are factored in. What remains is a sigmoidal curve that crosses zero at ε_1, which is illustrated in Figure 1.2B.

The 2D FS spectrum of a monomer is simply one peak located at (ε_1, ε_1), because that is the energy of the only transition available to the monomer within the wavelength range of interest (Figure 1.2C). Exciton coupling leads to a splitting of this transition, allowing for peaks at (ε_+,ε_+) and (ε_-,ε_-). These two 'diagonal peaks' correspond to the two peaks in the linear absorption spectrum and reflect pathways in which the dimer initially underwent a transition at $\varepsilon_{\pm}$ and then another transition at the same energy.

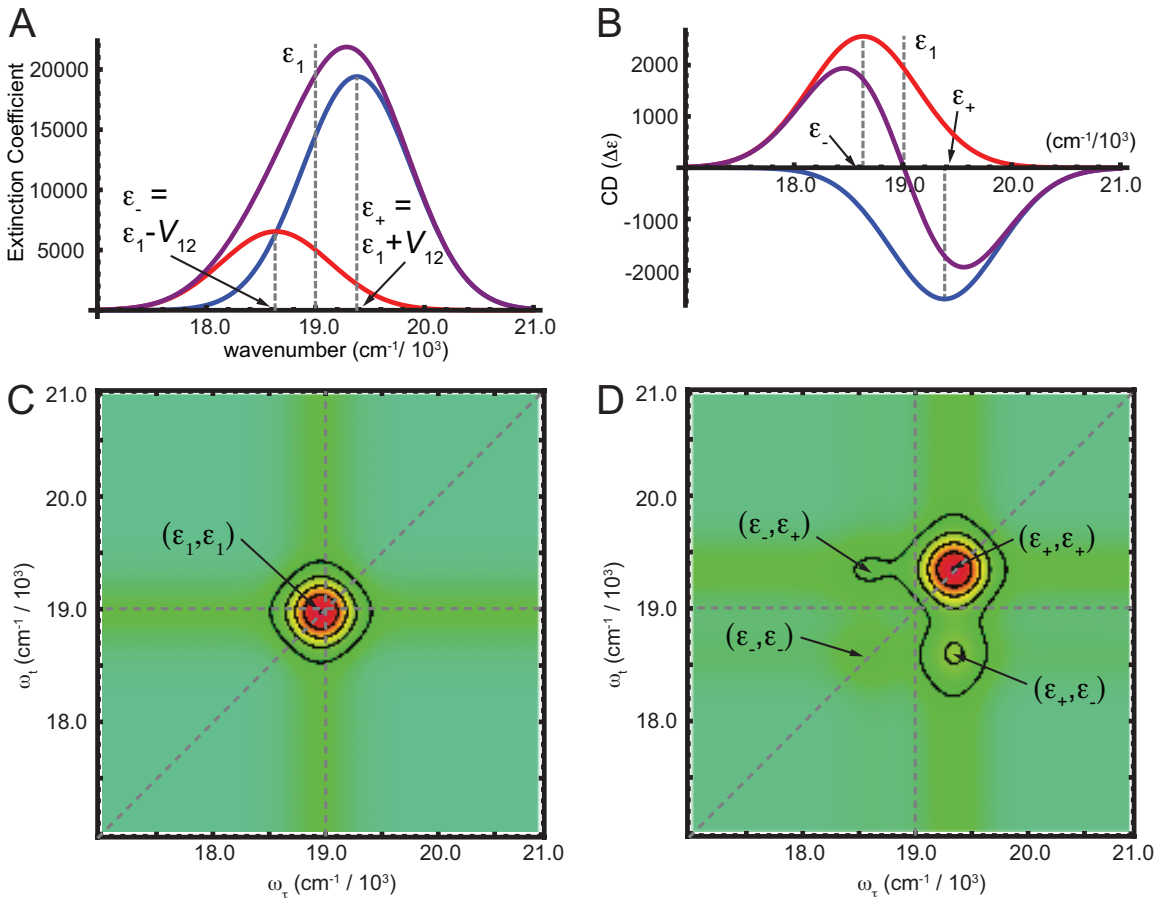

Figure 1.2. The effects of exciton coupling on spectroscopic signals. (A) The linear absorption spectrum of a dimer has two underlying absorption bands centered at $\varepsilon_- = \varepsilon_1 - V_{12}$ and $\varepsilon_+ = \varepsilon_1 + V_{12}$. (B) The CD spectrum has a sigmoidal shape resulting from the superposition of positive and negative bands centerd at ε_- and ε_+. (C) The 2D FS spectrum of a monomer has one feature centered at $(\varepsilon_1,\varepsilon_1)$. Crosshatches are placed at the monomer transition energy ε_1 and along the diagonal. (D) The 2D FS spectrum of a coupled dimer has diagonal peaks at $(\varepsilon_-,\varepsilon_-)$ and $(\varepsilon_+,\varepsilon_+)$, as well as cross peaks at $(\varepsilon_-,\varepsilon_+)$ and $(\varepsilon_+,\varepsilon_-)$. The dimer spectra were calculated for a monomer transition energy of 19000 cm^{-1}, an angle of 60° between monomer transition dipole moments (with $\vec{R}$ perpendicular to $\vec{\mu}_1$ and $\vec{\mu}_2$, $|\vec{R}| = 10$ Å and $|\vec{\mu}_1| = |\vec{\mu}_2| = 12.2D$), and a coupling strength of 373 cm^{-1}.

Furthermore, the coupling allows for 'cross peaks' at $(\varepsilon_+,\varepsilon_-)$ and $(\varepsilon_-,\varepsilon_+)$, which reflect pathways in which the dimer initially underwent a transition at $\varepsilon_\pm$ and then another transition at the other energy (Figure 1.2D). As in the linear absorption spectrum, the

splitting and relative intensities of these features are determined by V_{12} and δ, but due to the spreading out of the spectrum over a second dimension, the underlying transitions at ε_+ and ε_- can often be resolved. In addition, the four-pulse sequence and femtosecond time resolution of 2D FS allow excited state dynamics to be studied, and the lineshapes of spectral features contain information about the interactions of the chromophores with their surroundings.[15]

4. Porphyrins and Liposomes

Chapters II, III and VI discuss experiments performed on metalloporphyrin dimers embedded in liposomes.[9-10] Porphyrins are ubiquitous in biology. For example, the photosynthetic pigments chlorophyll a and b are magnesium porphyrins, and the oxygen carrier in blood is heme, an iron porphyrin.[16] The experiments described in this dissertation utilize magnesium tetraphenylporphyrin and zinc tetraphenylporphyrin. The absorption spectra of porphyrin chromophores exhibit a vibrational progression at low energy called the Q bands (the S_0 to S_1 transition), and a very strong transition at higher energy called the B or Soret band (S_0 to S_2).[17] Excitation in either the Q or B bands leads to fluorescence emission primarily from the Q band, exhibiting a vibrational progression. The exact intensities and energies of these features, as well as the fluorescence quantum yield, vary for different porphyrins. Figure 1.3B shows the absorption spectrum of ZnTPP in toluene, and Figure 1.3C shows its emission spectrum.

By embedding the porphyrin of interest in a membrane, we hope to uncover general principles governing the assembly and behavior of complex macromolecular machines that reside in membranes. Such machines include photosystems I and II, which

work together to use the energy from absorbed photons to oxidize water, and the complexes of the mitochondrial electron transport chain, which reduce oxygen to water while generating ATP.[16] When molecules such as porphyrins become concentrated in the hydrophobic region of the phospholipid bilayer, the surrounding lipid molecules induce them to adopt certain preferred conformations, leading to enhanced exciton coupling. For example, a flexible chiral molecule with two chromophores attached may exhibit no CD signal in solution, but when embedded in a membrane, it may exhibit a large CD signal that can be used to assign its absolute stereochemistry.[18]

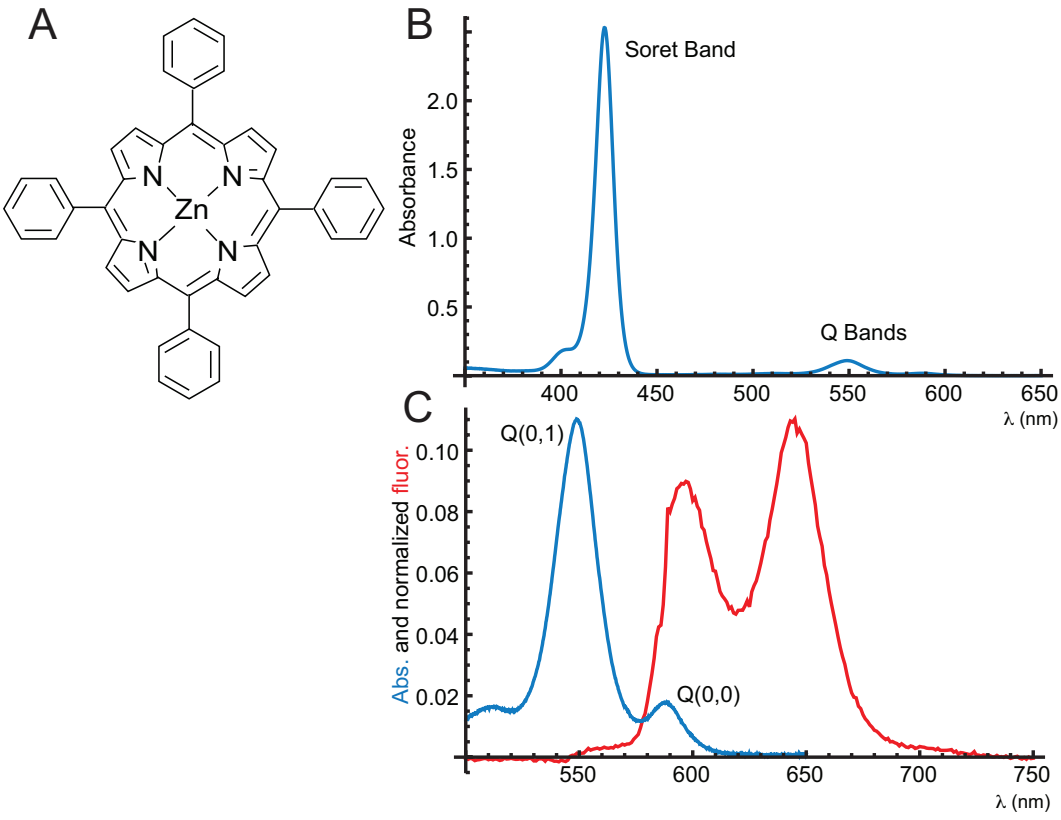

Figure 1.3. Optical properties of porphyrins. (A) The structure of zinc tetraphenylporphyrin (ZnTPP). (B) The linear absorption spectrum of ZnTPP in toluene, showing the Soret band and the Q bands. (C) Closeup of the Q bands of ZnTPP, showing the Q(0,1) and Q(0,0) vibronic progression of absorption bands (blue), and the corresponding vibronic progression in the emission spectrum (red).

Liposomes are spherical vesicles composed of phospholipid bilayers, and present a convenient platform in which to study the principles of membrane physical chemistry. In addition, they have been used for drug delivery due to their ability to transport both hydrophilic (in the encapsulated aqueous solution) and hydrophobic (in the lipid region of the membrane) molecules, and they can be used as simple models for cells.[19] Liposomes exhibit phase transitions as a function of temperature. Depending on lipid composition, liposomes undergo a gel to liquid crystal transition at temperatures ranging from -70 to 80°C.[20] The presence of unsaturated lipids and membrane additives like cholesterol act to increase membrane fluidity and decrease the phase transition temperature.

5. DNA Labeled with Cyanine Dyes and Fluorescent Base Analogues

Being the carrier of genetic information in cells, DNA is central to processes such as transcription and replication, in which one DNA strand is used as a template for the synthesis of a new strand of RNA or DNA. Additional processes include the repair of damaged DNA and the packaging of DNA into chromatin. Each of these involves numerous protein-DNA interactions that depend in different ways on the local conformation and dynamics of the DNA. Understanding these processes therefore requires probes that are sensitive to DNA conformation and dynamics. In this dissertation, I describe experiments utilizing cyanine dyes and fluorescent base analogues to study DNA conformation and protein-DNA interactions.

A. Cyanine Dyes

Chapter IV describes experiments investigating DNA labeled with the cyanine dyes Cy3 and Cy5 (structure shown in Figure 1.4A). Cyanine dyes are widely used as

labels for nucleic acids and proteins in single molecule spectroscopy[21] and fluorescence microscopy. Cy3 and Cy5 are commonly used as a fluorescence resonance energy transfer (FRET) pair, taking advantage of the distance dependence of energy transfer from Cy3 to Cy5. Cyanine dyes are usually connected to DNA via a flexible linker attached to a thymine base. In the studies presented in this dissertation, however, they are 'internally labeled' by incorporating the dye into the phosphodiester backbone.[21]

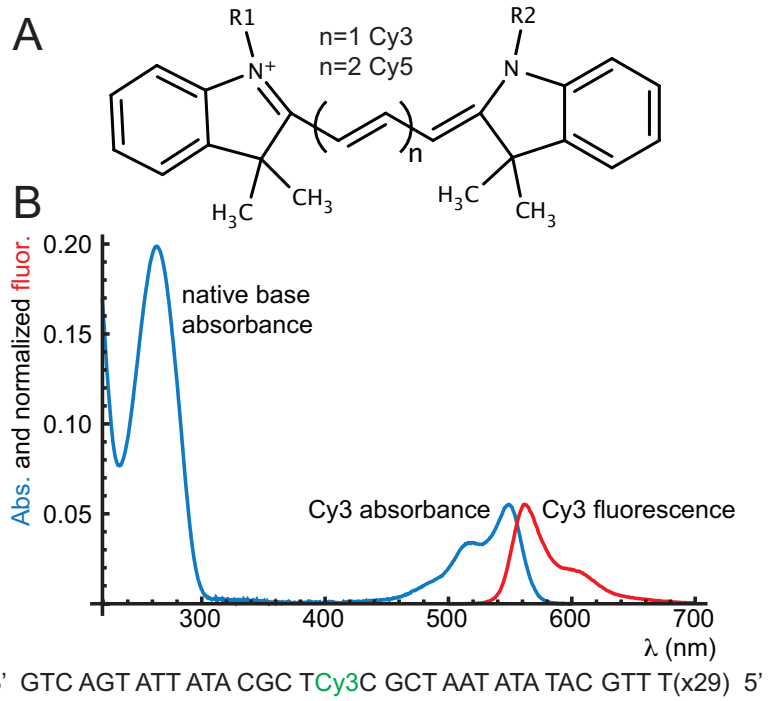

Figure 1.4. Spectra of cyanine-labeled DNA. (A) The structures of the "Cy" series of dyes. Cy3 has three carbons bridging the two ring structures, while Cy5 has five. (B) The absorption spectrum of a single-stranded DNA construct labeled with Cy3 (blue) and its emission spectrum when excited in the Cy3 band (red). The sequence of the DNA construct is shown below the spectra.

The spectra of cyanine dyes are dominated by a vibrational progression at low energy (the wavelength at which this progression occurs is determined by the length of the chain linking the two ring structures: three carbons for Cy3 and five for Cy5). This

vibrational progression is mirrored in the fluorescence spectrum (Figure 1.4B). Cyanine dyes self-assemble in solution, forming dimers and eventually extended aggregates as the concentration is increased.[22] These aggregates exhibit very strong exciton coupling due to the exceptionally strong oscillator strengths of the dyes. In Chapter IV, I report similar changes when two Cy3 residues are placed at close proximity in DNA, and I take advantage of these changes to study the effect of gp41 and gp61 (see Figure 1.1) binding on the DNA conformation.

B. Fluorescent Base Analogues

A disadvantage of using cyanine dyes to study DNA structure and dynamics is that their structures do not resemble those of any component of the DNA. Therefore, it is inevitable that they disrupt the DNA structure to some degree. Fluorescent base analogues are modified nucleic acid bases that base pair with their usual partners (Figure 1.5A), but exhibit desirable spectroscopic properties like redshifted absorption (allowing them to be excited selectively) and a fluorescence quantum yield that depends on the local conformation. Because they closely resemble native bases, base analogues are expected to perturb the DNA structure minimally and to report on the conformations of the bases they replace. In addition, base analogues can be site specifically placed at positions of interest, such as in a protein binding sequence, in order to gain information about the conformation at a specific position in the DNA.

Extensive experiments have used fluorescence intensity and CD to investigate the conformations of DNA labeled with two adjacent fluorescent base analogues, taking advantage of the conformation dependence of exciton coupling between the two probes.[11-12, 23-24] Chapter V applies 2D FS to a simple system of this type, investigating

the conformation of a dinucleotide of the fluorescent adenine analogue 2-aminopurine (structure shown in Figure 1.5A).[13] These experiments pave the way for future experiments utilizing 2D FS to study the role of local DNA conformation in processes like replication and transcription.

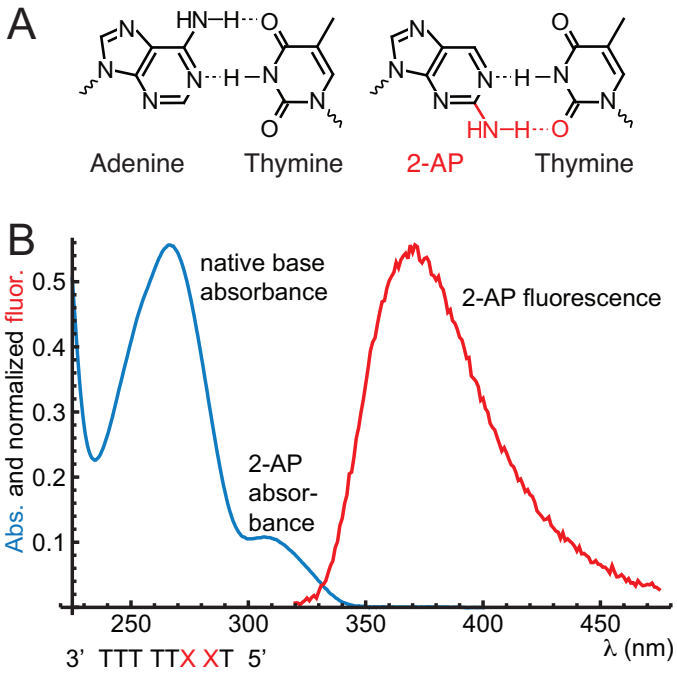

Figure 1.5. Structure and spectra of the fluorescent base analogue 2-aminopurine (2-AP). (A) Comparison of the structures and hydrogen-bonding arrangements of adenine and 2-AP.[13] (B) The absorption (blue) and emission (red) spectra of a single-stranded DNA construct labeled with two adjacent 2-AP residues. The sequence of the DNA construct is shown below the spectra, with 2-AP residues indicated by the letter X.

6. Outline and Acknowledgement of Contributions by Others to this Dissertation

This dissertation describes research done in the lab of Dr. Andrew Marcus, with whom the experiments and calculations were co-developed and the material was co-written. This dissertation also includes the contributions of numerous co-workers and collaborators.

Chapter II presents the theory for the spectroscopy of an exciton-coupled molecular dimer, and contains material co-authored with A. Perdomo-Ortiz, G. A. Lott, A. Aspuru-Guzik and A. H. Marcus.[9] We define a Hamiltonian for a system of two coupled two-level or three-level systems and use this to calculate linear absorption and circular dichroism signals, as well as the time-dependent nonlinear signals measured in 2D FS. The three-level system model calculations were performed by A. Perdomo-Ortiz.

Chapter III presents measurements on a tethered dimer of zinc tetraphenylporphyrin embedded in a phospholipid membrane, and contains material co-authored with W. Lee, A. Perdomo-Ortiz, D. Rappoport, T. F. Molinski, A. Aspuru-Guzik and A. H. Marcus.[10] In these experiments, a variety of spectroscopic techniques were utilized to measure the thermodynamics of interconversion between two different dimer conformations. In this work, the fluorometry was performed by W. Lee, and the data fitting procedure was developed by A. Perdomo-Ortiz. D. Rappoport performed the UFF structure optimizations, and the zinc porphyrin dimer was synthesized by the lab of T. F. Molinski.

Chapter IV presents studies of the conformations adopted by cyanine-labeled DNA, and it contains unpublished material co-authored with A. H. Marcus and P. H. von Hippel. We present proof-of-principle "FRET-filtered 2D FS" experiments in which the 2D FS signal was filtered in order to detect emission only from the fluorophore that was excited, or from an acceptor fluorophore to which the excitation had been transferred. Other spectroscopic techniques are used to study the conformations adopted by cyanine-labeled forked DNA in the presence of the bacteriophage T4 proteins gp41 (helicase) and gp61 (primase).

Chapter V discusses the adaptation of the 2D FS experiment for the study of ultraviolet chromophores, and contains material co-authored with N. P. Johnson, P. H. von Hippel and A. H. Marcus.[13] We present the technique of site-specifically labeling DNA with fluorescent base analogues such as the adenine analogue 2-aminopurine in order to study the local conformations and fluctuations of the DNA. 2D FS is used to determine the conformation of 2-aminopurine dinucleotide. The application of 2D FS to fluorescent base analogues was conceived in collaboration with A. H. Marcus, and builds on earlier experiments by N. P. Johnson and P. H. von Hippel.

Chapter VI presents the theory for excited state population transfer in exciton-coupled molecular dimers and contains material co-authored with A. Perdomo-Ortiz, G. A. Lott, A. Aspuru-Guzik and A. H. Marcus.[9] This theory is applied to a dimer of magnesium tetraphenylporphyrin embedded in a membrane. For this system, G. A. Lott recorded the experimental data and A. Perdomo-Ortiz did the conformational modeling. I also present unpublished results investigating spectral diffusion and population transfer in membrane supported ZnTPP dimers, work which was performed in collaboration with A. H. Marcus.

Chapter VII includes model calculations for a proposed experiment that would use entangled photons as the excitation source for 2D FS, and contains material co-authored with M. G. Raymer, A. H. Marcus and D. L. P. Vitullo.[14] M. G. Raymer and A. H. Marcus incorporated entanglement into the theoretical framework for 2D FS with the assistance of D. L. P. Vitullo, and I performed calculations investigating the effects of using entangled photons on the spectroscopy of an exciton-coupled dimer.

CHAPTER II

THEORY FOR THE SPECTROSCOPY OF EXCITON-COUPLED MOLECULAR DIMERS

1. Overview

As an overview of the theory that will be used throughout this dissertation, I present an excerpt from Perdomo-Ortiz, A.; Widom, J. R.; Lott, G. A.; Aspuru-Guzik, A.; Marcus, A. H. Conformation and Electronic Population Transfer in Membrane-Supported Self-Assembled Porphyrin Dimers by 2D Fluorescence Spectroscopy. *J. Phys. Chem. B.* **2012**, *116*, 10757-10770. This excerpt was co-written with Drs. G. A. Lott, A. Perdomo-Ortiz and Andrew Marcus and contains a derivation of the equations used to model 2D FS signals as well as model calculations using a two-dipole model (performed by me) and a four-dipole model (performed by A. Perdomo-Ortiz). It also includes an extensive comparison of 2D FS to the more common technique of 2-dimensional electronic spectroscopy (2D ES). This theory will be discussed in the context of self-assembled magnesium tetraphenylporphyrin (MgTPP) dimers, although this chapter will not present any experimental results. The remainder of the article from which this chapter is derived will be presented in Chapter VI as part of the discussion of excited state dynamics.

2. Introduction

The spontaneous assembly of aromatic and hetero-aromatic groups into structured, non-covalent oligomers is an example of molecular ‘stacking’ interactions, which are of central importance to the stability of macromolecular complexes such as

DNA, light harvesting antennas, and viruses.[25-29] Complexes composed of porphyrin chromophores, in particular, are ubiquitous to biochemical processes that involve electronic charge or energy transport. For example, the chlorosomes of green sulfur bacteria contain hundreds of thousands of bacterio-chlorophyll pigments, which self-assemble into ordered arrays that extend for hundreds of nanometers.[30-32] The remarkable efficiency with which these structures direct electronic excitation energy to photosynthetic reaction centers suggests the possibility to develop self-assembly strategies for new molecular electronics technologies.[30, 33-34] Such approaches aim to tailor electronic properties, such as state-to-state couplings, coherence lengths, and transition rates, by controlling inter-molecular conformation.

Given the direct connection between the electronic properties of a molecular complex and its architecture, experiments that simultaneously probe conformation-dependent electronic couplings and excited state dynamics can provide new insights to structure-property relationships. In this paper, we use two-dimensional fluorescence spectroscopy (2D FS) to determine the three-dimensional spatial conformation and femtosecond population transfer dynamics of magnesium meso tetraphenylporphyrin dimers [$(MgTPP)_2$], which self-assemble in the non-polar region of a phospholipid bilayer membrane. It has been established that by using membranes to induce chromophore assembly, it is possible to exert a moderate level of control over structural parameters, such as the degree of oligomerization, the placement of the porphyrins within different dielectric regions of the membrane, and the inter-chromophore conformation.[26] Related membrane-porphyrin systems have appeared in the literature, including biomimetic models for mitochondrial electron transport reactions,[26] drug delivery

vehicles for photo-dynamic cancer therapies,[35-36] and platforms for artificial light harvesting devices.[37]

In such membrane-porphyrin systems, the hydrophobic MgTPP monomers enter the aliphatic region of the phospholipid bilayer, and at elevated concentration the monomers self-assemble into dimers.[8] Within the membrane environment the dimer adopts a preferred conformation, in which the exciton-coupling strength exceeds the spectral width of site energy disorder. The stability of the dimer is sufficient to offset the loss of translational entropy of each monomer subunit, in addition to the disruption of favorable interactions between phospholipid acyl chains and the porphyrin macrocycles. A central issue pertains to the nature of the dimer stability. One possibility is that dimerization is driven by the formation of favorable monomer-monomer interactions, while an alternative picture attributes dimer stability to an increase in entropy resulting from the release of phospholipid acyl chains from their MgTPP contacts. Although a precise determination of the thermodynamic forces of dimerization is beyond the scope of the current study, an indication of the role played by the local membrane environment can be gleaned from the relative 'compactness' of the dimer conformation. For example, a relatively open structure, which does not maximize monomer-monomer surface contacts, would suggest that membrane-mediated dimer assembly is primarily entropy driven.

Here we present a general framework to describe how porphyrin dimer conformation and electronic population transfer can be elucidated using 2D FS. Although we focus here on one specific membrane supported $(MgTPP)_2$ system, our approach can be similarly applied to any electronically coupled dimer-solvent system. The electronic

states of adjacent MgTPP subunits couple through electronic interactions, which under conditions of moderate disorder leads to delocalization of the exciton-coupled states and splitting of the energy levels.[38] 2D FS is a variation of two-dimensional electronic spectroscopy (2D ES) that employs a sequence of four collinear femtosecond optical pulses to resonantly excite exciton-coupled states, and which probes correlations between successive optical transitions.[39] The 2D FS experiment monitors fluorescence, which is proportional to the fourth-order electronically excited populations induced by the four-pulse sequence.[8] A phase-modulation lock-in detection scheme is used to obtain phase-sensitive spectroscopic information.[4, 40] In contrast, the primary observable associated with 2D ES is the third-order polarization excited by three incident non-collinear pulses, which is phase-sensitively detected using a wave vector-matched geometry. This fundamental difference between the two methods can lead to 2D spectra with very different appearances.

The remainder of this chapter is organized in the following manner. In section 3, we review theoretical models to describe exciton-coupled molecular dimers, in which individual monomer sites can support either one or two degenerate electronic transitions. In section 4, we present a theoretical framework to describe 2D FS experiments that probe dimer conformation (zero population time limit) and electronic energy transport (non-zero population time). The relationship between 2D FS and 2D ES methods is established. In the remaining chapters of this dissertation, the theoretical results presented here are applied to analyze the spectra of porphyrin dimers and nucleic acids.

3. Models for Exciton-Coupled Dimers

Monomers of MgTPP have two equivalent perpendicular transition dipole moments contained within the plane of the porphyrin macrocycle (see Figure 2.1A, *Inset*). These define the directions of degenerate Q_x and Q_y transitions between ground and lowest lying excited states.[17, 41-43] Both transition moments contribute to the collective exciton interactions in a molecular complex. To specify dimer conformations, we adopt a molecular-frame coordinate system similar to that described in refs. [41] and [42] and which is depicted in Figure 2.1A. For each monomer, a right-handed coordinate system is taken with the *x* and *y* axes lying parallel to the Q_x and Q_y transition directions, and the *z* axis perpendicular to the porphyrin plane. A conformation is specified by the monomer center-to-center vector $\vec{R}$, which is oriented relative to molecule 1 according to the polar and azimuthal angles θ and ϕ, respectively. The relative orientation of molecule 2 is given by the Euler angles α and β. Because of the degeneracy of the Q_x and Q_y transitions, all exciton interactions are independent of the third Euler angle γ, we set to zero for all of our subsequent considerations.[42]

The Hamiltonian for a dimer of chemically identical *n*-level molecules, in which system-bath interactions are neglected, can be written

$$\hat{H} = \hat{H}^{(1)} + \hat{H}^{(2)} + \hat{V} = \hat{H}_0 + \hat{V} \tag{2.1}$$

where $\hat{H}^{(1)}$ $\left[\hat{H}^{(2)}\right]$ is the Hamiltonian associated with monomer 1 (monomer 2).

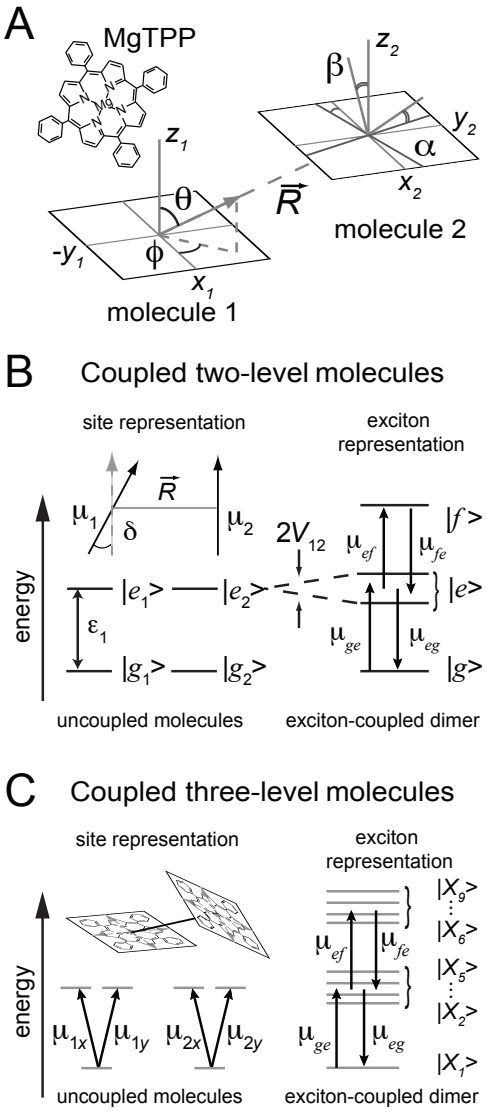

Figure 2.1. (A) Coordinate system used to describe two MgTPP monomers, whose relative conformation is defined by the molecular center-to-center vector ***R*** and the angles θ, ϕ, α and β. (*Inset*) Molecular formula for the MgTPP monomer. (B) Energy level diagram of two chemically identical two-level molecules. (*Inset*) An example configuration with relative transition dipole angle δ. Electronic interactions result in an exciton coupled four-level dimer with a single ground state, two singly-excited states, and a single doubly-excited state. Multi-pulse excitation can excite transitions between ground, singly-excited and doubly-excited state manifolds. The conformation of the dimer determines the energy level spacing and the strengths of the transitions. (C) Energy level diagram of two chemically identical three-level molecules, each with degenerate transition dipole moments directed along the x and y axes of the molecular frames. (*Inset*) An example configuration of a $(MgTPP)_2$ dimer. Electronic interactions result in an exciton-coupled nine-level system, with a single ground state, four singly-excited states, and four doubly-excited states. Exciton states are labeled $|X_1\rangle ... |X_9\rangle$.

Within the point-dipole approximation, the electronic coupling can be expressed

$$\hat{V} = \frac{1}{4\pi\varepsilon_0 R^3}\hat{\mu}_1(1-3\frac{\vec{R}\vec{R}}{R^2})\hat{\mu}_2 \tag{2.2}$$

where $\vec{R}$ is the inter-monomer center-to-center vector, $\hat{\mu}_1$ ($\hat{\mu}_2$) the dipole operator for monomer 1 (monomer 2), and ε_0 is the vacuum permittivity. Although more accurate electronic coupling models can be readily implemented, the point-dipole approximation is a useful starting point for our calculations.

A. Dimer of Two-Level Molecules (Coupled Two-Dipole Model)

We first consider the simplest case in which each monomer subunit supports a single electronic transition with energy ε_1. In Figure 2.1B (*Inset*), we illustrate two transition dipole moments, $\vec{\mu}_1$ and $\vec{\mu}_2$, with relative angle δ. In the exciton representation, the effect of the electronic coupling is to create a four-level system comprised of a common ground state $|g\rangle$, two non-degenerate singly-excited states $|\pm\rangle$ with $\varepsilon_\pm = \varepsilon_1 \pm V_{12}$ (referred to as the $|e\rangle$ state manifold), and a doubly-excited state $|f\rangle$ with $\varepsilon_f \cong 2\varepsilon_1$ (see Figure 2.1B). The coupling strength V_{12} is determined by the transition dipole moment magnitude $|\mu|^2$ and dimer conformation according to eq 2.2 (see SI section for details). The singly-excited states are related to the site basis according to $|\pm\rangle = \frac{1}{\sqrt{2}}\left[|e\rangle|g\rangle \pm |g\rangle|e\rangle\right]$. We define the tensor product states $|ij\rangle$ where $i,j = g,e$. $|ij\rangle$ respectively label the states on monomer 1 and 2, and $\{|ij\rangle\}$ is the dimer Hilbert space basis. Notice $g(e)$ is shorthand notation for the ground (excited) electronic state

associated with each monomer. These symmetric and anti-symmetric states have wave functions delocalized among the chromophore sites. The collective transition dipole moments between ground and singly-excited states are given by $\hat{\mu}_{\pm} = \frac{1}{2}\left[\hat{\mu}_1 \pm \hat{\mu}_2\right]$, which can be written $\hat{\mu}_{\pm} = \frac{|\mu|}{\sqrt{2}}\left[\boldsymbol{x}(\cos\delta \pm 1) + \boldsymbol{y}\sin\delta\right]$, where we have taken $\hat{\mu}_1$ to be oriented along the *x*-axis and $\hat{\mu}_2$ contained within the *x*-*y* plane. Moreover, the transition dipole moments that mediate excited state absorption between singly- and doubly-excited states are $\hat{\mu}_{+f} = \hat{\mu}_+$, and $\hat{\mu}_{-f} = -\hat{\mu}_-$. The intensities of ground-state accessible transitions depend on the relative orientation of the dipoles in the complex. For example, an H-type configuration *i.e.* $\uparrow\uparrow$ with $\delta = 0$ results in a blue-shifted absorption spectrum, while a J-type configuration *i.e.* $\rightarrow\rightarrow$ results in a red-shifted spectrum.[38] The effect of non-zero δ is to partition intensity to the otherwise dipole forbidden transition, according to $I_{\pm} = |\mu|^2 (1 \pm \cos\delta)$.

B. Dimer of Three-Level Molecules (Coupled Four-Dipole Model)

For a dimer of chemically identical three-level molecules, we define the tensor product states $\{|ij\rangle\}$ where $i, j = g, x, y$ respectively label the states on monomer 1 and 2, and $\{|ij\rangle\}$ is the dimer Hilbert space basis. Notice x (y) is shorthand notation for the excited electronic state associated with the Q_x (Q_y) transition on each monomer.

We simplify our notation by denoting the nine basis states $\{|l_i\rangle\}$, with $|l_1\rangle = |gg\rangle$, $|l_2\rangle = |xg\rangle$, $|l_3\rangle = |yg\rangle$, $|l_4\rangle = |gx\rangle$, $|l_5\rangle = |gy\rangle$, $|l_6\rangle = |xx\rangle$, $|l_7\rangle = |xy\rangle$, $|l_8\rangle = |yx\rangle$ and

$|l_9\rangle = |yy\rangle$. In this basis, the total Hamiltonian can be written as a nine-by-nine matrix of the form[41]

$$H \approx \begin{bmatrix} 0 & & & & & & & & \\ & \varepsilon_1 & V_{23} & V_{24} & V_{25} & & & & \\ & V_{32} & \varepsilon_1 & V_{34} & V_{35} & & & & \\ & V_{42} & V_{43} & \varepsilon_1 & V_{45} & & & & \\ & V_{52} & V_{53} & V_{54} & \varepsilon_1 & & & & \\ & & & & & 2\varepsilon_1 & & & \\ & & & & & & 2\varepsilon_1 & & \\ & & & & & & & 2\varepsilon_1 & \\ & & & & & & & & 2\varepsilon_1 \end{bmatrix} \tag{2.3}$$

In eq 2.3 we have assumed that $\langle l_i|\hat{V}|l_i\rangle = 0$ for all l_i, i.e. all of the diagonal contributions are associated with $\hat{H}_0$. To set the reference energy scale, we set $\varepsilon_g^{(1)} = 0$ with $\hat{H}^{(i)}|g\rangle = \varepsilon_g^{(i)}|g\rangle$, and therefore $\hat{H}_0|gg\rangle = (\varepsilon_g^{(i)} + \varepsilon_g^{(2)})|gg\rangle = 0|gg\rangle$. The value of ε_1 corresponds to the excitation energy associated with either the degenerate Q_x or Q_y transition of the uncoupled monomer. Then $\hat{H}_0|l_k\rangle = \varepsilon_k|l_k\rangle$ with $\varepsilon_k = \varepsilon_1$ for any of the states containing one excitation $(k = 2-5)$ and $\varepsilon_k = 2\varepsilon_1$ for the states containing two excitations $(k = 6-9)$. As we discuss below, we determined the value of $\bar{\nu}_1 = \varepsilon_1 / hc$ = 16,501 cm^{-1} from the linear absorption spectrum of uncoupled monomers suspended in liposomal membranes. Diagonalization of the Hamiltonian is straightforward since it involves only the 4x4 block associated with the singly excited state manifold (see Figure 2.1C). The eigen-energies of the singly excited state manifold correspond to the exciton

transitions underlying the region of interest in the experimental linear spectra. The positions and intensities of these features depend on the structural parameters of the dimer through the dependence on the couplings:

$$V_{ij} = \frac{1}{4\pi\varepsilon_0 R^3}(\vec{\mu}_1)_{ij} \cdot \left(1 - 3\frac{\vec{R}\vec{R}}{R^2}\right) \cdot (\vec{\mu}_2)_{ij} = \frac{\mu^2}{4\pi\varepsilon_0 R^3}\kappa_{ij}^2 \tag{2.4}$$

Here the orientation factor κ_{ij}^2 is related to the directions of the transition dipole moments and the vector connecting their centers according to $\kappa_{ij}^2 = (\underline{\mu}_1)_{ij} \cdot (\underline{\mu}_2)_{ij} - 3\left[(\underline{\mu}_1)_{ij} \cdot \underline{R}\underline{R} \cdot (\underline{\mu}_2)_{ij}\right]$, where $\hat{R} = (\sin\theta\cos\phi, \sin\theta\sin\phi, \cos\theta)$ is the monomer center-to-center unit vector, and $(\underline{\mu}_n)_{ij} = \langle l_i | \hat{\mu}_n | l_j \rangle / |\mu|$ is the normalized transition dipole moment operator. The relationship between the square of the monomer transition dipole moment and its absorption coefficient α, is given by

$$|\mu|^2 = \frac{3\varepsilon_0 \hbar c}{\pi N_A} \int_{-\infty}^{\infty} d\bar{\nu} \frac{\alpha(\bar{\nu})}{\bar{\nu}} \tag{2.5}$$

In eq 2.5, ε_0 is the dielectric constant, $\hbar$ is Planck's constant divided by 2π, c is the speed of light, and N_A is Avogadro's number. The factor $\int_{-\infty}^{\infty} d\bar{\nu} \frac{\alpha(\bar{\nu})}{\bar{\nu}}$ is the integrated optical line shape of the $Q(0,0)$ transition, measured in wave numbers, and divided by its frequency. We estimated this number by numerical integration of the experimental

absorption line shape to be 44.3 M^{-1} cm^{-1}, which corresponds to a value of the monomer transition dipole moment of 1.33 *D*.

4. Comparison between 2D Fluorescence and 2D Electronic Spectroscopy

2D FS and 2D ES are conceptually similar methods, yet important distinguishing factors can result in their non-equivalence. The 2D ES signal can be interpreted as the third-order polarization of the sample, which is the source of the detected signal field. In contrast, 2D FS is a technique based on fluorescence detection.[4] The signal may be considered proportional to the fourth-order excited state population. We thus compare the signals of the two methods based on interpretation of 2D ES signals using third-order perturbation theory, and 2D FS signals using fourth-order perturbation theory.

We consider the semiclassical light-matter interaction Hamiltonian,

$$\hat{H}_{SC} = \hat{H}_0 + \hat{H}_{\text{int}}(t), \text{ where } \hat{H}_{\text{int}} = -\hat{\mu} \cdot E(t) \tag{2.6}$$

In 2D FS experiments, the electric field for *P* sequential collinear pulses polarized in the *x* direction can be described by $E(t) = \boldsymbol{x}\sum_j^P E_j(t)$ where the electric field of the *j*th pulse is given by

$$E_j(t) = \lambda_j A_j(t - t_j)\cos\left[\omega_j(t - t_j) + \phi_j\right] \tag{2.7}$$

Here λ_j is the maximum intensity of the electric field, $A_j(t-t_j)=e^{-\frac{4\ln 2}{\tau_{fwhm}^2}(t-t_j)^2}$ is the temporal envelope, ω_j is the pulse frequency, and ϕ_j is its phase. In 2D ES experiments, the non-collinear pulses are analogously described by $E_j(t)=\lambda_j A_j(t-t_j)\cos\left[\omega_j(t-t_j)-\boldsymbol{k}_j\cdot\boldsymbol{r}\right]$, where the phase of the *j*th pulse depends on its wave vector $\boldsymbol{k}_j$.

Using the density matrix formulism, the evolution of the system is described by the Liouville-von Neumann equation

$$i\hbar\frac{\partial\hat{\rho}_i(t)}{\partial t}=\left[\hat{H}_{I,\text{int}},\hat{\rho}_I(t)\right] \tag{2.8}$$

written in the interaction picture, such that $\hat{\mathrm{O}}_I(t)\equiv e^{i\hat{H}_0(t-t_0)}\hat{\mathrm{O}}e^{-i\hat{H}_0(t-t_0)}$. A formal solution to eq 2.8 is

$$\hat{\rho}_I(t)=\hat{\rho}_I(t_0)+\sum_{n=1}^{\infty}\hat{\rho}_I^{(n)}(t) \tag{2.9}$$

with

$$\hat{\rho}_I^{(n)}(t)=(-1)^n\left(\frac{i}{\hbar}\right)^n\int_{t_0}^{t}d\tau_n\int_{t_0}^{\tau_n}d\tau_{n-1}\cdots\int_{t_0}^{\tau_2}d\tau_1\Big[\hat{H}_{I,\text{int}}(\tau_n),\\ \times\Big[\hat{H}_{I,\text{int}}(\tau_{n-1}),\Big[\cdots,\Big[\hat{H}_{I,\text{int}}(\tau_1),\hat{\rho}_I(t_0)\Big]\cdots\Big]\Big]\Big]. \tag{2.10}$$

The expectation of any observable, $\left\langle \hat{O}(t) \right\rangle \equiv tr\left\{ \hat{O}(t)\hat{\rho}(t) \right\} = tr\left\{ \hat{O}_I(t)\hat{\rho}_I(t) \right\}$, can be expressed as $\left\langle \hat{O}_I(t) \right\rangle \equiv \sum_{n=0}^{\infty} \left\langle \hat{O}_I^{(n)}(t) \right\rangle$ with $\left\langle \hat{O}_I^{(n)}(t) \right\rangle \equiv tr\left\{ \hat{O}_I(t)\hat{\rho}_I^{(n)}(t) \right\}$.

As mentioned previously, the 2D ES signal is associated with the third-order polarization

$$\mathbf{P}^{(3)}(t) \equiv \left\langle \hat{\mu}^{(3)}(t) \right\rangle \equiv tr\left\{ \hat{\mu}_I(t)\hat{\rho}_I^{(3)}(t) \right\}, \tag{2.11}$$

while the 2D FS signal is associated with the fourth-order excited state population,

$$\hat{A}^{(4)}(t) \equiv \left\langle \hat{A}^{(4)}(t) \right\rangle \equiv tr\left\{ \hat{A}_I(t)\hat{\rho}_I^{(4)}(t) \right\} \tag{2.12}$$

with $\hat{A} = \sum_{\upsilon} \Gamma_{\upsilon} |\upsilon\rangle\langle\upsilon|$ a projector onto all the states $\left\{ |\upsilon\rangle \right\} = \left\{ |e\rangle, |f\rangle \right\}$ of the excited state manifold, weighted by their respective fluorescence quantum yield coefficients, Γ_{υ}. Here we assume that the fluorescence quantum yield of all the singly-excited (excitonic) states are the same and equal to 1.0, i.e., $\Gamma_e = 1.0$ for all $\left\{ |e\rangle \right\}$. If we further assume that $\Gamma_f = \Gamma$ for all $\left\{ |f\rangle \right\}$, then $0 \le \Gamma \le 2$. The case of $\Gamma = 2$ corresponds to an ideal coherent case, where two photons are emitted via the pathway $|f\rangle \to |e\rangle \to |g\rangle$. In a more common scenario, one expects the relative quantum yield of the doubly excited states to be significantly smaller than for the singly-excited state, $\Gamma \approx 0$, due to the abundance of non-radiative relaxation pathways for highly excited states.

We consider the cases for which each monomer may support either one or two ground state allowed electronic transitions, as depicted in Figures 2.1B and 2.1C, respectively. As described in Sec. II above, couplings between monomer transitions result in a multi-level Hamiltonian described in the diagonal exciton basis as a single ground state $|g\rangle$, a manifold of singly-excited states $|e\rangle$, and a manifold of doubly-excited states $|f\rangle$. Signals for 2D ES and 2D FS experiments are expressed by expanding third- and fourth-order terms given by eqs 2.11 and 2.12, respectively. The 2D ES signals have been derived and studied for these dimer models.[15, 39] In Figure 2.2A, we show double sided Feynman diagrams (DSFDs) contributing to the nonrephasing (NRP) and rephasing (RP) signals, respectively, and in Figure 2.2B for the double quantum coherence (DQC) signals. In 2D ES, these signals correspond to detection in the wave vector-matched directions $\mathbf{K}_{NRP} = \boldsymbol{k}_1 - \boldsymbol{k}_2 + \boldsymbol{k}_3$, $\mathbf{K}_{RP} = -\boldsymbol{k}_1 + \boldsymbol{k}_2 + \boldsymbol{k}_3$, and $\mathbf{K}_{DQC} = \boldsymbol{k}_1 + \boldsymbol{k}_2 - \boldsymbol{k}_3$. Neglecting dissipation for the moment, and assuming the rotating wave approximation in the impulsive limit,[39] one obtains for 2D ES signals the following expressions for the nonrephasing terms:

$$\mathrm{R}_{1a}^{*} \propto \sum_{e,e'} \left[\mu_{eg}\mu_{ge}\mu_{e'g}\mu_{ge'} \right]_{\mathbf{e}_1\mathbf{e}_2\mathbf{e}_3\mathbf{e}_4} e^{-i\omega_{eg}\tau} e^{-i\omega_{e'g}t} \tag{2.13}$$

$$\mathrm{R}_{2a} \propto \sum_{e,e'} \left[\mu_{eg}\mu_{ge'}\mu_{e'g}\mu_{ge} \right]_{\mathbf{e}_1\mathbf{e}_2\mathbf{e}_3\mathbf{e}_4} e^{-i\omega_{eg}\tau} e^{-i\omega_{ee'}T} e^{-i\omega_{e'g}t} \tag{2.14}$$

and

$$\mathrm{R}_{3b}^{*} \propto \sum_{e,e',f} \left[\mu_{eg}\mu_{ge'}\mu_{fe}\mu_{e'f} \right]_{\mathbf{e}_1\mathbf{e}_2\mathbf{e}_3\mathbf{e}_4} e^{-i\omega_{eg}\tau} e^{-i\omega_{ee'}T} e^{-i\omega_{fe'}t} \tag{2.15}$$

Similarly, the rephasing terms are given by

$$\mathrm{R}_{4a} \propto \sum_{e,e'} \left[\mu_{ge}\mu_{eg}\mu_{ge'}\mu_{ge'} \right]_{\mathbf{e}_1\mathbf{e}_2\mathbf{e}_3\mathbf{e}_4} e^{-i\omega_{ge}\tau} e^{-i\omega_{e'g}t} \tag{2.16}$$

$$\mathrm{R}_{3a} \propto \sum_{e,e'} \left[\mu_{ge}\mu_{e'g}\mu_{eg}\mu_{ge'} \right]_{\mathbf{e}_1\mathbf{e}_2\mathbf{e}_3\mathbf{e}_4} e^{-i\omega_{ge}\tau} e^{-i\omega_{e'e}T} e^{-i\omega_{e'g}t} \tag{2.17}$$

and

$$\mathrm{R}^{*}_{2b} \propto \sum_{e,e',f} \left[\mu_{ge}\mu_{e'g}\mu_{fe'}\mu_{ef} \right]_{\mathbf{e}_1\mathbf{e}_2\mathbf{e}_3\mathbf{e}_4} e^{-i\omega_{ge}\tau} e^{-i\omega_{e'e}T} e^{-i\omega_{fe}t} \tag{2.18}$$

The double quantum coherence terms are given by

$$\mathrm{R}^{*}_{1b} \propto \sum_{e,e',f} \left[\mu_{eg}\mu_{fe}\mu_{e'f}\mu_{ge'} \right]_{\mathbf{e}_1\mathbf{e}_2\mathbf{e}_3\mathbf{e}_4} e^{-i\omega_{eg}\tau} e^{-i\omega_{fg}T} e^{-i\omega_{e'g}t} \tag{2.19}$$

and

$$\mathrm{R}^{*}_{4b} \propto \sum_{e,e',f} \left[\mu_{eg}\mu_{fe}\mu_{ge'}\mu_{e'f} \right]_{\mathbf{e}_1\mathbf{e}_2\mathbf{e}_3\mathbf{e}_4} e^{-i\omega_{eg}\tau} e^{-i\omega_{fg}T} e^{-i\omega_{fe'}t} \tag{2.20}$$

Here, e, e' label the states of the singly excited manifold, f labels the doubly excited states, and $\left[\mu_{ab}\mu_{cd}\mu_{jk}\mu_{lm} \right]_{\mathbf{e}_1\mathbf{e}_2\mathbf{e}_3\mathbf{e}_4}$ denotes the three-dimensional orientational average product $\left\langle (\boldsymbol{\mu}_{ab}\cdot\boldsymbol{e}_1)(\boldsymbol{\mu}_{cd}\cdot\boldsymbol{e}_2)(\boldsymbol{\mu}_{jk}\cdot\boldsymbol{e}_3)(\boldsymbol{\mu}_{lm}\cdot\boldsymbol{e}_4) \right\rangle$ where $\boldsymbol{e}_i$ is the polarization of the *i*th pulse. We calculated the above orientation factors using established methods.[15, 44] We

note that for the coupled two-dipole model, the orientation factors are simple functions of the relative dipole angle δ (see Figure 2.1B), while for the four-dipole model the orientation factors depend on all of the structural angles $\alpha, \beta, \theta,$ and ϕ (see Figure 2.1A). In the current experiments, all laser pulses have the same polarization. In eqs 2.13 – 2.20, we have adopted the convention of naming the intervals between pulses $t_2 - t_1 = \tau, t_3 - t_2 = T,$ and $t_4 - t_3 = t$. For the coupled two-level molecules depicted in Figure 2.1B, $e, e' \in \{+,-\}$ are the symmetric and anti-symmetric states. For the coupled three-level molecules of Figure 2.1C, $e, e' \in \{X_2, X_3, X_4, X_5\}$ is the singly excited manifold after diagonalization of the 4x4 block of the Hamiltonian in eq 2.3, and $f \in \{X_6, X_7, X_8, X_9\}$ is the doubly excited state manifold.

Figure 2.2 (next page). (A) Double sided Feynman diagrams (DSFDs) representing the light-matter interactions contributing to the rephasing and nonrephasing signals measured experimentally by 2D ES (top row) and by 2D FS (bottom row). The four- and nine-level models used to describe coupled dimers are shown in Figures 2.1B and 2.1C, respectively. The collective dipole moment allows transitions from the ground state to the singly-excited manifold, and from the latter to the final doubly-excited state. The sign associated with each diagram is determined by the number of arrows (dipole interactions) on the right vertical line of each ladder diagram ("bra" side). An even (odd) number of interactions picks up a positive (negative) sign for the term under consideration. The nonrephasing and rephasing 2D ES signals are $S_{NRP}^{2DES}(\tau,T,t) \propto \mathrm{R}_{1a}^{*} + \mathrm{R}_{2a} - \mathrm{R}_{3b}^{*}$ and $S_{RP}^{2DES}(\tau,T,t) \propto \mathrm{R}_{4a} + \mathrm{R}_{3a} - \mathrm{R}_{2b}^{*}$, respectively. The corresponding 2D FS signals are $S_{NRP}^{2DFS}(\tau,T,t) \propto -(\mathrm{Q}_{5a}^{*} + \mathrm{Q}_{2a} + \mathrm{Q}_{3b}^{*} - \Gamma\mathrm{Q}_{7b})$ and $S_{RP}^{2DFS}(\tau,T,t) \propto -(\mathrm{Q}_{4a} + \mathrm{Q}_{3a} + \mathrm{Q}_{2b}^{*} - \Gamma\mathrm{Q}_{8b}^{*})$. The parameter Γ accounts for different quantum yields between doubly- and singly-excited state manifolds. (B) DSFDs contributing to the double quantum coherence signals measured by 2D ES (top row) and 2D FS (bottom row). The 2D ES signal is $S_{DQC}^{2DES}(\tau,T,t) \propto \mathrm{R}_{1b}^{*} - \mathrm{R}_{4b}^{*}$, whereas the 2D FS signal is $S_{DQC}^{2DFS}(\tau,T,t) \propto -(\mathrm{Q}_{5b}^{*} + \mathrm{Q}_{4b}^{*} - \Gamma\mathrm{Q}_{6b})$.

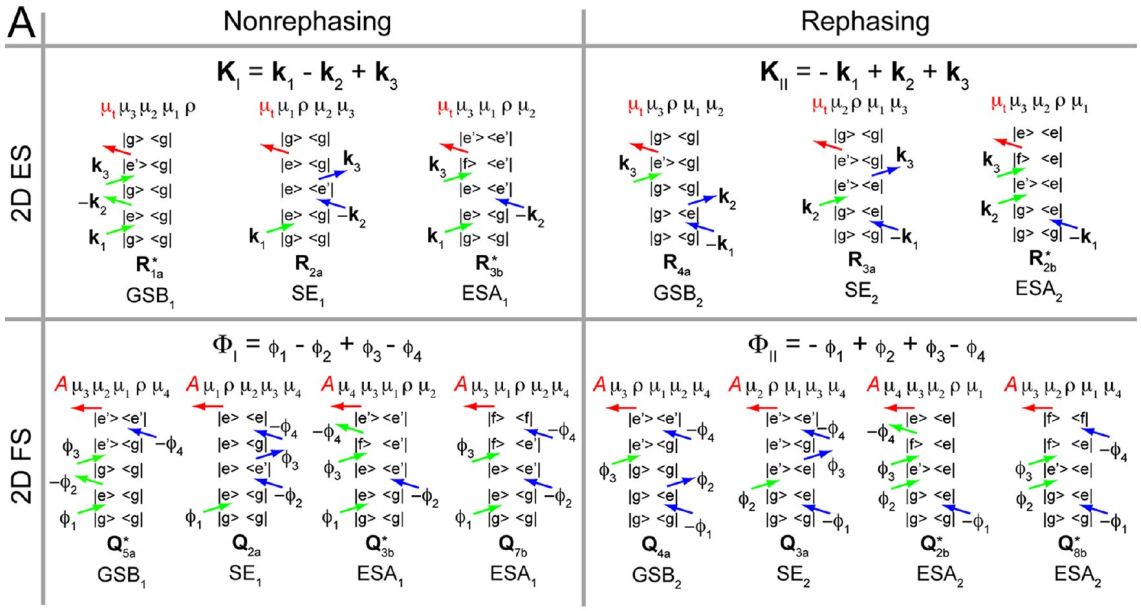
A
Nonrephasing
Rephasing
2D ES
2D FS
$\mathbf{K}_{I} = \mathbf{k}_1 - \mathbf{k}_2 + \mathbf{k}_3$
$\mathbf{K}_{II} = -\mathbf{k}_1 + \mathbf{k}_2 + \mathbf{k}_3$
$\Phi_{I} = \phi_1 - \phi_2 + \phi_3 - \phi_4$
$\Phi_{II} = -\phi_1 + \phi_2 + \phi_3 - \phi_4$
$\mathbf{R}^{*}_{1a}$ GSB$_1$
$\mathbf{R}_{2a}$ SE$_1$
$\mathbf{R}^{*}_{3b}$ ESA$_1$
$\mathbf{R}_{4a}$ GSB$_2$
$\mathbf{R}_{3a}$ SE$_2$
$\mathbf{R}^{*}_{2b}$ ESA$_2$
$\mathbf{Q}^{*}_{5a}$ GSB$_1$
$\mathbf{Q}_{2a}$ SE$_1$
$\mathbf{Q}^{*}_{3b}$ ESA$_1$
$\mathbf{Q}_{7b}$ ESA$_1$
$\mathbf{Q}_{4a}$ GSB$_2$
$\mathbf{Q}_{3a}$ SE$_2$
$\mathbf{Q}^{*}_{2b}$ ESA$_2$
$\mathbf{Q}^{*}_{8b}$ ESA$_2$

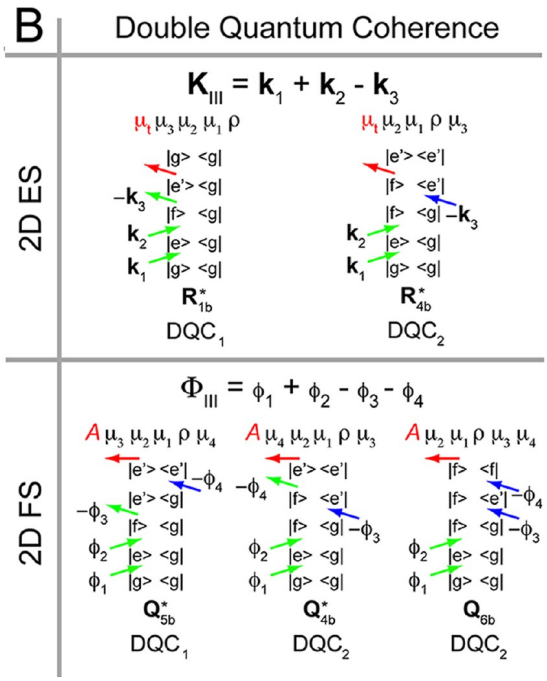
B
Double Quantum Coherence
2D ES
2D FS
$\mathbf{K}_{III} = \mathbf{k}_1 + \mathbf{k}_2 - \mathbf{k}_3$
$\Phi_{III} = \phi_1 + \phi_2 - \phi_3 - \phi_4$
$\mathbf{R}^{*}_{1b}$ DQC$_1$
$\mathbf{R}^{*}_{4b}$ DQC$_2$
$\mathbf{Q}^{*}_{5b}$ DQC$_1$
$\mathbf{Q}^{*}_{4b}$ DQC$_2$
$\mathbf{Q}_{6b}$ DQC$_2$

For 2D FS, the signals are phase-synchronously detected with respect to the modulated laser fields, and are separated according to $\Phi_{NRP} = -(\phi_1 - \phi_2 + \phi_3 - \phi_4)$, $\Phi_{RP} = -(-\phi_1 + \phi_2 + \phi_3 - \phi_4)$, and $\Phi_{DQC} = \phi_1 + \phi_2 - \phi_3 - \phi_4$.[4, 8] In Figure 2.2A are shown the 2D FS nonrephasing and rephasing DSFDs obtained from the fourth-order perturbation expansion given by eq 2.12. In Figure 2.2B are shown the analogous DSFDs for the double quantum coherence terms. In contrast to 2D ES, the DSFDs for 2D FS all terminate with excited population in either the $|e\rangle$-state or $|f\rangle$-state manifolds. Nevertheless, there is a direct correspondence between 2D ES and 2D FS signal terms. It is easy to see that for the case of nonrephasing contributions, the following relations hold: $\mathrm{R}_{1a}^{*} = \mathrm{Q}_{5a}^{*} \equiv \mathrm{GSB}_1$, $\mathrm{R}_{2a} = \mathrm{Q}_{2a} \equiv \mathrm{SE}_1$, $\mathrm{R}_{3b}^{*} = \mathrm{Q}_{3b}^{*} \equiv \mathrm{ESA}_1$, and also that $\mathrm{Q}_{3b}^{*} = \mathrm{Q}_{7b}$. For the rephasing contributions, we have $\mathrm{R}_{4a} = \mathrm{Q}_{4a} \equiv \mathrm{GSB}_2$, $\mathrm{R}_{3a} = \mathrm{Q}_{3a} \equiv \mathrm{SE}_2$, $\mathrm{R}_{2b}^{*} = \mathrm{Q}_{2b}^{*} \equiv \mathrm{ESA}_2$, and that $\mathrm{Q}_{2b}^{*} = \mathrm{Q}_{8b}^{*}$. For double quantum coherence contributions, we have $\mathrm{R}_{1b}^{*} = \mathrm{Q}_{5b}^{*} \equiv \mathrm{DQC}_1$, $\mathrm{R}_{4b}^{*} = \mathrm{Q}_{4b}^{*} \equiv \mathrm{DQC}_2$, and $\mathrm{Q}_{4b}^{*} = \mathrm{Q}_{6b}$.

The nonrephasing, rephasing, and double quantum coherence 2D ES signals are written:

$$\begin{aligned} S_{NRP}^{2DES}(\tau,T,t) &\propto \mathrm{R}_{1a}^{*} + \mathrm{R}_{2a} - \mathrm{R}_{3b}^{*} \\ &\propto \mathrm{GSB}_1 + \mathrm{SE}_1 - \mathrm{ESA}_1, \end{aligned} \tag{2.21}$$

$$\begin{aligned} S_{RP}^{2DES}(\tau,T,t) &\propto \mathrm{R}_{4a} + \mathrm{R}_{3a} - \mathrm{R}_{2b}^{*} \\ &\propto \mathrm{GSB}_2 + \mathrm{SE}_2 - \mathrm{ESA}_2, \end{aligned} \tag{2.22}$$

$$S_{DQC}^{2DES}(\tau,T,t) \propto \mathrm{R}_{1b}^{*} - \mathrm{R}_{4b}^{*}$$
$$\propto \mathrm{DQC}_1 - \mathrm{DQC}_2 \,. \tag{2.23}$$

There are two key differences between 2D ES and 2D FS that lead to non-equivalence of the two methods:

1. Since the 2D FS experiment is based on fluorescence detection, it is important to consider the nature of the resulting excited state of the system after its interaction with the four ultrafast pulses. Consequently, we must consider the relative impact of terms ending in the doubly excited state $|f\rangle$ to those ending in the singly excited manifold $\{|e\rangle\}$. Even though mathematically we have $\mathrm{Q}_{3b}^{*} = \mathrm{Q}_{7b}$, $\mathrm{Q}_{2b}^{*} = \mathrm{Q}_{8b}^{*}$, and $\mathrm{Q}_{4b}^{*} = \mathrm{Q}_{6b}$, these terms do not contribute equally because the terms Q_{6b}, Q_{3b}^{*}, and Q_{4b}^{*} end up in the singly excited manifold, while the terms Q_{7b}, Q_{8b}^{*}, and Q_{6b} end up in the doubly excited state. Since the quantum yields of singly and doubly excited states are generally different, we must account for this fact when simulating the signals. We therefore introduce a multiplicative factor Γ in front of the diagrams ending in a doubly excited population (see Q_{7b}, Q_{8b}^{*}, and Q_{6b} in Figure 2.2A and 2.2B) to capture the relative quantum yield of this doubly-excited state compared to the singly excited states. Due to the abundance of non-radiative relaxation pathways for highly excited states, one expects the relative quantum yield of the doubly excited states to be significantly smaller than for the singly excited states. In a fully ideal

coherent case, where two photons are emitted via the pathway $|f\rangle \rightarrow |e\rangle \rightarrow |g\rangle$, then $\Gamma = 2$. In general, we expect at least partial self-quenching of the doubly excited state for systems in contact with a thermal environment, such that $0 \leq \Gamma \leq 2$. As discussed further below, for the dimer studied in the current work, the value $\Gamma = 0.31$ was obtained from a global optimization analysis that compared simulated to experimental spectra.[8] A visual illustration of these differences is presented in Figures 2.3 and 2.4, where we compare for several different conformations 2D FS spectra (with $\Gamma = 0.31$) to the corresponding 2D ES spectra (with $\Gamma = 2$).

2. The GSB, SE, ESA, and DQC terms add up differently for 2D ES and 2D FS. This is a consequence of the third-order versus fourth-order perturbation approach, respectively. This is the primary reason for the different appearances of 2D FS versus 2D ES spectra.

After accounting for the differences between the two methods addressed in points 1 and 2 above, the 2D FS signals are written:

$$\begin{aligned} S_{NRP}^{2DFS}(\tau,T,t) &\propto -(\mathrm{Q}_{5a}^{*} + \mathrm{Q}_{2a} + \mathrm{Q}_{3b}^{*} - \Gamma \mathrm{Q}_{7b}) \\ &\propto -\left[\mathrm{GSB}_1 + \mathrm{SE}_1 + (1-\Gamma)\cdot \mathrm{ESA}_1\right], \end{aligned} \tag{2.24}$$

$$S_{RP}^{2DFS}(\tau,T,t) \propto -(\mathrm{Q}_{4a}+\mathrm{Q}_{3a}+\mathrm{Q}_{2b}^{*}-\Gamma\mathrm{Q}_{8b}^{*})$$
$$\propto -\left[\mathrm{GSB}_2+\mathrm{SE}_2+(1-\Gamma)\cdot\mathrm{ESA}_2\right], \tag{2.25}$$

$$S_{DQC}^{2DFS}(\tau,T,t) \propto -(\mathrm{Q}_{5b}^{*}+\mathrm{Q}_{4b}^{*}-\Gamma\mathrm{Q}_{6b})$$
$$\propto -\left[\mathrm{DQC}_1+(1-\Gamma)\cdot\mathrm{DQC}_2\right]. \tag{2.26}$$

Although the signal expressions corresponding to the two methods are closely related, the variable sign contribution of the ESA and DQC_2 terms in the 2D FS expressions (eqs 2.24 – 2.26), in comparison to the well-known negative sign ESA contributions and DQC relationships[45] in 2D ES spectroscopy (eqs 2.21 – 2.23), can lead to considerable differences in the appearance of 2D spectra. We emphasize that the differences in sign assignments between these terms arises from the commutator expansions of eq 2.10.

We first consider the case where the interval between the second and third pulses, the so-called population time T, is equal to zero. In this limit, the 2D spectral line shape should depend predominantly on the static energy level structure of the exciton-coupled dimer, with little contribution from electronic population transfer. To account for optical dephasing, inhomogeneous broadening, and other dissipative processes, we multiply each term given by eqs 2.21 – 2.26 by a phenomenological line-broadening function, which is assumed to be Gaussian with respect to both coherence times, τ and t. That is, the rephasing signals are multiplied by the factors e^{τ^2/σ_{RP}^2} and e^{t^2/κ_{RP}^2}. Similarly, we use factors containing the parameters σ_{NRP}^2 (σ_{DQC}^2) and κ_{NRP}^2 (κ_{DQC}^2) to describe the

broadening of the nonrephasing (double quantum coherence) optical line-shapes. Fourier transformation of these equations to the ω_τ and ω_t domains provides the complex-valued 2D spectra $S_{NRP}^{2DFS}(\omega_\tau, T, \omega_t)$ (with similar expressions for rephasing and double quantum coherence spectra). Complex-valued rephasing and non-rephasing spectra were summed to construct the total correlation spectra (TCS), according to $S_{NRP}^{2DFS}(\omega_\tau, T, \omega_t) + S_{RP}^{2DFS}(\omega_\tau, T, \omega_t) = S_{TCF}^{2DFS}(\omega_\tau, T, \omega_t)$.[46] The real and imaginary parts of the total correlation spectra effectively partition the absorptive and dispersive contributions to the nonlinear optical response.

In Figure 2.3, we present model calculations of absorbance, CD, 2D FS and 2D ES total correlation spectra corresponding to four example conformations using the coupled two-dipole model. These calculations illustrate the sensitivity of a selected set of spectroscopic observables to, for example, different local arrangements of adjacent bases in a single strand of DNA. The figure compares adjacent "stacked," "T-shaped," "sheared," and in-line "side-to-side" conformations. For these calculations, we assumed a flat laser spectrum, and we used values for the relative dipole angle $\delta = 30°$ (with the exception of the "T-shaped" structure, for which we used $\delta = 60°$), inter-dipole separation $R = 3.6$ Å, dipolar strength $|\mu| = 1.33D$, and monomer transition frequency $\varepsilon_1/hc = 16{,}501$ cm^{-1}. For the "sheared" conformation, the angle subtending the parallel planes containing the dipoles and the inter-dipole vector was set to 45°. Exciton features underlying the absorption spectral line shapes were modeled as Gaussians, with fwhm = 700 cm^{-1}. 2D line shapes were modeled using a line width with fwhm = 175 cm^{-1}. CD was calculated using standard methods[47] which are briefly described in Appendix A.

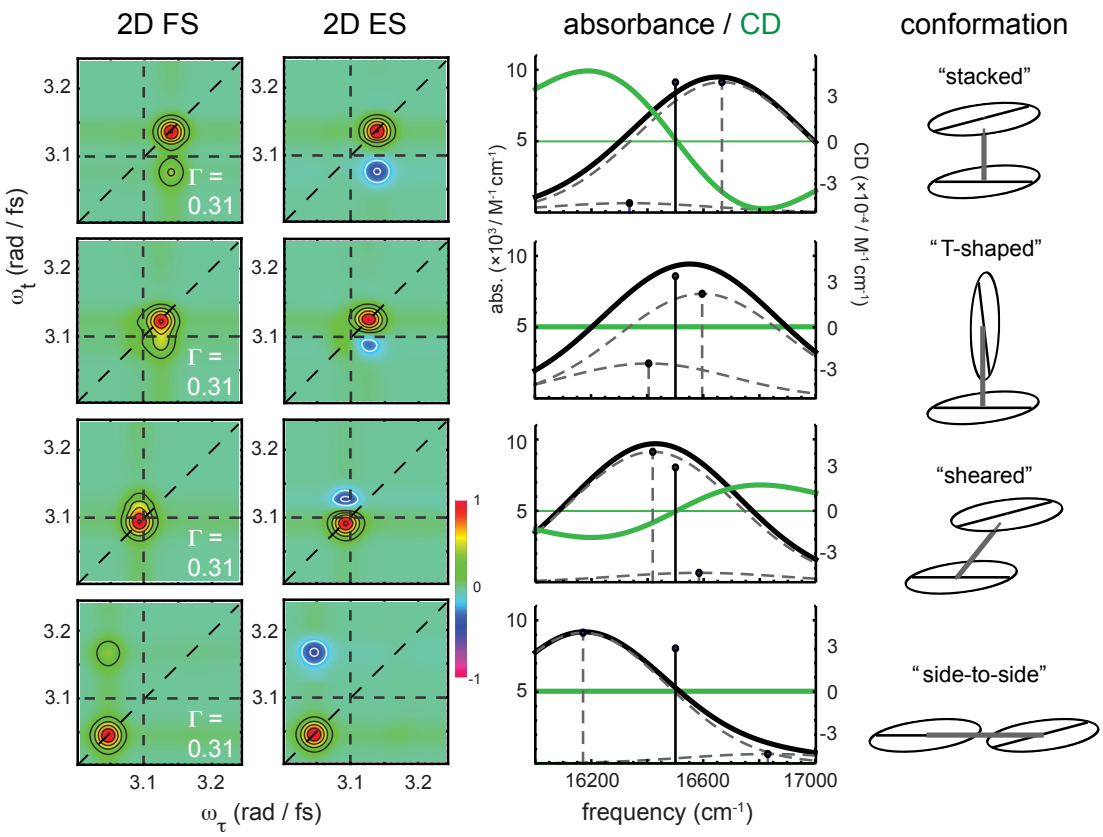

Figure 2.3. Comparison between simulated 2D FS and 2D ES total correlation spectra (real part), linear absorption, and circular dichroism (CD) using the coupled two-level model. Calculations for four selected dimer conformations are shown. Linear absorption (shown as solid black curves) and CD spectra (green curves) were calculated using standard procedures (detailed in SI section) with structural parameters $R = 3.4$ Å, $\delta = 30°$, and dipole moment $|\mu| = 1.33D$. Also shown are the positions of the underlying exciton features (dashed gray curves), which are evenly spaced about the monomer transition frequency $\bar{\nu}_1 =$ 16501 cm^{-1} = 3.11 rad fs^{-1}. 2D spectra were calculated assuming a uniform laser spectral density, and using eqs 2.21 and 2.22 for 2D ES, and eqs 2.24 and 2.25 for 2D FS. Horizontal and vertical dashed lines indicate the monomer transition frequency.

For the "stacked" conformation (top row), the helical H-type arrangement of transition dipoles results in a strong blue-shifted transition, and a relatively weak red-shifted one. This conformation also exhibits a strong CD signal, and blue-shifted diagonal peaks in the 2D FS and 2D ES spectra. The appearance of cross-peaks in the 2D FS and

2D ES spectra indicate coupling between excitons. In general, conformations that result in strong blue-shifted transitions also give rise to 2D spectral cross-peaks below the diagonal line. Conversely, conformations resulting in red-shifted spectra exhibit cross-peaks above the diagonal line. The effect of changing dimer conformation is to alter the coupling interaction V_{12}, defined in eq 2.4. For the case of the "T-shaped" conformation (second row), the magnitude of V_{12} is diminished due to the larger relative angle $\delta = 60°$ between transition dipole moments. Moreover, the lack of helicity in this conformation leads to loss of the CD signal. For the helical "sheared" conformation (third row), the sign of the coupling V_{12} is inverted relative to the "stacked" conformation, which results in a shift of the primary transition strength to the lower energy exciton. This effect is accompanied by a change in sign of the CD spectrum, and intense red-shifted diagonal peaks in both 2D FS and 2D ES. The "side-to-side" conformation (bottom row) results in a red-shifted pattern similar to the "sheared" structure. However, in this case the exciton splitting is enhanced due to its greater coupling strength. The absence of helicity in the "side-by-side" conformation leads to loss of the CD signal.

For each of the conformations depicted in Figure 2.3, the primary difference between 2D FS and 2D ES spectra is the sign of the cross-peak. For the case of 2D FS, the cross peak is positive, while for 2D ES the cross peak is negative. This difference arises due to the influence of the parameter $\Gamma = 0.31$ for 2D FS, and $\Gamma = 2$ for 2D ES. In the case of 2D ES, the ESA terms contribute with negative sign to the cross peak amplitude (see eqs 2.21 and 2.22). The analogous ESA terms contribute with positive sign to the cross-peak amplitude in 2D FS. We emphasize that although it is not possible to determine a particular conformation using any one of these spectroscopic observables,

the combination of absorbance, CD and 2D FS (or, alternatively 2D ES) is in principle sufficient to distinguish between conformations.

We next consider the effects of varying dimer conformation in the context of the coupled four-dipole model. In Figure 2.4 we present simulated spectra for nine different achiral structures of the exciton-coupled porphyrin dimer. Values for the structural parameters used in these calculations are given in the figure legend. The effect of coupling two dipoles from each monomer subunit is to increase the number of possible exciton-split ground-state allowed transitions to four. For many of the cases examined, the spectra exhibit degeneracies and / or transitions that carry no oscillator strength.

We note interesting similarities and differences predicted by the two models. For example, the "face-to-face" conformation (top left) results in linear and 2D spectra dominated by H-type coupling, which is similar to that of the "stacked" conformation in the two-dipole model. In contrast, the coplanar "side-to-side" conformation (bottom left) appears different from its two-dipole counterpart. For the four-dipole system, a combination of H-type and J-type coupling gives rise to significant blue- and red-shifted transitions, with each characterized by a unique splitting. The 2D spectrum corresponding to the "side-to-side" conformation exhibits cross-peaks above and below the diagonal line reflecting the two types of coupling. Similarly, both H- and J-type couplings contribute simultaneously to the spectra of the "bent T-shaped" conformation (center) and the "sheared face-to-face" conformation (middle left), although in the latter case the coupling strengths are significantly reduced.

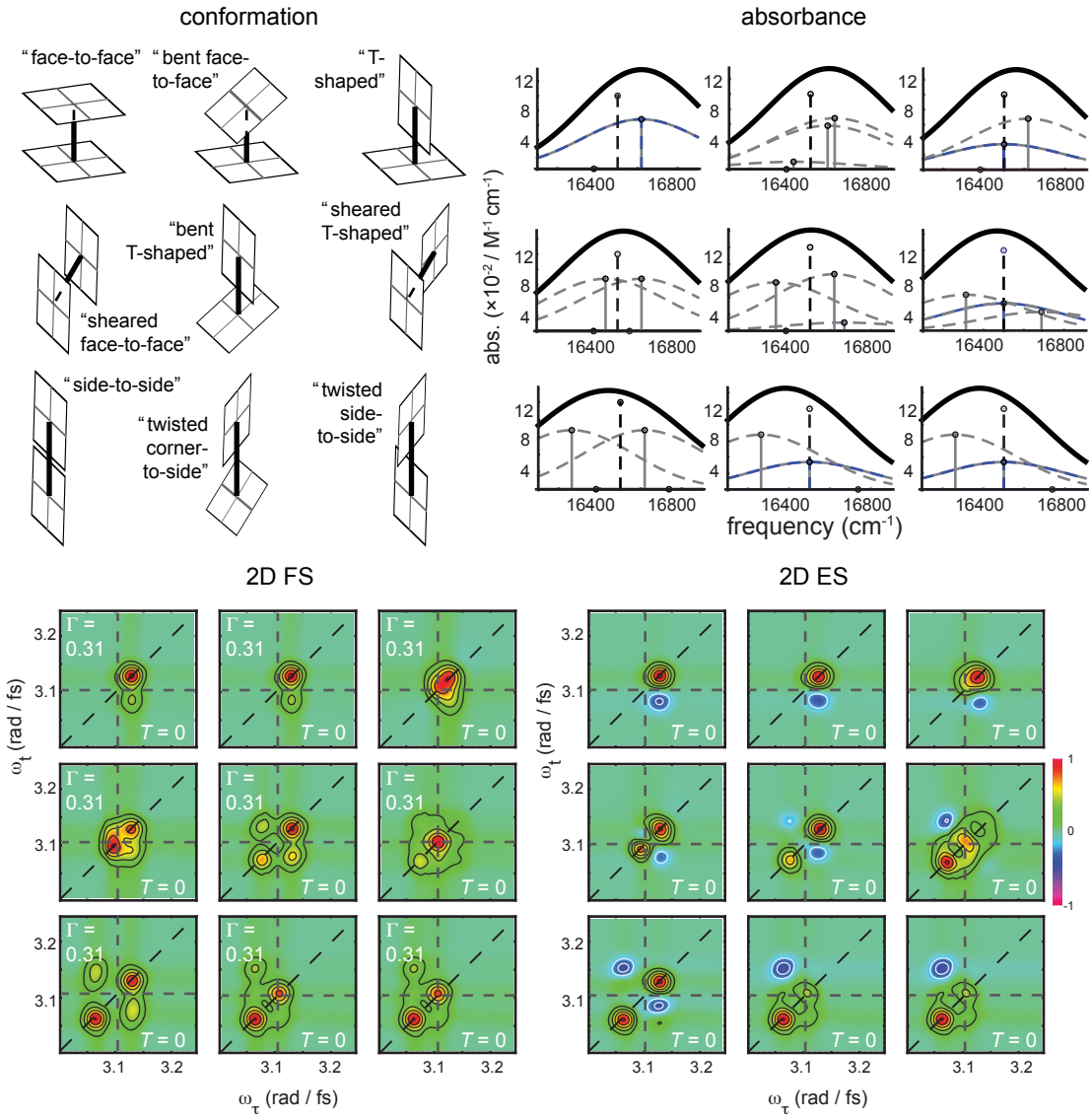

Figure 2.4. Comparison between simulated 2D FS and 2D ES total correlation spectra (real part), and linear absorption using the coupled three-level model for nine selected dimer conformations. Linear and 2D spectra were calculated according to the same procedures used for the calculations shown in Figure 2.3 and displayed in a similar fashion.

The effect of tilting the plane of a monomer subunit in the "face-to-face" dimer can be seen from the horizontal progression across the top row. The symmetric "T-shaped" conformation (top right) contains one pair of H-type coupled dipoles. Since the

remaining dipoles of this structure are perpendicular, they do not couple and their transition energies are unperturbed from that of the monomer. In the case of the "bent face-to-face" conformation (top middle), the two pairs of dipoles each contribute H-type coupling to the linear and 2D spectra.

The remaining three conformations – "sheared T-shaped" (middle right), "twisted corner-to-side" (bottom middle), and "twisted side-to-side" (bottom right) share common spectroscopic characteristics. Each of these structures exhibits one pair of J-type coupled dipoles and another pair whose lack of coupling leads to transitions at the monomer frequencies. We note that the spectra of these last two conformations are identical. This is due to the high symmetry of the metallo-porphyrin molecule, which leads to invariance of the Hamiltonian with respect to rotation of one of the monomer subunits within the plane of its macrocycle.[42]

The results presented in Figures 2.3 and 2.4 show that 2D FS and 2D ES are similarly sensitive to dimer conformation. As stated previously, the primary difference between the two methods is manifest in the sign of the cross-peaks of the real total correlation spectra, which are positive in the current case of 2D FS ($\Gamma = 0.31$) and negative in 2D ES ($\Gamma = 2$).

5. Conclusions

We have presented a theoretical framework for 2D fluorescence spectroscopy (2D FS), which is a highly sensitive approach to examine the conformations of electronically coupled molecular dimers in disordered complex environments. We considered two different exciton coupling models, the case of coupled two-level molecules and that of

coupled three-level molecules. We demonstrated that by combining 2D FS with linear absorption and / or circular dichroism spectroscopy, it is possible to distinguish between various different dimer conformations, including enantiomers of opposite handedness. We compared the 2D FS observables to those of 2D electronic spectroscopy (2D ES) performed by four-wave mixing. We determined that the 2D spectra measured by the two methods often appear very different due to a modification of the relative sign and magnitude of the ESA contribution in 2D FS signals. The origin of the dissimilarity is due to rapid self-quenching of the fluorescence from population on doubly-excited excitons relative to the fluorescence from population on singly-excited excitons.

6. Summary and Bridge to Chapter III

2D FS signals can be readily computed by applying fourth-order perturbation theory to the interactions of a coupled dimer with four laser pulses. Sixteen double-sided Feynman diagrams reflect all of the possible pathways through molecular state space, four of which contribute to the rephasing signal and four of which contribute to the nonrephasing signal. Under both two-dipole and four-dipole models, the 2D FS spectrum is found to be sensitive to the relative distance and angle between two coupled chromophores, and to contain similar information to the 2D ES spectrum computed using third-order perturbation theory. This chapter has laid the foundations for the studies presented in the remainder of this dissertation, in which I take advantage of the conformational sensitivity of 2D FS to study a variety of systems. In Chapter III, I apply 2D FS to a similar system to the membrane-bound MgTPP dimer discussed here, a tethered dimer of zinc tetraphenlyporphyrin (ZnTPP) embedded in a phospholipid

membrane, and I use the theory presented here to determine its conformations as a function of temperature.

CHAPTER III

TEMPERATURE-DEPENDENT CONFORMATIONS OF A MEMBRANE SUPPORTED ZINC PORPHYRIN TWEEZER BY 2D FLUORESCENCE SPECTROSCOPY

1. Overview

This chapter contains material published as Widom, J. R.; Lee, W.; Perdomo-Ortiz, A.; Rappoport, D.; Molinski, T. F.; Aspuru-Guzik, A.; Marcus, A. H. Temperature-Dependent Conformations of a Membrane Supported Zinc Porphyrin Tweezer by 2D Fluorescence Spectroscopy. *J. Phys. Chem. A*. **2013**, *117*, 6171-6184. In these experiments, a tethered dimer of zinc tetraphenylporphyrin embedded in a membrane was found to adopt a mixture of folded and extended conformations. The relative populations of these two conformations were determined at a series of temperatures, allowing us to calculate the overall changes in enthalpy and entropy upon folding of the dimer. Among the experiments presented in this chapter, W. Lee performed the fluorometry. I performed the data fitting using a procedure developed by A. Perdomo-Ortiz, which utilizes an extension of the theory presented in Chapter II. D. Rappoport performed the UFF structure optimizations, and the zinc porphyrin tweezer was synthesized by the lab of T. F. Molinski. The paper was written in collaboration with A. H. Marcus, with editorial assistance from the other co-authors.

2. Introduction

The properties of biological macromolecular complexes are to a great extent influenced by non-covalent interactions between proteins, nucleic acids, sugars, and

lipids.[26-29, 48] These interactions take many different forms. For example, proteins that bind to nucleic acids utilize hydrogen bonding and stacking between amino acid side chains and bases. The chromophore arrays of photosynthetic complexes are held in specific three-dimensional arrangements through their contacts with proteins, and through direct interactions between pigments. The folding of many proteins is driven, not only by the formation of favorable non-covalent bonds between amino acids, but also by the increasing entropy of water liberated from contacts with hydrophobic surfaces.

Significant work in molecular biology has focused on developing a better understanding of the various contributions to the stability of specific macromolecular complexes.[49-51] The function of such systems often relies on their ability to exist in different conformational states. For example, the fidelity of DNA replication is thought to involve rapid interconversion between two conformational end-states of the DNA polymerase – primer-template DNA complex; a 'proofreading' conformation and a processive 'polymerization' conformation.[12] Studies that seek to understand the mechanisms of such processes must determine the identities of the end-states, their relative stabilities, and the kinetics of their interconversion. A significant experimental challenge is to separate signals from the different end-states so that structural, thermodynamic and kinetic parameters can be accurately ascertained.

Changes in stability associated with the formation of a macromolecular complex are often governed by a delicate balance between large and opposing changes in enthalpy and entropy.[48-49, 51] Contributions to the enthalpy depend on direct interactions between components of the complex, in addition to contacts between the solvent and those components that become more or less solvent-exposed. Entropic contributions are due to

changes in conformational degrees of freedom of the components (i.e., translational, rotational, vibrational, etc.), as well as those of solvent molecules, which may be tightly bound to exposed component surfaces. For our current purposes, we consider the dimerization reaction between two monomers $2M \rightleftharpoons M_2$. In this case, the free energy of association can be partitioned into enthalpic and entropic terms reflecting solvent-solvent interactions, monomer-monomer interactions, and monomer-solvent interactions, allowing for different mechanisms to lead to dimer stability. For example, dimer formation might be driven by favorable monomer-monomer enthalpic interactions, sufficient to offset the loss of entropic degrees of freedom of the 'free' monomer subunits. Alternatively, a favorable change in the solvent entropy upon dimerization might be large enough to compensate for the disruption of otherwise stable enthalpic contacts between solvent and exposed monomer surfaces.

In earlier work,[52] one of us (TFM) found that dimeric esters of TPP linked by acyclic C_2 symmetric1,5-, 1,7- and 1,9-diols formulated in highly uniform unilamellar liposomes (DSSC, f_{ave} = 26±5.1 nm) exhibited strong circular dichroism (CD) signals at room temperature. These observations suggested the presence of organized bilayer-TPP structures supported by lipid bilayer-TPP interactions, or bilayer-constrained TPP-TPP interactions. Moreover, even simple long-chain naphthamides, when formulated in liposomes, exhibited complex temperature-dependent CD spectra[53-54] suggesting the assembly of multi-chromophore structures.

Two-dimensional electronic spectroscopy (2D ES) is a method that probes the correlations between successive electronic transitions, and it has been used to investigate energy transfer pathways in photosynthetic protein-pigment complexes,[6, 55-57] conjugated

polymers[58] and semiconductors.[59-60] In principle, 2D ES experiments are sensitive to the relative orientations of resonantly excited electronic transition dipole moments of coupled multi-chromophore systems, suggesting its general application as an analytical tool for structural elucidation. Recently, a fluorescence-detected version of 2D ES, called two-dimensional fluorescence spectroscopy (2D FS), was used to elucidate the conformation of a self-assembled magnesium meso tetraphenylporphyrin (MgTPP) dimer in a biological membrane.[8-9] Subsequent extension of the method to ultraviolet wavelengths made it possible to solve the solution conformation of a dinucleotide of the fluorescent adenine analogue 2-aminopurine (2-AP).[13]

In previous 2D FS experiments performed on MgTPP chromophores embedded in the amphiphilic regions of 1,2-distearoyl-sn-glycero-3-phosphocholine (DSPC) liposomes, we found that self-assembled MgTPP dimers formed relatively open "T-shaped" structures, suggesting that the association process was driven primarily by an increase in the entropy of the local membrane environment (i.e., the monomer-solvent entropy term).[9] However, those experiments were not sufficient to determine the values of the different contributions to the free energy of dimerization. Measurements performed over a range of temperatures should yield separately the enthalpic and entropic contributions to dimer assembly. Moreover, by using a dimer consisting of two chemically tethered monomers instead of the previously studied self-assembled dimer, it is possible to work under dilute solute conditions to minimize the perturbation of solvent-solvent interactions, and to avoid the process of higher-order aggregation.

In this paper, we present 2D FS experiments on a chemically tethered dimer – a 'zinc porphyrin tweezer' [herein designated as $(ZnTPP)_2$], which was synthesized by

coupling two zinc 5-(p-carboxylphenyl)-10,15,20-triphenylporphyrin subunits using a 1,4 butyndiol spacer (see Figure 3.1A). We studied the zinc porphyrin tweezer $(ZnTPP)_2$ in the same DSPC liposomes as in our previous experiments on the self-assembled magnesium porphyrin dimer,[8-9] and we expect both systems to exhibit similar enthalpic and entropic interactions with the local membrane environment. We combined a broad range of experimental data obtained from 2D FS experiments, linear absorption, and fluorimetry, which we compared to dimer conformation models based on the exciton coupling between the porphyrin subunits. Our results indicate that the zinc porphyrin tweezer adopts a mixture of 'extended' and 'folded' conformations in the membrane, and that the relative populations of these two states are temperature-dependent. By performing these experiments over a range of temperatures, we separately determined the relevant enthalpic and entropic contributions to the overall free energy change of the folding process.

3. Experimental Methods

A. Preparation of the $(ZnTPP)_2$ Dimer

1,4-Butanediol, but-2-yn-1,4-diol, zinc acetate dihydrate, and dicyclohexylcarbodiimide (DCC) were purchased from Sigma Aldrich (Milwaukee, WI) and used as received. Dry dichloromethane (DCM) and tetrahydrofuran (THF) were prepared by passage over activated alumina or molecular sieves under an argon atmosphere. ^1H NMR spectra were recorded on Varian Mercury 400 or Jeol ECA 500 MHz spectrometers. Samples were measured in $CDCl_3$ solution (referenced to residual solvent, d = 7.24 ppm). Accurate mass spectra measurements were made using an Agilent

6230 time of flight mass spectrometer (TOFMS). TLC was carried out on aluminum plates thin-coated with silica (0.1 mm, EM Merck) and visualized under UV-light (254 nm).

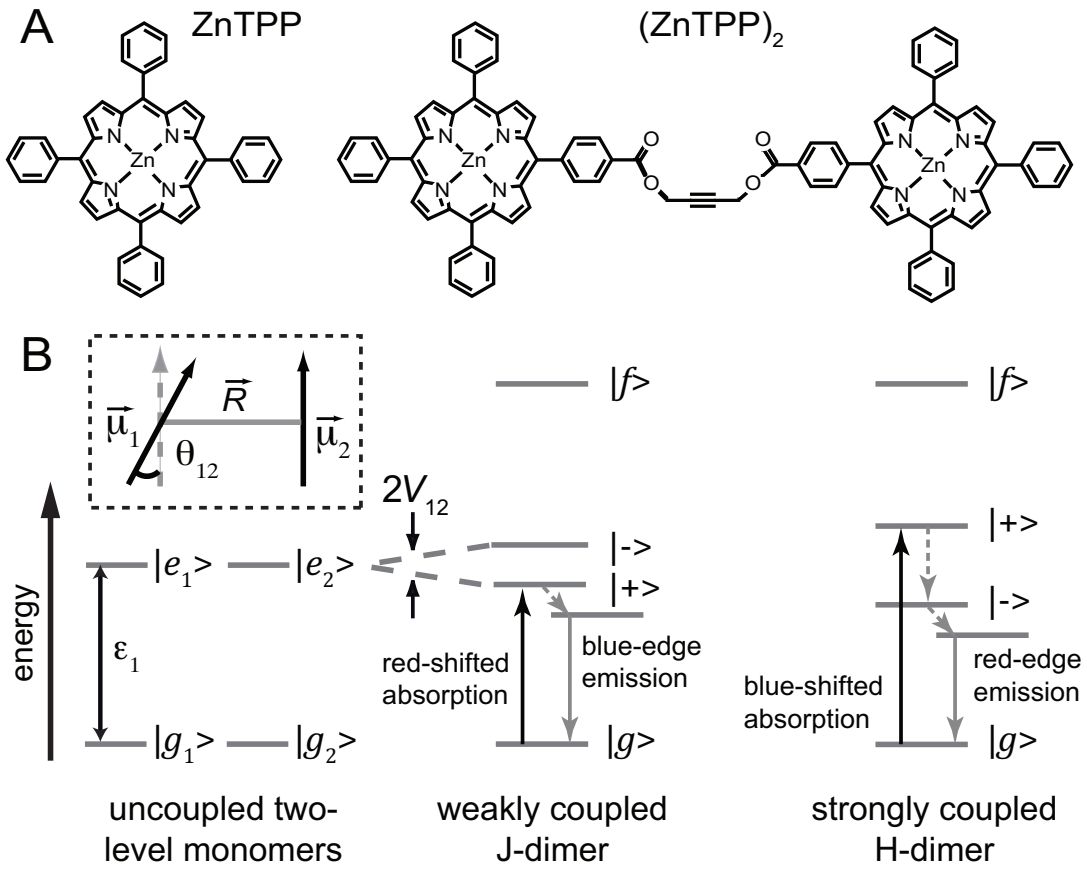

Figure 3.1. (A) Structures of the chromophores used in this study, zinc tetraphenylporphyrin (ZnTPP) and a covalently linked dimer of ZnTPP $(ZnTPP)_2$. (B) Energy level diagrams of two degenerate two-level molecules. Electronic coupling results in a four-level dimer with a single ground state $|g\rangle$, two non-degenerate singly-excited states $|\pm\rangle$, and a doubly-excited state $|f\rangle$. For a 'weakly coupled J-dimer' (i.e., with a head-to-tail dipole arrangement), the $|+\rangle$ state is shifted to lower energy. The situation is juxtaposed for a 'strongly coupled H-dimer' (i.e., a side-by-side dipole arrangement). Because transitions involving the $|+\rangle$ state are favored, absorption is red-shifted for a J-dimer, while it is blue-shifted for an H-dimer. After excited state relaxation, emission occurs from the lowest-energy singly-excited state, which is lower in energy for the H-dimer than the J-dimer due to the H-dimer's stronger coupling. Therefore, fluorescence from the H-dimer occurs on the red edge of the emission line shape while emission from the J-dimer occurs on the blue edge of the emission line shape.

Dimer $(TPP)_2$ was prepared using a modification of the procedure of Nakanishi and coworkers.[61] To a solution of 5-*p*-carboxyphenyl)-10,15,20-triphenylporphyrin (2.2 equiv), prepared as previously described,[62] in DCM (approximately 0.1-0.2 M) and DCC (2.2 equiv) was added but-2-yn-1,4-diol (1 equiv) and the mixture was stirred at room temperature until TLC of a sample of the mixture showed absence of starting material (overnight). The mixture was diluted with DCM (10 volumes), washed with $NaHCO_3$ (aqueous, saturated) and dried over Na_2SO_4. Removal of the volatiles under reduced pressure gave a residue that was subjected to flash chromatography (silica, hexane: ethyl acetate) to provide pure TPP-diester $(TPP)_2$ with TOFMS and NMR data consistent with the assigned structure.

A solution of $(TPP)_2$ in DCM (0.1 M) was stirred rapidly with excess zinc acetate dihydrate ($Zn(C_2H_3O_2)_2 \bullet 2H_2O$) overnight at room temperature.[61] The mixture was filtered and concentrated to give a highly colored residue that was purified by flash chromatography to give $(ZnTPP)_2$ with TOFMS and NMR data consistent with the assigned structure.

Control experiments were performed using zinc meso tetraphenylporphyrin (ZnTPP) as a monomer, which was purchased from Sigma Aldrich and used as received. We prepared porphyrin / liposome samples using DSPC as the lipid according to established procedures.[8, 18] We prepared samples containing the zinc porphyrin tweezer using a 30:1 DSPC : $(ZnTPP)_2$ molar ratio, and samples containing monomeric ZnTPP using the ratios 20:1 and 70:1 DSPC : ZnTPP. Before performing our measurements, we annealed each liposome sample by heating it to 70°C and allowing it to slowly cool back

to room temperature (23°C). We prepared solution phase samples by dissolving $(ZnTPP)_2$ or ZnTPP in spectroscopic grade chloroform.

B. Differential Scanning Calorimetry (DSC)

We performed DSC measurements using a TA instruments DSC 2920. We prepared a 30:1 DSPC : $(ZnTPP)_2$ liposome sample in addition to a control blank DSPC liposome sample using the procedures described above. The samples were centrifuged for 5 minutes at 5000 RPM and the supernatant liquid equal to 96% of the total volume was removed. The resulting samples (weighing ~ 10 mg) were placed in aluminum hermitic pans and crimped shut. An empty pan was used as a reference and the temperature was scanned from 10°C to 80°C at a rate of 10°C / minute. After performing an initial run to anneal the sample, we recorded data on the second consecutive run.

C. Linear Absorption and Fluorescence Spectroscopy

We measured the linear absorption spectra of our samples using a Cary 3E UV-visible spectrophotometer, which was equipped with a computer-interfaced temperature control system. There was significant non-resonant background underlying the $Q(0,0)$ line shape (~ 600 nm), which was due to the strong *B*- (Soret) band transition (~ 430 nm). To obtain the line shapes used for our data analysis, we performed a background subtraction by fitting a line to the blue-edge (513 – 538 nm) and to the red-edge (650 – 700 nm) of the $Q(0,0)$ and $Q(0,1)$ features, and by subtracting this fit from the raw data. We recorded fluorescence spectra using a Jobin-Yvon FluoroMax-3 spectrofluorometer, which was equipped with a manual temperature control system. Fluorescence spectra were measured by exciting, in separate experiments, the blue and the red edges of the

$Q(0,0)$ band (596 and 602 nm), the $Q(0,1)$ band (551 and 570 nm), and the *B*-band (418 and 452 nm).

D. Two-Dimensional Fluorescence Spectroscopy

The 2D FS instrumentation and method is described in detail elsewhere.[4, 8-9] Briefly, the sample was resonantly excited using a sequence of four phase-modulated collinear femtosecond optical pulses. The ensuing nonlinear excited state populations were phase-synchronously detected by monitoring fluorescence. The laser pulses were prepared using two optical parametric amplifiers (OPAs), which were driven with the output of a 250 kHz amplified Ti:Sapphire oscillator (Coherent, RegA 9000, pulse energy ~ 10 mJ). The tunable output of each OPA was passed through a pair of SF10 prisms (double pass geometry) for pre-dispersion compensation, and subsequently directed into a Mach-Zehnder interferometer (MZI). The input of each MZI was split, and the resulting two beams were each passed through an acousto-optic Bragg cell (AOBC), which imparted a continuous phase sweep to the pulse. The relative beam paths were controlled using a retro-reflective mirror that was mounted to a computer-interfaced optical delay stage, and the beams were recombined and made collinear at the exit beam-splitters. The output of one of the MZIs was passed through an additional computer-interfaced delay stage before it was combined at a beam-splitter with the output of the other MZI, to create a train of four collinear pulses with controllable inter-pulse time delays. The AOBCs were detuned from each other such that the relative phase of pulses 1 and 2 was swept at 8 kHz and the relative phase of pulses 3 and 4 was swept at 5 kHz. A replica of each pulse pair was spectrally filtered using a monochromator and detected using an avalanche photodiode (APD). The 8 and 5 kHz reference signals created from the first

and second pulse pairs, respectively, were input to a custom-built waveform mixer, which generated sum (13 kHz) and difference (3 kHz) sidebands. These waveforms were used as references for lock-in detection of the fourth-order population signals, analogous to the nonrephasing (NRP) and rephasing (RP) signals measured in 2D ES.[4, 8-9] To collect a 2D FS spectrum, the delays between pulses 1 and 2 (designated $t_{21} = \tau$) and between pulses 3 and 4 ($t_{43} = t$) were scanned from 0 to 250 fs, while the delay between pulses 2 and 3 ($t_{32} = T$) was held fixed. The cosine and sine projections of the 13 and 3 kHz signals were thus recorded, and the Fourier transform of the resulting 2D interferogram, with respect to the variables τ and t, yielded the 2D FS spectrum. For all of the experiments discussed in this paper, we set $T = 0$. Before each series of experiments, the pulse durations and delay stage positions at which the pulses were maximally overlapped were determined through second harmonic generation autocorrelation using a beta barium borate (BBO) crystal. Before each data set, the phase calibrations of the lock-in amplifiers were adjusted to maximize the cosine projection of the signal at the time origin.

For all of our 2D FS measurements, we circulated the sample through a quartz flow cell using a peristaltic pump. The fluorescence was spectrally filtered, and detected using an APD. We used various filters and filter combinations for different experiments, which were a 610 – 680 nm band-pass filter (Chroma HQ645/75m), a 620 nm long-pass filter (Omega 3RD 620LP), a 635 nm long-pass filter (Chroma HQ635LP), a 645 nm long-pass filter (Chroma HQ645LP), and the above 620 nm long-pass filter combined with a 650 nm short-pass filter (ThorLabs FE S0650). The temperature was controlled by circulating water from a heat bath through a copper block in which the sample flow cell was mounted. The heat bath was calibrated by measuring the temperature of a blank

sample using a thermocouple. For our temperature-dependent measurements, we annealed the liposome samples as described above, before recording successive data sets in order of increasing temperature at 23, 28, 46, 63, 72, and 85°C. After reaching the highest temperature, the sample was slowly cooled to 17°C for the final sets of measurements. At each temperature, we recorded 2D fluorescence spectra with the laser spectrum centered at four different frequencies: 16 620, 16 470, 16 340 and 16 220 cm^{-1}.

E. Molecular Modeling Calculations

We performed thermodynamic calculations on the zinc porphyrin tweezer in the 'folded' and 'extended' conformations based on the Universal Force Field (UFF).[63] The UFF was used for optimizations of model structures for the 'folded' and 'extended' conformations. Subsequently, enthalpies and entropies of these conformations were computed in the harmonic approximation using UFF Hessian matrices. The UFF model was designed to provide consistent accuracy across the periodic table and yields rather accurate structure predictions for organic molecules[63] as well as transition-metal complexes.[64] While the UFF model lacks parameterization to correctly describe planar Zn-porphyrin complexes, we expect it to provide useful estimates for differences in thermodynamic parameters between 'folded' and 'extended' conformations. All calculations were performed using the TURBOMOLE suite of programs.[65]

4. Modeling Linear Absorption and 2D FS Data

A. Exciton-Coupled Four Level Dimer Model

Models that we previously used to simulate linear absorption and 2D FS spectra of metal porphyrin dimers, which depend on dimer conformation, are described in detail

elsewhere.[8-9, 13] For the current study, we used the coupled two-dipole model[9, 38] with some additional modifications. Here, each monomer subunit of the zinc porphyrin tweezer supports a single ground state accessible electronic transition $|e_n\rangle \leftarrow |g_n\rangle$, with electric dipole transition moment (EDTM) $\vec{\mu}_n$ [$n \in \{1,2\}$], and energy ε_1 (see Figure 3.1B). The effect of coupling between transitions is to create a four-level system consisting of a common ground state $|g\rangle$, two singly excited states $|\pm\rangle$ with $\varepsilon_\pm = \varepsilon_1 \pm V_{12}$, and a doubly excited state $|f\rangle$ with $\varepsilon_f \cong 2\varepsilon_1$. The symmetric and anti-symmetric singly excited states have wave functions delocalized among the monomer sites, which are related to the site basis according to $|\pm\rangle = \frac{1}{\sqrt{2}}\left[|e\rangle|g\rangle \pm |g\rangle|e\rangle\right]$. We used the point-dipole approximation to calculate the electronic coupling between EDTMs of each monomer

$$V_{12} = \frac{1}{4\pi\varepsilon_0 R_{12}^3}(\vec{\mu}_1)\cdot\left(1-3\frac{\vec{R}_{12}\vec{R}_{12}}{R_{12}^2}\right)\cdot(\vec{\mu}_2) \tag{3.1}$$

In eq 3.1, $\vec{R}_{12}$ is the vector connecting the centers of the EDTMs, and ε_0 is the vacuum permittivity. The collective EDTMs that mediate transitions between ground and singly excited states are given by $\vec{\mu}_\pm = (1/2)\left[\vec{\mu}_1 \pm \vec{\mu}_2\right]$, and between singly excited states and doubly excited states by $\vec{\mu}_{\pm f} = \pm\vec{\mu}_\pm$. The intensities of the transitions between the various levels depend on the relative orientations of the dipoles within the complex. For example, the amplitudes of the ground state allowed transitions are given by $I_\pm = |\mu|^2(1 \pm \cos\theta_{12})$, where $|\mu|^2$ is the square magnitude of the monomer EDTM, and θ_{12} is the relative dipole

angle. We note that an 'H-type' side-by-side configuration (i.e., $\uparrow\uparrow$) with $\theta_{12} = 0$ has the majority of its oscillator strength carried by the higher energy (blue-shifted) transition, whereas a 'J-type' head-to-tail configuration (i.e., $\rightarrow\rightarrow$) has the majority of its oscillator strength carried by the lower energy (red-shifted) transition. The effect of non-zero θ_{12} is to partition some intensity to the otherwise 'dark' transition. Moreover, the conformation of the dimer affects its emission spectrum. As illustrated in Figure 3.1B, a weakly coupled J-dimer results in fluorescence on the blue edge of the emission line shape, while a strongly coupled H-dimer leads to self-quenching and relatively weak fluorescence on the red edge of the emission line shape.

We performed a series of 2D FS measurements with the laser spectrum centered at different wavelengths, ranging from the peak of the $Q(0,0)$ absorption band to its red shoulder. For all of these measurements, we observed that the peaks of the 2D FS spectra shifted systematically with changing laser center wavelength, suggesting that the $Q(0,0)$ line shapes were inhomogeneously broadened. To account for static disorder, we included in our model a correction based on the spectral overlap between the laser and components of the absorption spectrum.[13] We modeled the laser spectrum $g(\omega)$ and individual spectral features $a_{nm}(\omega)$, due to a transition bridging the *m*th and *n*th state, as Gaussians

$$g(\omega) = \exp\left[-\frac{(\omega-\omega_L)^2}{2\sigma_L^2}\right] \tag{3.2}$$

and

$$a_{nm}(\omega) = \exp\left[-\frac{(\omega-\omega_{nm})^2}{2\sigma_1^2}\right] \tag{3.3}$$

In eqs 3.2 and 3.3, ω_L is the center frequency of the laser spectrum, σ_1 is the standard deviation of the component of the absorption line shape that results in the shift, and σ_L ($\approx$ 220 cm^{-1}) is the standard deviation of the laser spectrum. For a given transition, we determined the simulated 2D FS spectrum from the spectral overlap function $g(\omega)\cdot a_{nm}(\omega)$. We thus adjusted the transition center frequency according to

$$\omega_{nm} \rightarrow \tilde{\omega}_{nm} \equiv \frac{\omega_L \sigma_1^2 + \omega_{nm}\sigma_L^2}{\sigma_1^2 + \sigma_L^2}, \tag{3.4}$$

and we adjusted the weight of the transition, which was determined by the laser amplitude, according to

$$\alpha(\omega) \rightarrow \tilde{\alpha}(\omega) = \exp\left[-\frac{(\omega-\omega_L)^2}{2(\sigma_L^2+\sigma_1^2)}\right] \tag{3.5}$$

We used the above model to calculate the center frequency for each 2D FS feature, assuming a Gaussian line shape with line width characterized by its phenomenological dephasing time τ. In addition to the correction given by eq 3.5, we applied the usual contributions to the signal from each coherence pathway, weighted according to the rotational average of the sequence of transition dipole moments involved in that pathway, $\langle \mu_1\mu_2\mu_3\mu_4 \rangle$. We assumed that the orthogonal Q_x and Q_y EDTMs on

each porphyrin monomer could be represented by one "effective" EDTM (discussed further in Results). We therefore modeled the linear absorption spectrum according to

$$A(\bar{\nu}) = a_0 + \delta|\mu|^2\left[(1+\cos\theta_{12})\, e^{-\frac{(\bar{\nu}-\varepsilon_+)^2}{2\sigma_{lin}^2}} + (1-\cos\theta_{12})\, e^{-\frac{(\bar{\nu}-\varepsilon_-)^2}{2\sigma_{lin}^2}}\right], \tag{3.6}$$

where a_0 is a baseline offset, δ is the intensity, σ_{lin} is the spectral line width, and the parameters μ, θ_{12}, and $\varepsilon_\pm$ are defined above.

B. Fitting Procedures

We used our temperature-dependent linear absorption and 2D FS data sets, taken at four different laser center wavelengths, to constrain the structural parameters that determine the zinc porphyrin tweezer conformations. The fitting procedure involved a 16-parameter nonlinear global optimization, which we performed using the aid of the software package KNITRO.[66] As we discuss further below, we determined from our fluorometry and spectrally filtered 2D FS experiments that our data could not be modeled in terms of a single dimer conformation. We concluded that there must be two structures present in the membrane, one 'folded' conformation, which we modeled as an H-dimer, and one 'extended' conformation, which we modeled as a J-dimer. We used the model described above to simultaneously fit the linear absorption spectrum and both real and imaginary parts of the RP and NRP spectra, with the laser center frequency set to 16 620 cm^{-1} and 16 470 cm^{-1}. The configurations that optimized these fits to our data also yielded spectra that matched our 2D FS measurements recorded with laser center frequency set to 16 340 cm^{-1} and 16 220 cm^{-1}. Nevertheless, when the laser was significantly detuned

from the $Q(0,0)$ absorption maximum, as was the case with 16 340 cm^{-1} and 16 220 cm^{-1} excitation, the model slightly underestimated the extent to which the peaks were red-shifted towards the laser center frequency. For this reason, we only included in our optimizations the linear absorption and the 2DFS spectra with the laser center frequency tuned to 16 620 cm^{-1} and 16 470 cm^{-1}.

We performed the following procedure to obtain optimized solutions for a mixture of H- and J-dimer species. The H- and J-dimer conformations were each characterized by five variables: i) the electronic coupling strength $V_{H(J)}$, ii) the relative dipole angle of the two monomers $\theta_{H(J)}$, iii) the phenomenological dephasing time $\tau_{H(J)}$, iv) the fluorescence quantum yield of the doubly excited state relative to the singly excited states $\Gamma_{H(J)}$, and v) the line shape overlap parameter $\sigma_{H(J)}$. In addition, six parameters characterized the collective system: vi) the linear spectrum baseline offset a_0, vii) the linear spectrum intensity δ, viii) the linear spectrum line width σ_{lin}, ix) the monomer transition energy ε_1, x) the ratio b of H-dimer to J-dimer conformational populations, and xi) the ratio d of H-dimer to J-dimer fluorescence quantum yields. Initially, we calculated the linear absorption and 2D spectra for independent H- and J-dimer conformations. We treated these single species spectra as basis functions from which we obtained the linear spectrum of the mixture taking a linear combination of the two, weighted by the relative population of the H-dimer to that of the J-dimer. We thus obtained the 2D spectrum of the mixture by weighting the 2D spectrum of the H-dimer by its relative population and its relative fluorescence quantum yield, and combining this with the spectrum of the J-dimer.

We optimized the sixteen model parameters to find a global minimum of the least-squares cost function χ^2_{tot}, which we constructed as follows.

$$\begin{aligned}\chi^2_{2D} = \sum_{\omega_\tau,\omega_t} \Big\{ &\Big[\mathrm{Re}(NRP_{\mathrm{sim}}(\omega_\tau,\omega_t) - \mathrm{Re}(NRP_{\mathrm{exp}}(\omega_\tau,\omega_t)\Big]^2 \\ &+\Big[\mathrm{Im}(NRP_{\mathrm{sim}}(\omega_\tau,\omega_t)) - \mathrm{Im}(NRP_{\mathrm{exp}}(\omega_\tau,\omega_t))\Big]^2 \\ &+\Big[\mathrm{Re}(RP_{\mathrm{sim}}(\omega_\tau,\omega_t)) - \mathrm{Re}(RP_{\mathrm{exp}}(\omega_\tau,\omega_t))\Big]^2 \\ &+\Big[\mathrm{Im}(RP_{\mathrm{sim}}(\omega_\tau,\omega_t)) - \mathrm{Im}(RP_{\mathrm{exp}}(\omega_\tau,\omega_t))\Big]^2\end{aligned} \tag{3.7}$$

$$\chi^2_{lin} = \sum_{\bar{\nu}} \Big[A_{\mathrm{sim}}(\bar{\nu}) - A_{\mathrm{exp}}(\bar{\nu})\Big]^2 \tag{3.8}$$

$$\chi^2_{tot} = \chi^2_{2D,16620} + \chi^2_{2D,16470} + n \cdot \chi^2_{lin} \tag{3.9}$$

In eq 3.7, $NRP(RP)_{\mathrm{sim(exp)}}(\omega_\tau,\omega_t)$ is the simulated (experimental) NRP (RP) signal at frequencies (ω_τ,ω_t). In eq 3.8, $A_{\mathrm{sim(exp)}}(\bar{\nu})$ is the simulated (experimental) linear spectrum. In eq 3.9, $\chi^2_{2D,16620(16470)}$ is χ^2_{2D} for the simulated and experimental spectra using 16 620 (16 470) cm^{-1} excitation, and n is a weighting factor used to make the contribution of χ^2_{lin} to the cost function comparable to that of χ^2_{2D}. We set n = 10 000 in order to fit our data taken at 17, 23, 28, 46, and 63°C. For the fits to data taken at 72 and 85°C, we increased the value of n to 20 000 and to 50 000, respectively, in order to maintain a good fit to the linear spectrum. We first minimized the cost function χ^2_{tot} for the room temperature (23°C) data set to find an optimized sixteen-parameter solution. For

the remaining temperature data sets, we fixed the parameters ε_1, V_H, V_J, θ_H, θ_J and d to their room temperature values. We then varied the remaining parameters to minimize the cost function.

In Figure 3.2, we show an example of simulated spectra obtained from the fitting procedure described above. For brevity, we show here only the 2D FS NRP spectra under 16 470 cm^{-1} excitation. However, we performed all of our optimizations by minimizing the cost function (eq 3.9), which used as simultaneous constraints the linear absorbance, RP and NRP 2D FS spectra obtained with laser center frequency tuned to 16 620 and 16 470 cm^{-1}. RP and NRP 2D FS spectra were routinely combined to obtain the total correlation spectra.[9]

5. Results

In Figure 3.3, we present temperature-dependent absorption and fluorescence spectra of the DSPC liposome / $(ZnTPP)_2$ system. We recorded the absorption spectra over the range 400 – 650 nm and observed the three characteristic features associated with metal porphyrins in solution.[17] These are the $Q(0,0)$- and $Q(0,1)$-bands centered at 600 nm and 560 nm, respectively, and the *B*-band centered at 430 nm. We recorded fluorescence spectra by exciting the blue-edge of the *B*-band at 420 nm, and we observed two major features centered at ~ 610 and 650 nm. We performed these measurements at temperatures ranging from 17 – 85°C.

The fluorescence line shapes of the liposome / $(ZnTPP)_2$ system were broad and asymmetric for all of the temperatures we investigated, suggesting that they might be a

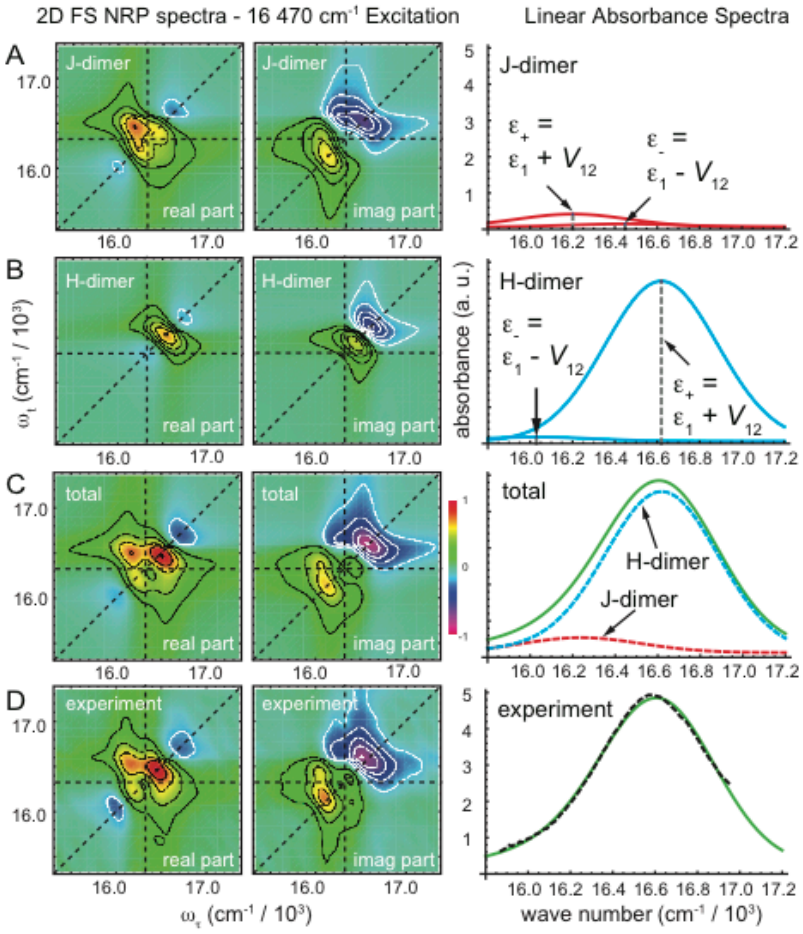

Figure 3.2. Binary mixture decomposition analysis based on minimization of the cost function described by eq 3.9. Simulated contribution to 2D FS NRP and linear absorbance spectra are shown for (A) the J-dimer, (B) the H-dimer, and (C) the combined components of the mixture. (D) The experimental 2D FS and linear absorbance are to be compared to the simulated spectra shown in (C).

superposition of two bands. This is to be compared to the relatively narrow and symmetric line shapes of monomeric ZnTPP in solution, and at low concentration in liposomes. When we selectively excited the liposome / $(ZnTPP)_2$ system on the red-edge of the absorption bands [i.e., the *B*-band at 452 nm and the $Q(0,1)$-band at 570 nm], we found that the blue-edge of the emission spectrum was enhanced. Conversely, when we excited on the blue-edge of the absorption bands, the red-edge of the emission spectrum was enhanced. Moreover, both the *B*-band and the fluorescence line shapes were sensitive

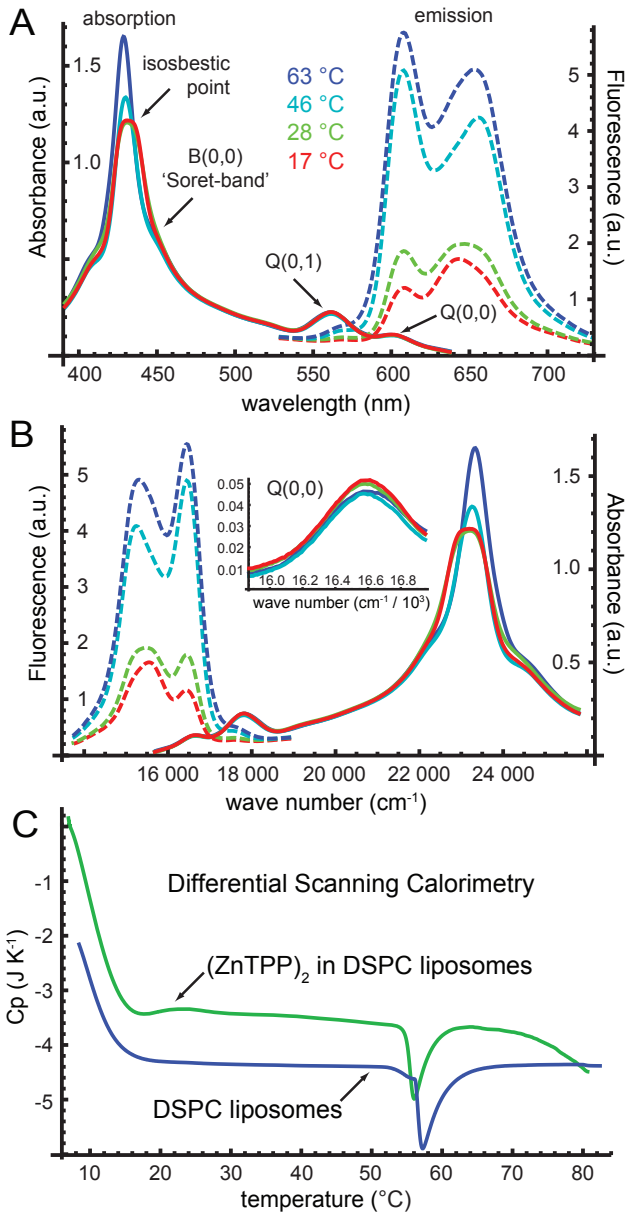

Figure 3.3. (A) The linear absorption (solid curves) and fluorescence spectra (dashed curves) of the zinc porphyrin tweezer $(ZnTPP)_2$ in DSPC liposomes are shown for different temperatures, ranging from 17 °C to 63 °C. The spectra are plotted versus wavelength. The *B*-band narrows and blue-shifts at elevated temperatures, while the low-energy fluorescence band red-shifts at elevated temperatures. A single isosbestic point occurs in the *B*-band close to ~ 440 nm. (B) The same spectra shown in the preceding panel are plotted versus wave number. The inset shows an expanded view of the $Q(0,0)$ band, which is the absorption band excited in our 2D FS measurements. The $Q(0,0)$ band broadens slightly at elevated temperatures, but does not change shape significantly. (C) Differential scanning calorimetry data are shown for DSPC liposome samples prepared in the absence and presence of the $(ZnTPP)_2$ dimer. The gel-to-liquid-crystal phase transition occurs near 57 °C in DSPC.[67]

to temperature. We observed that the blue-edge of the *B*-band and the red-edge of the emission line shape became increasingly more pronounced as the temperature was raised, and that a single isosbestic point was present in the absorption spectrum of the *B*-band. These observations further suggest the existence of two equilibrium populations of species with blue-edge excitation correlated to red-edge emission, and red-edge excitation correlated to blue-edge emission. While these temperature-dependent changes of the spectral line shapes were significant, the $Q(0,0)$ and $Q(0,1)$ features exhibited very little sensitivity to temperature (see Figure 3.3B, inset). We further note that the DSPC liposome system undergoes a gel-to-liquid-crystal phase transition close to 57°C.[67] We determined by differential scanning calorimetry (DSC) that the transition temperature was shifted only slightly (~2°C) by the presence of the $(ZnTPP)_2$ chromophore (see Figure 3.3C).

In chloroform solution, the 2D FS spectra of $(ZnTPP)_2$ exhibited only a single diagonal feature, similar to those observed from monomeric ZnTPP. In low viscosity solvents, the $(ZnTPP)_2$ molecule can adopt a broad distribution of conformations, so that the exciton-coupling strength under these conditions is small compared to the spectral width of dynamic site energy disorder. However, depending on experimental conditions, the 2D spectra of $(ZnTPP)_2$ in DSPC liposomes exhibited multiple diagonal peaks and off-diagonal cross peaks. This suggested that interactions between the dimer and its local membrane environment resulted in preferred dimer conformations, which were reflected by specific couplings between the electronic transitions of the porphyrin residues. Thus the strengths of the electronic couplings in the membrane / $(ZnTPP)_2$ system were comparable to the spectral width of site energy disorder.

In order to test whether two major sub-populations of $(ZnTPP)_2$ conformations existed in our samples, we performed 2D FS experiments in which the lowest-energy emission band was spectrally filtered to selectively detect signals from different species. Figure 3.4 summarizes the results of these measurements, which were carried out at 17°C with the laser center frequency set to 16 470 cm^{-1} (607 nm). When we collected the entire low-energy emission band (using a 620 nm long-pass filter), we observed in the 2D FS total correlation function (TCF) spectrum well-separated blue- and red-shifted diagonal peaks (relative to the monomer), in addition to a cross peak positioned above the diagonal (see Figure 3.4A). However, when we selectively detected the blue-edge of the emission band (using a 620 nm long-pass filter in combination with a 650 nm short-pass filter), the intensity of the red-shifted diagonal peak was enhanced relative to that of the blue-shifted feature (see Figure 3.4B). Finally, when we isolated the red-edge of the emission band (using a 645 nm long-pass filter), we observed only the blue-shifted diagonal feature in the 2D FS spectrum (see Figure 3.4C).

The observations summarized in Figure 3.4 serve to illustrate an important principle of fluorescence-detected 2D optical coherence spectroscopy. While the 2D optical spectrum provides information about exciton coupled $Q(0,0)$ transitions resonant with the laser spectral bandwidth (~ 16 200 – 16 700 cm^{-1}), the signal can be selectively filtered by monitoring different regions of the emission line shape. We see that by detecting either the blue-edge or the red-edge of the lowest energy emission band (spanning the range 14 300 – 16 000 cm^{-1}), we obtained two qualitatively different sets of 2D optical spectra. These results are consistent with our temperature-dependent fluorimetry measurements (see Figure 3.3, and associated discussion), as they show that

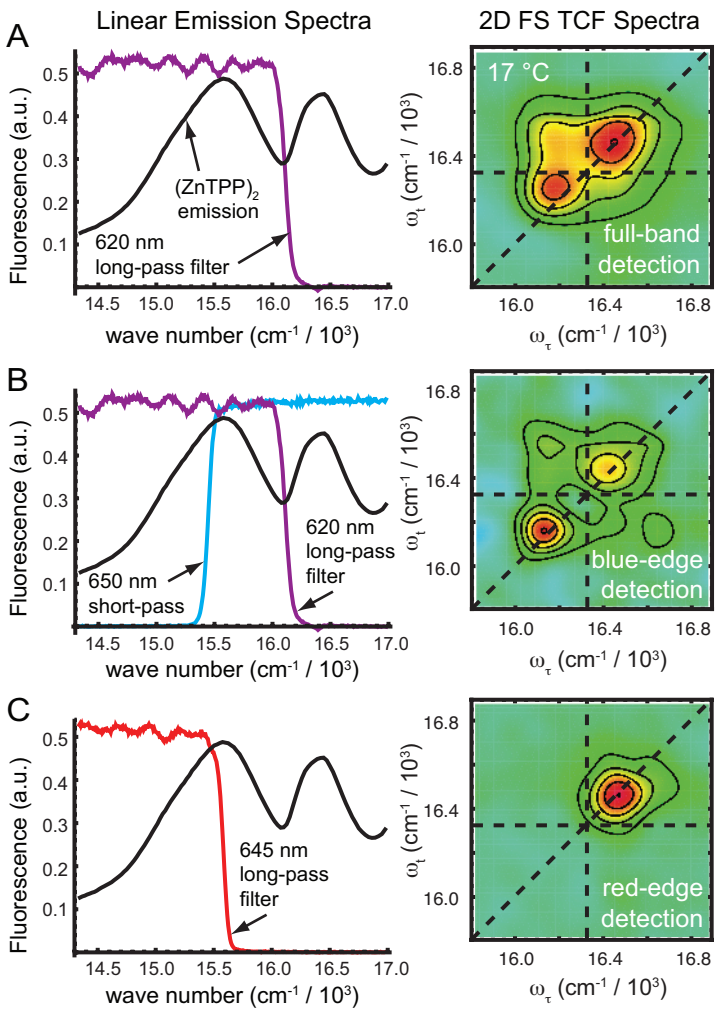

Figure 3.4. Spectral selection of conformational sub-populations by 2D FS. (A) Left panel: The transmission spectrum of a 620 nm long-pass filter (purple) is shown superimposed with the emission spectrum (black) of $(ZnTPP)_2$ in DSPC liposomes at 23 °C while exciting at 570 nm near the red edge of the $Q(0,1)$ band. This filter passes the majority of the lowest-energy emission band. Right panel: The real part of the 2D FS total correlation function (TCF) spectrum is shown, which was obtained using the 620 nm long-pass filter. For these data, the laser center frequency was 16 470 cm^{-1} (607 nm). The dashed horizontal and vertical lines indicate the monomer transition energy. (B) Left panel: The transmission spectra of the 620 nm long-pass filter (purple) and a 650 nm short-pass filter (blue) are shown superimposed with the emission spectrum. This filter combination passes mostly the blue-edge of the emission line shape. Right panel: The 2D FS spectrum obtained using this filter combination has an enhanced red-shifted feature. (C) Left panel: A 645 nm long-pass filter (red) passes mostly the red side of the emission line shape. Right panel: The 2D FS spectrum obtained with this filter exhibits an enhanced blue-shifted feature. The 2D spectra appear to be very different depending on whether the blue-edge or the red-edge of the emission line shape is detected.

fluorescence occurring on the blue-edge of the emission line shape is correlated to red-edge absorption of the $Q(0,0)$ feature (Figure 3.4B), and conversely that red-edge emission is correlated to blue-edge absorption (Figure 3.4C). Furthermore, these data provide strong support for our conjecture that the zinc porphyrin tweezer $(ZnTPP)_2$ adopts two very different conformations in DSPC liposomes, i.e., a weakly coupled J-dimer and a strongly coupled H-dimer with distinct absorption and emission properties, as illustrated in Figure 3.1B.

As we discussed above, we modeled the system in terms of a mixture of 'extended' and 'folded' conformations, which can be described as an electronically coupled H- and J-dimer, respectively, in the coupled two-dipole model. This model assumes that each ZnTPP monomer supports just a single "effective" EDTM, and it neglects relatively minor contributions to the electronic spectra due to the presence of orthogonally polarized degenerate Q_x and Q_y transitions within the planes of the ZnTPP macrocycles. Supporting this approximation, in our previous 2D FS theoretical modeling of self-assembled MgTPP dimers,[9] we found that most extended conformations gave rise to predominantly red-shifted absorption, which can be reasonably approximated as a four-level J-dimer, while most folded conformations gave rise to predominantly blue-shifted absorption, which can be approximated as a four-level H-dimer (see Figure 3.1B).

Because the spectral width of the $Q(0,0)$ feature of the $(ZnTPP)_2$ / liposome system was broader than the laser spectrum, we performed a series of 2D FS measurements in which the laser was progressively tuned across the absorption band (see Figure 3.5, right column). These 2D data served to fully characterize the exciton-split spectral features underlying the linear $Q(0,0)$ absorption line shape. Figure 5

summarizes the results of our measurements carried out at 23°C, although we performed the same set of measurements at seven different temperatures spanning 17 – 85°C. When the laser was tuned close to the $Q(0,0)$ absorption maximum (16 620 cm^{-1}, 602 nm), the 2D spectra exhibited a single diagonal feature, which was blue-shifted relative to the monomer transition energy (Figure 3.5A). When the laser was detuned just to the red of the $Q(0,0)$ maximum (16 470 cm^{-1}, 607 nm), the 2D spectra exhibited an intense blue-shifted diagonal peak, a relatively weak red-shifted diagonal peak, and an intense cross peak above the diagonal (Figure 3.5B). For the above two laser excitation frequencies, a 620 nm long-pass filter was sufficient to shield the detector from scattered laser light. Upon further detuning of the laser toward the red side of the absorption maximum, it was necessary to use a 635 nm long-pass filter to remove scattered laser light from the detection path. We found that as we progressively detuned the laser toward the red-edge of the $Q(0,0)$ maximum, the red-shifted peaks in the 2D spectra became correspondingly enhanced. At the same time, the effect of using the red-shifted emission filter was to

---

Figure 3.5 (next page)**.** Laser center frequency-dependence of 2D spectra, and optimized fits. Right column: The linear absorbance spectrum of the $Q(0,0)$ band of the $(ZnTPP)_2$ dimer in DSPC liposomes at 23°C is shown (dashed black curve), superimposed with Gaussian fits to the laser spectrum at four different center frequencies, as indicated. Left and center columns: (A) Experimental and simulated 2D FS spectra are shown for the laser center frequency set to 16 620 cm^{-1}. The simulated spectra were obtained by simultaneously fitting the linear absorbance spectrum and the 2D spectra using both 16 620 and 16 470 cm^{-1} excitation. (B) Experimental and simulated 2D FS spectra are shown for the laser center frequency set to 16 470 cm^{-1}. (C) Experimental and simulated 2D FS spectra corresponding to 16 340 cm^{-1} excitation. The simulated spectra were determined using the same parameters obtained from the fit to the data shown in panels (A) and (B), however the parameter d (ratio of H- to J-dimer fluorescence quantum yield) was adjusted to reflect the necessary change of the emission filter (discussed in text). (D) Experimental and simulated 2D FS spectra corresponding to 16 220 cm^{-1} excitation. These simulated spectra were determined using the same parameters as those used to simulate the 2D spectra shown in panel (C).

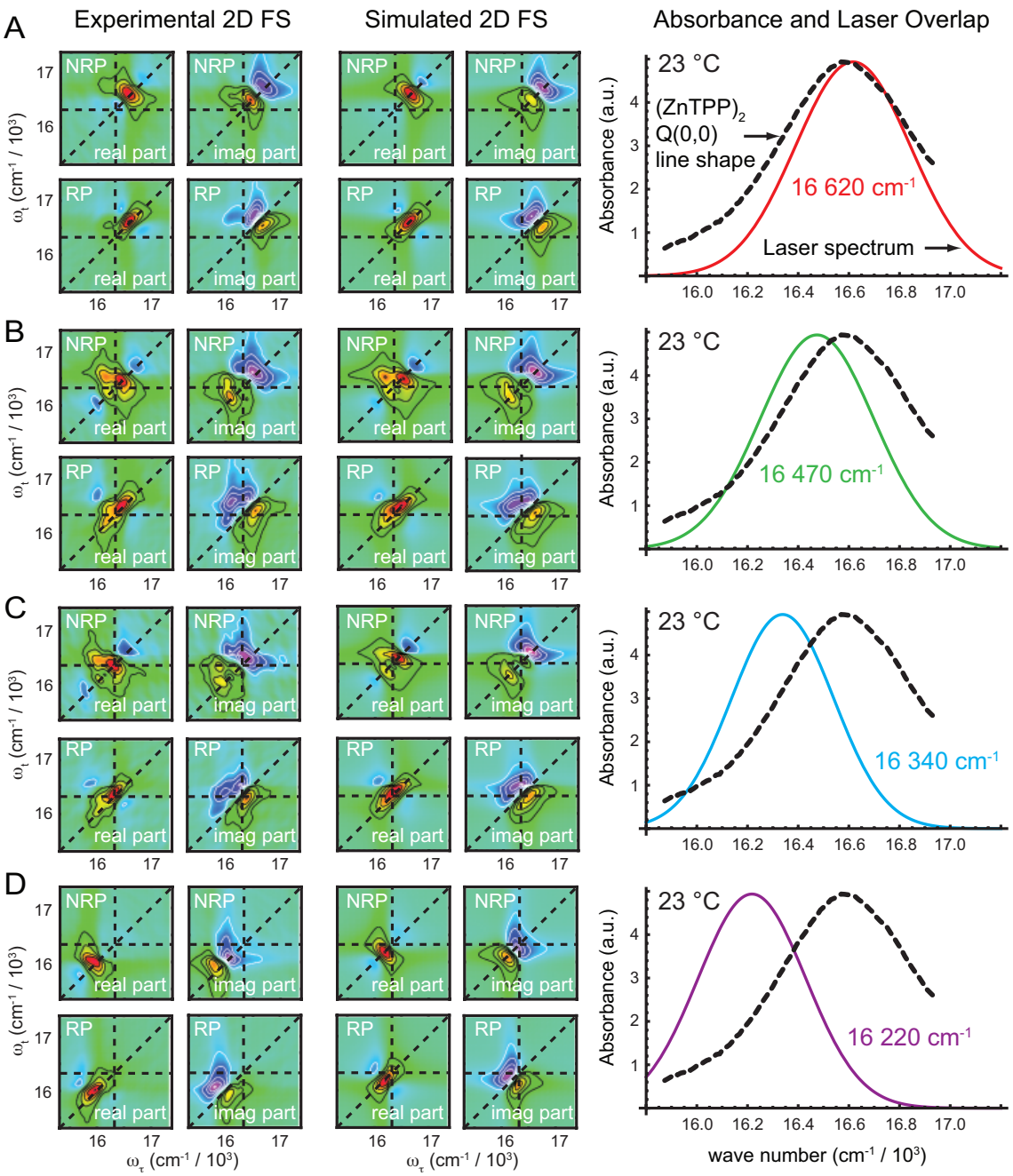
A
Experimental 2D FS
Simulated 2D FS
Absorbance and Laser Overlap
NRP
RP
real part
imag part
23 °C
(ZnTPP)2
Q(0,0)
line shape
16 620 cm-1
Laser spectrum
16 470 cm-1
16 340 cm-1
16 220 cm-1
Absorbance (a.u.)
ωt (cm-1 / 10³)
ωτ (cm-1 / 10³)
wave number (cm-1 / 10³)
B
C
D

enhance the blue-shifted features in the 2D spectra, as we previously discussed (see Figure 3.4). When the laser was further detuned to 16 340 cm^{-1} (612 nm), the two effects tended to cancel, leaving the relative intensities of the peaks nearly unchanged from the prior laser setting, while their absolute positions were somewhat shifted (Figure 3.5C). Finally, when the laser was detuned to 16 220 cm^{-1} (617 nm, still using a 635 nm long-pass filter), we observed in the 2D spectra an intense red-shifted diagonal peak and a weak cross peak above the diagonal (Figure 3.5D).

We performed model optimizations to the full set of temperature-dependent 2D FS and linear absorption data, assuming a binary mixture of H- and J-dimer species, as described in the Methods Section. For each of the 2D data sets that employed different laser excitation frequencies, we simulated the 2D spectra using the same sets of values for the model parameters (listed in Table 3.1), with one exception. For the cases with the laser frequency tuned to 16 340 cm^{-1} and 16 220 cm^{-1}, we allowed for a change in the parameter d, which described the ratio of detected fluorescence from the H-dimer relative to the J-dimer, from 0.0079 to 0.198. This change reflects the fact that for the experiments carried out with the laser tuned to 16 340 and 16 220 cm^{-1}, our use of the red-shifted detection filter (relative to the one used for 16 620 and 16 470 cm^{-1} excitation) resulted in a larger fraction of the detected fluorescence emanating from the H-dimer. Taking this experimental difference into account, we assumed that all other properties of the system were unchanged relative to those in experiments carried out with the laser tuned to 16 620 and 16 470 cm^{-1}. The simulated 2D FS spectra obtained using these parameters are shown along with the corresponding experimental data in Figure 3.5.

The results of our multi-parameter optimization over the complete range of temperatures investigated are summarized in Table 3.1, and a comparison between simulated and experimental data (for 607 nm excitation only) are shown in Figure 3.6. The optimized values reported for each temperature are solutions corresponding to the

Table 3.1. Optimized parameter values

Temp (°C)	17	23 (RT)	28	46	63	72	85
V_H (cm^{-1})[a]	[b]	295					
θ_H (°)[c]		18					
τ_H (fs)[d]	71	62	65	66	66	67	68
Γ_H [e]	0.94	1.33	1.48	1.04	1.02	0.90	0.63
σ_H (cm^{-1})[f]	354	374	384	393	416	431	413
V_J (cm^{-1})[g]		-123					
θ_J (°)		52					
τ_J (fs)	69	65	69	71	72	71	69
Γ_J	0.38	0.58	0.59	0.57	0.49	0.40	0.46
σ_J (cm^{-1})	57	50	50	50	60	50	50
σ_{lin} [h]	354	374	384	393	416	431	413
ε_1 (cm^{-1})[i]		16325					
b [j]	**8.56** ±0.07	**10.31** ±0.06	**10.40** ±0.06	**12.46** ±0.07	**13.81** ±0.08	**19.59** ±0.08	**21.69** ±0.06
d [k]		0.0079					

[a]Electronic coupling strength. Parameters with subscript H refer to the H-dimer species. [b]Empty boxes indicate that a given parameter was fixed at its room temperature value when performing the fit at another temperature. [c]Relative dipole angle of the two monomers. [d]Phenomenological dephasing time. [e]Fluorescence quantum yield of doubly-excited state relatively to singly-excited states. [f]Line shape overlap parameter. [g]Parameters with subscript J refer to the J-dimer. [h]Linear spectrum line width. [i]Monomer transition energy. [j]Ratio of H-dimer to J-dimer conformational popultions. Error bars determined according to the method of Lott et al.[8] [k]Ratio of H-dimer to J-dimer fluorescence quantum yields.

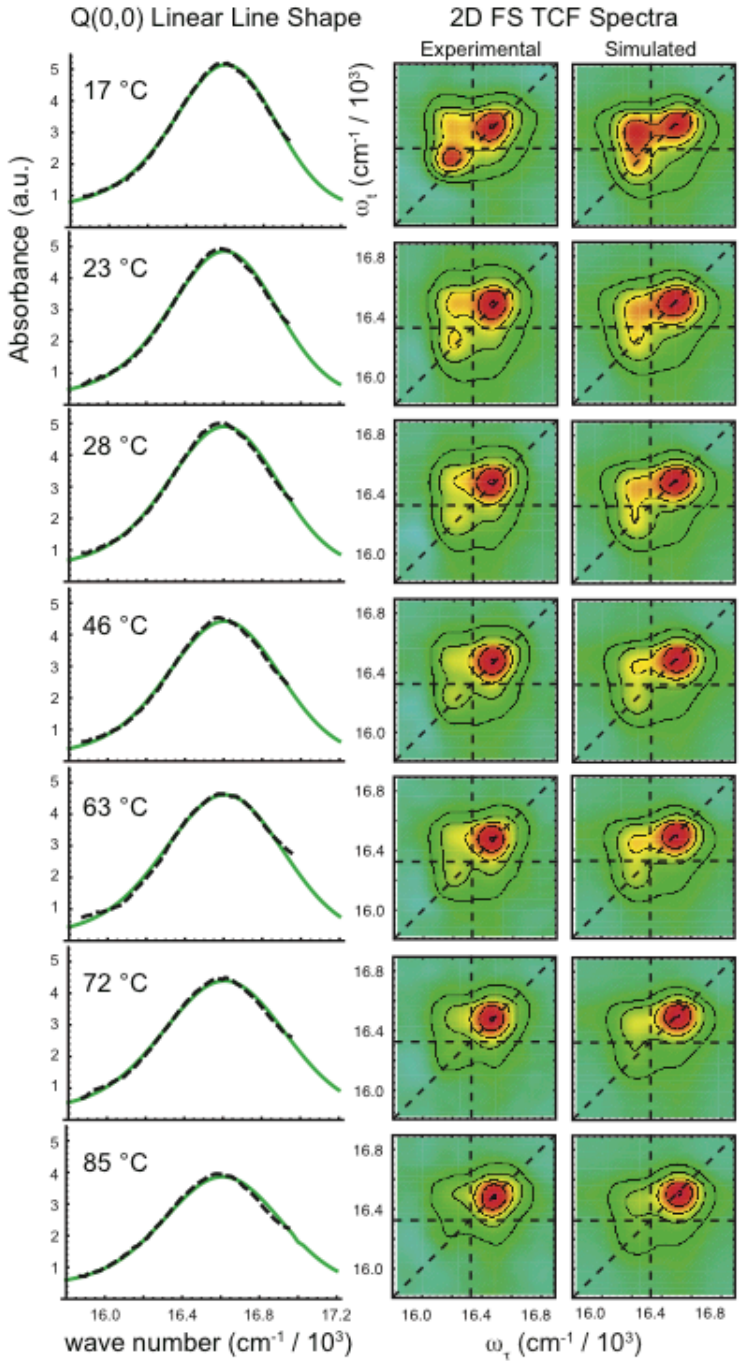

Figure 3.6. Temperature-dependent 2D FS and linear absorption data, and optimized fits. Left column: The linear absorption spectrum of the $Q(0,0)$ band of $(ZnTPP)_2$ dimers in DSPC liposomes (dashed black) is overlaid with its optimized fit (green) for each of the seven temperatures investigated. Right column: The real part of the 2D FS total correlation spectra is compared to its optimized fit for each temperature. As the temperature is increased, the red-shifted diagonal peak and the above diagonal cross peak decrease in intensity, corresponding to a loss in the relative population of J-dimer conformation. These temperature-dependent changes in the 2D spectral line shapes are consistent with those observed in the *B*-band of the linear absorption spectra.

minimized cost function χ^2_{tot}. The most striking change with temperature occurs in the parameter b, the relative population of H- to J-dimer (shown in bold font in Table 3.1). Error bars for b were determined according to a procedure we developed previously,[8] which we discuss further below (see Discussion Section). We emphasize that our best attempts to model these data using only a single dimer conformation were unsuccessful. Nevertheless, the full range of experimental data could be readily fit to the binary mixture model.

We note that the optimized room temperature solution exhibits a smaller exciton splitting for the J-dimer than for the H-dimer. This makes physical sense because the porphyrin residues are likely to be separated by a larger distance in the 'extended' conformation than in the 'folded' conformation (see Figure 3.7A). This is also consistent with our experimental observation that selective excitation of the blue-edge of the $Q(0,0)$ band (favoring excitation of the H-dimer) leads to red-edge emission, which follows from the fact that the larger coupling strength of the H-dimer places its lowest-energy singly-excited state at a lower energy than that of the J-dimer (see Figure 3.1B for energy level diagrams that illustrate this). Immediately after the H-dimer is excited, nonradiative relaxation to the lowest energy singly-excited state followed by solvation results in a larger fluorescence Stokes-shift than that of the corresponding J-dimer.

The 2D FS spectra reveal significant changes with temperature, despite the fact that they were obtained by exciting in the $Q(0,0)$ band, where the linear absorption spectrum changes very little (Figure 3.3B, inset). The temperature-dependent changes in the 2D FS spectra follow very closely to those seen in the *B*-band of the linear absorption spectrum, with the relative intensity of the blue-shifted peak increasing with raising

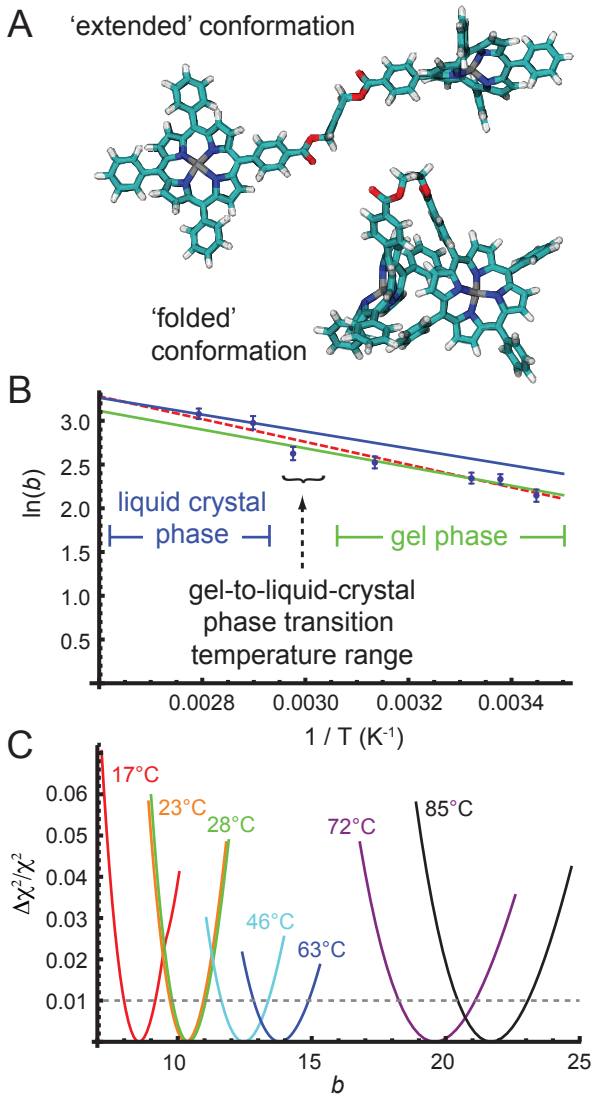

Figure 3.7. (A) Models of 'extended' and 'folded' conformations of the zinc porphyrin tweezer from the UFF structure optimizations. (B) Van't Hoff plot of the parameter ln(b) versus inverse temperature, where b is the ratio of H- to J-dimer population. Blue points with error bars are the values of b obtained from the optimizations to the linear absorption and 2D FS spectra over the full range of temperatures shown in Figure 3.6. The linear fits to these points (green and blue lines) yield the standard state changes in entropy and enthalpy associated with the 'extended'-to-'folded' conformational transitions in the gel and liquid-crystal phases, respectively. See Table 3.2 for values. (C) The relative deviation of the cost function $\Delta\chi^2_{tot}/\chi^2_{tot}$ from the optimized reference value $\chi^2_{tot,ref}$ is plotted as a function of the parameter b. Cross-sections of the cost function at each temperature have minima corresponding to the optimized value b_{ref}. The cross-section curvatures indicate the sensitivity of the optimizations to the uncertainty $\Delta b = b - b_{ref}$. Trust intervals were directly read out from these plots based on the approximately 1% relative error associated with the experimental data quality (indicated by the dashed horizontal black line).

temperature. All of these changes are consistent with an increase in the population of H-dimer at elevated temperatures, which is reflected by the temperature-dependence of the parameter b (see Table 3.1).

6. Discussion

The parameter b is the ratio of H- to J-dimer population, and is therefore equal to the equilibrium constant for the process by which the 'extended' conformation is converted into the 'folded' one. In Figure 3.7B, we present our results in the form of a Van't Hoff plot – i.e., the natural logarithm of b versus the inverse temperature. The error bars associated with the values of b are also shown in Figure 3.7B. Our determination of these uncertainties was based on a procedure we previously demonstrated for self-assembled porphyrin dimers, for which the data quality is very similar to that of the current study.[8] For each temperature, the relative deviation of the cost function $\Delta\chi^2_{tot}/\chi^2_{tot}$ from the optimized reference value $\chi^2_{tot,ref}$ was determined as a function of the parameter b. In Figure 3.7C are shown temperature-dependent cross-sections of the cost function over a range of values of b in the vicinity of the optimized value b_{ref}. Trust intervals were directly read out from these plots, based on the approximately 1% relative error associated with the experimental data quality (as indicated by the horizontal dashed line).

Taking error bars into account, the data shown in Figure 3.7B can be fit very well to a line over the full range of temperatures we investigated (17 – 85°C), with the exception of the point corresponding to 63°C. This was the only data set recorded at a temperature in the vicinity of the gel-to-liquid-crystal phase transition of the DSPC

liposomes, which occurs near 57°C. We note that the data presented in Figure 3.7B show a slight discontinuity close to the phase transition temperature.

Each of the linear fits to the data shown in Figure 3.7B has slope and y-intercept proportional to, respectively, the standard state changes in enthalpy and entropy of the monomer association process:

$$\ln b = -\frac{\Delta H_a^\circ}{RT} + \frac{\Delta S_a^\circ}{R} \tag{3.10}$$

We thus obtained values of ΔS_a° and ΔH_a° for the gel and the liquid crystal phases separately, as well as the values that result from considering the full range of temperatures. These results are listed in Table 3.2. For both the gel and the liquid crystal phases, we find $\Delta H_a^\circ \approx 50$ J mol^{-1} K^{-1} and $\Delta S_a^\circ \approx 10$ kJ mol^{-1}. For comparison, the enthalpy change upon breaking a single hydrogen bond in liquid water is 11 kJ mol^{-1}.[68]

Table 3.2. Thermodynamic parameters

	ΔS_a° (J mol^{-1} K^{-1})	ΔH_a° (kJ mol^{-1})
Gel phase[a]	49 ± 8	9 ± 2
Liquid crystal phase[b]	48 ± 22	8 ± 8
All points[c]	56 ± 3	10.9 ± 0.9

[a]Fit to 17, 23, 28 and 46°C data points. [b]Fit to 72 and 85°C data points. [c]Fit to 17, 23, 28, 46, 63, 72 and 85°C data points.

It is useful to decompose the thermodynamic parameters into contributions resulting from monomer-monomer and monomer-solvent interactions: $\Delta H_a^\circ = \Delta H_{a,M-M}^\circ + \Delta H_{a,M-solv}^\circ$ and $\Delta S_a^\circ = \Delta S_{a,M-M}^\circ + \Delta S_{a,M-solv}^\circ$. We have assumed that

contributions resulting from solvent-solvent interactions are negligible due to the low concentration of the porphyrin in the membrane. Since the association process is expected to lead to favorable contacts between the porphyrin residues, we may conclude that $\Delta H^{\circ}_{a,M-solv} \geq 10$ kJ mol^{-1} (considering the approximate values of $\Delta S^{\circ}_{a} \approx$ 50 J mol^{-1} K^{-1} and $\Delta H^{\circ}_{a} \approx$ 10 kJ mol^{-1}), where the equality holds in the limit $\Delta H^{\circ}_{a,M-M} \rightarrow 0$. Thus, the association process is opposed by the disruption of favorable enthalpic interactions between previously exposed porphyrin surfaces and the acyl chains of the membrane. The change in monomer-solvent enthalpic interactions upon association must therefore be larger in magnitude than the corresponding change in monomer-monomer interactions. The entropy change of the association process can be understood in a similar fashion. Because the porphyrin residues are connected together by a flexible linker, we expect the monomer-monomer entropy change of association to be small and negative, as relatively little conformational freedom is lost by the dimer in this process. Thus, the observed positive entropy change of association must be dominated by the monomer-solvent term: $\Delta S^{\circ}_{a,M-solv} \geq$ 50 J mol^{-1} K^{-1}, where the equality holds in the limit $\Delta S^{\circ}_{a,M-M} \rightarrow 0$. We therefore conclude that in both the gel and liquid crystal phases, the association process is largely driven by the increase in entropy of acyl side chains, which are liberated from their contacts with the porphyrin surfaces when the dimer folds. This membrane-facilitated association process is analogous to the hydrophobic effect that drives the folding of many proteins, in which folding is driven by the increase in entropy of water molecules that are liberated when the surfaces of the protein are buried.

We attempted to obtain rough estimates for the values of $\Delta H^{\circ}_{a,M-solv}$ and $\Delta S^{\circ}_{a,M-solv}$ by performing simple force field computer calculations. We carried out energy

minimizations for the models of the 'extended' and 'folded' conformations of the zinc porphyrin tweezer using the Universal Force Field (UFF) (shown in Figure 3.7A). From these calculations, we obtained the values $\Delta H^{\circ}_{a,M-M} \approx -238$ kJ mol^{-1} and $\Delta S^{\circ}_{a,M-M} \approx -115$ J mol^{-1} K^{-1}, which in turn allowed us to estimate $\Delta H^{\circ}_{a,M-solv} \approx 248$ kJ mol^{-1} and $\Delta S^{\circ}_{a,M-solv} \approx 165$ J mol^{-1} K^{-1} = 40 e.u., respectively. Since UFF fails to correctly predict the planar Zn-porphyrin coordination, the enthalpy estimates should be treated with caution. However, the entropy of the conformational change arises primarily from vibrational frequency changes in the flexible linker, for which UFF is expected to provide useful estimates.

The results of the current study provide further insights to, and are consistent with, the results of our previous experiments on self-assembled MgTPP dimers in DSPC liposomes.[8-9] In that work, we observed that monomers of MgTPP could spontaneously assemble into dimers, which adopted an open T-shaped structure within the membrane. The T-shaped conformation of the self-assembled porphyrin dimer did not form a compact structure to maximize porphyrin-porphyrin stacking interactions, suggesting that the association process was not driven by the direct interactions between porphyrin monomers. There would be a significant entropic cost to the association of the monomers, which in contrast to our current work were not linked together. Furthermore, there is a sizable enthalpic cost to bury the porphyrin surfaces, which could otherwise interact favorably with the acyl side chains. It is therefore very likely that the self-assembly of MgTPP dimers in DSPC liposomes is also driven by an increase in entropy of the acyl chains, which are liberated from their local contacts with the porphyrin residues, similar to protein assembly in membranes.[69-70]

It is important to reconsider at this stage the validity of the point-dipole approximation that we have implemented to model our data. Although the point-dipole model is proven to be useful to describe electronic coupling in a variety of chemical systems, its accuracy is questionable when the inter-chromophores separation is very small. We believe that the approach we have outlined could be applied in future studies to experimentally test the accuracy of higher levels of electronic structure theory and the limitations of point-dipole models.

The experiments presented in this paper illustrate a significant advantage of fluorescence-detected 2D electronic spectroscopy – different contributions to the nonlinear signal can be separated based on their fluorescence properties, such as emission wavelength (demonstrated here), fluorescence lifetime, or polarization. A particularly interesting application of this principle would involve placing a Förster resonance energy transfer (FRET) 'acceptor' chromophore on a molecule that binds to the 'donor' chromophore being excited. For example, the donor chromophore could be a pair of fluorescent nucleic acid base analogs such as 2-aminopurine (2-AP) dinucleotide incorporated into DNA,[11, 13] and the FRET acceptor chromophore could be placed on a protein that binds to DNA. Recording 2D FS spectra while using filters to collect either fluorescence directly from the 2-AP dinucleotide labeled DNA or from the FRET acceptor labeled protein would allow one to separately measure the 2D FS spectra of local DNA conformations in the unbound and bound states, respectively.

7. Conclusions

Using linear absorption, fluorescence and 2D FS, we studied the equilibrium conformations of a dimer composed of two ZnTPP residues connected by a flexible linker – i.e., a 'zinc porphyrin tweezer', which was suspended within the amphiphilic regions of a liposome membrane. We determined that the porphyrin tweezer exists within the membrane as a mixture of 'extended' and 'folded' conformations. This was accomplished using a novel approach to 2D FS in which the fluorescence was spectrally filtered to select signals from different components of the mixture. By fitting the linear absorption and 2D FS spectra over a series of temperatures, we determined the values of the enthalpy and entropy changes associated with the conformational transition between 'extended' and 'folded' states. Our results indicate that the enhanced stability of the folded state at elevated temperatures is driven by an increase in entropy of the membrane acyl chains, which are liberated from their local contacts with porphyrin surfaces when the dimer folds. Future work on this system will investigate the excited state relaxation pathways of the zinc porphyrin tweezer within its local membrane environment, the kinetics of interconversion between conformational sub-states, and the relationship between conformational transitions and spectral diffusion.

8. Summary and Bridge to Chapter IV

It was shown by a combination of absorption spectroscopy, fluorometry and 2D FS that $(ZnTPP)_2$ adopts a mixture of folded and extended structures when incorporated into a membrane, and that the relative population of the folded structure increases with temperature. By applying a Van't Hoff analysis to the temperature-dependent data, it was

found that the folding of $(ZnTPP)_2$ is driven by an increase in the entropy of lipid side chains that are liberated from their contacts with the porphyrins upon folding. This is analogous to the hydrophobic effect, which drives the folding of many proteins in aqueous solution. A key experiment that allowed us to make these conclusions was the measurement of 2D FS spectra in which the sample's fluorescence was filtered so as to separate the signals from the folded and extended subpopulations. Any property related to fluorescence, such as lifetime or polarization, could potentially be used to separate signals from the components of a mixture. As proposed in the final paragraph of section VI above, I have performed proof-of-principle experiments in which a FRET acceptor was incorporated into the sample and 2D FS spectra were measured by collecting only signal from the donor or only from the acceptor. These experiments are described in Chapter IV, along with other experiments aimed at understanding the interactions of forked DNA with bacteriophage T4 helicase and primase.

CHAPTER IV

SPECTROSCOPIC INVESTIGATION OF CY3-LABELED DNA IN COMPLEXES WITH BACTERIOPHAGE T4 HELICASE AND PRIMASE

1. Overview

In Chapter III, I described experiments in which 2D FS signals were measured while filtering the fluorescence emission in order to selectively record signals from different subpopulations of the sample. It was suggested in the discussion section that any fluorescence property could be used in a similar manner to separate signals from mixtures. This chapter describes experiments demonstrating this using the property of fluorescence resonance energy transfer (FRET), and this approach is applied to the study of cyanine-labeled DNA constructs. Linear spectroscopic approaches using these constructs are also applied to study protein-DNA interactions in the bacteriophage T4 primosome. This chapter contains unpublished co-authored material. The experiments were conceived and planned in collaboration with A. H. Marcus and P. H. von Hippel, and the data collection was performed with help from L. Kringle and D. Jose.

2. Introduction

The bacteriophage T4 DNA replication system is often used as a model for the replication systems of higher organisms, because it operates in the same basic manner with a helicase unwinding the DNA, a primase laying down RNA primers on the lagging strand, and two polymerases replicating the leading and lagging strands in an antiparallel fashion (see Figure 1.1).[3] The 'primosome,' which performs the function of processively

unwinding double-stranded DNA so that it can be replicated as well as synthesizing RNA primers, includes six helicase (gp41) subunits, one primase (gp61) subunit, and six molecules of guanosine triphosphate (GTP). The primosome preferentially binds to fork junctions between single-stranded and double-stranded DNA. In the absence of gp61, the gp41/GTP hexamer exists in equilibrium between fork-bound and unbound states and unwinds DNA in a non-processive manner through the hydrolysis of GTP. Upon the addition of gp61 the equilibrium collapses to the bound state, and the helicase can unwind DNA processively through GTP hydrolysis. Numerous experiments have revealed the subunit stoichiometry (6 gp41 : 6 GTP : 1 gp61) and assembly pathway of the functional primosome, as well as how it unwinds DNA by taking advantage of 'breathing' fluctuations at the fork.[24, 71]

'Internal' cyanine dye labels (Figure 4.1A) have found utility in the field of single molecule spectroscopy due to their greatly enhanced photostability in comparison with the more widely used 'external' labels.[21] They also have the benefit of a low spatial profile, which can be important for the T4 primosome, in which the lagging strand of DNA passes through the center of the gp41 hexameric ring.[3] Because of these benefits, it is important to characterize the conformations adopted by these internal labels in positions of interest, such as in duplex regions of DNA and at replication forks. In doing so, we will learn what aspects of DNA conformation these labels report on and to what extent they perturb the native DNA conformation.

In the experiments described in this chapter, I investigate the effects of gp41 and gp61 on the conformations adopted by Cy3-labeled DNA. This was accomplished by comparing the absorption, fluorescence and circular dichroism spectra of forked DNA

constructs labeled with two cyanine dye fluorophores placed either in the duplex region or at the fork junction. This system was also used to demonstrate the feasibility of FRET-filtered 2D FS using high- and low-FRET DNA control samples.

A

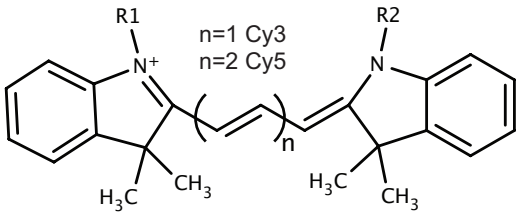

B

D1 3' GTC AGT ATT ATA CGC TCy3C GCT AAT ATA TAC GTT TTT TTT TTT TTT TTT TTT TTT TTT TTT T 5'
D2 5' CAG TCA TAA TAT GCG ACy3G CGA TTA TAT ATG CTT TTA CCA CTT TCA CTC ACG TGC TTA C 3'
D3 5' CAG TCA TAA TAT GCG ATG CGA TTA TAT ATG CTT TTA CCA CTT TCA CTC ACG TGC TTA C 3'
D4 3' GTC AGT ATT ATA CGC TCy5C GCT AAT ATA TAC GTT TTT TTT TTT TTT TTT TTT TTT TTT TTT T 5'
D5 5' CAG TCA TAA TAT GCG ACy5G CGA TTA TAT ATG CTT TTA CCA CTT TCA CTC ACG TGC TTA C 3'

F1 3' AGA GGA GCA GAG GGA GCA CAG CAG AGG TCA GTA TTA TAC GCT Cy3CG CTG GTA TAC CAC GTT T (x29) 5'
F2 5' CTC CCT CGT GTC GTC TCC AGT CAT AAT ATG CGA Cy3AT GCT TTT ACC ACT TTC ACT CAC GTG CTT A 3'
F3 5' CTC CCT CGT GTC GTC TCC AGT CAT AAT ATG CGA TAT GCT TTT ACC ACT TTC ACT CAC GTG CTT A 3'

C

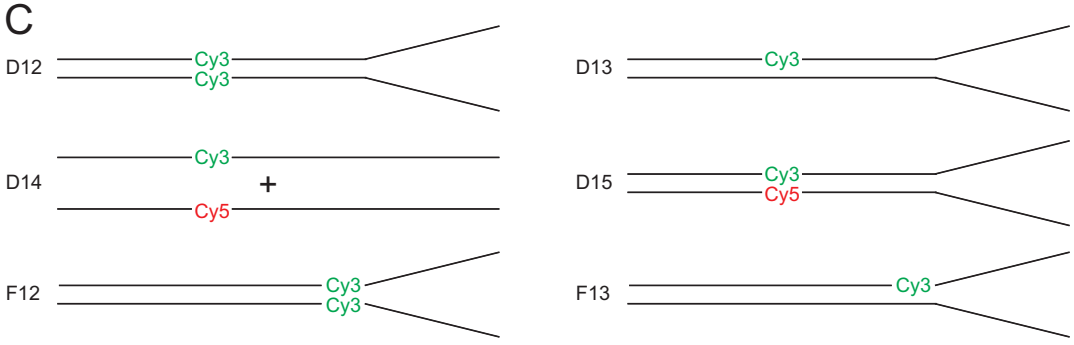

Figure 4.1. Samples used in studies of T4 primosome interactions with forked DNA. (A) Structures of the dyes used in these studies: internally labeled Cy3 and Cy5. Cy3 has three carbons connecting the two fused ring structures; Cy5 has five carbons. (B) Oligonucleotide sequences used. "D" stands for "duplex" and "F" stands for "fork," indicating the location of the dye(s) once the oligo is annealed to its complimentary strand. (C) Schematics of the structures formed from different combinations of the oligos shown in B. Closely spaced parallel lines indicate a duplex region.

3. Experimental Methods

The samples used in these studies were oligonucleotides that were 'internally labeled' with the cyanine dyes Cy3 or Cy5. The sequences and structures (and the nomenclature that will be used to refer to them) are shown in Figure 4.1. The samples used for absorption and fluorescence experiments were 400 nM or 500 nM, the samples used for 2D FS were 500 nM, and the samples used for CD were 1 μM. All double-stranded samples were annealed before use by heating the sample to 95°C for 3 minutes, then allowing it to cool overnight.

For all experiments using protein, a solution of DNA (500 nM), GTP-γS (60 μM) and gp41 (3 μM) was prepared and measured, with the gp41 being added last. Then gp61 was added so as to attain a concentration of 500 nM and the sample was measured again. A 500 nM solution of DNA alone was prepared separately and measured. The 0.6% dilution that resulted when gp61 was added was accounted for in the data processing. All fluorescence measurements were performed by exciting the sample at the peak of its absorption spectrum in the absence of protein, and scanning the emission wavelength. HPLC-purified oligonucleotides were purchased from Integrated DNA Technologies and used as received. HPLC-purified GTP-γS was purchased from Sigma Aldrich and used as received. gp41 was stored at -80°C in aqueous buffer, and gp61 was stored at -20°C in glycerol.

A. Fluorescence Resonance Energy Transfer (FRET)

When a molecule absorbs a photon in the visible or ultraviolet wavelength range, it enters an electronic excited state, which may return to the ground state through nonradiative relaxation or fluorescence. Under certain conditions, other pathways are

available. If another fluorophore (the 'acceptor') is present in the vicinity of the excited one and absorbs light at the wavelengths at which the first fluorophore (the 'donor') emits, the excitation can be transferred from the donor to the acceptor in a process called fluorescence resonance energy transfer (FRET). This process happens with an efficiency E given by eq 4.1,

$$E = \frac{1}{1+(r/R_0)^6} \tag{4.1}$$

where r is the distance between the donor and the acceptor and R_0 is the Förster critical transfer distance for that donor-acceptor pair. This distance is given by eq 4.2,

$$R_0^{\,6} = \frac{9Q_0 \ln(10)\kappa^2 J}{128\pi^5 \eta^4 N_A} \tag{4.2}$$

where Q_0 is the fluorescence quantum yield of the isolated donor, κ^2 is the orientation factor, which equals 2/3 for randomly oriented donors and acceptors, J is the overlap integral, which reflects how well the emission spectrum of the donor overlaps with the absorption spectrum of the acceptor, η is the refractive index of the medium, and N_A is Avogadro's number.[72]

Due to the $(r/R_0)^6$ term in the denominator of eq 4.2, E is sensitive to r over a range around $r = R_0$, and approaches 1 for $r << R_0$ and 0 for $r >> R_0$. This sensitivity to r can be used to study the distances between different components of a macromolecular

machine or different parts of a single macromolecule. Doing so involves exciting the donor fluorophore and monitoring the emission from both the donor and the acceptor.

B. FRET-Filtered 2-Dimensional Fluorescence Spectroscopy

FRET-filtered 2D FS involves exciting a donor chromophore and comparing the 2D FS signals obtained while using filters to selectively record donor or acceptor fluorescence. For example, the donor chromophore could be an exciton-coupled dimer of Cy3 dyes incorporated into a DNA construct, and the acceptor chromophore could be a Cy5 dye placed on a protein that binds to the DNA. A conventional 2D FS experiment would reveal the average conformation of the Cy3 dimer. A FRET-filtered 2D FS experiment, on the other hand, would separately reveal the conformations of the Cy3 dimer when the protein is not bound (if the Cy3 fluorescence is detected) or when the protein is bound (if the Cy5 fluorescence is detected).

A control experiment is shown in Figure 4.2. Figure 4.2A shows the absorption and fluorescence spectra of a mixture of single-stranded DNA molecules that are identical except that half contain Cy3 and half contain Cy5 (sample D14, see Figure 4.1). The donor and acceptor are therefore far apart, and excitation of the donor leads to emission primarily from the donor. Figure 4.2B shows the signals from a sample in which the Cy3 and Cy5 are on complimentary regions of a forked DNA construct (D15). They are therefore held rigidly in close proximity to each other, and excitation of the donor leads to emission primarily from the acceptor.

The same behavior can be seen through the lens of 2D FS. For a sample containing only Cy3 (D12), similar spectra are seen through the Cy3 and Cy5 filters but the signal is 30 times more intense through the Cy3 filter. This suggests that about 1/30

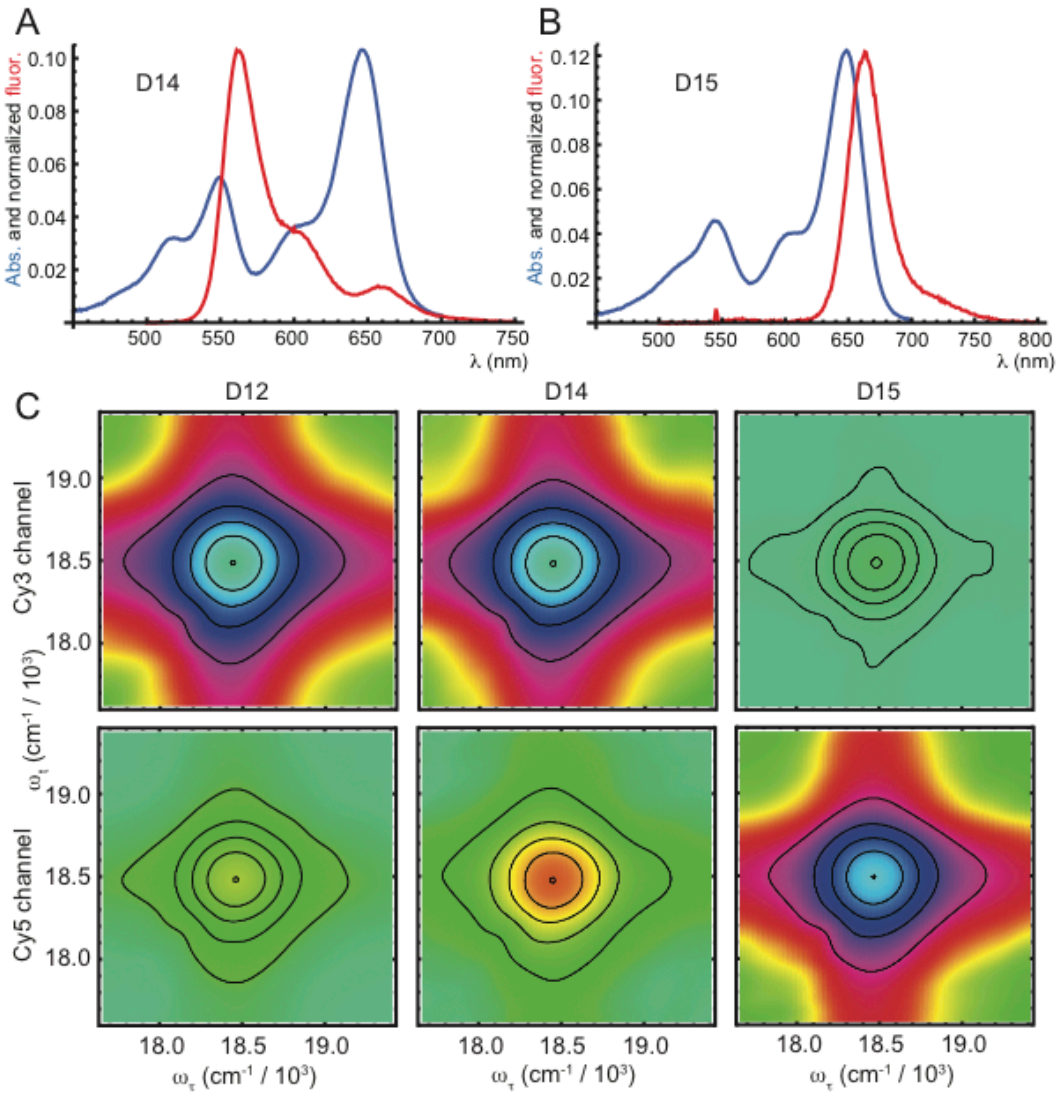

Figure 4.2. Fluorescence and 2D FS spectra of control samples demonstrating FRET-filtered 2D FS. (A) Absorption (blue) and fluorescence (red) spectra of the sample D14, which is a mixture of non-complimentary single-stranded oligos containing Cy3 (D1) and Cy5 (D4). When Cy3 is excited in this sample, nearly all the fluorescence observed is emission from Cy3. (B) Absorption and fluorescence spectra of D15, in which a Cy3 and Cy5 are placed directly opposite each other in a duplex region of the construct. In this sample, when Cy3 is excited, the fluorescence observed is almost exclusively emission from Cy5, indicating a FRET efficiency close to 100%. (C) Control FRET-filtered 2D FS spectra (absolute value of difference signal). The sample J12, which contains Cy3 but not Cy5, exhibits a strong signal in the Cy3 channel and a small amount of leakage in the Cy5 channel. The low-FRET control J14 exhibits strong Cy3 signal and a weak Cy5 signal that is nevertheless about 2x stronger than J12's Cy5 signal. High-FRET control J15 exhibits a very weak Cy3 signal and a strong Cy5 signal. The Cy5 signal captures the 2D FS excitation spectrum of the Cy3 dye. In these spectra, the density plot uses an Arcsinh scale to allow the weaker spectra to be seen, and the contours are placed at 20, 40, 60, 80 and 100% of the raw signal amplitude.

as much Cy3 fluorescence leaks through the Cy5 filter as the Cy3 filter. For the low FRET sample containing Cy3 and Cy5 (D14), the Cy3 signal is 15 times more intense than the Cy5 signal, consistent with the small but detectable amount of FRET seen in this sample by linear fluorescence spectroscopy, in addition to the leakage seen in the Cy3 only sample. For the high FRET control sample (D15), the Cy3 signal is about 150 times *less* intense than the Cy5 signal, but the 2D spectrum looks nearly identical through both channels. Figure 4.2C and Table 4.1 summarize these results. These control measurements establish the feasibility of FRET-filtered 2D FS by showing that the 2D spectrum of the donor can be accurately recorded by monitoring the fluorescence of the acceptor.

Table 4.1. FRET-filtered 2D FS signal intensities

Sample[a]	Cy3 channel inten.[b]	Cy5 channel inten.[c]	Cy3/Cy5 ratio[d]
D12	3.78	0.12	31.5
D14	3.73	0.26	14.3
D15	0.02	2.71	1/135.5

[a]See Figure 4.1C. [b,c]Max intensity of the absolute value of the difference signal using a filter that passes primarily Cy3 (b) or Cy5 (c) fluorescence. [d]Column 2/Column 3.

4. Results and Discussion

A. Absorption and Fluorescence Spectroscopy

Single-stranded constructs like D1 as well as double-stranded constructs containing only one Cy3 such as D13 show the expected spectra for DNA containing a Cy3 monomer (Figure 4.3A). This consists of a peak at 260 nm resulting from the

absorption of the native bases and a vibronic progression with its most intense peak centered at 549 nm resulting from the Cy3 absorption. When a second Cy3 is added, the results vary depending on whether the two Cy3s are in the duplex region or at the fork. When compared to the Cy3 monomer constructs, both Cy3 dimer constructs exhibit an increase in intensity near the wavelength of the second vibronic peak, about 515 nm. Changes similar to this have been observed in cyanine aggregates that self-assemble in solution, and this peak is often called the 'dimer peak'.[22, 73] In the duplex-labeled construct D12, the lowest-energy Cy3 peak broadens and redshifts, with a shoulder at the original absorption maximum of 549 nm. In contrast, in the fork-labeled construct F12 this peak exhibits no shift and only slight broadening.

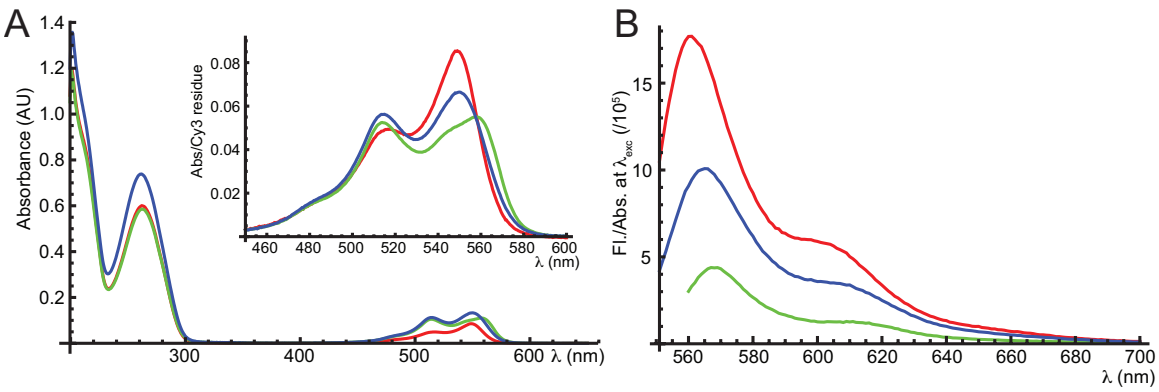

Figure 4.3. Absorption and fluorescence spectra of Cy3-labeled DNA constructs. (A) Absorption spectra of duplex-labeled Cy3 monomer D13 (red), duplex-labeled Cy3 dimer D12 (green) and fork-labeled Cy3 dimer F12 (blue). The inset shows a closeup of the Cy3 absorption region, scaled by the number of Cy3s in the molecule. (B) Emission spectra, scaled by absorbance at the excitation wavelength, of D13 (red), D12 (green) and F12 (blue). These spectra were obtained by exciting in the Cy3 band at the wavelength of maximum absorbance.

The fluorescence spectra of all the constructs investigated are roughly the mirror image of the monomer absorption spectrum, and each construct has a Stokes shift of

approximately 20 nm (Figure 4.3B). Even D12 and F12, whose absorption spectra are so different from those of the monomeric samples, exhibit similar fluorescence lineshapes to the monomers as a result of the fact that fluorescence emission occurs primarily from the lower-energy single-exciton state. The intensity of emission varies between constructs, though. When scaled by the absorbance at the excitation wavelength, D12's emission is quenched by a factor of about 4 relative to single-stranded samples, and F12's emission is quenched by about a factor of 2. This fluorescence quenching is consistent with the formation of H-type dimers in the case of D12 and F12, as explained in Chapter III. Double-stranded monomeric samples D13 and F13 may have slightly higher fluorescence intensities than the single-stranded samples, though this is a much smaller effect.

B. Circular Dichroism Spectroscopy

All samples investigated exhibit the expected sigmoidal signals in the native base region of the spectrum (Figure 4.4A). In the Cy3 region of the spectrum, single-stranded monomer D1 exhibits a weak positive signal ($\Delta\varepsilon \sim 5$) with the same shape as the Cy3 absorption spectrum. In duplex-labeled monomer D13, the signal remains weak but changes sign ($\Delta\varepsilon \sim -8$). In D12, exciton coupling between the Cy3 residues leads to a strong couplet ($\Delta\varepsilon \sim 400$ at 560 nm) with a positive feature centered near the absorption maximum and a negative feature centered near the secondary maximum of 515 nm (Figure 4.4B). F12 also exhibits an exciton couplet, but both of its peaks are redshifted by about 5 nm relative to those of D12, and their signs are opposite. This suggests a drastic change in conformation, perhaps even an inversion of chirality, upon moving the Cy3s from the duplex to the fork.

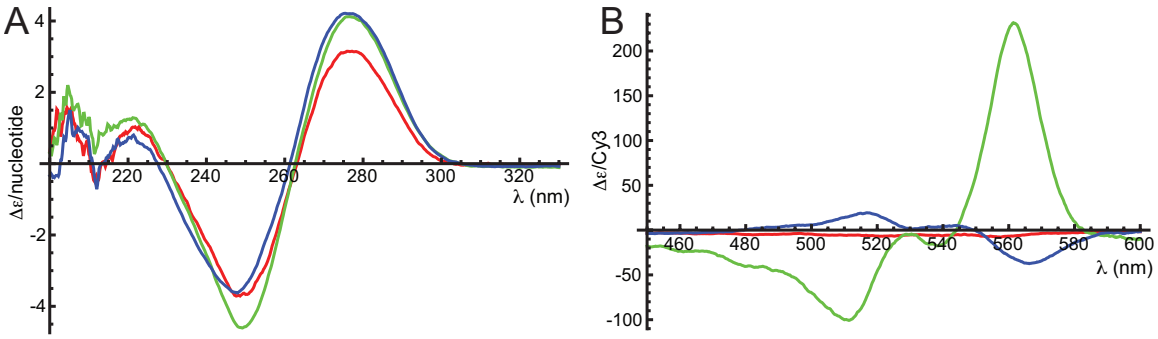

Figure 4.4. Circular dichroism spectra of Cy3-labeled DNA constructs. (A) CD signal per nucleotide of D13 (red), D12 (green) and F12 (blue) in the native base absorption region. (B) CD signal per Cy3 residue of D13 (red), D12 (green) and F12 (blue) in the Cy3 region.

C. Temperature-Dependent Spectroscopy

The absorption spectra of D12 and F12 show significant changes with temperature, reflecting pre-transitions as well as the melting of the double-stranded region of the DNA construct. In D12, as the temperature is increased, there is a significant decrease in intensity on the red edge of the lowest-energy absorption peak at low temperature (15 - 55°C). Then, over the range of 60 - 70°C, the 549 nm peak increases in intensity and the 515 nm peak decreases, yielding a spectrum that looks much like the monomer spectrum. Over the same temperature range, the native base absorption at 260 nm increases. We therefore assign these changes to the melting of the duplex region of the DNA, while the decrease in the red edge of the lowest-energy absorption peak must result from a pre-transition that is local to the Cy3 dimer. F12 exhibits similar changes over the dsDNA melting range, which is higher in temperature (75 - 85°C) due to the fact that F12 has a longer duplex region (33 vs. 26 base pairs) with higher G-C content (52% vs 35% G-C) than D12. F12 shows changes at temperatures lower than the main melting transition (small decreases in the 549 and 515 nm Cy3

peaks), but these changes are much smaller in magnitude than those seen in D12. This may be due to the fact that because there are only base pairs to one side of the Cy3 dimer in F12, the dimer itself is already 'melted' to some extent even at room temperature.

D. Effects of gp41 and gp61

The changes in the spectra of D12 and F12 upon addition of gp41 and gp61 indicate that the proteins bind to the fork, with the binding being enhanced by the presence of gp61. The changes in signal upon adding gp41 and GTP-γS to D12 are minimal. There is perhaps a slight decrease in the intensity of the 515 nm absorption peak (Figure 4.6A). When gp61 is added, there is a slight further decrease in the intensity of the 515 nm peak and perhaps a slight increase in fluorescence intensity. No shifts in the absorption or fluorescence spectra are observed. These results were expected because in the presence of the non-hydrolysable GTP analogue GTP-γS, gp41 is unable to unwind

---

Figure 4.5 (next page). Temperature-dependent absorption spectra of D12 and F12. (A) The Cy3 (left column) and native base (right column) regions of the absorption spectrum of D12 as a function of temperature. In the Cy3 region, the lowest-energy feature decreases in intensity over the range of 15 - 55°C, then the spectrum converts to a monomer-like spectrum (see Figure 4.3A) over the range of 60 - 70°C. In the native base region, the intensity increases over the range of 60 - 70°C. The temperatures plotted are 15 (red), 25 (orange), 35 (green), 45 (cyan), 55 (blue), 65 (purple), 75 (brown) and 85°C (black). (B) The Cy3 and native base regions of the absorption spectrum of F12 as a function of temperature. F12 shows only minor changes in its absorption spectrum at low temperature, then melts over the range of 75 - 85°C. The temperatures plotted are 15 (red), 25 (orange), 35 (yellow), 45 (green), 55 (cyan), 65 (blue), 75 (purple), 80 (brown) and 85°C (black). (C) Melting curves of D12 tracking the absorption at 549 nm (left column) and 260 nm (right column). Both show cooperative melting in the range of 60 - 70°C. (D) Melting curves of F12 tracking the absorption at 549 nm and 260 nm. Both show cooperative melting over the range of 75 - 85°C.

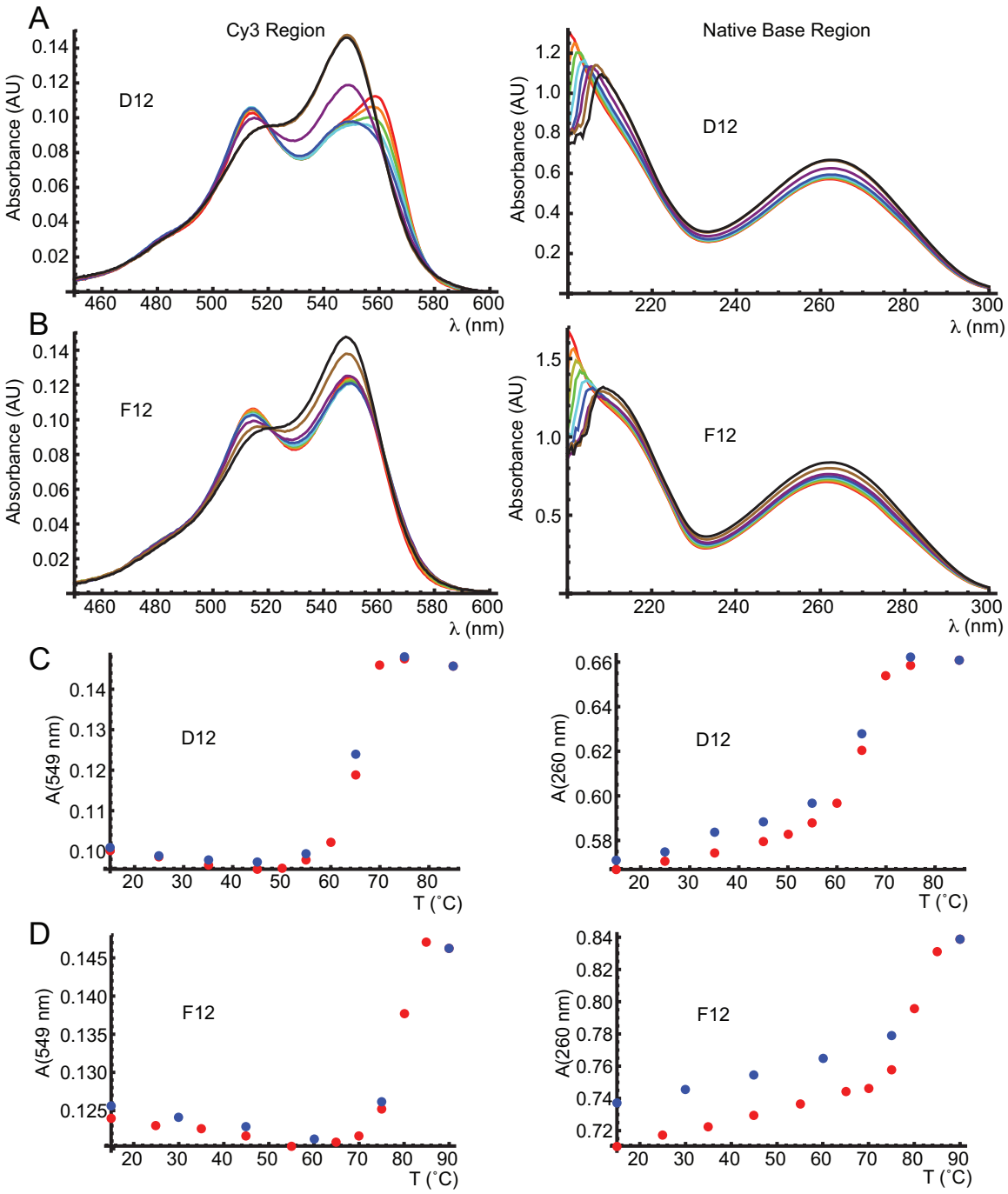
A
Cy3 Region
Native Base Region
D12
Absorbance (AU)
λ (nm)
B
F12
C
A(549 nm)
A(260 nm)
T (˚C)
D

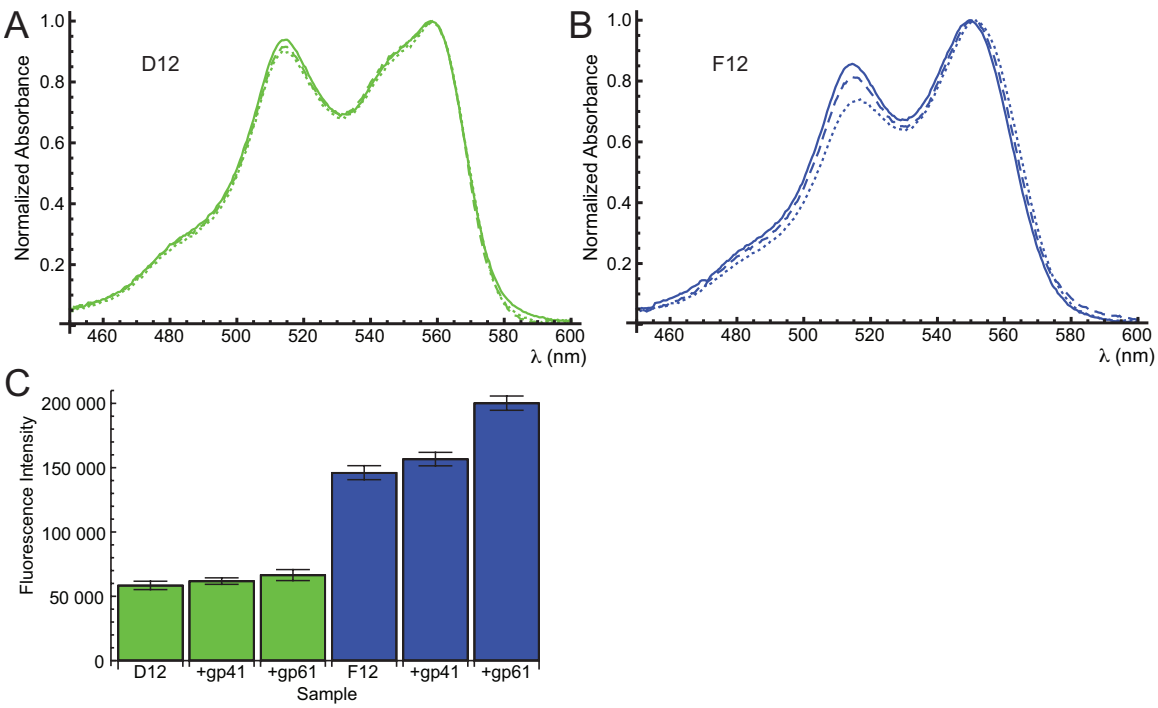

Figure 4.6. Effects of gp41 and gp61 on duplex- and fork-labeled DNA constructs. (A) Absorption spectra of D12 (solid), 1:6 D12:gp41 with excess GTP-γS (dashed), and 1:6:1 D12:gp41:gp61 with excess GTP-γS (dotted). There is very little change in the spectrum upon addition of the proteins. (B) Absorption spectra of F12 (solid), 1:6 F12:gp41 with excess GTP-γS (dashed), and 1:6:1 F12:gp41:gp61 with excess GTP-γS (dotted). The relative intensity of the 515 nm peak decreases and the 550 nm peak redshifts upon addition of the proteins. (C) Fluorescence intensities of D12 (green bars) and F12 (blue bars) in the presence of gp41 and gp61. The fluorescence intensity of F12 increases when gp61 is added.

DNA. The dyes, which are buried in the duplex region in D12, were therefore expected to be unperturbed by the presence of protein. The results are very different in the case of F12. The addition of gp41 and GTP-γS results in a larger decrease in the intensity of the 515 nm absorption peak than that seen in D12, as well as a slight redshift in the 549 nm peak (Figure 4.6B). The fluorescence intensity increases slightly. When gp61 is added, there is a further decrease in the intensity of the 515 nm absorption peak and a further redshift in the 549 nm peak, as well as a 26% increase in fluorescence (Figure 4.6C). These changes are consistent with the Cy3 dyes at the fork being separated from one

another by the presence of the gp41, whose binding to the fork is stabilized by gp61. The decrease in the intensity of the 515 nm absorption peak and the increase in fluorescence both suggest that the Cy3s are behaving more like monomers in the presence of protein than in the bare F12 construct. When compared to the spectra of the single-stranded Cy3 monomer strands that F12 is constructed from, however, the spectrum of F12 in the presence of gp61 still has a significantly more intense 515 nm peak, a broadened and redshifted 549 nm peak, and quenched fluorescence. This suggests that the Cy3s remain close enough to exhibit coupling even in the presence of the primosome.

Binding of gp41 and gp61 does not change the sign of the CD spectrum of either D12 or F12 (data not shown), indicating that the difference in conformation between the probes in these two constructs is preserved upon protein binding. This suggests that the 'inverted' conformation of F12 is the conformation needed for binding, and that it perhaps contributes to the recognition of the fork by gp41 and gp61.

5. Conclusions

The experiments presented in this chapter confirm the results of earlier experiments that studied the behavior of gp41 and gp61 using different probes. They show that Cy3 dimers are a sensitive probe of DNA conformation, revealing differences in DNA conformation between the duplex and the fork, and changes in the fork conformation upon protein binding. In addition, the Cy3 signal of D12 exhibits a pre-melting transition at low temperature, while in F12 it melts along with the double-stranded DNA. In F12, the increase in fluorescence and decrease in 515 nm peak intensity upon gp61 binding suggest that the presence of the proteins leads to a partial

opening of the fork. Ongoing work applying 2D FS to D12 and F12 will yield more detailed understanding of the differences in conformation between the duplex region and the fork, and how these conformations are recognized by gp41 and gp61.

Control experiments on Cy3 and Cy5-labeled DNA showed that FRET-filtered 2D FS can be used to distinguish between the 2D signals of high- and low-FRET states in the sample, and that the appearance of the 2D spectrum is preserved when it is detected through the acceptor channel after energy transfer. Applying FRET-filtered 2D FS to D12 and F12 using Cy5-labeled gp61 will allow us to dissect the differences in conformation between the bound and unbound species.

6. Summary and Bridge to Chapter V

In this chapter, I have presented experiments utilizing cyanine dyes as probes to investigate the interactions of bacteriophage T4 helicase and primase with forked DNA. Absorption and fluorescence spectroscopy showed that the proteins affect the conformation of the dyes in fork-labeled constructs, but not duplex-labeled constructs, particularly after the addition of gp61. This supports the conclusions of previous studies that gp41 binds only weakly to the fork, and that this binding is stabilized by gp61. I also used a control system to demonstrate the feasibility of FRET-filtered 2D FS, which has the potential to be a powerful tool for separating signals from mixtures. Cy3 and Cy5 have the advantage that they absorb light in the visible range of the spectrum and have very high oscillator strength, facilitating their use as fluorescent probes. They have the significant disadvantage, however, that they do not closely resemble any component of DNA. It is therefore unclear what aspect of DNA conformation they report on, and it is

inevitable that they disrupt the DNA structure to some extent. A different set of probes, the fluorescent nucleic acid base analogues, address these difficulties in that their structures closely resemble those of native bases. They present the challenges, however, that they absorb in the UV rather than the visible and have much weaker oscillator strengths than the cyanine dyes. In Chapter V, I present work in which the 2D FS system was modified in order to excite UV chromophores, and used to determine the conformation of a dinucleotide of the fluorescent adenine analogue 2-aminopurine.

CHAPTER V

SOLUTION CONFORMATION OF 2-AMINOPURINE DINUCLEOTIDE DETERMINED BY ULTRAVIOLET TWO-DIMENSIONAL FLUORESCENCE SPECTROSCOPY

1. Overview

This chapter describes the extension of the 2D FS method to the ultraviolet regime and contains material published as Widom, J. R.; Johnson, N. P.; von Hippel, P. H., Marcus, A. H. Solution Conformation of 2-Aminopurine Dinucleotide Determined By Ultraviolet Two-Dimensional Fluorescence Spectroscopy. *New J. Phys.* **2013**, *15*, 025028-1 – 025028-16. It describes the modification of the 2D FS apparatus to perform experiments with ultraviolet excitation, which was used to determine the conformation of a dinucleotide of the fluorescent adenine analogue 2-aminopurine. I performed all of the experiments and data fitting reported in this chapter in collaboration with P. H. von Hippel and A. H. Marcus. N. P. Johnson provided insight into the interpretation of the results.

2. Introduction

The conformational manipulation of nucleic acid bases within functioning 'macromolecular machines' is a central feature of DNA replication and RNA transcription reactions. In many cases, these manipulations involve the unwinding of DNA-DNA (or DNA-RNA, or RNA-RNA) duplexes at single-stranded-double-stranded (ss-ds) replication forks, or at Primer-Template (P/T) junctions. Such unwinding

processes provide access for the relevant DNA or RNA polymerases to the duplex 'interior,' and expose ss DNA or RNA sequences that serve as templates for replication and transcription. Thermally driven conformational fluctuations (i.e. 'breathing') within duplex DNA play a prominent role in these processes, although it has been difficult to directly probe these motions and to determine their influence on the activities of protein-nucleic acid complexes. In this work, we introduce two-dimensional fluorescence spectroscopy (2D FS) in the ultraviolet (UV) regime to measure the electronic coupling between the subunits of a dinucleotide of the fluorescent nucleic acid base analog 2-aminopurine (2-AP).[23, 74] These experiments establish the feasibility to measure the relative separation and orientation of a selected pair of 2-AP bases that has been site-specifically substituted for designated canonical adenine bases within a DNA molecule. Such analog dinucleotide-substituted DNA constructs have previously been studied using linear spectroscopic methods to probe local equilibrium and steady-state conformational changes of defined DNA bases within functioning protein-nucleic acid complexes.[11, 24] Nevertheless, these earlier experiments did not permit the interpretation of linear spectroscopic signals in either structural or dynamic terms.

2D FS belongs to a class of two-dimensional Fourier transform spectroscopies widely used to analyze molecular structure and dynamics.[75-76] Such experiments measure correlations between field-induced quantum transitions, which are excited by sequences of phase-related electromagnetic pulses. The resulting spectra are functions of two independent frequency variables, and can provide information about the couplings between excitation transition dipole moments. For example, 2D NMR is a well established structural tool for solution phase studies.[75] More recently, 2D IR experiments

have provided structural and dynamic information about local vibrational modes in proteins[9, 77-78] and DNA.[79] 2D electronic spectroscopy (2D ES) is sensitive to correlations between electronic transition dipole moments, and has been used to study mechanisms of energy redistribution in photosynthetic protein-pigment complexes,[6, 55] semiconductors,[60] and conjugated polymers.[58] The 2D FS method we apply here is a fluorescence-detected variation of 2D electronic spectroscopy, which we recently used to elucidate the conformation and characterize the excited state population transfer of an electronically coupled porphyrin dimer in a biological membrane.[8]

In order to apply 2D FS to study nucleic acid base conformation and excited state dynamics in these systems, it was necessary to extend the capabilities of this method to excite the lowest energy UV transitions of nucleotide base analog probes. Although considerable progress has been made towards performing 2D ES at UV and shorter wavelengths,[80-84] a significant challenge is due to the occurrence of a large non-resonant background, which limits S/N when pulses are temporally overlapped.[82, 84] For example, Raleigh scattering, which scales as the fourth power of the frequency, is especially severe for experiments using multiple UV pulses. This problem can be addressed using 2D FS. As a fluorescence-based method, 2D FS is an effective strategy to elevate signal levels by enhancing contrast, because Stokes-shifted fluorescence can be effectively separated from non-resonant background and scattered laser light. Moreover, because of the inherent sensitivity of fluorescence, 2D FS can be employed under low signal conditions (e.g. low sample concentration, low laser power, moderate extinction coefficient, etc.). These considerations make 2D FS an appealing approach for solution phase structural

studies of macromolecular complexes, which are very often only marginally stable at physiological concentrations ($\leq 1\mu M$).

Most 2D optical experiments are based on four-wave mixing (FWM), in which three non-collinear pulses coherently excite a third-order polarization in the sample. The FWM signal is phase-selectively detected using wave vector matching and optical homodyne interferometry. The phase-selectivity of 2D ES allows for different non-linear signal contributions to be spatially isolated according to their wave vector matching conditions. The so-called non-rephasing (NRP) signal satisfies $\boldsymbol{k}_S^{NRP} = \boldsymbol{k}_1 - \boldsymbol{k}_2 + \boldsymbol{k}_3$, the rephasing (RP) signal $\boldsymbol{k}_S^{RP} = -\boldsymbol{k}_1 + \boldsymbol{k}_2 + \boldsymbol{k}_3$, and the double quantum coherence (DQC) signal $\boldsymbol{k}_S^{DQC} = \boldsymbol{k}_1 + \boldsymbol{k}_2 - \boldsymbol{k}_3$, where $\boldsymbol{k}_i$ with $i \in \{1,2,3\}$ is the wave vector of the i^{th} pulse, and $\boldsymbol{k}_S$ is that of the signal field.[39]

2D FS uses a sequence of four collinear pulses to excite fourth-order populations,[4, 7-9, 85] which are detected by monitoring a suitable action signal (e.g., fluorescence). Isolation of the desired fourth-order signal terms (i.e. NRP, RP and DQC) is accomplished by phase-cycling[7] or, in the case of 2D FS, by phase-modulation.[4] In 2D FS, the phases of the excitation pulses are swept at kilohertz frequencies such that the NRP, RP and DQC signals uniquely oscillate at modulation frequencies that satisfy energy conservation. Thus, the nonlinear signals of interest can be distinguished according to their phase-modulation frequencies: i.e., $S_S^{NRP} \propto \exp\left[i(\Omega_1 - \Omega_2 + \Omega_3 - \Omega_4)\right]$, $S_S^{RP} \propto \exp\left[i(-\Omega_1 + \Omega_2 + \Omega_3 - \Omega_4)\right]$, and $S_S^{DQC} \propto \exp\left[i(\Omega_1 + \Omega_2 - \Omega_3 - \Omega_4)\right]$, where Ω_i with $i \in \{1,2,3,4\}$ is the phase imparted to the vibronic wave function upon interaction with the i^{th} laser pulse. For the experiments presented below, we focus on the NRP and

RP signals, which we write $S_S^{NRP} \propto \exp\left[i(\Omega_{43} + \Omega_{21})\right]$ and $S_S^{RP} \propto \exp\left[i(\Omega_{43} - \Omega_{21})\right]$, respectively, where $\Omega_{ij} = \Omega_i - \Omega_j$ is the relative phase-modulation frequency associated with the i^{th} and j^{th} pulses. In our current experiments, we have set Ω_{21} = 5 kHz and Ω_{43} = 8 kHz, such that the NRP and RP signals oscillate at the 'sum' and 'difference' frequencies 13 kHz and 3 kHz, respectively. By using a lock-in amplifier to phase-synchronously detect these nonlinear signals, the measurement achieves a signal-to-noise (S/N) ratio of approximately 50:1.

3. Experimental Methods

We performed 2D FS experiments on a dinucleotide of 2-aminopurine (2-AP), a fluorescent nucleic acid base analog of adenine (A) (see Figure 5.1A). The 2-AP ribonucleoside [r(2-AP)] has peak absorbance at $\lambda_{\max}^{Abs} = 303$ nm, although this is significantly red-shifted to the value $\lambda_{\max}^{Abs} = 315$ nm upon incorporation into ss or ds DNA constructs.[74] 2-AP fluorescence has a large Stokes-shift, with peak emission at $\lambda_{\max}^{Fl} = 370$ nm. The fluorescence quantum yield of the free probe in solution is $Q_{Fl} = 0.68$, although this is significantly reduced upon incorporation into DNA constructs.[86] 2-AP is a useful probe of local nucleic acid base environment, since it may be readily substituted for A in various DNA sequence contexts. The chemical structure of the 2-AP base is similar to A, and it selectively forms a two-hydrogen-bonded base pair with thymine (T) (see Figure 5.1B), although we note that one of the hydrogen bonds of the (2-AP)-T base pair involves a different set of hydrogen bond donors and acceptors than in the canonical Watson-Crick A-T base pair.[87]

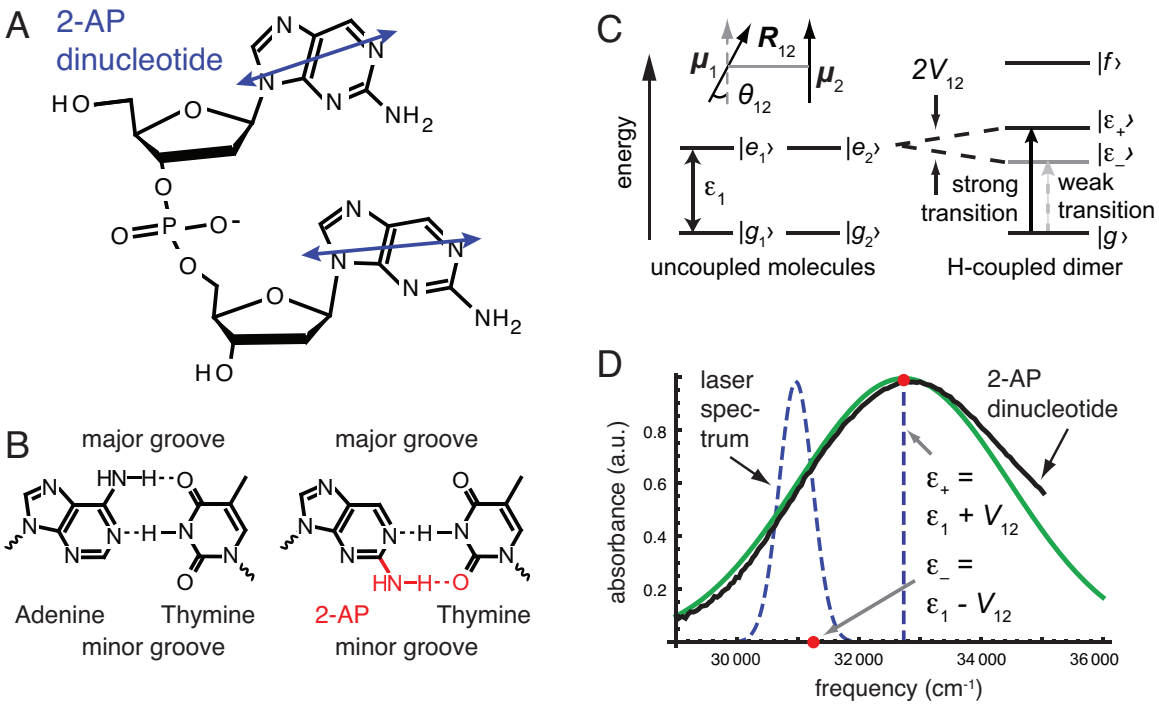

Figure 5.1. (A) The molecular structure of the 2-AP dinucleotide. The lowest-energy electric dipole transition moments (EDTMs) are indicated as blue arrows. (B) The molecular structures of 2-AP-thymine and adenine-thymine base pairs (bp). Note that while Watson-Crick base pairing is maintained, the 2-AP-T bp involves a different hydrogen-bonding pattern than that utilized in A-T. (C) Energy level diagram of two chemically identical two-level molecules. (Inset) An example configuration with relative transition dipole angle θ_{12}. Electronic interactions result in an exciton-coupled four-level dimer with a single ground state, two singly excited states, and a single doubly excited state. Multi-pulse excitation can excite transitions between ground, singly excited and doubly excited state manifolds. The conformation of the dimer determines the energy level spacing and the strengths of the transitions. For an H-dimer, which has a side-by-side arrangement of transition EDTMs, the red-shifted transition will be weak, while the blue-shifted transition will be strong. (D) The lowest-energy absorption band of 2-AP dinucleotide is shown (black) along with the optimized spectrum obtained by simultaneously fitting the linear absorption and 2D FS spectra to the point-features dipole model (green) (described in the text). The energies of the underlying exciton transitions [$\varepsilon_+ = 32\ 742$ cm^{-1} (305.4 nm) and $\varepsilon_- = 31\ 258$ cm^{-1} (319.9 nm)] are indicated by red dots and a dashed blue line. The value obtained for the optimized monomer transition energy is $\varepsilon_1 = 32\ 000$ cm^{-1} (312.5 nm). The laser spectrum used in the 2D FS measurements [center frequency 30 960 cm^{-1} (323 nm)] is shown as a dashed blue curve.

Recent studies have shown that exciton coupling between 2-AP dinucleotide substituted DNA constructs can be used to spectroscopically monitor local base conformation in protein-DNA complexes.[11, 23-24] These experiments take advantage of the electronic interaction between adjacent 2-AP residues, which is sensitive to the magnitude, separation, and relative orientation of the 2-AP electric dipole transition moments (EDTMs). A model that we used to simulate dimer conformation-dependent linear absorption and 2D FS spectra is described in detail elsewhere.[8-9] This model uses the point-dipole approximation to describe electronic coupling between the EDTMs of the monomeric 2-AP chromophores. Here, the coupling is given by

$$V_{12} = \frac{1}{4\pi\varepsilon_0 R_{12}^3}(\vec{\mu}_1)\cdot\left(1-3\frac{\vec{R}_{12}\vec{R}_{12}}{R_{12}^2}\right)\cdot(\vec{\mu}_2) \tag{5.1}$$

Where $\vec{\mu}_{1(2)}$ is the EDTM of the 1st (2nd) 2-AP residue, $\vec{R}_{12}$ is the vector connecting their centers, and ε_0 is the vacuum permittivity. Although more accurate electronic coupling models can be readily implemented, the point-dipole approximation is a useful starting point for our calculations.

In Figure 5.1C, we illustrate the energy levels of two EDTMs with relative angle θ_{12}. In the absence of coupling, the two EDTMs have degenerate electronic transition energy ε_1. The effect of the electronic coupling is to create a four-level system consisting of a common ground state $|g\rangle$, two non-degenerate singly excited states $|e_\pm\rangle$ with energies $\varepsilon_\pm = \varepsilon_1 \pm V_{12}$, and a doubly excited state $|f\rangle$ with $\varepsilon_f \cong 2\varepsilon_1$. The coupling

strength V_{12} is determined by the EDTM magnitude $|\mu|^2$ and dimer conformation according to eq 5.1. In our modeling for the 2-AP dinucleotide, we used the known magnitudes and directions of the EDTMs within the 2-AP molecular frame.[88] The singly excited states are related to the monomer site basis according to $|\varepsilon_{\pm}\rangle = (1/\sqrt{2})\left[|e_1\rangle|g_2\rangle \pm |g_1\rangle|e_2\rangle\right]$, where $g_{1(2)}$ and $e_{1(2)}$ label the ground and excited states, respectively, of monomer 1 (2). These symmetric and anti-symmetric states have wave functions delocalized among the chromophore sites. The collective transition dipole moments between ground and singly excited states are given by $\vec{\mu}_{\pm} = (1/2)\left[\vec{\mu}_1 \pm \vec{\mu}_2\right]$, such that the intensities of ground state accessible transitions depend on the relative orientation of the EDTMs in the dimer. For example, a side-by-side H-type conformation (i.e., $\uparrow\uparrow$) with $\theta_{12} = 0$ results in a purely blue-shifted absorbance spectrum. On the other hand, a head-to-tail J-type conformation (i.e., $\rightarrow\rightarrow$) results in a purely red-shifted spectrum. The effect of nonzero θ_{12} is to partition intensity to the otherwise dipole forbidden (dark) transition, according to $I_{\pm} = |\mu|^2 (1 \pm \cos\theta_{12})$. On the right side of Figure 5.1C, we depict an energy level diagram for an H-type dimer – the case in which the 2-AP residues are at least partially stacked. The side-by-side configuration results in blue-shifted absorbance. Furthermore, fluorescence self-quenching of the H-dimer occurs due to rapid internal conversion of the initially excited population in the $|\varepsilon_{+}\rangle$ level to the lowest excited $|\varepsilon_{-}\rangle$ level. Because the $|\varepsilon_{-}\rangle$ state carries little oscillator strength, slow relaxation to the ground state occurs predominantly by internal conversion.

In Figure 5.1D are shown the experimental linear absorption spectrum of the 2-AP dinucleotide, and the simulated spectrum obtained by performing an optimization of

the point-dipole model to the linear and 2D FS data (see Discussion below). Also shown is the laser spectrum used in these experiments with center energy at 30 960 cm^{-1} (323 nm). The optimization procedure we performed was similar to that used for porphyrin dimers in membranes.[8-9] As we discuss further below, our results indicate that the 2-AP dinucleotide adopts an H-type conformation, with bright and nearly dark transitions occurring, respectively, at the energies $\varepsilon_+ = 32\ 742\ cm^{-1}$ (305.4 nm) and $\varepsilon_- = 31\ 258\ cm^{-1}$ (319.9 nm) (indicated by red dots), and with monomer transition energy $\varepsilon_1 = 32\ 000\ cm^{-1}$ (312.5 nm). We note that the fluorescence intensity of the 2-AP dinucleotide in solution is known to be quenched 20-fold relative to that of the monomeric 2-AP nucleoside,[23] which is the expected outcome for an H-type dimer conformation.

Linear absorption and 2D FS measurements were performed using 50 mM 2-AP dinucleotide in aqueous buffer containing 20 mM HEPES (pH 7.5), 150 mM KOAc, 10 mM $Mg(OAc)_2$, 0.1 mM EDTA and 1 mM DTT. Control measurements were performed using the fluorescent dye POPOP in cyclohexane.

A. Two-Dimensional Fluorescence Spectroscopy in the Ultraviolet Regime

The principles of 2D FS are described in detail elsewhere.[4, 8-9] Here we briefly outline the approach for experiments in the UV. The collinear four-pulse sequence with inter-pulse delays and phase-modulation frequencies is depicted in Figure 5.2A. A schematic of the instrument is shown in Figure 5.2B. A 250 kHz regenerative amplifier (Coherent RegA 9000, 9 mJ / pulse, 790 nm) was used to simultaneously drive two collinear optical parametric amplifiers (Coherent OPA 9400). The output of each OPA was tuned to 646 nm (~ 18 nm bandwidth), and directed through a pair of fused silica prisms using double-pass geometry for pre-dispersion compensation. Each beam entered

a Mach-Zehnder interferometer (MZI), where an acousto-optic Bragg cell (Gooch & Housego R46200-2.2-.25-.7-LTD-XQ) was placed within each interferometer arm to impart a continuous phase-sweep to the incident pulses. After the Bragg cells, the pulses were frequency doubled using beta barium borate (BBO) crystals (0.1 mm thickness), and recombined at the exit beam-splitters of each MZI to form collinear trains of 323 nm pulse-pairs.

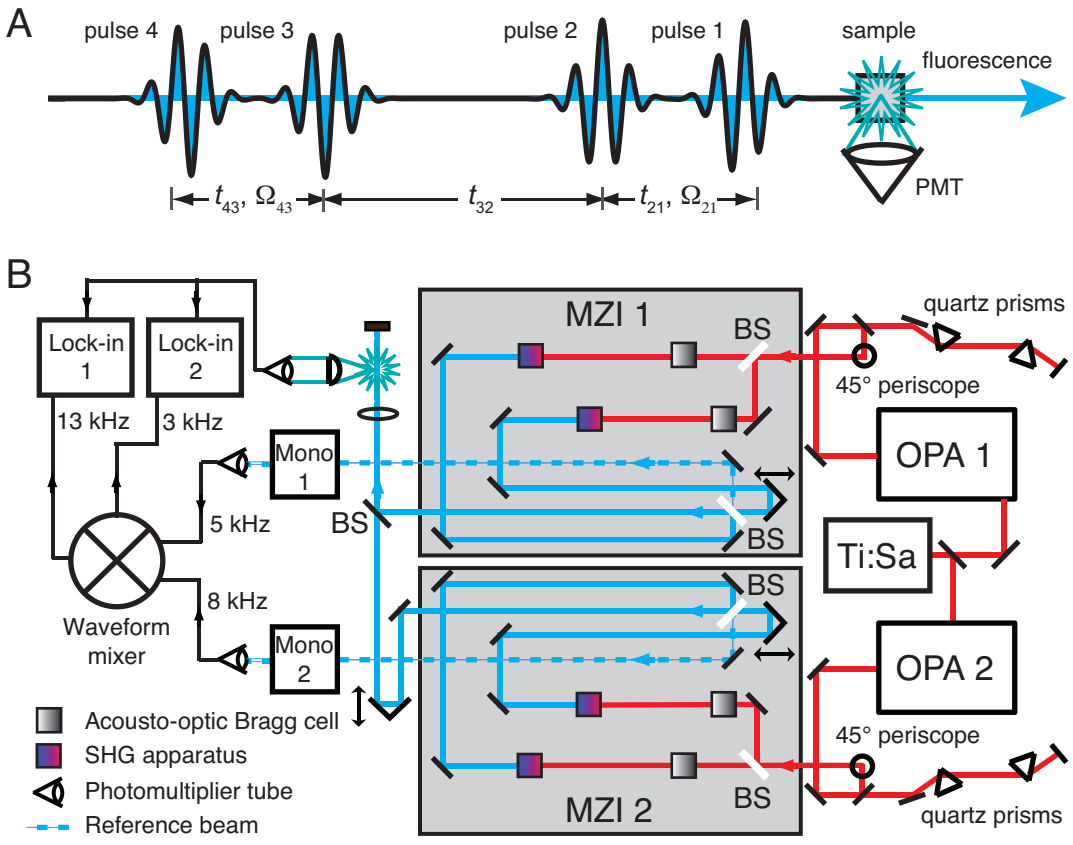

Figure 5.2. (A) UV-2D FS pulse sequence. (B) Schematic of the 2D FS instrument for experiments at UV wavelengths.

The two independently generated pulse-pairs were combined downstream to form a sequence of four collinear pulses that were focused into the sample using a 5 cm focal

length fused silica lens. A pair of dichroic mirrors (Semrock FF409-Di03) was placed in the beam path just prior to sample incidence to remove residual 646 nm light. Retro-reflective mirrors (PLX 533511) mounted onto computer-controlled delay stages (Aerotech ALS130-050, 20 nm step size) were used to control the inter-pulse delay times. We note that after the BBO crystals, all mirrors used UV-enhanced aluminum coatings, all lenses were made from fused silica, and all transmissive optics used UV anti-reflection coatings.

Phase selective detection of the nonlinear signals was carried out using the 2D FS phase-modulation technique.[4] Each of the four Bragg cells were driven continuously at unique frequencies, which were detuned from their resonances (~ 175 MHz) such that a relative phase sweep was applied between the first and second pulses at 5 kHz, and between the third and fourth pulses at 8 kHz. Replicas of the output pulse-trains from each MZI were directed to separate monochromators (Acton SpectraPro 150 and SpectraPro 2150i, 1200 grooves/mm grating blazed to 500 nm, < 0.4 nm resolution), and the spectrally filtered time-varying pulse intensities (5 kHz at 326 nm, 8 kHz at 326 nm) were detected using photomultiplier tubes (PMT, Hamamatsu R1527), which were mounted in air-cooled housings (Products for Research PC202CE). The photocurrent signals were pre-amplified and filtered to produce high quality AC references for lock-in detection, as described below.

Pulse widths were characterized on a daily basis using the two-photon absorption (2PA) autocorrelation method of Tian and Warren[89] (see Figure 5.3). A silicon photodiode (Thor Labs DET10A) was placed at the sample position where a train of phase-modulated pulse pairs was incident. The signal was detected using a lock-in

amplifier (Stanford Research Systems SR830), which was referenced to the AC carrier signal matching the excitation pulse-pair. The 2PA response was measured as a function of inter-pulse delay by locking to the photodiode signal at twice the pulse pair modulation frequency (i.e., using second harmonic detection). This procedure was carried out in turn for pulses 1 and 2, for pulses 3 and 4, and for pulses 2 and 3 to determine the pulse widths and stage positions at which the pulses were maximally overlapped (i.e., the zero-time delays). Upon optimization of the prism compensators, 2PA autocorrelation pulse-widths on the order of ~33 fs were obtained, which corresponds to approximately 1.1 times the value for Fourier transform-limited pulses. Autocorrelation signals detected at twice the carrier frequency were significantly narrowed relative to those detected at the pulse pair modulation frequency, which confirms that our measurements isolate the 2PA signal.

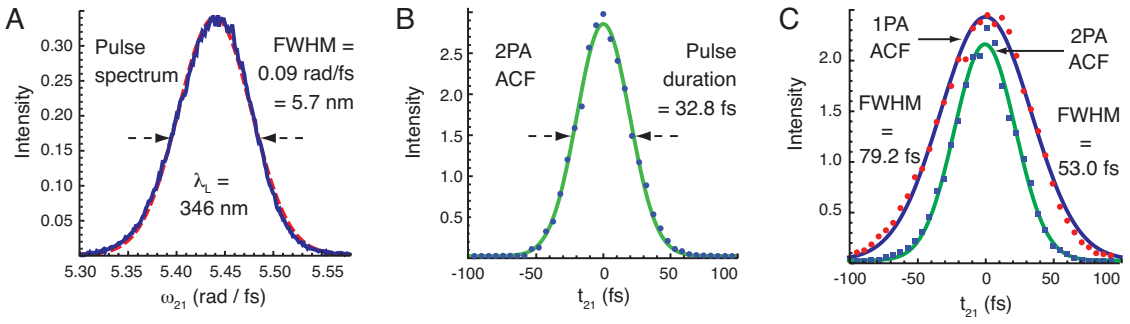

Figure 5.3. (A) A typical pulse spectrum, and (B) two-photon absorption (2PA) intensity auto-correlation function are shown for the case with laser center wavelength λ_L = 346 nm. The pulse duration is 33 fs, the pulse spectrum FWHM is 5.7 nm. The time-bandwidth product is 0.47. (C) The 2PA autocorrelation is narrower than the one-photon absorption (1PA) autocorrelation, which demonstrates that our measurements isolate the 2PA signal, and not simply leakage of the 1PA signal.

For our 2D FS experiments, we placed a sample containing 2-AP dinucleotide in a fused silica flow cell at the sample position, and the fluorescence was collected at a right angle using a fused silica lens (6 cm focal length, 2 inch diameter). The fluorescence was filtered from scattered laser light (Semrock, 364LP) and imaged onto an air-cooled PMT (Hamamatsu R3896). The photocurrent signal was pre-amplified and filtered before it was split into two signals. The NRP and RP contributions to the fluorescence signal were separately detected using two identical lock-in amplifiers, which were referenced, respectively, to sum- and difference-frequency waveforms. These reference waveforms were constructed from the 5 kHz and 8 kHz pulse pair modulation signals using a custom-built waveform mixer that generated the sum (13 kHz) and difference (3 kHz) frequency sidebands.[4] The time delays t_{21} (between pulses 1 and 2), and t_{43} (between pulses 3 and 4) were scanned from 0 to 200 fs, while setting $t_{32} = 0$. The cosine and sine projections of the NRP and RP signals were simultaneously measured at each time point. Fourier transformation of the resulting signal interferograms, with respect to t_{21} and t_{43}, yielded the 2D fluorescence spectra.

We emphasize that the fluorescence-detected population signal contains NRP, RP and DQC contributions, as well as majority contributions from linear population terms. In our current experiments, we measured the NRP and RP terms by separately locking to the sum and difference frequency side bands, $\Omega_{21} \pm \Omega_{43}$, respectively. We note that in principle, double quantum coherence signals could also be measured using this instrument with minor adjustment to the electronic filters to create a reference waveform with modulation frequency $(\Omega_4 + \Omega_3) - (\Omega_2 + \Omega_1)$. The selection of phase-matching condition is accomplished through the electronic synchronization of a modulated signal

with its corresponding reference waveform. Thus, calibration of the signal phase is a simple matter of adjusting the lock-in detector to maximize the cosine projection and minimize the sine projection at the time origin (i.e $t_{21} = t_{32} = t_{43} = 0$).[4]

An important advantage of UV-2D FS is that the fluorescence-detected nonlinear signal is free of non-resonant background contributions from the solvent response, as recently noted by West and Moran.[82, 84] In FWM approaches to 2D ES, a large non-resonant background degrades signal-to-noise when UV pulses are temporally overlapped (e.g., for $t_{32} = 0$), which limits the time-resolution of the measurement. In Figure 5.4A, we present control 2D FS data obtained from a sample containing the UV chromophore POPOP, where we have set the inter-pulse delay $t_{32} = 0$ fs and we used the same laser spectrum as that shown in Figure 5.1D. In these measurements, we observed only a single resonant feature in the RP and NRP 2D line shapes, which were peaked at the positions of the laser spectrum. The appearance of just a single resonant feature in the 2D spectrum is consistent with the behavior of an uncoupled two-level molecule. Total correlation function (TCF) spectra were constructed by combining RP and NRP spectra, as is customary.[46] In Figure 5.4B, we show the t_{32} -dependence of the absolute value of the RP and NRP signals (for fixed $t_{21} = t_{43} = 0$). In contrast to FWM,[82] the 2D FS signal is free of non-resonant contributions for inter-pulse delays close to $t_{32} = 0$.

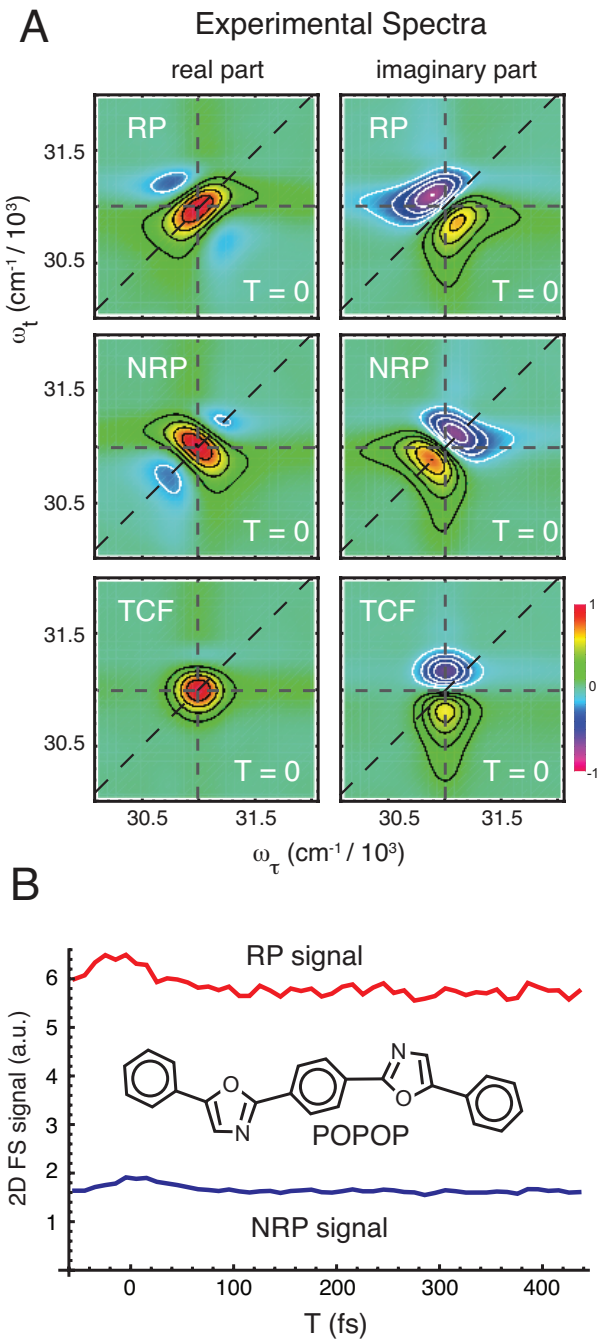

Figure 5.4. (A) Control experimental UV-2D FS data for POPOP dissolved in cyclohexane. The top row shows RP spectra, the middle row shows NRP spectra, and the bottom row shows TCF spectra. Only a single feature in the 2D FS line shape is observed. (B) The absolute values of the RP (red) and NRP (blue) signals of POPOP for $t_{21} = t_{43} = 0$ are plotted as a function of population time t_{32}. Because the 2D FS method is based on fluorescence detection, non-resonant background is effectively suppressed from the population signal at short inter-pulse delays $t_{32} = 0$ fs. (Inset) The chemical structure of POPOP is shown.

4. Discussion

In Figure 5.5A, we present the UV-2D FS measurements that we performed on the 2-AP dinucleotide. The first electronic transition of 2-AP residues, when incorporated into various DNA constructs, is close to 315 nm,[74] which allows it to be selectively excited in protein-nucleic acid complexes because the natural nucleotides and amino acids are transparent at these wavelengths. It has been shown using circular dichroism (CD) spectroscopy that when two adjacent base residues in a DNA construct are substituted with 2-AP, interaction between the chromophores leads to exciton-coupling of the electronic states and splitting of the energy levels.[23] This exciton-induced energy level splitting is clearly evident in the experimental 2D FS data shown in Figure 5.5A. Both real and imaginary 2D spectra exhibit a strong resonant feature lying approximately on the diagonal, close to the laser center frequency at $\omega_\tau = \omega_t =$ 31 000 cm^{-1}. The presence of exciton coupling gives rise to an additional weak resonant feature that lies just below the diagonal at $\omega_\tau =$ 31 000 cm^{-1} and $\omega_t =$ 30 600 cm^{-1}. This qualitative pattern in the 2D FS line shapes, in addition to the blue-shifted linear absorbance of the dinucleotide relative to the monomer (shown in Figure 5.1D), suggests that the dinucleotide adopts an average side-by-side H-type arrangement of coupled transition dipoles, as expected for a base-stacked conformation.[9] In Figure 5.5D, we show the simulated 2D FS spectra corresponding to the optimized base-stacked conformation most consistent with our data (discussed further below). These simulated 2D spectra exhibit the same intense diagonal and weak cross-peak features evident in the experimental 2D spectra. For comparison, we also show in Figure 5.5C simulated 2D spectra corresponding to the J-dimer conformation, in which the laser and linear absorbance

spectra are assumed to be the same as in Figure 5.1D. The J-dimer exhibits only a single diagonal feature, and does not resemble the experimental 2D spectra.

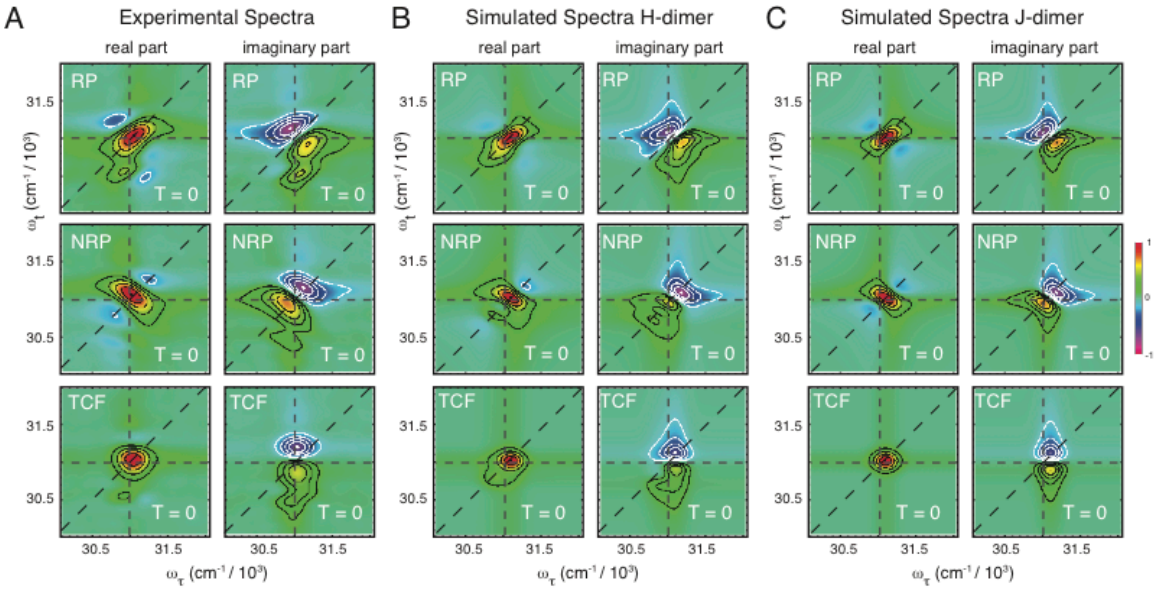

Figure 5.5. (A) Experimental, and (B) simulated, UV-2D FS spectra of 2-AP dinucleotide in aqueous buffer. The experimental 2D spectra exhibit a diagonal peak and a cross-peak below the diagonal, indicating the existence of exciton splitting in the dinucleotide. Horizontal and vertical dashed lines indicate the center frequency of the laser 30 960 cm^{-1} (323 nm). The simulated 2D spectra are the result of an optimization of the point-dipole model to the experimental 2D FS and linear absorbance data shown in Figure 5.1D. The structural parameters so obtained are the inter-base distance $R_{12} = 3.5$ Å ± 0.5Å and relative twist angle $\theta_{12} = 5° \pm 5°$ between EDTMs of the 2-AP residues. The top row shows RP spectra, the middle row shows NRP spectra, and the bottom row shows TCF spectra. (C) Simulated UV-2D FS spectra corresponding to a J-dimer conformation with laser and linear spectrum the same as in Figure 5.1D.

As was previously demonstrated for membrane-supported MgTPP dimers,[8-9] 2D FS can be used to find a globally optimized solution for the relative conformation of the two coupled probe residues. Here we apply a similar approach to solve for the conformation of the 2-AP dinucleotide. These experiments demonstrated that excellent signal-to-noise was obtained for this system. Scattered laser light and non-resonant

background were effectively removed from the signal using two stacked long-pass emission filters. Control measurements, in which the fluorescent sample was replaced with buffer, yielded no detectable signal.

We followed a procedure similar to one we used previously for porphyrin dimers[8-9] to perform a geometry optimization using the combined linear absorption and 2D FS data as the minimization target function. In our previous work, we simulated the 1D and 2D spectra for a given dimer conformation, which was based on the calculated coupling strengths. It was assumed that an individual exciton feature in the simulated 2D fluorescence spectrum was positioned at its eigen-frequency ω_{nm} that bridges transitions between the various exciton states (i.e., ground to singly-excited, and singly-excited states to doubly-excited states). The line width of each feature was characterized by its phenomenological dephasing time τ. The contribution to the signal from each coherence pathway was weighted according to the rotational average corresponding to the sequence of transition dipole moments involved in that pathway, $\langle \mu_1 \mu_2 \mu_3 \mu_4 \rangle$, as well as the amplitude of the laser spectrum at the center frequency of the transition, $\alpha(\omega_{nm})$.

In the current work, the laser spectral bandwidth was significantly narrower than the spectral bandwidths of the underlying exciton features (see Figure 5.1D). Furthermore, the laser spectrum was positioned near the low-energy shoulder of the 2-AP absorption band in order to emphasize the weaker red-shifted exciton. The features in the resulting 2D FS signal were observed to be red-shifted relative to the linear absorption maximum, and slightly blue-shifted relative to the laser maximum (see Figure 5.5A). To account for the effects of the finite laser bandwidth, the laser detuning from the absorption maximum, and the observed peak shifts in our data, we included in our model corrections based on

the spectral overlap between the laser and absorption spectrum. We modeled the laser spectrum $g(\omega)$ and the individual spectral features $a_{nm}(\omega)$ as Gaussians

$$g(\omega) = \exp\left[-\frac{(\omega-\omega_L)^2}{2\sigma_L^2}\right] \tag{5.2}$$

and

$$a_{nm}(\omega) = \exp\left[-\frac{(\omega-\omega_{nm})^2}{2\sigma_1^2}\right] \tag{5.3}$$

where ω_L is the center frequency of the laser spectrum, σ_1 is the standard deviation of the exciton line shape (= 658 cm^{-1}, obtained from optimization), and σ_L (= 277 cm^{-1}) is the standard deviation of the laser spectrum. For a given transition, the simulated 2D FS spectrum was determined from the spectral overlap function $g(\omega)\cdot a_{nm}(\omega)$. The transition frequency was thus adjusted to

$$\omega_{nm} \rightarrow \tilde{\omega}_{nm} \equiv \frac{\omega_L\sigma_1^2 + \omega_{nm}\sigma_L^2}{\sigma_1^2 + \sigma_L^2} \tag{4}$$

and the weight of the transition determined by the laser amplitude was adjusted to

$$\alpha(\omega) \rightarrow \tilde{\alpha}(\omega) = \exp\left[-\frac{(\omega-\omega_L)^2}{2(\sigma_L^2+\sigma_1^2)}\right] \tag{5}$$

We have implemented the above model to describe a wide range of experimental 2D FS data for a membrane-supported porphyrin dimer in which the subunits were connected by a flexible linker. In these studies, the laser center frequency was systematically tuned across the absorption band, and we obtained very good agreement between our experimental results and the corrections predicted by eqs 5.4 and 5.5 when the laser was centered near the absorption maximum. This work will be published elsewhere. When the laser was detuned further from the absorption maximum, the model reproduced the relative intensities of peaks in the 2D FS spectra very well, but slightly underestimated the extent to which the peak positions were red-shifted toward the laser's peak position. To account for this inaccuracy, we included in our fit an additional shift parameter that allowed for the 2D FS peak positions to be optimized beyond the predictions of the above model. Our optimized peak positions were thus further red-shifted relative to the prediction given by eq 5.4: $\tilde{\omega}_{nm} -$ 191 cm^{-1}.

Using the above model, we simultaneously fit the linear absorption spectrum (results shown in Figure 5.1D) and the RP and NRP 2D FS spectra (results shown in Figure 5.5B). Our results yielded a coupling $V_{12} = 742$ cm^{-1} between 2-AP residues and an angle $\theta_{12} = 5° \pm 5°$ between EDTMs. The lowest-energy EDTM of 2-AP has magnitude $|\mu| = 2.55$ D.[88] For a side-to-side EDTM geometry, these parameters yielded an average distance $R_{12} = 3.5 \pm 0.5$ Å between the 2-AP bases of the dinucleotide, which we obtained by inversion of eq 5.1. These values for θ_{12} and R_{12} are to be compared to the known twist angle 36° and distance 3.4 Å between adjacent bases in B-form duplex DNA. Previous CD studies of the 2-AP dinucleotide suggested that the molecule adopts a right-handed helical conformation with moderate base stacking.[23] The CD intensity of the

lowest-energy transition of the 2-AP dinucleotide is five times weaker than in the corresponding 2-AP dinucleotide-substituted dsDNA construct. When the sample was heated or placed in a denaturing solvent, the exciton-coupling contribution to the CD signal was observed to decrease. Although these data were originally interpreted to indicate that the dinucleotide is partially un-stacked, the structural parameters determined in this work ($R_{12} = 3.5\ \text{Å} \pm 0.5\ \text{Å}$ and $\theta_{12} = 5° \pm 5°$) suggest that the weak CD signal of the dinucleotide may be the result of its reduced chirality in comparison to dsDNA. In addition, the dinucleotide fluorescence is quenched 20-fold relative to the monomeric nucleoside,[23] as expected for an H-coupled dimer, thus providing further evidence that there is significant base stacking in this system. The combination of these results with the previous CD and fluorescence quenching experiments suggests that at room temperature, in aqueous solvent, there is significant base stacking in the dinucleotide with relatively small twist angle.

These results are significant in the context of the energetics of base stacking in duplex DNA. Our observations imply that optimal nearest-neighbor stacking of a dinucleotide in aqueous solution may involve as much surface occlusion of the bases as possible, consistent with the small twist angle that we measure (see Figure 5.6A). This is the expected outcome for the dinucleotide, provided that the hydrophobic forces favoring stacking exceed the opposing strain that such maximal stacking may induce in the connecting sugar-phosphate backbone.[90-91] The reduced stacking (surface occlusion) seen between neighboring bases in longer dsDNA (twist angle ~ 36° in B-form dsDNA, see Figure 5.6B), where of course both "faces" of the bases are significantly removed from contact with the aqueous solvent by stacking, may reflect the energetic requirement to

accommodate the stiffness of the sugar-phosphate backbones by simultaneously maximizing base stacking and minimizing backbone strain, resulting in the formation of base-stacked double helical structures of duplex DNA of the type introduced by Watson and Crick (see Figure 5.6C). We note that because the 2D FS measurement is sensitive to the absolute value of the twist angle, and not the sign of the chirality, the relatively small magnitude for θ_{12} we observe cannot reflect a cancellation between signal contributions from either a pair of static or dynamic structures of B-form geometry and opposing chirality, as might be the case for a comparable CD result.

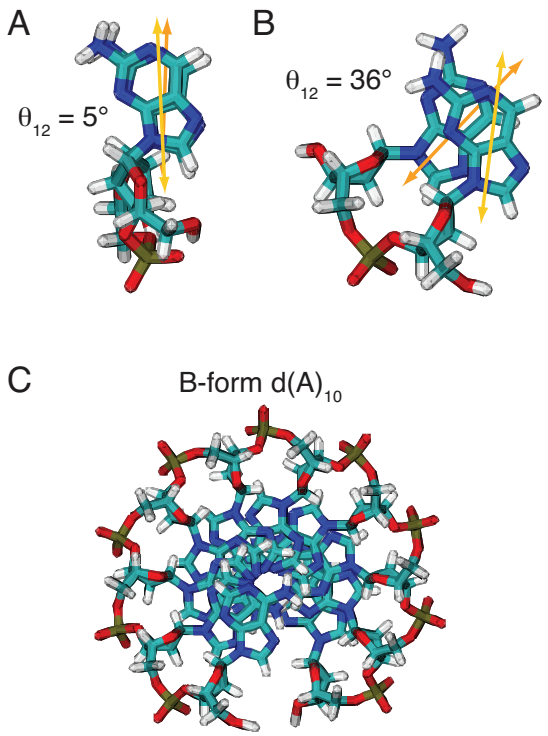

Figure 5.6. (A) Schematic illustration of the nearly maximal occluded surfaces of adjacent nucleic acid bases with twist angle $\theta_{12} = 5°$. (B) The degree of stacking (occluded surface area) is much less for neighboring bases in oligomeric B-form dsDNA, which has $\theta_{12} = 36°$. (C) A decomeric segment of B-form duplex DNA containing A-T pairs. Only the $d(A)_{10}$ strand is shown, viewed along the helical axis.

5. Conclusions

We have determined the average solution conformation of the dinucleotide of the fluorescent nucleic acid base analog 2-AP, which is a useful probe of local nucleic acid base structure. This was accomplished by implementing the 2D FS method in the UV regime, which allowed us to directly observe the effects of conformation-dependent exciton coupling between the 2-AP bases of the dinucleotide. 2D FS presents important advantages for experiments in the UV, such as the relatively high sensitivity associated with fluorescence measurements and the straightforward separation of signal from non-resonant background. Future work will involve altering the pulse polarization sequences used for 2D FS measurements to enhance cross peaks, and using 2D FS to determine the local conformations of DNA and RNA within protein-nucleic acid complexes.

6. Summary and Bridge to Chapter VI

Fluorescence-detected 2D spectroscopy is well suited to applications using ultraviolet excitation due to its high sensitivity and the ease of separating the desired signal from non-resonant background. By fitting its absorbance and 2D FS spectra, it was found that a dinucleotide of 2-aminopurine adopts a nearly parallel, stacked conformation. This suggests that the 36° twist observed in B-form DNA is the result of the constraints of backbone connectivity, while the smaller dinucleotide is free to adopt a more parallel conformation that maximizes stacking.

2-dimensional electronic spectroscopy experiments have yielded a wealth of knowledge about the excited state dynamics of systems like photosynthetic protein-pigment complexes[6] and conjugated polymers.[58] In Chapter VI, I present the application

of 2D FS to study the excited state dynamics of two systems: the MgTPP dimer discussed in the introduction to Chapter II, and the ZnTPP dimer discussed in Chapter III. I also discuss the theory that predicts the effects of electronic population transfer on 2D spectra.

CHAPTER VI

EXCITED STATE DYNAMICS IN EXCITON-COUPLED DIMERS

1. Overview

This chapter presents studies on two different systems in which 2D FS was used to probe excited state dynamics. The first system discussed is a membrane bound self-assembled MgTPP dimer. This section contains material published as Perdomo-Ortiz, A.; Widom, J. R.; Lott, G. A.; Aspuru-Guzik, A.; Marcus, A. H. Conformation and Electronic Population Transfer in Membrane-Supported Self-Assembled Porphyrin Dimers by 2D Fluorescence Spectroscopy. *J. Phys. Chem. B.* **2012**, *116*, 10757-10770. In this work, G. A. Lott performed the experiments, A. Perdomo-Ortiz performed the data fitting and I performed the modeling of electronic population transfer, the focus of this section. The remainder of the chapter consists of unpublished material investigating the excited state dynamics of the membrane bound ZnTPP dimer discussed in Chapter III. I performed the experiments and modeling for this system in collaboration with A. H. Marcus.

2. Conformation and Electronic Population Transfer in Membrane-Supported Self-Assembled MgTPP Dimers

A. Conformation of Self-Assembled $(MgTPP)_2$ Dimer in Liposomal Membranes

In Figure 6.1 are shown the results of experiments performed on $(MgTPP)_2$ samples, which were prepared in 7:1 1,2-distearoyl-sn-glycero-3-phosphocholine (DSPC):MgTPP liposomes.[8] In these studies, a comparison was made between the line

shapes of the lowest energy electronic transitions (i.e. the Q(0,0) features) for three different samples: a solution of MgTPP in toluene, a low concentration monomer sample in liposomes (70:1 DSPC:MgTPP), and the dimer sample in liposomes. From the linear spectra, we observed that the liposomal membrane stabilizes the monomer transition energy relative to toluene. From the monomer liposome spectrum, we determined the values of the unperturbed transition frequency $\bar{\nu}_1$ = 16,500.7 cm^{-1} and the dipole strength $|\mu|$ = 1.33 *D*. In comparison to the monomer samples, the line shape of the $(MgTPP)_2$ sample (shown in Figure 6.1A) was asymmetrically broadened, suggesting the presence of electronic interactions between monomer subunits that lead to splitting of the Q(0,0) transitions. This was confirmed by 2D FS measurements of these samples, in which individual exciton-split features underlying the linear absorption line shape and associated cross-peaks were observed directly.

As described in Chapter II, it is possible to model the linear absorption spectrum in terms of the structural parameters $\boldsymbol{R}$, α and β (see Figure 2.1A) that determine the couplings V_{kl} (eq 2.4) and the collective dipole moments, and which ultimately determine the energies and intensities of the ground-state accessible transitions. We numerically generated approximately 1,000 representative conformations and simulated their linear spectra. By comparing experimental and simulated data, we established that a wide distribution of approximately 100 conformations could reasonably explain the linear absorption spectrum. In Figure 6.1A is shown the simulated linear spectrum and the four underlying component transitions of the optimized "bent T-shaped" dimer conformation (shown in Figure 6.1B). The linear spectrum is composed of two intense spectral features at 16,283 and 16,619 cm^{-1}, one weak feature at 16,718 cm^{-1}, and one effectively dark

feature at 16,382 cm^{-1}. The relatively unrestricted constraint imposed on dimer conformation by the linear spectrum is a consequence of the many possible arrangements and weights that can be assigned to the four overlapping Gaussian features with broad spectral width.

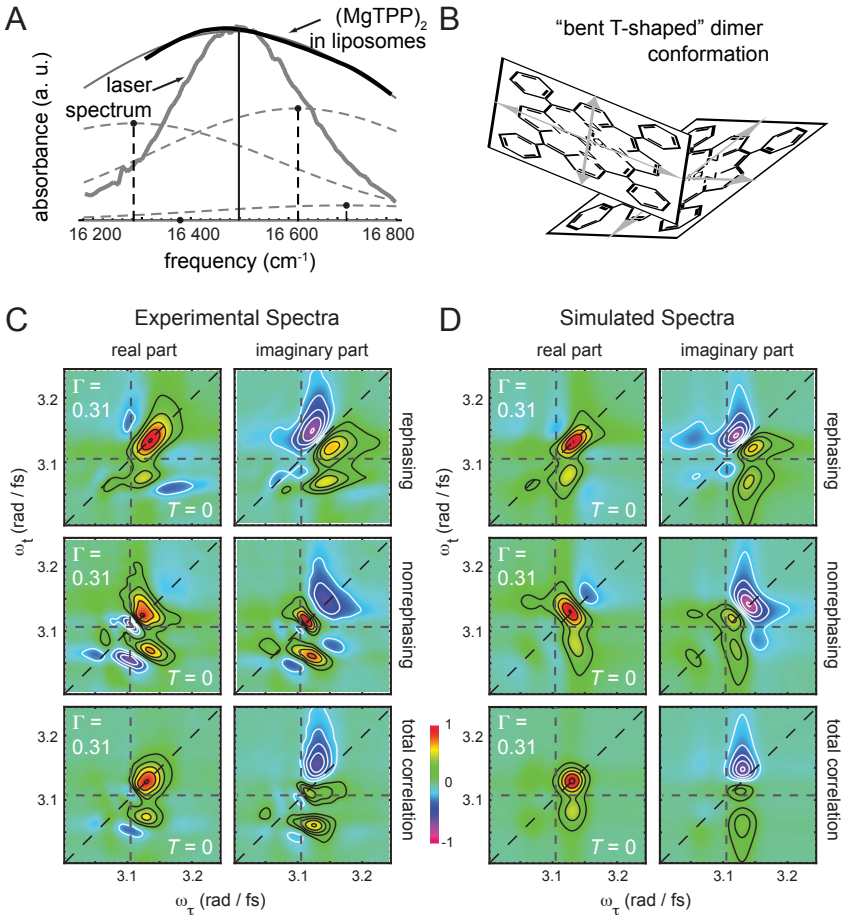

Figure 6.1. (A) Overlay of the $(MgTPP)_2$ in liposome absorbance and the laser pulse spectrum. The laser spectrum (solid gray curve) was fit to a Gaussian centered at the monomer transition frequency $\bar{\nu}_1 = 16{,}501$ cm^{-1} (606 nm), and with FWHM = 327 cm^{-1} (12 nm). The linear absorbance (solid black curve) is compared to the simulated spectrum (solid gray curve), which is based on the "bent T-shaped" dimer conformation depicted in (B). The optimized dimer conformation corresponds to the structural parameter assignments $R = 4.2$ Å, $\theta = 117.4°$, $\phi = 225.2°$, $\alpha = 135.2°$, and $\beta = 137.2°$. (C) and (D) Comparison between experimental (C) and simulated (D) rephasing (top row) nonrephasing (middle row) and total correlation (bottom row) spectra. The simulated spectra correspond to the optimized conformation depicted in (B) with $\Gamma = 0.31$.

In Figure 6.1C are shown the complex-valued 2D FS data for the $(MgTPP)_2$ liposome sample. The 2D FS spectra depend on the overlap between the $Q(0,0)$ feature and the laser pulse spectrum (shown in Figure 6.1A). Rephasing and nonrephasing data (top and middle rows, respectively) were processed from independently detected signals according to their unique phase-matching conditions. The two types of spectra provide complementary structural information because each depends on a different set of nonlinear coherence terms. Rephasing and nonrephasing spectra were summed together to construct the total correlation spectrum (bottom row).[46] The 2D spectra are asymmetrically shaped, with the most prominent features a high-energy diagonal peak and a coupling peak directly below it with an apparent splitting of approximately ~ 340 cm^{-1}. We note the similarities between the general appearance of the experimental linear and 2D spectra, and the model spectra associated with "T-shaped" and closely related dimer conformations shown in Figure 2.3 (for two-dipole coupled models) and in Figure 2.4 (for four-dipole coupled models).

By extending the procedure to simulate linear spectra, we numerically simulated the 2D spectra for a broad distribution of conformations. We performed a least-squares analysis that compared simulated and experimental spectra to obtain an optimized conformation consistent with both the 2D and linear datasets. In our optimization procedure, we treated the fluorescence efficiency Γ of doubly excited excitons as a parameter to find the value that best represents the experimental data. In Figure 6.1D, we directly compare our experimental and simulated 2D FS spectra for the optimized "bent T-shaped" conformation shown in Figure 6.1B. The values obtained for the parameters of this conformation are $\theta = 117.4°$, $\phi = 225.2°$, $\alpha = 135.2°$, $\beta = 137.2°$, $R = 4.2$ Å, and

$\Gamma = 0.31$, with associated trust intervals: $-16° < \Delta\theta < 4°$, $-11° < \Delta\phi < 11°$, $-11° < \alpha < 11°$, $-2° < \Delta\beta < 2°$, $-0.05\,\text{Å} < \Delta R < 0.05\,\text{Å}$ and $-0.1 < \Gamma < 0$. For rephasing, nonrephasing and total correlation spectra, the agreement between experiment and theory is very good, with an intense diagonal peak and a weaker coupling peak (below the diagonal) clearly reproduced in the simulation. A notable feature of the experimental 2D spectra is the asymmetric line shape, which is most apparent in the coupling peak. One possible explanation for these asymmetries is the existence of distinct interactions between the various exciton states and the membrane environment. The discrepancy between experimental and simulated 2D line shapes is an indication of a shortfall in the model Hamiltonian. We address this issue below in our consideration of the population time dependence of the 2D FS data. As we discuss below, this feature appears to be related to the presence of the dark transition at 16,382 cm^{-1}.

Our confidence in the conformational assignment we made was quantified by the numerical value of the regression analysis target parameter $\chi^2_{tot} = \chi^2_{linear} + \chi^2_{2D}$, which includes contributions from both linear and 2D FS spectra.[8] By starting with this conformation and incrementally scanning the structural parameters θ, ϕ, α and β, we observed that χ^2_{tot} increased, indicating that the favored conformation is a local minimum when both linear and 2D spectra were included in the analysis. Similarly, we found that the value $\Gamma = 0.31$ correspond to a local minimum. If only one of the two types of spectra is included, the restrictions placed on the dimer conformation are significantly relaxed.

B. The Influence of Excited State Population Transfer on 2D FS Spectra

For non-zero population time *T*, transfer of population between singly-excited excitons can influence the 2D optical spectra of molecular aggregates.[92-95] Here we examine how energy transfer processes affect 2D FS versus 2D ES experimental data.

To describe exciton population dynamics, we employed the quantum master equation in the secular approximation, which neglects the effects of short-lived coherences[15]

$$\frac{\partial G_{kj}(T)}{\partial T} = \sum_{l \neq k} K_{kl} G_{lj}(T) - \left(\sum_{l \neq k} K_{lk} \right) G_{kj}(T) \tag{6.1}$$

Here, $G_{kj}(T)$ is the Green's function probability that population is in state $|k\rangle$ at time *T*, provided that state $|j\rangle$ was originally populated at $T = 0$. For the coupled three-level dimer model (see Figure 2.1C), the indices label the singly-excited excitons $j,k,l \in \{X_2, X_3, X_4, X_5\}$ The rate constants K_{kl} (K_{lk}) are parameters that describe forward (backward) population transfer between pairs of states, subject to the detailed balance condition

$$\frac{K_{kl}}{K_{lk}} = e^{-(\varepsilon_k - \varepsilon_l)/k_B T} \tag{6.2}$$

The Green's function solution to eq 6.1 provides time-dependent matrix elements that weight the coherence term contributions to the 2D optical spectra.[15] For example, if

we consider a particular pair of singly-excited states, $|m\rangle$ and $|n\rangle$ with $\varepsilon_m > \varepsilon_n$, the associated peaks and cross-peaks of the 2D total correlation function have the following forms:

$$S_{TCF}^{Dm}(\omega_\tau, T, \omega_t) \propto \mathrm{GSB} + \mathrm{SE} \cdot G_{mm}(T) + (1-\Gamma) \cdot \mathrm{ESA} \cdot G_{nm}(T) \tag{6.3a}$$

$$S_{TCF}^{Dn}(\omega_\tau, T, \omega_t) \propto \mathrm{GSB} + \mathrm{SE} \cdot G_{nn}(T) + (1-\Gamma) \cdot \mathrm{ESA} \cdot G_{mn}(T) \tag{6.3b}$$

$$S_{TCF}^{Cmn}(\omega_\tau, T, \omega_t) \propto \mathrm{GSB} + \mathrm{SE} \cdot G_{nm}(T) + (1-\Gamma) \cdot \mathrm{ESA} \cdot G_{mm}(T) \tag{6.3c}$$

$$S_{TCF}^{Cnm}(\omega_\tau, T, \omega_t) \propto \mathrm{GSB} + \mathrm{SE} \cdot G_{mn}(T) + (1-\Gamma) \cdot \mathrm{ESA} \cdot G_{nn}(T) \tag{6.3d}$$

In the above expressions, we combined nonrephasing and rephasing coherence terms (defined by eqs 2.24 – 2.26) to calculate the total correlation spectra, such that $\mathrm{GSB} = \mathrm{GSB}_1 + \mathrm{GSB}_2$, $\mathrm{SE} = \mathrm{SE}_1 + \mathrm{SE}_2$, and $\mathrm{ESA} = \mathrm{ESA}_1 + \mathrm{ESA}_2$. Equations 6.3a and 6.3b represent diagonal peaks (superscript *Dm*, *Dn*) at the transition frequencies of states $|m\rangle$ and $|n\rangle$, respectively, while eqs 6.3c and 6.3d represent cross peaks (*Cmn*, *Cnm*), below and above the diagonal, respectively. As described previously, in 2D FS the parameter Γ is the average number of photons emitted from ESA pathways resulting in population in doubly-excited excitons relative to the number of photons emitted from ESA pathways that lead to singly-excited exciton population. Self-quenching of doubly-

excited excitons reduces the fluorescence quantum yield, such that $0 \le \Gamma \le 2$. For the $T = 0$ data presented in Figure 6.1, we found the optimized value for $\Gamma = 0.31$.

Equations 6.3a – 6.3d serve to illustrate differences between *T*-dependent 2D FS and 2D ES experiments. Each of the four peaks of the 2D spectrum consists of a stationary positive GSB term, a *T*-dependent positive SE term, and a *T*-dependent ESA term whose sign depends on the magnitude of Γ. In the case of 2D ES experiments, the ESA term has opposite sign with respect to the SE term. Turning to the behavior of the Green's function matrix elements, we see that downhill population transfer (i.e. $|n\rangle\langle n| \leftarrow |m\rangle\langle m|$) leads to a *T*-dependent increase in the matrix element $G_{nm}(T)$, and a corresponding decrease in $G_{mm}(T)$. Thus the intensity of the higher energy diagonal peak given by eq 6.3a, for example, will diminish with increasing *T* due to cancellation between a decaying positive SE term and an increasing negative ESA term. Similarly, the cross-peak given by eq 6.3c, which represents coupling from the higher to lower energy state, will increase in time due to the growth of the SE term and the decay of the ESA term. Cancellation between SE and ESA terms of opposite signs in 2D ES experiments makes these measurements sensitive to electronic population transfer. This is compared to 2D FS experiments, in which case the relative signs of SE and ESA terms need not be opposite. For $\Gamma \le 1$, the factor $1 - \Gamma$ that multiplies the ESA term will have the same sign as the SE term. Thus, contrast between the two terms will occur to a lesser extent. In these situations, the growth and decay of 2D FS spectral features are expected to be somewhat less sensitive to population transfer dynamics in comparison to 2D ES.

By varying the transfer rate constants defined by eqs 6.1 – 6.3, we simulated time-dependent 2D FS spectra, which we optimized to obtain the best agreement with our data.

This procedure was accomplished using the nonlinear global optimization package KNITRO.[66] In our experience with other problems, and this particular problem, the optimization algorithms and features of the KNITRO package allow for more robust optimization than built-in methods of computer algebra systems. In Figure 6.2A, we present experimental data for population times T = 0, 15, 45, 150, 600 and 1,200 fs. These spectra were normalized to the highest intensity feature within the T = 0 fs dataset. We note the following general trends. At T = 0 fs, there is a significantly intense peak along the diagonal centered at $\omega_\tau = \omega_t \approx 16{,}620$ cm^{-1}, and a cross-peak below the diagonal at $\omega_\tau \approx 16{,}620$ cm^{-1} and $\omega_t \approx 16{,}280$ cm^{-1}. A second, relatively weak diagonal peak is present at $\omega_\tau = \omega_t \approx 16{,}280$ cm^{-1}. These 2D spectral features are fully accounted for by the optimized "bent T-shaped" dimer conformation, whose linear spectrum is shown in Figure 6.1A. For population times T = 15 fs and T = 45 fs, the intensities of the lower-diagonal peak and the cross peak increase, while the intensity of the upper-diagonal peak decreases to a minor extent. We further note the appearance at these short times of a weak diagonal peak at $\omega_\tau = \omega_t \approx 16{,}393$ cm^{-1}, and an associated cross-peak at $\omega_\tau \approx 16{,}393$ cm^{-1} and $\omega_t \approx 16{,}280$ cm^{-1}. Interestingly, this third feature occurs at a frequency very close to that of the dark state of the bent T-shaped dimer (16,382 cm^{-1}), and not far from that of the uncoupled monomer transition (16,501 cm^{-1}). As the population time is further increased, approaching the value T = 1,200 fs, the intensities of all the observed features in the 2D spectra gradually decrease.

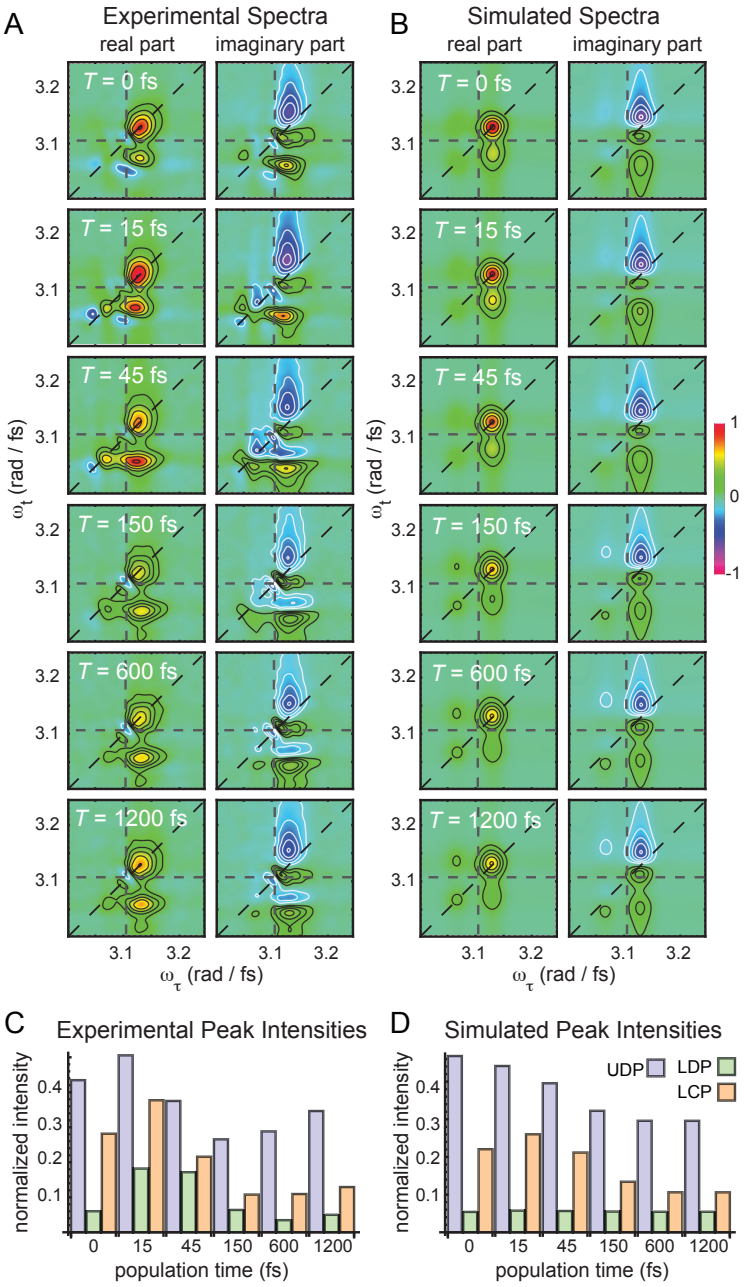

Figure 6.2. Comparison between experimental (A) and simulated (B) time-dependent 2D FS total correlation spectra of the $(MgTPP)_2$ / liposome system. Horizontal and vertical dashed lines indicate the monomer transition frequency $\bar{\nu}_1 = 16{,}501\ cm^{-1} = 3.11\ rad\ fs^{-1}$. The simulated spectra are based on using the optimized structural and spectroscopic parameters as input. Population transfer among singly-excited excitons was modeled using a Green's function solution to the quantum master equation (see eqs 6.1 – 6.3), and rapid decay of the parameter Γ due to vibrational dephasing. (C) Time-dependent intensities of experimental 2D line shapes (UDP = upper diagonal peak, LDP = lower diagonal peak, LCP = lower cross-peak). (D) Time-dependent intensities of simulated 2D line shapes.

As discussed above, a multi-variable regression analysis was implemented on the $T = 0$ datasets to obtain the optimized structural and spectroscopic parameters.[8] These parameters (i.e. $\boldsymbol{R}$, α, β, Γ, etc.) were used as input to our analysis of the time-dependent data. For the optimized conformation, only two of the singly-excited excitons, with ε_{X_2} = 16,283 cm^{-1} and $\varepsilon_{X_4} = 16{,}619$ cm^{-1}, appear to contribute. The weaker transition at ε_{X_5} = 16,718 cm^{-1} occurs near the blue edge of the laser spectrum, and does not appear as a diagonal peak in the 2D FS spectra. The transition at $\varepsilon_{X_3} = 16{,}382$ cm^{-1} is effectively dark according to our $T = 0$ optimization (see Figure 6.1A). We therefore adopted a model that included only the $|X_2\rangle$, $|X_3\rangle$ and $|X_4\rangle$ states. We found that because the state $|X_3\rangle$ carries no oscillator strength, its presence has a negligible effect on the calculated spectra. Nevertheless, we included it in our calculations for completeness.

Using the simplified model described above, the population transfer rate constants were optimized using the full set of time-dependent 2D FS data shown in Figure 6.2A. We found that the slow decay of all experimentally observed peak intensities could be well modeled using eqs 6.1 – 6.3. However, the rise of the cross-peak amplitude at $T = 15$ fs and $T = 45$ fs could not be reproduced using this approach alone. We therefore consider the possibility that in addition to the population transfer mechanism described by the master equation, we must also account for the effects of fast electronic dephasing due to electron-nuclear coupling. Figure 6.3 illustrates the two relaxation pathways that affect the 2D FS spectra. Population is initially excited by pulses 1 and 2 within the singly-excited state manifold. During the time interval T, both population transfer and rapid dephasing of electronic states coupled to nuclear motion occurs. At time T, pulses 3 and 4 excite the two possible ESA pathways; the first producing population on the

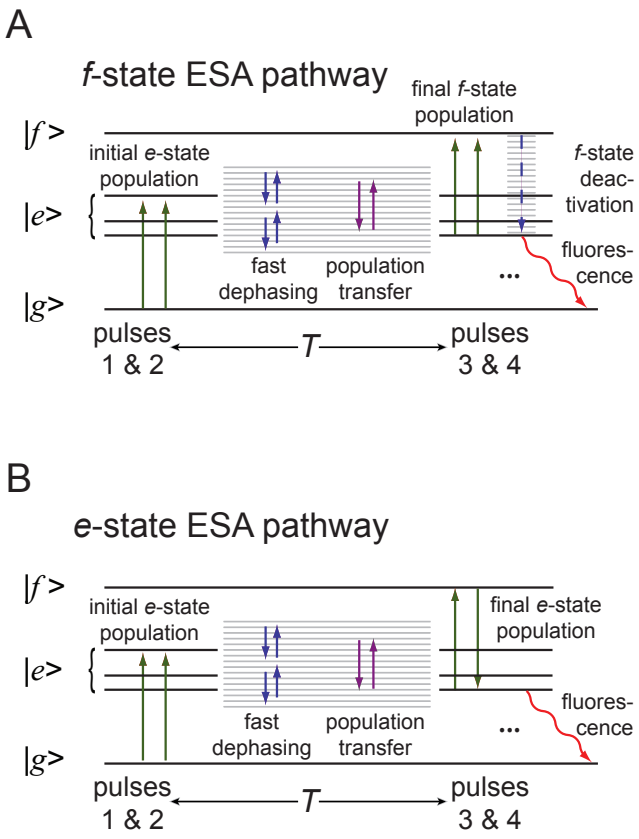

Figure 6.3. Energy level diagrams depicting the effects of population transfer and rapid electronic dephasing on excited state absorption (ESA) terms of the 2D FS signal. Pulses 1 and 2 excite initial population in the singly-excited $|e\rangle$-state manifold, which can subsequently relax during the population period T by two primary mechanisms. These are coupling to nuclear modes and rapid electronic dephasing, in addition to downhill population transfer between electronic levels. Relaxation within the $|e\rangle$-state manifold is expected to have different effects on the two types of ESA pathways that contribute to 2D FS. (A) ESA signal pathways that result in population on the doubly-excited $|f\rangle$-state are susceptible to deactivation pathways, which involve coupling to nuclear coordinates. (B) ESA signal pathways that directly excite population on the $|e\rangle$-state manifold are expected to experience a comparatively weaker dependence on electron-nuclear coupling.

doubly-excited state $|f\rangle$, the second producing population on the singly-excited state manifold $|e\rangle$. Because the fluorescence quantum yield resulting from doubly-excited state population ultimately depends on deactivation pathways that couple the $|f\rangle$-state to

lower-lying electronic levels, we anticipate that the extent of electronic dephasing can reduce this pathway's importance relative to those that populate $|e\rangle$-state levels directly. Taken in this context, we define the parameter $\Gamma \equiv Q^{f}_{ESA}/Q^{e}_{ESA}$ as the ratio of fluorescence quantum efficiencies due to ESA pathways that produce population in the $|f\rangle$-state to those that produce population in the $|e\rangle$-state. We propose that the value of Γ can exhibit a time-dependent decay $\Gamma = 0.31e^{-K_{ed}T}$ that reflects the fast electronic dephasing within the $|e\rangle$-state manifold.

Figure 6.2B shows the results of our optimization using as parameters the transfer rate constants $K_{X_2X_3}$, $K_{X_2X_4}$, $K_{X_3X_4}$, and the electronic dephasing rate constant K_{ed}. We followed standard procedures to calculate the Green's function matrix elements based on diagonalization of the rate matrix (see Appendix B for details).[15] Our nonlinear optimization included in its target function χ^2 a comparison between simulated and experimental 2D peak intensities for the most prominent features, the higher energy diagonal peak (labeled DX_4) and cross peak (CX_4X_2).

$$\chi^2 = \sum_T \left[S^{DX_4}_{TCF,\exp} - S^{DX_4}_{TCF,sim} \right]^2 + \left[S^{CX_4X_2}_{TCF,\exp} - S^{CX_4X_2}_{TCF,sim} \right]^2 \qquad (6.4)$$

The values of the rate constants that minimize eq 6.4 were found to be $K_{X_2X_3} = 3.6\times10^{-9}\,\mathrm{fs}^{-1}$, $K_{X_2X_4} = 0.0105\ \mathrm{fs}^{-1}$, $K_{X_4X_3} = 2.56\times10^{-9}\,\mathrm{fs}^{-1}$, and $K_{ed} = 0.86\ fs^{-1}$. By using the detailed balance condition (eq 6.2), we determined the remaining rate constants according to $K_{X_3X_2} = 0.616\times K_{X_2X_3} = 2.22\times10^{-9}\,\mathrm{fs}^{-1}$, $K_{X_4X_2} = 0.201\times K_{X_2X_4} =$

$2.11\times10^{-3}\,\mathrm{fs}^{-1}$, $K_{X_3X_4} = 3.067\times K_{X_4X_3} = 7.85\times10^{-9}\,\mathrm{fs}^{-1}$, $K_{X_2X_2} = K_{X_3X_2} + K_{X_4X_2} \cong$ $2.11\times10^{-3}\,\mathrm{fs}^{-1}$, $K_{X_3X_3} = K_{X_2X_3} + K_{X_4X_3} \cong 6.16\times10^{-9}\,\mathrm{fs}^{-1}$, $K_{X_4X_4} = K_{X_2X_4} + K_{X_3X_4} \cong 0.0105\ \mathrm{fs}^{-1}$.

This model appears to reproduce the general trends in the experimental data. Population transfer is dominated by coupling between the $|X_2\rangle$ and $|X_4\rangle$ states, with the downhill process occuring on the time scale ~ 95 fs, and the uphill process ~ 474 fs. The rise of the cross-peak intensity at short population times is accounted for by electronic dephasing with time constant ~ 1.2 fs. An interesting feature observed in the experimental spectra, which the current model does not reproduce, is the appearance at short times of a weak diagonal peak at $\omega_\tau = \omega_t \approx 16{,}393$ cm^{-1} and an associated cross-peak at $\omega_\tau \approx$ 16,393 cm^{-1} and $\omega_t \approx$ 16,280 cm^{-1}. These features could be due to greater oscillator strength in transitions to the $|X_3\rangle$ state (16,382 cm^{-1}) than is allowed by the optimized structural parameters. This could be an indication that the true conformation is slightly different from the one resulting from our $T = 0$ fs analysis. A second possibility is that a minor component of MgTPP monomer is also present in the sample. This seems less likely as the monomer transition frequency (16,501 cm^{-1}) is further removed from the observed feature, and there is no indication of its presence in the $T = 0$ fs dataset.

C. Thermodynamic Considerations of Membrane Induced Porphyrin Dimer Self-Assembly

We found that the average conformation for the $(MgTPP)_2$ dimer is a "bent T-shaped" structure with mean separation between Mg centers $R = 4.2$ Å. Close packing considerations alone would suggest that the most stable structure should maximize $\pi-\pi$ stacking interactions. However, entropic contributions to the free energy due to

fluctuations of the amphiphilic interior of the phospholipid membrane must also be taken into account. To understand the conditions that determine dimer stability, we dissect the thermodynamic contributions to dimer assembly.[48]

We consider the association reaction of a dimer $2M \leftrightharpoons M_2$ within its local membrane environment. The standard state Gibb's free energy of association $\Delta G^{\circ}_{a,tot}$ can be written as the sum of contributions:

$$\Delta G^{\circ}_{a,tot} = \Delta G^{\circ}_{a,\text{M-solv}} + \Delta G^{\circ}_{a,\text{M-M}} + \Delta G^{\circ}_{a,\text{solv-solv}} \,. \tag{6.5}$$

In eq 6.5, the first term on the right represents the contribution of monomer-solvent interactions, the second term represents monomer-monomer interactions, and the last term represents solvent-solvent interactions. The solvent-solvent term is approximated to be small, since at low monomer concentration the majority of solvent molecules do not come into contact with monomer or dimer species. The balance of enthalpic and entropic contributions to the first two terms determines the stability of the dimer. We write these, respectively

$$\Delta H^{\circ}_{a,tot} = \Delta H^{\circ}_{a,\text{M-solv}} + \Delta H^{\circ}_{a,\text{M-M}} \tag{6.6}$$

$$\Delta S^{\circ}_{a,tot} = \Delta S^{\circ}_{a,\text{M-solv}} + \Delta S^{\circ}_{a,\text{M-M}} \tag{6.7}$$

We next estimate the relative signs and magnitudes of the enthalpic and entropic contributions described by eqs 6.6 and 6.7. We observed that at very low concentrations

of MgTPP in aqueous liposome suspensions, essentially all of the monomer is partitioned into the lipid phase, indicating favorable monomer-solvent interactions. Upon association of the dimer, fewer contacts must be formed between monomer and solvent, such that $\Delta H^{\circ}_{a,\text{M-solv}} > 0$. This factor, taken alone, should oppose dimer assembly. On the other hand, the enthalpic contribution due to forming new monomer-monomer contacts is not known. If interactions between monomers were highly favorable, this might drive dimer assembly. However, our determination of the bent T-shaped dimer conformation – a relatively open structure – suggests that the dimer does not maximize monomer-monomer surface contacts. Based on this observation, we infer that $\Delta H^{\circ}_{a,\text{M-M}} \approx 0$.

We next consider the entropic contributions. We expect $\Delta S^{\circ}_{a,\text{M-M}} < 0$. This term represents the entropic cost of dimer assembly, which is due to the loss of translational and rotational freedom of monomers in comparison to the dimer.[29] An approximate lower bound for this value, which is based on a loosely associated dimer and ignores the confining effects of the membrane, is $\Delta S^{\circ}_{a,\text{M-M}} \geq -36 \text{ e.u.} = -151 \text{ J K}^{-1}\text{mol}^{-1}$. The true value is expected to be smaller in magnitude because of the reduced translational and rotational degrees of freedom of the monomer in the membrane. Lastly, we consider the effect on the entropy of monomer-solvent interactions upon dimer dissociation. In the associated state, the number of monomer-solvent contacts is expected to decrease, corresponding to an increase in the conformational freedom of the solvent. This suggests that entropic monomer-solvent interactions favors dimer assembly, such that $\Delta S^{\circ}_{a,\text{M-solv}} > 0$.

The relevant thermodynamic factors that determine dimer assembly can be summarized as follows. 1) Dimer assembly requires monomer-solvent contacts to be

disrupted, resulting in a loss in enthalpic stability. 2) Condensation of the monomers to form a dimer corresponds to a loss of entropic freedom. Both factors 1) and 2) are energetic barriers to dimer assembly, which must be compensated for by a gain in conformational entropy of the local solvent environment. The balance of factors can be written

$$T\Delta S^{\circ}_{a,\text{M-solv}} > \left(\Delta H^{\circ}_{a,\text{M-solv}} - T\Delta S^{\circ}_{a,\text{M-M}}\right). \tag{6.8}$$

Currently, the magnitudes of the monomer-solvent interaction terms of eq 6.8 are not known. The monomer-monomer entropy term can be accurately calculated from theory.[29] Knowledge of the three terms in eq 6.8 could provide insights about dimer assembly in terms of the chemical nature of the membrane-monomer interactions. One might expect temperature to be a useful control parameter. By applying a conformational analysis to temperature-dependent 2D FS measurements, it should be possible to separate enthalpic from entropic contributions to the Gibb's free energy. We have performed follow-up experiments (described in Chapter III) that examine the adopted conformations of a pair of ZnTPP monomers that are chemically tethered by a flexible linker. This allows for low concentrations of the exciton-coupled chromophores to be studied over a range of temperatures without the complication of higher order aggregate formation. The results of these experiments will be reported in a separate publication. We anticipate the energetics of "folding" of a tethered dimer to exhibit nearly identical values for $\Delta S^{\circ}_{a,\text{M-solv}}$ and $\Delta H^{\circ}_{a,\text{M-solv}}$ as the current system, and the value of $\Delta S^{\circ}_{a,\text{M-M}}$ can be accurately determined from theory.

D. Conclusions

Using a combination of 2D FS and multivariable nonlinear global analysis, we determined the conformation of spontaneously self-assembled $(MgTPP)_2$ dimers in the hydrophobic regions of phospholipid bilayer membranes at room temperature. We found that the average conformation adopted by the system is that of a "bent T-shaped" dimer. Furthermore, we studied the time-dependence of the 2D FS total correlation spectra on time scales ranging between 15 fs – 1.2 ps. These measurements are well described using a quantum master equation to model the population transfer among singly-excited exciton states and rapid electronic dephasing. The relatively "open" structure of the dimer conformation suggests that the thermodynamic factors that favor dimer assembly are closely related to the interactions of the system with the local membrane environment. The experiments described in Chapter III extended this work by using a tethered ZnTPP dimer to make a clean separation between entropic and enthalpic contributions to the thermodynamic driving forces of membrane-induced dimer self-assembly. The population time dependence of the signals from this system was measured as well, and are discussed in the following section.

3. Electronic Population Transfer and Spectral Diffusion in a Membrane-Supported Zinc Porphyrin Tweezer

As an extension of the experiments described in Chapter III, 2D FS spectra were recorded at a series of values of the population time T for $(ZnTPP)_2$ embedded in liposomes. These spectra were recorded at 17° C under 16,470 cm^{-1} excitation. The results are shown in Figure 6.4, which shows the real part of the 2D total correlation

spectrum for values of T ranging from 0 to 195 fs. As the population time is increased, the upper cross peak increases in intensity, and the spectral linewidths of the peaks broaden. The spectrum reverts to its original appearance when T is returned to 0 fs at the end, confirming that the observed changes result from changing the population time.

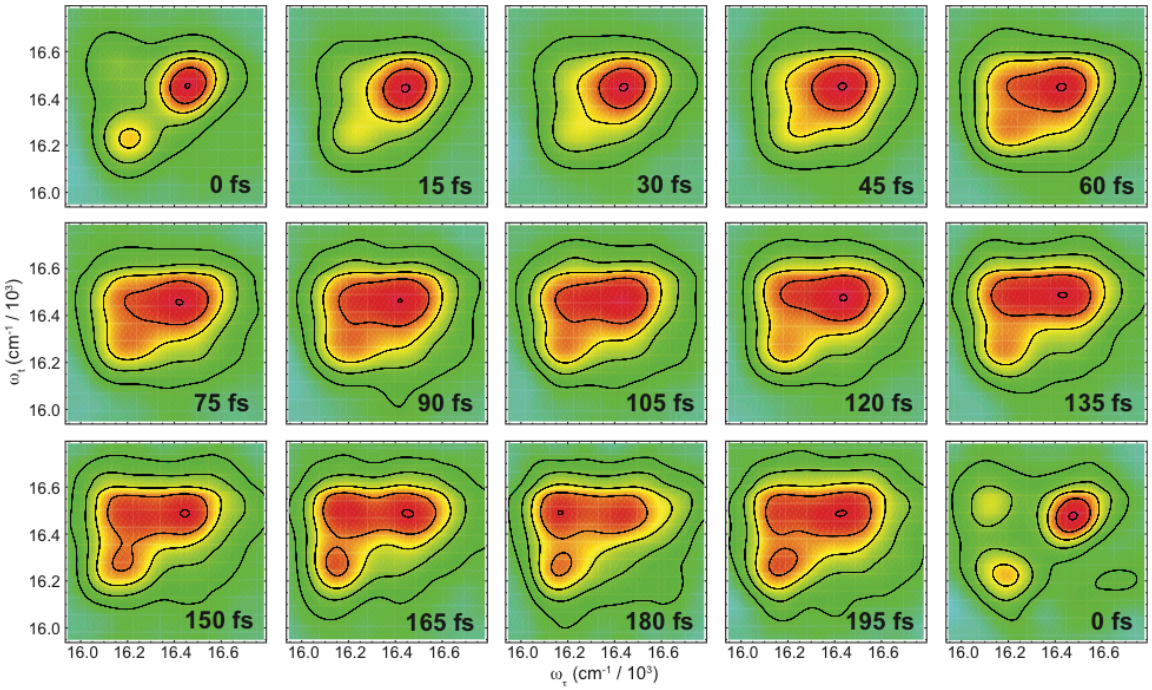

Figure 6.4. Population time-dependent 2D FS spectra of $(ZnTPP)_2$ in liposomes. The real part of the total correlation spectrum is plotted. As T is increased, the relative intensity of the upper off-diagonal peak increases. The spectrum in the lower right-hand corner was obtained by returning the delay stages to 0 fs population time after recording all of the other data. These spectra were formed by adding together sum and difference spectra that were each normalized to the intensities of its upper diagonal peak (at $\omega_\tau = \omega_t = 16{,}463\ \mathrm{cm}^{-1}$).

A. Changes in Relative Peak Intensity

Prior to attempting to model the T-dependence of the data, the fitting procedure used for the 17° C data in Chapter III was repeated using the initial T=0 fs spectra from the dataset presented in this chapter. The results were similar to those obtained in Chapter

III: τ_H = 73 fs, Γ_H = 1.32, σ_H = 367 cm^{-1}, τ_J = 87 fs, Γ_J = 0.82, σ_J = 50 cm^{-1}, σ_{lin} = 367 cm^{-1}, b = 9.82, with the remaining variables being fixed at their 23° C values as in Chapter III. The quality of the fit is reflected in the calculated and experimental total correlation spectra in the lower left-hand corner of Figure 6.5. Performing this initial optimization of the T=0 fit ensured that we would model true T-dependent changes in the subsequent fit, rather than compensating for imperfections in the T=0 fit.

The changes in relative intensities of the peaks were modeled in the same manner as the MgTPP data presented in section 2. Redfield theory was used to predict the T-dependence of excited state populations,[15, 95] and an additional time constant was included that allowed the parameter Γ to vary with T.[9] At each value of T, spectra were calculated separately for the J-dimer and H-dimer, then combined, taking into account the relative populations and fluorescence quantum yields of the J- and H- dimer as well as T-dependent changes in intensity predicted by the theory. Each dimer had two free parameters that were varied to optimize a fit to the data: the time constants for population transfer and electronic dephasing (manifested as a change in Γ with T). A cost function (eq 6.9) was generated, taking into account the deviation of the calculated signal from the experimental signal for the real and imaginary parts of the rephasing and nonrephasing signals at each population time point.

$$\begin{aligned}\chi^2_{2D} = \sum_{\omega_\tau,\omega_t,T} \Big\{ &\Big[\mathrm{Re}\big(NRP_{sim}(\omega_\tau,\omega_t,T)\big) - \mathrm{Re}\big(NRP_{\exp}(\omega_\tau,\omega_t,T)\big)\Big]^2 \\ &+\Big[\mathrm{Im}\big(NRP_{sim}(\omega_\tau,\omega_t,T)\big) - \mathrm{Im}\big(NRP_{\exp}(\omega_\tau,\omega_t,T)\big)\Big]^2 \\ &+\Big[\mathrm{Re}\big(RP_{sim}(\omega_\tau,\omega_t,T)\big) - \mathrm{Re}\big(RP_{\exp}(\omega_\tau,\omega_t,T)\big)\Big]^2 \\ &+\Big[\mathrm{Im}\big(RP_{sim}(\omega_\tau,\omega_t,T)\big) - \mathrm{Im}\big(RP_{\exp}(\omega_\tau,\omega_t,T)\big)\Big]^2 \Big\}\end{aligned} \tag{6.9}$$

Figure 6.5 shows separately the H- and J-dimer spectra calculated at three different population times, and compares them to experiment. It is immediately apparent that the theory captures the increase in the upper off-diagonal peak intensity quite well.

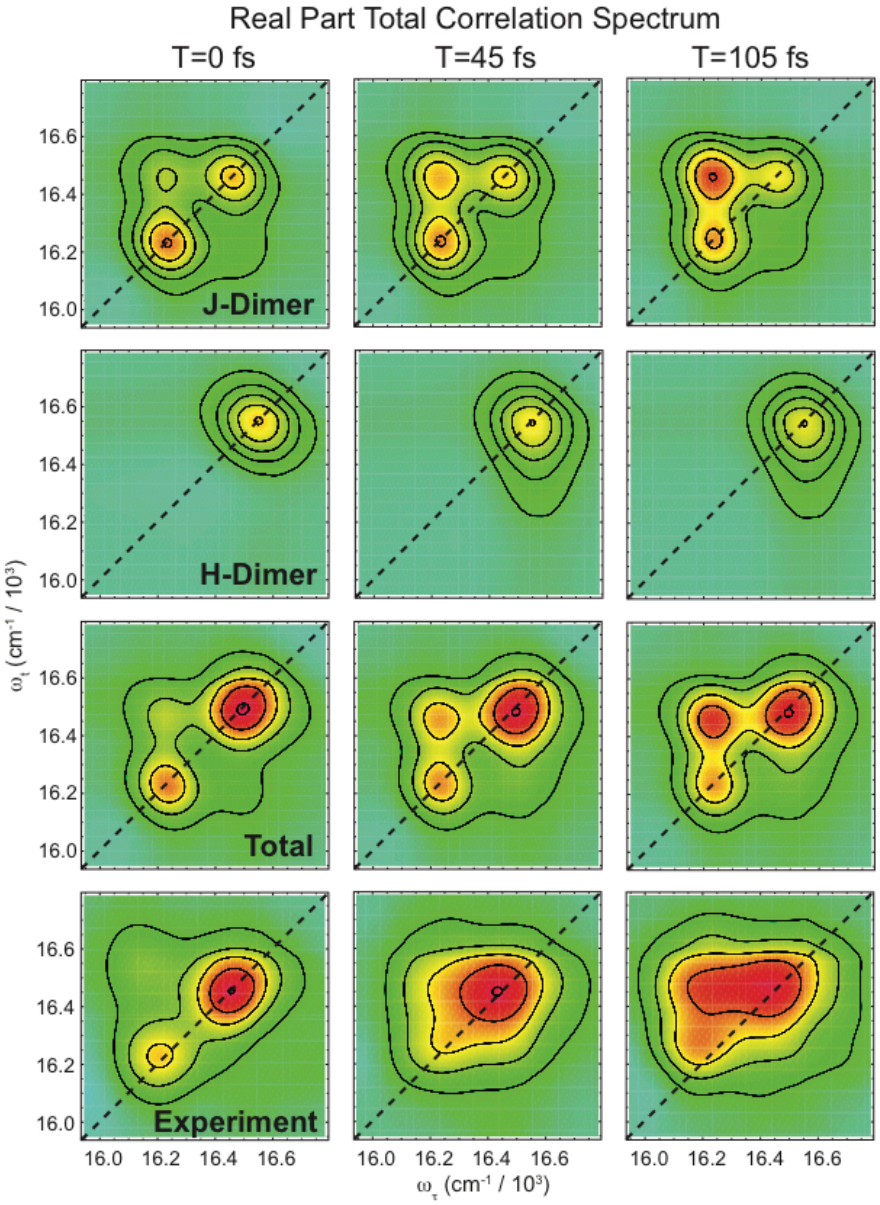

Figure 6.5. Modeling of population time-dependent $(ZnTPP)_2$ data. For each population time point, the J- and H-dimer signals were calculated separately and then combined in the proper ratio. The optimal values of the parameters $K_{X_2X_3,J}$, $K_{X_2X_3,H}$, $K_{ed,J}$ and $K_{ed,H}$ were obtained and used to calculate the *T*-dependent spectra plotted here.

Figure 6.6 further explores the experimental and calculated spectra by tracking the amplitudes of the lower diagonal peak (LDP), lower cross peak (LCP), and upper cross peak (UCP) in the experimental and theoretical total correlation spectra as a function of *T* (positions indicated in Figure 6.6A). The upper diagonal peak (UDP) was not tracked because all spectra were normalized to its intensity. Figure 6.6 shows that in addition to the increase in the upper cross peak in the real part, the theory also captures more subtle changes like the imaginary part's slight increase in LDP amplitude, while the UCP becomes more negative with increasing *T*. The parameter values corresponding to these fits are $K_{X_2X_3,J} = 0.00018$ fs^{-1}, $K_{X_2X_3,H} = 0.0034$ fs^{-1}, $K_{ed,J} = 0.0058$ fs^{-1} and $K_{ed,H} = 2.52$ fs^{-1}, where $X_2 = |-\rangle$ and $X_3 = |+\rangle$. As was done for MgTPP, the reverse rate constants were calculated by applying detailed balance to the energy gaps between excited states 2 and 3 (eq 6.2). The changes in the spectrum are dominated by $K_{ed,J}$, which is responsible for most of the increase in intensity of the UCP with increasing *T*.

B. Changes in Spectral Lineshape

The above calculations did not take into account changes to the spectral lineshapes, and therefore they do not capture the 'blurring together' of the features with increasing population time. This was investigated by performing fits to diagonal and antidiagonal slices through the spectra and comparing their linewidths. Figure 6.7 shows the *T*-dependent changes in the real part of the difference signal. The signal along the diagonal shows little change in linewidth as *T* is increased, while the signal along the antidiagonal broadens significantly. To quantify this behavior, the diagonal slice of the spectrum at each population time was fit to two Gaussians to take into account the UDP

and LDP, while an antidiagonal slice through the UDP was fit to one Gaussian. Representative fits are shown in Figures 6.7B and 6.7C.

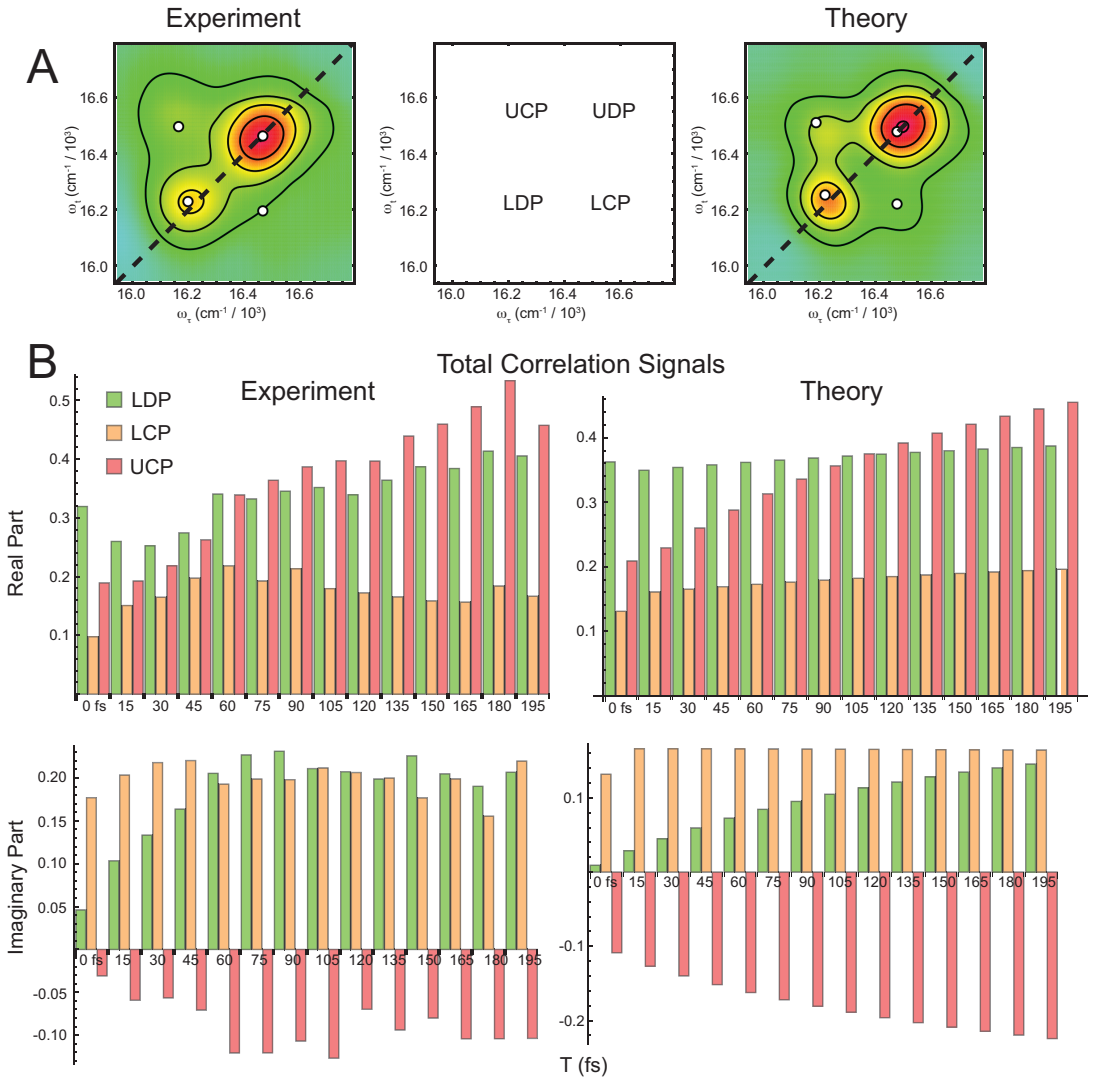

Figure 6.6. *T*-dependent peak intensities using the fits summarized in Figure 6.5. (A) Experimental and theoretical *T*=0 spectra, with white dots showing the positions used to track the lower diagonal peak (LDP), upper diagonal peak (UDP), lower cross peak (LCP) and upper cross peak (UCP). The center plot is a schematic associating the names of the four peaks with their approximate positions in the spectrum. (B) Bar graphs showing the *T*-dependence of LDP, LCP and UCP in the real and imaginary parts of the total correlation spectrum. The left column is experiment and the right column is theory; the upper row is the real part and the lower row is the imaginary part. The amplitude of LDP is plotted in green, LCP in orange and UCP in red, with *T* on the x-axis. All spectra were normalized to the UDP, which is therefore not included in the bar graphs.

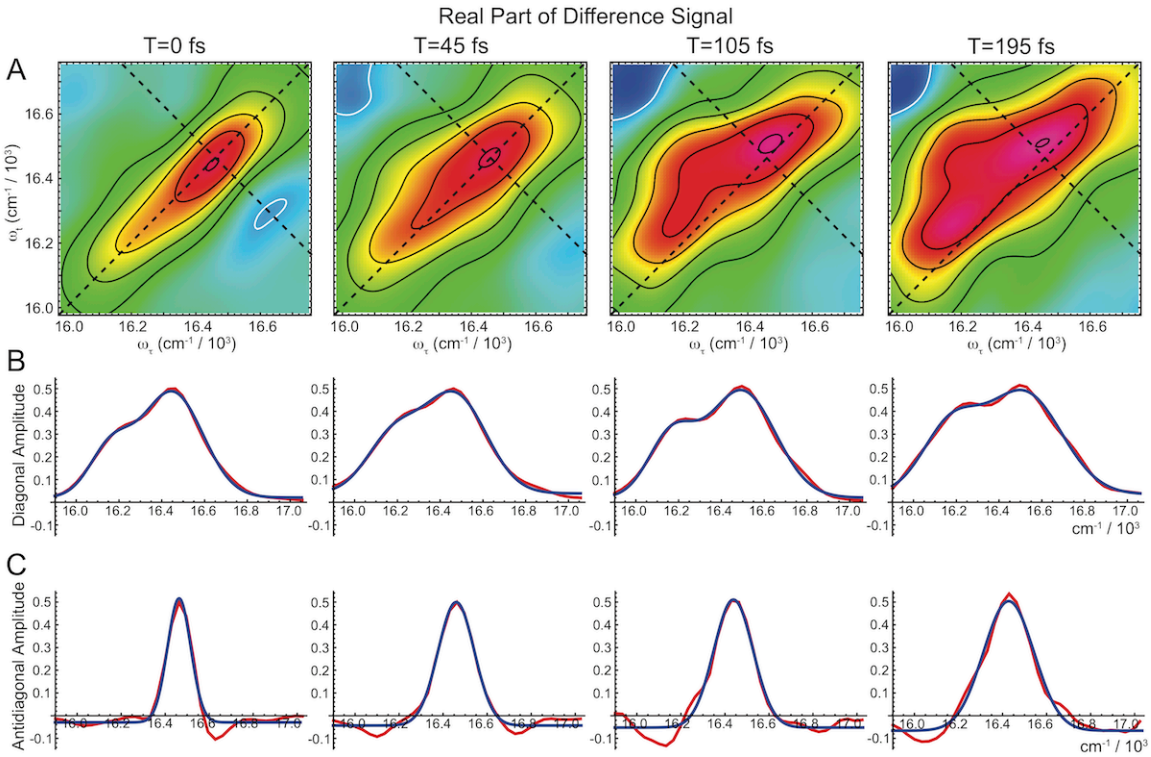

Figure 6.7. *T*-dependent lineshapes in the real part of the difference signal. (A) 2D spectra show changes in relative peak intensities (discussed above) as well as a broadening of the spectral features in the antidiagonal direction. The diagonal and antidiagonal slices that were utilized for fitting are indicated by dashed lines. (B) Slices along the diagonal show little change in width as *T* is increased. Data shown in red; fit to two Gaussians shown in blue. (C) Slices along the antidiagonal increase in width as *T* is increased. Data shown in red; fit to one Gaussian shown in blue.

These fits are summarized in Figure 6.8. Figure 6.8A shows the full width at half max (FWHM) of different spectral features as a function of population time. In red are shown the FWHMs obtained from fitting diagonal slices to two Gaussians (solid = higher energy peak, dashed = lower energy peak). In blue, the FWHMs obtained from fitting antidiagonal slices to one Gaussian are shown. Figure 6.8B presents the ratio between the antidiagonal FWHM and the weighted average of the diagonal FWHMs (weighted by the intensity of that feature in the fit to two Gaussians). This figure shows that the ratio of the antidiagonal to diagonal linewidth increases roughly exponentially with a time constant of about 60 fs. It should be noted that the time constant does not depend on where one

chooses to draw the antidiagonal slice. This increase in the 'roundness' of spectral features is observed frequently in 2D spectroscopy and is attributed to the process of spectral diffusion leading to decorrelation between the initial (ω_τ) and final (ω_t) transition frequencies.[15] The ratio does not reach 1, however, even at the longest population time investigated (195 fs). This suggests that while there is a process that leads to rapid loss of correlation between transition frequencies (perhaps reflecting small solvent-induced fluctuations in the transition frequency of each dimer), static disorder results in some correlation remaining after 195 fs (perhaps reflecting J- and H-dimers that only interconvert on much longer timescales). Experiments at larger values of *T* could yield insight into these slower processes.

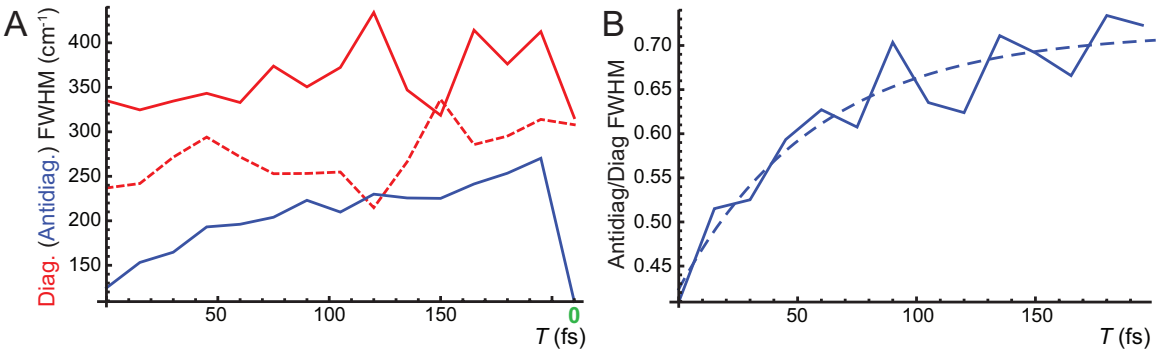

Figure 6.8. *T*-dependent linewidths in the real part of the difference signal. (A) The diagonal FWHM of the UDP (solid red) and LDP (dashed red), and the antidiagonal FWHM of the UDP (solid blue) at a series of values of *T*. The rightmost data point (labeled on the x-axis with a green zero) shows the return of the antidiagonal linewidth to its original value upon returning to *T*=0 fs, accompanied by little change in the diagonal linewidth. (B) *T*-dependence of the ratio of the UDP antidiagonal FWHM to the weighted average of the UDP and LDP diagonal FWHMs (solid blue) and an exponential fit to it (dashed blue).

C. Discussion

Both MgTPP and ZnTPP dimers in liposomes show sub-100 fs excited state dynamics that cannot be modeled with Redfield theory alone. In both cases, an additional electronic dephasing process that leads to *T*-dependent changes in the parameter Γ must to be invoked in order to explain the spectra. In particular, in both MgTPP and ZnTPP there is a stronger increase in the intensity of the predominant cross peak than can be reproduced under Redfield theory for any set of parameters. Another possible explanation for this observation in the case of ZnTPP is an electronic excitation transport (EET) process between different dimers in the liposome.[96] To investigate this possibility, we estimated the Förster radius (eqs 4.1 and 4.2) for ZnTPP dimers at the 30:1 lipid:porphyrin ratio used for these experiments. In this calculation, we used the average fluorescence quantum yield of ZnTPP in solution (0.033)[97] and calculated the overlap integral using the full absorption and emission spectra of $(ZnTPP)_2$ in liposomes. The H-dimer's fluorescence is quenched, leading to a lower quantum yield than that of monomeric ZnTPP, a fact that was taken into consideration when calculating the Förster radius for H-dimer donors. Using these quantities, we obtain Förster radii of 1.89 nm for the J-dimer and 0.85 nm for the H-dimer. The use of the full absorption and emission spectra is expected to overestimate the energy transfer probability. The J-dimer emits on the blue edge of the emission spectrum and absorbs on the red edge of the absorption spectrum, making the overlap integral of J-to-J transfer larger than that of H-to-H, H-to-J or J-to-H transfer. However, J-to-J transfer is significantly disfavored by the low number of J-dimers relative to H-dimers (1:9.8).

Using the Förster radii determined as described above, the formalism of ref [96] was used to calculate the probability that the initially excited dimer is still excited after a time t in each of the four transfer scenarios listed above. These calculations suggest that J-to-H transfer will be the fastest of the four, and may result in as high as an 80% probability that an initially excited J-dimer will transfer its excitation to an H-dimer within a delay equal to its fluorescence lifetime. Meanwhile, H-to-J transfer depopulates only 3% of initially excited H-dimers. Details of the calculations are presented in Appendix B.

J-to-H and H-to-J transfer would be expected to have the largest impact on the *T*-dependence of the 2D FS signals, because a different dimer conformation could be excited before and after *T*. J-to-H transfer during *T* could account for some of the increase in the UCP, because J-dimers would be initially excited at relatively low frequency, and after transfer, the higher-frequency transitions in the H-dimer would be excited by pulses 3 and 4. Assuming a fluorescence lifetime on the order of 1 ns, these calculations predict that only about 5% of initially excited J-dimers have transferred their excitation to H-dimers on the 200 fs timescale investigated in this work. These calculations assume a fully incoherent inter-dimer energy transfer mechanism. It is conceivable that the fast timescale of UCP growth observed in this system results from a coherent inter-dimer energy transfer process. Further experiments and more extensive modeling could reveal whether this inter-dimer energy transfer process is responsible for the increase in the UCP beyond that predicted by Redfield theory, and whether it proceeds by a coherent or incoherent mechanism.

Analogues of the broadening of the antidiagonal linewidth of the difference spectrum observed in $(ZnTPP)_2$ have been observed by four-wave mixing 2D electronic

spectroscopy in numerous different systems. Full relaxation of the spectrum to a circular shape is typically observed within a few hundred femtoseconds for monomeric chromophores in solution.[98-99] $(ZnTPP)_2$ in liposomes exhibits rapid broadening in the antidiagonal direction on a similar timescale, but the spectrum does not relax to a fully circular shape over the 195 fs population time range investigated. Instead, the broadening plateaus with an antidiagonal/diagonal ratio of about 0.7 (Figure 6.8), suggesting that slower processes must take place before the final transition frequency can become fully decorrelated from the initial transition frequency.

4. Summary and Bridge to Chapter VII

This chapter has demonstrated that similar excited state dynamics are at play in the self-assembled MgTPP and tethered ZnTPP dimer systems. Population relaxation timescales can be extracted from changes in peak intensity as a function of population time, while spectral diffusion timescales can be extracted from changes in the lineshapes of 2D spectra. These timescales reflect both the photophysical properties of the chromophore itself and its interactions with its environment.

Broad spectral lineshapes present challenges for all spectroscopic measurements, particularly those performed with UV excitation. Broad lineshapes limit the amount of information that can be extracted from spectra, because changes manifest themselves as small changes to the shape of one broad peak, rather than changes in the positions and intensities of multiple discreet peaks. Chapter VII presents theoretical investigations into a version of 2D FS that has the potential to yield significantly narrower lineshapes than conventional 2D FS. The proposed experiment would use entangled photon pairs as the

excitation source, and model calculations suggest that it could significantly suppress diagonal peaks in 2D spectra, in addition to yielding narrower lineshapes. These differences could allow significantly more information to be extracted from the spectra of systems for which conventional 2D spectra are highly congested.

CHAPTER VII

ENTANGLED PHOTON-PAIR TWO-DIMENSIONAL FLUORESCENCE SPECTROSCOPY

1. Overview

In the previous chapters of this dissertation, I presented new experimental developments that have expanded the capabilities of 2D FS and yielded new insight into systems like porphyrins and DNA. In this chapter, I present a theoretical investigation into another potential extension of 2D FS – the use of entangled photons as the excitation source. This chapter is based on material published as Raymer, M. G.; Marcus, A. H.; Widom, J. R.; Vitullo, D. L. P. Entangled Photon-Pair Two-Dimensional Fluorescence Spectroscopy (EPP-2DFS). *J. Phys. Chem. B.*, **2013**, DOI 10.1021/jp405829n. M. G. Raymer and A. H. Marcus developed the theory with help from D. L. P. Vitullo, and I performed the model calculations. This chapter presents those model calculations along with an overview of the background and theory. Further details can be found in [14].

2. Introduction

Entanglement is a central tenet of quantum mechanics, and developments in the field of quantum information science have utilized entanglement for the purposes of quantum computing, cryptography and teleportation.[100-102] In this work, we investigate the potential of quantum-entangled light in the area of molecular spectroscopy. In particular, we propose an experiment called entangled photon-pair two-dimensional fluorescence spectroscopy (EPP-2DFS) that would utilize time-frequency entangled

photon pairs as the excitation source for a 2D FS experiment. The photons are directed through a 'Franson interferometer' with controllable phase shifts and delays in both arms.[103-105] This entangled photon pair is used to induce two-photon absorption in a sample, and the ensuing fluorescence is monitored as a function of the interferometer delays. Our calculations suggest that this approach will yield significant advantages in comparison to standard 2D spectroscopy techniques. In particular, 1) the intensities of nonlinear optical signals will be greatly enhanced relative to those of linear 'background' signals. 2) The time-frequency entanglement of the light source will allow simultaneous temporal and spectral resolution that is not attainable using 'classical' light sources. 3) The 2D spectral lineshapes of resonant transitions will be proportional to the inverse population relaxation time scale, rather than the coherence dephasing time scale, thus providing considerable enhancements to spectral resolution. 4) The approach facilitates the isolation of the two-photon absorption (TPA) signal from signals yielding population on singly-excited states, which has the effect of greatly reducing the diagonal contributions to the 2D spectrum. While points 1 and 2 are extensions of well-known properties of entangled light,[106-109] points 3 and 4 are unique to our specific experimental arrangement.

3. The Franson Separated Two-Photon Interferometer

The Franson interferometer demonstrates quantum entanglement of photons by yielding a nonlocal quantum interference effect that cannot be fully simulated with a classical model of light.[103-105] As shown schematically in Figure 7.1, entangled photon pairs (from a source such as a parametric downconversion (PDC) crystal) enter separate

interferometers, labeled *A* and *B*. While each interferometer has one arm that is delayed by a time much greater than the coherence time of the light, the relative delays of the *A* and *B* interferometers are set equal to within the coherence time of the light. Coincidence counts at detectors D_A and D_B are monitored, and are found to depend on phase shifts in either the *A* or *B* interferometer. Classical theory predicts up to 50% fringe visibility upon variation of the phase, while quantum theory predicts 100% fringe visibility for certain two-photon states.

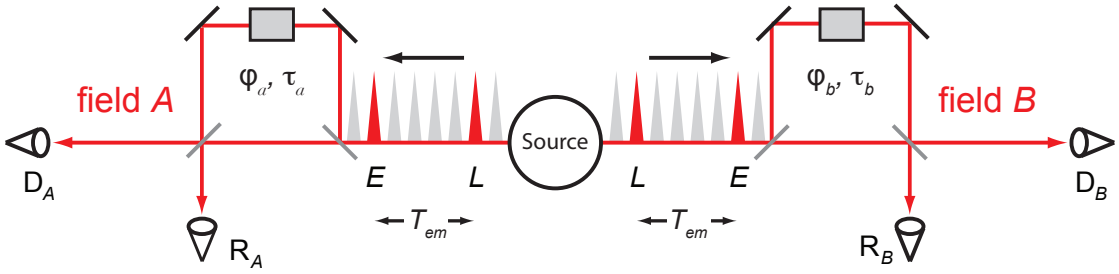

Figure 7.1. Franson interferometer. A stationary source creates two fields *A* and *B*, each of which enters an interferometer that introduces a relative time delay (τ_a, τ_b) in the long path. Phases (φ_a, φ_b) are controlled using acousto-optic Bragg cells (shown as gray rectangles). Gray diagonal lines are 50/50 beam splitters. Detectors D_A, D_B, R_A and R_B generate photoelectric counts, and both coincident and individual detector count rates are recorded. The source emission-time difference, denoted by T_{em}, is defined as the time between an 'early' (*E*) occurrence of the photon-pair virtual emission event in the source, and a 'late' (*L*) virtual emission event.

This effect can be explained by describing the field as a superposition of quantum amplitudes for emission of the photon pair at different times.[105] A photon pair being emitted 'early' and traversing the 'long' paths through the interferometers is physically indistinguishable from one being emitted 'late' and traversing the 'short' paths. These two pathways can thus interfere, and for certain interferometer phases, destructive interference leads to a coincidence count rate of zero at detectors D_A and D_B.

4. Coupled Two-Level Molecules as a Quantum Two-Photon Coincidence Detector

The detectors in Franson's apparatus were assumed to have infinite spectral bandwidth and instantaneous response. Therefore, interference between different pathways could occur only if the photons were coincident to within the coherence time of the light, and the signals measured revealed information about the fields, not about the detectors. In this work, we investigate what the result would be if the detectors were replaced by a pair of electronically coupled two-level molecules. By monitoring the TPA signal, the pair of molecules can be used specifically as a coincidence detector, because the signal will be large only when the photons arrive within a time window set by the relaxation time scales of intermediate molecular states. In this case, interference between the two pathways discussed above can take place if the difference between the *A* and *B* interferometer delays is within the relevant relaxation timescale of the molecule.

Figure 7.2A shows a schematic of the proposed experiment. Packets of quantum amplitude from putative early ("E") or late ("L") emission events are shown, after traversing the short ("sh") or long ("lo") paths in the *A* and *B* interferometers. The outputs of the A and B interferometers are overlapped in a sample consisting of coupled dimers, and detectors are placed after the sample in the *A* and *B* beams to detect any photons that do not get absorbed by the sample. A third detector is used to detect fluorescence from the sample.

Figure 7.2B shows the energy level diagram of a pair of coupled two-level molecules, similar to the systems considered in the previous chapters of this dissertation. This dimer can undergo TPA to yield population on the doubly-excited ($|f\rangle$) state. This state can then undergo internal conversion to the lowest-energy singly-excited ($|e\rangle$) state,

which in turn emits fluorescence. This type of pathway leads to detection of a fluorescent photon coincident with zero detected photons in the *A* and *B* beams. In Figure 7.3, we consider the three pathways in classical 2D FS that can yield population on the $|f\rangle$ state, which are termed the double quantum coherence (DQC), rephasing (RP), and nonrephasing (NRP) pathways. These pathways can be isolated from background terms involving independent one-photon excitation of separated molecules, by their dependence on the phase shifts applied to the interferometer arms.

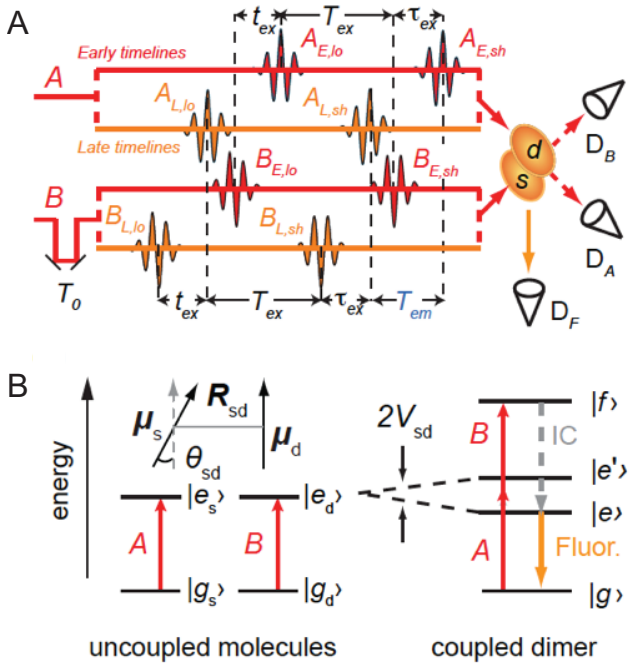

Figure 7.2. (A) Excitation and detection geometry for EPP-2DFS performed on a pair of electronically coupled molecules, labeled *s* and *d*. A variable delay T_0 is included in the B beam. There is perfect number correlation between the single-photon wave-packets (shown as short oscillatory pulses) in fields *A* and *B*. Eight packets are shown: those in the *A* and *B* fields that traversed the short (*sh*) and long (*lo*) interferometer paths, for "early" (*E*) and "late" (*L*) virtual emission events. As in Figure 7.1, these two emission events are separated by the variable emission time interval T_{em}. (B) Energy-level diagram of a pair of uncoupled two-level molecules (left), and that of a coupled molecular dimer (right). Two-photon absorption (TPA) yields population on the doubly-excited state, which undergoes internal conversion (IC) followed by fluorescence emission from the lowest-energy singly excited state.

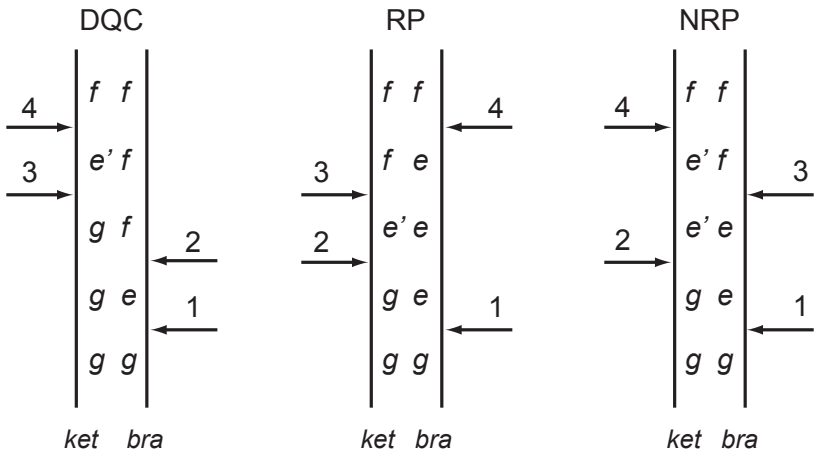

Figure 7.3. Double-sided Feynman diagrams for the molecular density matrix corresponding to the three possible TPA excitation pathways that produce population on the $|f\rangle$ state of an electronically coupled molecular dimer. The three different pathways are designated double-quantum coherence (DQC), rephasing (RP), and non-rephasing (NRP). Time increases in the upward direction. Horizontal arrows indicate field-molecule interactions, which induce transitions between populations and coherences during the time-evolution of the density operator. Arrows appearing on the left indicate an interaction on the ket side of the density matrix, while arrows appearing on the right indicate a bra-side interaction.

5. Time-Frequency Photon Entanglement – Avoiding the Time-Frequency Uncertainty Principle

The proposed experiment uses spectrally and temporally entangled photons produced by using a monochromatic laser to pump a parametric downconversion (PDC) crystal.[110] This process generates two broadband fields, *A* and *B*, with coherence times as short as femtoseconds and center frequencies ω_A and ω_B. Because the pump beam is monochromatic, the instantaneous frequencies of *A* and *B* photons are anticorrelated so that they add up to the pump frequency: $\omega + \omega' = \omega_p$. Meanwhile, the arrival times (*t* and *t'*) of the photons are correlated so that $t = t'$. While the Heisenberg uncertainty principle limits the simultaneous tightness of arrival time and frequency in a single classical pulse to $std(\omega_j)std(t_j) \geq 1/2$, there is no limit to the simultaneous tightness of *correlations*

between frequency and arrival time in two entangled photons. Therefore, for an entangled two-photon state, there is no lower bound to the uncertainty product $std(\omega+\omega')std(t-t')$, even though the individual components ω, ω', t and t' can vary. This is analogous to the EPR state of two entangled quantum particles, in which the uncertainty product $std(x+x')std(p-p')$ for position x and momentum p has no lower bound. The lack of a lower bound on this product indicates quantum entanglement, as for all separable (including all classical) states, the lower bound is $std(\omega+\omega')std(t-t')\geq 1$.[111-112] The equality holds only for two transform limited pulses of identical duration.

The spectral and temporal entanglement properties described above suggest two advantages of entangled photons in the area of molecular spectroscopy. First, the fact that the sum of the energies of any entangled pair of *A* and *B* photons is a constant, while their individual energies vary, suggests that entangled photons could be used to selectively excite a homogeneously broadened subgroup of molecules from within a broader inhomogeneous distribution. Second, the high temporal correlation means that two-photon transitions could be efficiently excited even in molecules with a very short lifetime of the intermediate state. The lack of a lower bound on the uncertainty product means that both of these advantages can be obtained simultaneously, which is not possible with any classical light source.

6. Two-Dimensional Fluorescence Spectroscopy using Entangled Photon Pairs

As mentioned above, the proposed experimental apparatus uses the combined output of the *A* and *B* interferometers (with relative delays of τ_a and τ_b, respectively,

between their arms) to excite a sample consisting of a coupled dimer of two-level molecules. There is an additional global delay, termed T_0, placed in the B beam. The global and interferometer delays lead to the possible interaction times shown in Figure 7.4, with the delays between them given by $\tau_{ex} \equiv T_0$, $T_{ex} \equiv \tau_a - T_0$, and $t_{ex} \equiv T_0 + \tau_b - \tau_a$.

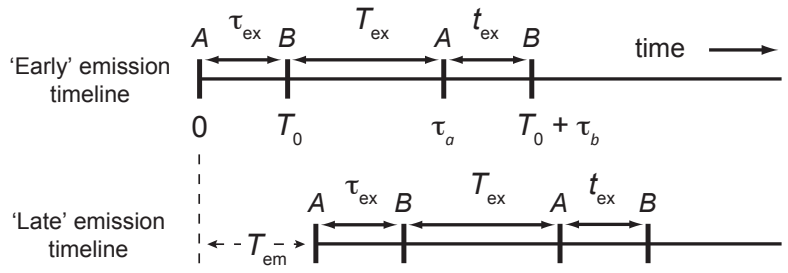

Figure 7.4. 'Early' and 'late' source emission event timelines. Top timeline: An early virtual emission event in the source creates a sequence of four possible interaction times with the molecule, with delays fixed by the experimental configuration. Bottom timeline: A later virtual emission event in the source, delayed by an indeterminate time T_{em}, creates another sequence of four possible interaction times with the molecule.

As described in Chapter II, time-dependent perturbation theory is typically used to track the time evolution of the sample's density operator in the interaction picture and thus predict the signals seen in 2D spectroscopy experiments.[9] In this work, we generalize the theory to describe the evolution of the composite light-molecule density operator. The interaction Hamiltonian is the electric dipole interaction, $\hat{d}(t) \cdot \hat{E}(t)$, as in Chapter II. Initially, the molecule is in its ground state $|g\rangle$ and the field is in a two-photon entangled state $|\Psi\rangle_F$. We consider only those pathways in which the final state is $|f\rangle|vac\rangle$, with the molecule in its doubly-excited state $|f\rangle$ and the field in the vacuum state (indicating that both incident photons have been absorbed). The perturbation theory

shows that the population of this final state created within a time window $[-\tau_w, \tau_w]$ is proportional to a weighted sum of three terms:

$$
\begin{aligned}
R_{DQC}^{e,e'} &= \int_{-\tau_w}^{\tau_w} dt_4 \int_{-\infty}^{t_4} dt_3 \int_{-\infty}^{t_3} dt_2 \int_{-\infty}^{t_2} dt_1 e^{-\gamma_{eg}(t_2-t_1)} e^{-\gamma_{fg}(t_3-t_2)} e^{-\gamma_{fe'}(t_4-t_3)} \cdot \langle vac | \hat{E}^{(+)}(t_4) \hat{E}^{(+)}(t_3) | \Psi \rangle_{F\ F} \langle \Psi | \hat{E}^{(-)}(t_1) \hat{E}^{(-)}(t_2) \\
R_{RP}^{e,e'} &= \int_{-\tau_w}^{\tau_w} dt_4 \int_{-\infty}^{t_4} dt_3 \int_{-\infty}^{t_3} dt_2 \int_{-\infty}^{t_2} dt_1 e^{-\gamma_{eg}(t_2-t_1)} e^{-\gamma_{ee'}(t_3-t_2)} e^{-\gamma^*_{fe}(t_4-t_3)} \cdot \langle vac | \hat{E}^{(+)}(t_3) \hat{E}^{(+)}(t_2) | \Psi \rangle_{F\ F} \langle \Psi | \hat{E}^{(-)}(t_1) \hat{E}^{(-)}(t_4) | \\
R_{NRP}^{e,e'} &= \int_{-\tau_w}^{\tau_w} dt_4 \int_{-\infty}^{t_4} dt_3 \int_{-\infty}^{t_3} dt_2 \int_{-\infty}^{t_2} dt_1 e^{-\gamma_{eg}(t_2-t_1)} e^{-\gamma_{ee'}(t_3-t_2)} e^{-\gamma_{fe'}(t_4-t_3)} \cdot \langle vac | \hat{E}^{(+)}(t_4) \hat{E}^{(+)}(t_2) | \Psi \rangle_{F\ F} \langle \Psi | \hat{E}^{(-)}(t_1) \hat{E}^{(-)}(t_3)
\end{aligned}
\tag{7.1}
$$

Here, *e* and *e'* indicate which intermediate states a particular pathway progresses through. Also, $\gamma_{nm} = \tilde{\gamma}_{nm} - i\omega_{nm}$, $\gamma^*_{nm} = \tilde{\gamma}_{nm} + i\omega_{nm}$; $\omega_{nm} = \varepsilon_{nm}/\hbar$, and $\tilde{\gamma}_{nm}$ is the dephasing rate of the *n*-to-*m* molecular transition, and the energy difference between two molecular states is $\varepsilon_{nm} = \varepsilon_n - \varepsilon_m$. DQC stands for 'double quantum coherence', RP stands for 'rephasing' and NRP stands for 'nonrephasing.' Note that the exponential functions in eq 7.1 are analogous to those in the molecular response functions presented in Chapter II.

In eq 7.1, each of the electric field operators is a sum of four operators: two from each of the *A* and *B* beams representing the short and long paths through the Franson interferometer. The excited state population therefore contains a total of 192 terms, plus their complex conjugates. This number of terms can be greatly reduced by implementing a similar phase-synchronous detection scheme to that used in 'classical' 2D FS.[4, 8] In the proposed experimental setup, an acousto-optic Bragg cell is placed in one arm of each interferometer, and is driven such that the phase of the corresponding beam is modulated at the frequency φ_a (for the *A* interferometer) or φ_b (for the *B* interferometer). It can be shown that in the Franson interferometer, the phase signature $\cos(\varphi_a + \varphi_b)$ acts as an

identifier for frequency anti-correlation, so we are interested in terms with this 'sum-phase' signature $\exp\left[\pm i\left(\varphi_a+\varphi_b\right)\right]$. In the limit of broad optical bandwidth (and therefore short correlation time) of the excitation field, six of the 192 terms have this phase signature, and we denote them $R^{e,e'}_{DQC(\pm)}$, $R^{e,e'}_{RP(\pm)}$, and $R^{e,e'}_{NRP(\pm)}$. In addition, the tight temporal correlation of the photon pairs emitted from the source can be well approximated using a delta function. Making this approximation, the sum phase signature terms are given in eq 7.2.

$$
\begin{aligned}
R^{e,e'}_{DQC(+)} &= e^{i(\varphi_a+\varphi_b)}e^{i\omega_p(T_{ex}+t_{ex})}\int_0^\infty dt_{43}e^{-(\gamma_{fe'}+i\omega_p)t_{43}}\delta(t_{43}-t_{ex})\cdot\int_0^\infty dt_{32}e^{-(\gamma_{fg}+i\omega_p)t_{32}}\cdot\int_0^\infty dt_{21}e^{-\gamma_{eg}t_{21}}\delta(t_{21}-\tau_{ex})\\
R^{e,e'}_{DQC(-)} &= e^{-i(\varphi_a+\varphi_b)}e^{-i\omega_p(T_{ex}+t_{ex})}\int_0^\infty dt_{43}e^{-(\gamma_{fe'}+i\omega_p)t_{43}}\delta(t_{43}-\tau_{ex})\cdot\int_0^\infty dt_{32}e^{-(\gamma_{fg}+i\omega_p)t_{32}}\cdot\int_0^\infty dt_{21}e^{-\gamma_{eg}t_{21}}\delta(t_{21}-t_{ex})\\
R^{e,e'}_{RP(+)} &= e^{i(\varphi_a+\varphi_b)}e^{i\omega_p(T_{ex}+t_{ex})}\int_0^\infty dt_{43}e^{-(\gamma^*_{fe}-i\omega_p)t_{43}}\int_0^\infty dt_{32}e^{-\gamma_{ee'}t_{32}}\delta(t_{32}-t_{ex})\int_0^\infty dt_{21}e^{-\gamma_{eg}t_{21}}\delta(t_{43}+t_{32}+t_{21}-\tau_{ex})\\
R^{e,e'}_{RP(-)} &= e^{-i(\varphi_a+\varphi_b)}e^{-i\omega_p(T_{ex}+t_{ex})}\int_0^\infty dt_{43}e^{-(\gamma^*_{fe}-i\omega_p)t_{43}}\int_0^\infty dt_{32}e^{-\gamma_{ee'}t_{32}}\delta(t_{32}-\tau_{ex})\int_0^\infty dt_{21}e^{-\gamma_{eg}t_{21}}\delta(t_{43}+t_{32}+t_{21}-t_{ex})\\
R^{e,e'}_{NRP(+)} &= e^{i(\varphi_a+\varphi_b)}e^{i\omega_p(T_{ex}+t_{ex})}\int_0^\infty dt_{43}e^{-(\gamma_{fe'}+i\omega_p)t_{43}}\int_0^\infty dt_{32}e^{-\gamma_{ee'}t_{32}}\int_0^\infty dt_{21}e^{-\gamma_{eg}t_{21}}\delta(t_{32}+t_{21}-\tau_{ex})\,\delta(t_{43}+t_{32}-t_{ex})\\
R^{e,e'}_{NRP(-)} &= e^{-i(\varphi_a+\varphi_b)}e^{-i\omega_p(T_{ex}+t_{ex})}\int_0^\infty dt_{43}e^{-(\gamma_{fe'}+i\omega_p)t_{43}}\int_0^\infty dt_{32}e^{-\gamma_{ee'}t_{32}}\int_0^\infty dt_{21}e^{-\gamma_{eg}t_{21}}\delta(t_{32}+t_{21}-t_{ex})\,\delta(t_{43}+t_{32}-\tau_{ex}).
\end{aligned}
\tag{7.2}
$$

Unlike in classical 2D FS, the time delays between light-matter interactions in EPP-2DFS are not fixed by the experimenter but rather depend on the source emission-time delay T_{em}. Each of the integrals in eq 7.2 can be re-written as an integral over T_{em}. In the $R^{e,e'}_{DQC(+)}$ term, two relations are enforced by delta functions: $t_{21}=\tau_{ex}$ and $t_{43}=t_{ex}$. Therefore, it is useful to make a change of variables from t_{32} to the emission-time delay T_{em}, where $T_{em}=t_{32}-T_{ex}$. The integral can then be written

$$R_{DQC(+)}^{e,e'} = e^{i(\varphi_a+\varphi_b)} e^{i\omega_p T_{ex}} \int_{-T_{ex}}^{\infty} dT_{em} e^{-\gamma_{eg}\tau_{ex}} e^{-(\gamma_{fg}+i\omega_p)t_{32}^{DQC(+)}[T_{em}]} e^{-\gamma_{fe'}t_{ex}} \tag{7.3}$$

where we introduced the function $t_{32}^{DQC(+)}[T_{em}] \equiv T_{em} + T_{ex}$, which is the delay between interactions 2 and 3 in the 'molecular-perspective.' The integral in eq 7.3 serves to sum over the many possible durations of this interval, in contrast to the classical case.

To interpret eq 7.3, recall that $\gamma_{nm} = \tilde{\gamma}_{nm} - i\omega_{nm}$, where $\tilde{\gamma}_{eg}$ is the damping rate (homogeneous line half-width) of the *n*-to-*m* molecular transition, and $\omega_{nm} = (\varepsilon_n - \varepsilon_m)/\hbar$. The terms in the integrand can therefore be interpreted as follows: the first *A* interaction creates a *g*-*e* coherence, which oscillates at ω_{eg} and damps at a rate $\tilde{\gamma}_{eg}$ for the duration τ_{ex}. The first *B* interaction then creates a *f*-*g* coherence, which oscillates at ω_p and decays at a rate $\tilde{\gamma}_{fg}$ for the indeterminate duration $t_{32}^{DQC(+)}[T_{em}]$ before the next *A* interaction occurs, creating an *f*-*e'* coherence. This damps for a duration t_{ex}, at which time the final *B* interaction creates population in the $|f\rangle$ state. The integration sums over the range of possible source-emission event delays.

$R_{DQC(+)}^{e,e'}$ can be represented uniquely by a double-sided Feynman diagram, labeled $DQC(+)$ in Figure 7.5. Here we have modified the diagrams shown in Figure 7.3 to emphasize several points: 1) Each ket represents the state of the composite molecule-field system: $|i,n_A,n_B\rangle$ means the molecule is in state *i*, where $i \in \{g,e,e',f\}$, the *A* field contains n_A photons, and the *B* field contains n_B photons. Each bra $\langle i',n_A',n_B'|$ has a

similar meaning. 2) The extra time axes on both sides of the ket-bra axes indicate the virtual source emission events that contribute to a given diagram. 3) The delay T_{em} between 'early' and 'late' virtual emission events in the source is indicated in each diagram, allowing the left source axis to 'slide,' within limits, relative to the right source axis. This reflects the fact that the four-time correlation function in each integral in eq 7.1 factors into the product of two separate two-time correlation functions. 4) The shaded gray regions indicate intervals whose durations are not fixed by the experimental delay parameters, and which must be integrated over. For the case of the $R^{e,e'}_{DQC(+)}$ term, the shaded gray region represents the $t_{32}^{DQC(+)}[T_{em}]$ interval.

In our proposed experiment, the delay T_{ex} is fixed while the other two controllable delays, τ_{ex} and t_{ex} are scanned. This data is then Fourier transformed with respect to τ_{ex} and t_{ex} to create EPP-2DFS spectra. Such a spectrum contains contributions from all six of the terms in eq 7.2. After Fourier transformation, the contribution of $R^{e,e'}_{DQC(+)}$ to the spectrum is:

$$\begin{aligned} S^{e,e'}_{DQC(+)}(\omega_\tau,\omega_t) &= \sum_{e,e'} \int_0^\infty d\tau_{ex} \int_0^\infty dt_{ex} e^{-i(\omega_\tau \tau_{ex} + \omega_t t_{ex})} R^{e,e'}_{DQC(+)} \\ &= e^{i(\varphi_a+\varphi_b)} e^{i\omega_p T_{ex}} \sum_{e,e'} \frac{1}{\tilde{\gamma}_{fg} - i(\omega_{fg} - \omega_p)} \frac{1}{\tilde{\gamma}_{eg} - i(\omega_{eg} - \omega_\tau)} \frac{1}{\tilde{\gamma}_{fe'} - i(\omega_{fe'} - \omega_t)} \end{aligned} \tag{7.4}$$

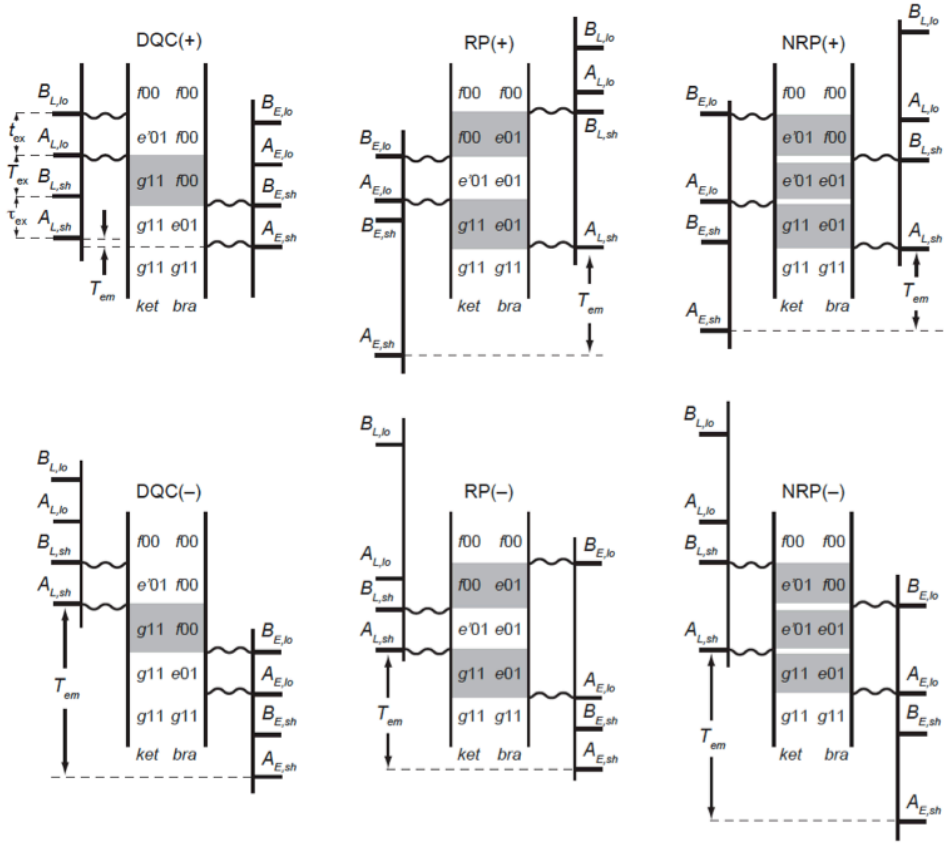

Figure 7.5. Double-sided Feynman diagrams for the composite field-molecule system, labeled DQC(±), RP(±), and NRP(±), represent the six nonzero integrals (eq 7.2) with the corresponding phase signatures $\exp\left[\pm i\left(\varphi_a+\varphi_b\right)\right]$. Each excitation pathway for the classical field – molecule system (shown in Figure 7.3) gives rise to two distinct field-molecule pathways for the composite system, which include information about the quantum numbers of the exciting fields. Pathways for 'early' (*E*) and 'late' (*L*) virtual emission events are shown, and the times of their field-molecule interactions are indicated by wavy horizontal lines. The shaded regions are those with indeterminate durations between any pair of 'early' and 'late' virtual emission events, which are integrated over specific limits for each term. For example, the DQC(±) term represents an integral in which the first two interactions are from a virtual emission event at the early time, and whose wave packets follow 'short' (*sh*) arms in their respective interferometers, while the third and fourth interactions are from a source virtual emission event at a later time, and whose wave packets follow 'long' (*lo*) arms in their interferometers.

As was demonstrated in this derivation of $S^{e,e'}_{DQC(+)}(\omega_\tau,\omega_t)$, each other term in eq 7.2 can be evaluated by first making a change of variables so as to integrate over T_{em} instead of t_{21}, t_{32} and t_{43}. This integral can then be evaluated, and the resulting expression

Fourier transformed with respect to τ_{ex} and t_{ex} to generate the frequency domain EPP-2DFS signal.

7. Model Spectra for an Electronically Coupled Molecular Dimer

We now consider the EPP-2DFS observable of an electronically coupled molecular dimer. The spectroscopic properties of an electronically coupled dimer depend sensitively on the spatial relationship between the component monomer electric transition dipole moments (i.e., its 'conformation'), in addition to the interactions between the internally coupled dimer and its local environment. Such dimers can be excellent spectroscopic probes of the local structure and dynamics of biological macromolecules, such as DNA,[13, 23, 113-114] and phospholipid membranes.[8-10, 53] Moreover, electronically coupled chromophore arrays play a central role in natural photosynthetic systems,[6, 115] and they are important to developing strategies for molecular electronics technologies.[33] The electronic interactions within a coupled dimer affect linear spectroscopic signals in a variety of ways, giving rise to spectral line shifts and line shape changes, circular dichroism signals (for chiral geometries), and variations in fluorescence quantum yields.[9, 38, 114] The effects of the electronic interactions within a molecular dimer are especially apparent in its 2D optical spectrum, which can reveal the couplings between electronic transitions that are often hidden under the overlapping spectral line shapes of the linear absorption spectrum.[8-9]

In principal, the conformation of a molecular dimer can be determined by optimizing a multi-parameter model under the constraints imposed by an experimental 2D spectrum, in combination with linear absorption and/or circular dichroism spectra.[8-9]

Such a fitting procedure is feasible only if the 2D spectrum can resolve the positions and intensities of individual peaks and cross-peaks. Unfortunately, in many situations of chemical interest, 2D spectral features are too congested to extract model Hamiltonian parameters. Broadening of the optical absorption line shape occurs as a result of the combined effects of inhomogeneous site energy disorder and rapid electronic dephasing, the latter resulting from significant electronic-vibrational coupling in condensed phase molecular systems. Progress has been made towards simplifying 2D optical spectra by manipulating the polarizations of the exciting laser fields,[116-118] and thereby reducing the signal contributions from resonant features that appear on the diagonal of the 2D spectrum. Nevertheless, this approach has the undesirable effect of reducing the overall signal strength and, under certain polarization conditions, reducing the sensitivity of the 2D spectrum to the angle between the coupled transition dipole moments of the dimer.

As discussed above in Sec. IV, in EPP-2DFS we isolate the two-photon absorption (TPA) signal proportional to the $|f\rangle$ state population by detecting only fluorescence photoelectron counts that are coincident with the absence of photoelectron counts from the *A* and *B* beams (see Figure 7.2A). This is possible using time-frequency-entangled photon-pairs, because for every photon in the *A* beam there is guaranteed to be a correlated photon in the *B* beam, and vice versa. Although the quality of these measurements will depend ultimately on the photo-detector efficiency, we assume ideal detection efficiency for our current purposes. A fluorescence photon that is detected with the 'sum-phase' signature, and which coincides with the destruction of both photons from the transmitted *A* and *B* fields must contribute to the TPA transition. A 'background' signal may also occur in which two separate dimer molecules each absorb one photon

from the fields. However, this 'background' fluorescence does not oscillate with the 'sum-phase' signature, and therefore it can be readily separated from the TPA signal.

In 'classical' 2DFS experiments performed on condensed phase molecular systems, it is not possible to isolate the TPA signal (i.e., fluorescence resulting from population on the $|f\rangle$ state) apart from the signals due to competing pathways that produce populations on the singly-excited $|e\rangle$ and $|e'\rangle$ states. The 'classical' TPA signal is the result of three excited state absorption (ESA) pathways, which are described by the Feynman diagrams shown in Figure 7.3. These terms can be written[9]

DQC (classical):
$$\frac{e^{-T\left(\tilde{\gamma}_{fg}-i\omega_{fg}\right)}}{\left[\tilde{\gamma}_{eg}+i\left(\omega_{\tau}-\omega_{eg}\right)\right]\left[\tilde{\gamma}_{fe'}+i\left(\omega_{t}-\omega_{fe'}\right)\right]}, \tag{7.5}$$

RP (classical):
$$\frac{e^{-T\left(\tilde{\gamma}_{ee'}-i\,\omega_{ee'}\right)}}{\left[\tilde{\gamma}_{eg}+i\left(\omega_{\tau}+\omega_{eg}\right)\right]\left[\tilde{\gamma}_{fe}+i\left(\omega_{t}-\omega_{fe}\right)\right]}, \tag{7.6}$$

and

NRP (classical):
$$\frac{e^{-T\left(\tilde{\gamma}_{ee'}-i\,\omega_{ee'}\right)}}{\left[\tilde{\gamma}_{eg}+i\left(\omega_{\tau}-\omega_{eg}\right)\right]\left[\tilde{\gamma}_{fe'}+i\left(\omega_{t}-\omega_{fe'}\right)\right]}, \tag{7.7}$$

where the frequencies ω_{τ} and ω_{t} are the Fourier transform variables of the scanned time delays τ and t, respectively. The eight remaining pathways that contribute to the classical 2DFS spectrum differ from the TPA pathways in that they absorb only a single photon from the field, although each diagram involves four field-matter interactions. These

pathways are well known, and they are referred to as ground-state bleach (GSB), stimulated emission (SE) and excited-state absorption (ESA).[9] In general, a weighted sum of GSB, SE, and ESA pathways contribute to the classical 2DFS spectrum, with each term proportional to the normalized fluorescence quantum yield of its final state: 0 for the $|g\rangle$ state, 1 for the $|e\rangle$ and $|e'\rangle$ states, and ~0.5 for the $|f\rangle$ state.[8] Here we assume the factor ~0.5 for the $|f\rangle$ state fluorescence quantum yield to account for the rapid deactivation and partial self-quenching of this state during the fluorescence lifetime. The GSB, SE, and ESA terms are additionally weighted according to their orientationally averaged four-point product $\left\langle (\boldsymbol{\mu}_{ab}\cdot\mathbf{e}_1)(\boldsymbol{\mu}_{cd}\cdot\mathbf{e}_2)(\boldsymbol{\mu}_{jk}\cdot\mathbf{e}_3)(\boldsymbol{\mu}_{lm}\cdot\mathbf{e}_4)\right\rangle$, which takes into account the projections of the transition dipole moments onto the polarization directions of the incident fields averaged over an isotropic distribution of dimer orientations, while keeping the relative angle between monomer transition dipole moments fixed. We note that in our calculations, we have assumed all fields to have parallel plane polarizations.

In Figure 7.6, we compare simulated linear and classical 2DFS spectra for an electronically coupled molecular dimer composed of chemically identical monomeric subunits. The spectra are plotted for different values of the homogeneous line width, which has been systematically varied from 0.08 – 0.11 fs^{-1} (columns A – D). The 2D spectra are presented as contour plots versus the frequency variables ω_τ and ω_t, and for a fixed value of the waiting time interval $T = 0$. The conformation-dependent transition strengths and eigen-energies are based on the point-dipole coupling model,[38] for which the details of these calculations are established in [9]. The monomer transition dipole moments are arranged side-to-side, with a relative twist angle $\theta_{sd} = 75°$ and electronic coupling strength $V_{sd} = +400\ cm^{-1}$ (see Figure 7.2B). The top row shows the linear

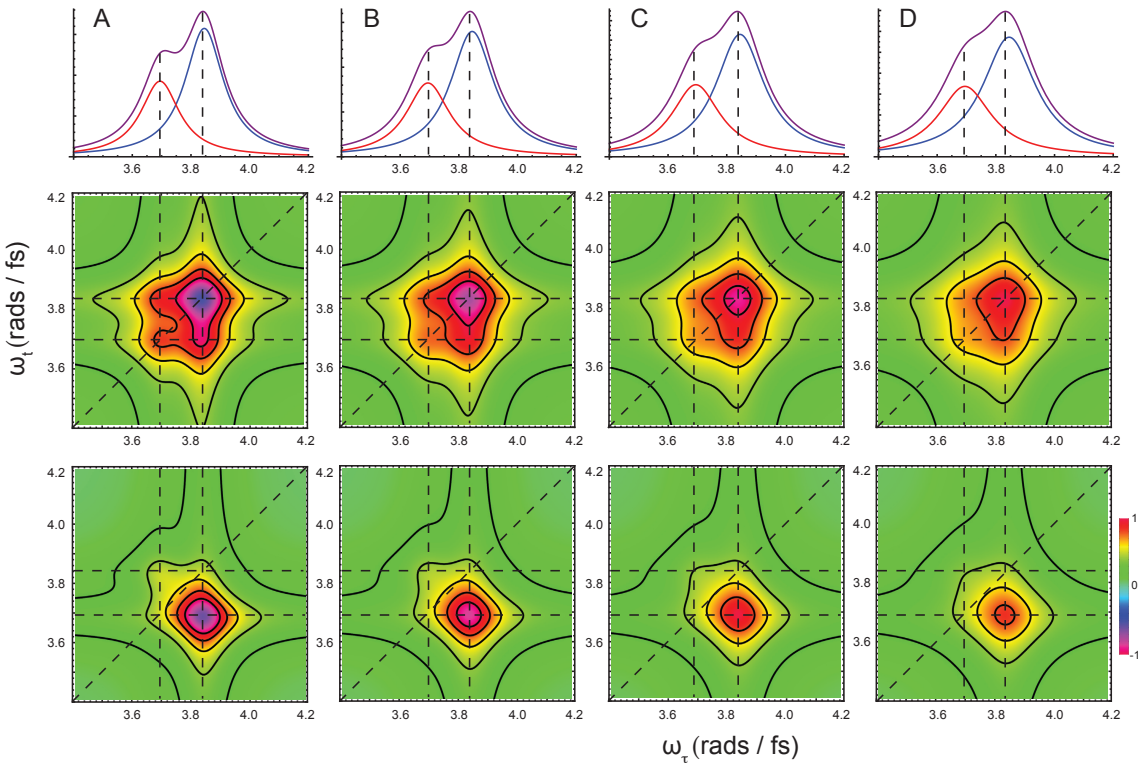

Figure 7.6. Simulated classical-light-excited linear and 2DFS spectra of an electronically coupled molecular dimer. The point dipole approximation was used to model a side-to-side arrangement of coupled transition dipole moments (H-dimer) with twist angle 75°, coupling strength +400 cm^{-1}, and monomer transition energy 3.77 rads fs^{-1} (500 nm). The $|e\rangle$ and $|e'\rangle$ state population relaxation rates have been set to $\tilde{\gamma}_{ee} = \tilde{\gamma}_{e'e'} = \Gamma =$ 0.03 fs^{-1}, and the dephasing rates $\tilde{\gamma}_{e'e} =$ 0.04 fs^{-1} and $\tilde{\gamma}_{fg} =$ 0.07 fs^{-1}. The remaining dephasing rates $\tilde{\gamma}_{e'g} = \tilde{\gamma}_{eg} = \tilde{\gamma}_{fe'} = \tilde{\gamma}_{fe}$ are adjusted according to (A) 0.08 fs^{-1}, (B) 0.09 fs^{-1}, (C) 0.10 fs^{-1}, and (D) 0.11 fs^{-1}. The middle row shows the real part of standard 2DFS total correlation spectra (RP + NRP), which exhibit overlapping diagonal peaks and off-diagonal cross-peaks. The bottom row shows only the contributions to the 2DFS spectra from Feynman pathways that result in population on the $|f\rangle$ state. These terms isolate the off-diagonal cross-peaks of the 2D spectra.

absorption spectra predicted for the dimer. The 2DFS spectra (middle row) are composed of two resonant diagonal features [at the points $(\omega_{eg},\omega_{eg})$ and $(\omega_{e'g},\omega_{e'g})$] and two off-diagonal cross-peaks [at the points $(\omega_{eg},\omega_{e'g})$ and $(\omega_{e'g},\omega_{eg})$], with relative intensities that depend on the weights assigned to the different excitation pathways. The overlapping

peaks and cross-peaks become progressively more difficult to resolve as the homogeneous line width (i.e. the electronic dephasing rate) is increased. In the bottom row, we plot the contributions to the classical 2DFS spectra that arise solely from the TPA ($|f\rangle$ state population) signal, given by eqs 7.5 – 7.7. In this case, the most pronounced features are the off-diagonal cross-peaks, and the diagonal peaks are greatly suppressed. Even the broadest of these spectra (panel D) still contains features that are clearly positioned off the diagonal, which allows for the magnitude of the coupling and the positions of the weaker peaks to be distinguished. Clearly, the extraction of model Hamiltonian parameters from experimental 2DFS spectra would be greatly simplified if it were possible to isolate the TPA signal from the remaining signal pathways.

The equations describing the quantum-light-excited EPP-2DFS signals obtained for an exciton-coupled dimer follow from Fourier transformation of eq 7.3 and its analogues for the other terms. Each of the resulting six terms is described by one of the double-sided Feynman diagrams shown in Figure 7.5.

DQC(+):

$$\frac{e^{iT_{ex}\omega_p}}{\left[\tilde{\gamma}_{eg}+i\left(\omega_{\tau_{ex}}-\omega_{eg}\right)\right]\left[\tilde{\gamma}_{fe'}+i\left(\omega_{t_{ex}}-\omega_{fe'}\right)\right]\left[\tilde{\gamma}_{fg}+i\left(\omega_p-\omega_{fg}\right)\right]}, \tag{7.8}$$

DQC(−):

$$\frac{e^{-iT_{ex}\omega_p}}{\left\{\tilde{\gamma}_{eg}+i\left[\omega_{t_{ex}}-\left(\omega_p-\omega_{eg}\right)\right]\right\}\left\{\tilde{\gamma}_{fe'}+i\left[\omega_{\tau_{ex}}-\left(\omega_p-\omega_{fe'}\right)\right]\right\}\left[\tilde{\gamma}_{fg}-i\left(\omega_p-\omega_{fg}\right)\right]}, \tag{7.9}$$

RP(+):

$$\frac{e^{iT_{ex}\omega_p}}{\left\{\tilde{\gamma}_{ee'}+i\left[\omega_{\tau_{ex}}+\omega_{t_{ex}}-\left(\omega_p+\omega_{ee'}\right)\right]\right\}\left[\tilde{\gamma}_{eg}+i\left(\omega_{\tau_{ex}}-\omega_{eg}\right)\right]\left\{\tilde{\gamma}_{fe}+i\left[\omega_{\tau_{ex}}-\left(\omega_p-\omega_{fe}\right)\right]\right\}}, \tag{7.10}$$

RP(−):

$$\frac{e^{-iT_{ex}\omega_p}}{\left\{\tilde{\gamma}_{ee'}+i\left[\omega_{\tau_{ex}}+\omega_{t_{ex}}-\left(\omega_p-\omega_{ee'}\right)\right]\right\}\left\{\tilde{\gamma}_{eg}+i\left[\omega_{t_{ex}}-\left(\omega_p-\omega_{eg}\right)\right]\right\}\left[\tilde{\gamma}_{fe}+i\left(\omega_{t_{ex}}-\omega_{fe}\right)\right]}, \tag{7.11}$$

NRP(+):

$$\frac{e^{iT_{ex}\omega_p}}{\left\{\tilde{\gamma}_{ee'}+i\left[\omega_{\tau_{ex}}+\omega_{t_{ex}}-\left(\omega_p+\omega_{ee'}\right)\right]\right\}\left[\tilde{\gamma}_{eg}+i\left(\omega_{\tau_{ex}}-\omega_{eg}\right)\right]\left[\tilde{\gamma}_{fe'}+i\left(\omega_{t_{ex}}-\omega_{fe'}\right)\right]}, \tag{7.12}$$

NRP(-):

$$\frac{e^{-iT_{ex}\omega_p}}{\left\{\tilde{\gamma}_{ee'}+i\left[\omega_{\tau_{ex}}+\omega_{t_{ex}}-\left(\omega_p-\omega_{ee'}\right)\right]\right\}\left\{\tilde{\gamma}_{eg}+i\left[\omega_{t_{ex}}-\left(\omega_p-\omega_{eg}\right)\right]\right\}\left\{\tilde{\gamma}_{fe'}+i\left[\omega_{\tau_{ex}}-\left(\omega_p-\omega_{fe'}\right)\right]\right\}} \tag{7.13}$$

In eqs 7.8 – 7.13, ω_{ij} is the transition frequency between states $|i\rangle$ and $|j\rangle$, where $i,j\in\{g,e,e',f\}$ refer to the four-level exciton-coupled dimer (see Figure 7.2B). $\tilde{\gamma}_{ij}$ is the rate of relaxation of the coherence $|i\rangle\langle j|$, and for the case $i=j=e=e'$, $\tilde{\gamma}_{ee}=\Gamma$ is the population time of state $|e\rangle$ or $|e'\rangle$. ω_p is the frequency of the pump laser prior to down-conversion, and $\omega_{\tau_{ex}}$ and $\omega_{t_{ex}}$ are the Fourier transform variables complementary to the experimentally controlled time delays τ_{ex} and t_{ex}, respectively. Similar to the classical 2DFS signal discussed above, the EPP-2DFS signal is obtained by summing each

pathway over the possible intermediate states, $|e\rangle$ and $|e'\rangle$, and weighting each term by the fluorescence quantum yields and orientation factors associated with the sequence of transition dipole moments involved in that pathway.

We note that for the classical 2DFS TPA spectrum (see eqs 7.5 – 7.7), each resonance occurs at values of ω_τ and ω_t equal to the transition frequencies of the dimer, with line widths determined by the dephasing rates of the single-quantum coherences (e.g., $\tilde{\gamma}_{eg}$). Furthermore, each of these signal terms oscillates and rapidly dampens as the waiting time *T* is increased. The EPP-2DFS signals described by eqs 7.8 – 7.13 show additional features not present in the classical 2DFS TPA signal. The natural resonances and dephasing rates are still present, however an additional third factor appears in the denominator of each term. The pump frequency ω_p, which has no analogue in the classical signals, is present in at least one of these factors. The DQC(+) term is identical to its classical analogue, apart from a constant factor that accounts for the TPA resonance condition $\omega_p = \omega_{fg}$. This is not the case for the RP(+) and NRP(+) terms, which contain additional factors in their respective denominators that depend on $\omega_{\tau_{ex}}$, $\omega_{t_{ex}}$, and the pump frequency ω_p. These additional factors place tighter restrictions on the line shapes of the EPP-2DFS spectra in comparison to those of classical 2DFS. The relationship between (+) and (–) terms, and the appearance of the pump frequency in eqs 7.8 – 7.13, are a consequence of the energy conservation condition imposed by the time-frequency entanglement of the photons. For example, whenever a resonant transition is probed at the frequency $\omega_{\tau_{ex}} = \omega_{eg}$, there is guaranteed to be an associated transition at the frequency $\omega_{t_{ex}} = \omega_p - \omega_{eg}$.

Equations 7.8 – 7.13 can be interpreted in terms of the diagrams in Figure 7.5. Consider for example the RP(+) term described by eq 7.10. During the interval τ_{ex} (the delay between A_{sh} and B_{sh}), the field-molecule system undergoes four successive interactions. The molecule is initially excited into a $|g\rangle\langle e|$ coherence described by the resonance condition $\omega_{\tau_{ex}} = \omega_{eg}$, then into the $|e\rangle\langle e|$ population (or the $|e'\rangle\langle e|$ coherence for $e \neq e'$), and then into the $|f\rangle\langle e|$ coherence described by the resonance condition $\omega_{\tau_{ex}} = \omega_p - \omega_{fe}$. The interval during which the molecule is in the coherence (or population) $|e'\rangle\langle e|$ falls within both the intervals τ_{ex} and t_{ex} (i.e., the delay between A_{lo} and B_{lo}), which leads to the resonance condition $\omega_{\tau_{ex}} + \omega_{t_{ex}} = \omega_p + \omega_{ee'}$.

The resonance condition $\omega_{\tau_{ex}} + \omega_{t_{ex}} = \omega_p \pm \omega_{ee'} \simeq \omega_p$ appears in both the RP($\pm$) and NRP($\pm$) terms, and has the effect of maximizing the signal along the anti-diagonal in the 2D spectrum, with a line width determined by $\tilde{\gamma}_{ee'}$. For cases in which $e = e'$, this is a population relaxation rate, rather than the coherence dephasing rates that would otherwise lead to broadening of the line shapes in the 2D spectra. The presence of population times within the line shape functions leads to greatly narrowed spectral features in EPP-2DFS, as illustrated in Figure 7.7. Although the DQC($\pm$) signals are nearly identical to their classical analogues (not shown), the RP($\pm$) and NRP($\pm$) spectra are significantly narrowed in the diagonal direction. Peaks that would otherwise appear on the diagonal are greatly suppressed due to the elimination of Feynman pathways that end with population on states other than $|f\rangle$.

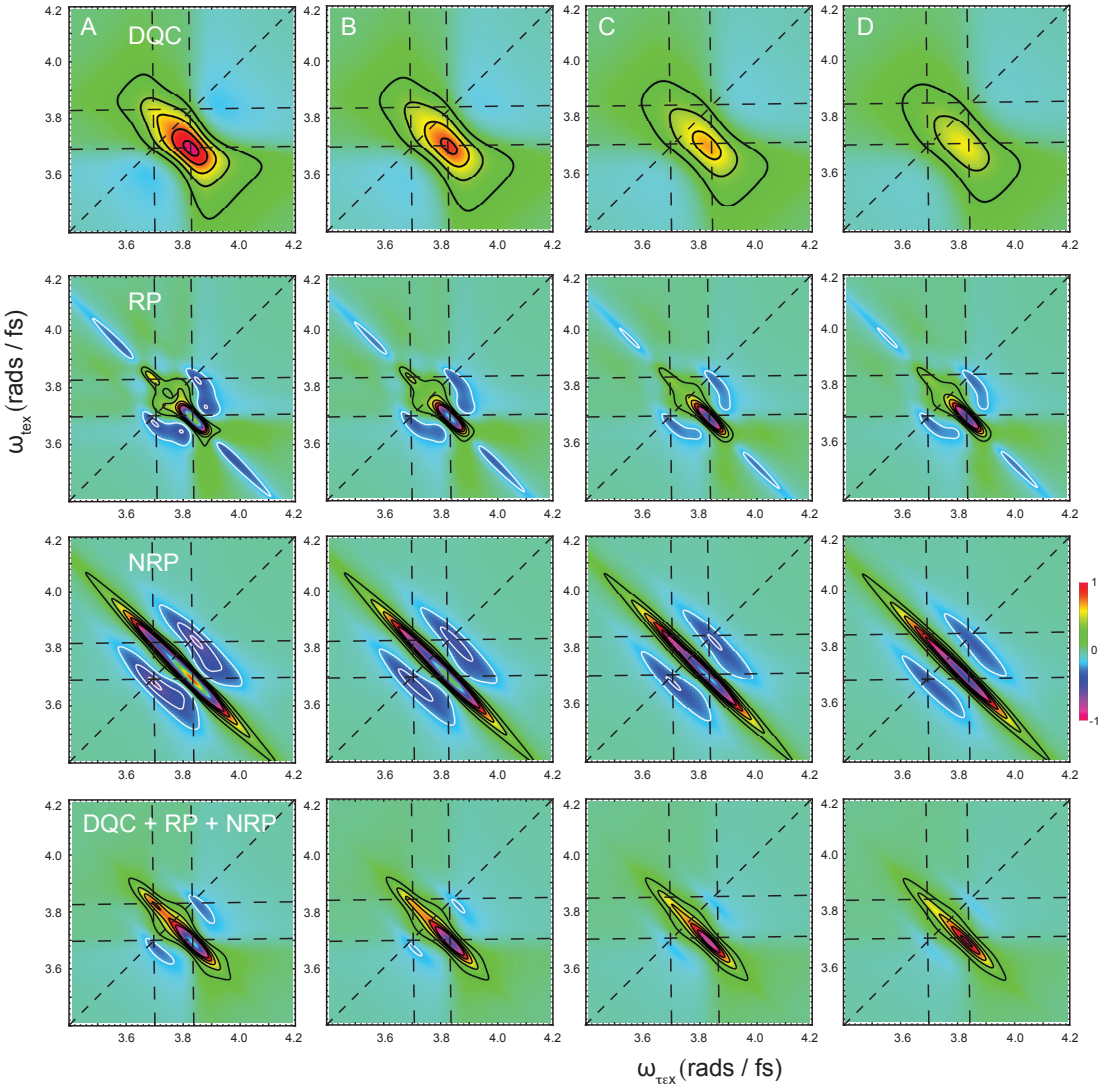

Figure 7.7. Simulated EPP-2DFS spectra of an electronically coupled molecular dimer using the same model parameters as for the spectra shown in Figure 6. The top row shows the DQC(±) terms, the second row shows the RP(±) terms, and third row shows the NRP(±) terms, and the bottom row shows the sum of all three terms. The off-diagonal cross-peaks dominate the EPP-2DFS spectra, and these features are much narrower than their classical counterparts.

The suppression of diagonal peaks and the narrowing of the 2D spectral line shapes make this method especially promising for the general extraction of model Hamiltonian parameters. For the specific case of the exciton-coupled molecular dimer, the peak positions are determined primarily by the magnitude of the electronic coupling,

and the relative peak intensities by the angle between the monomer transition dipole moments. The EPP-2DFS method should therefore be useful for the inversion of 2D spectra to obtain the conformation of the dimer. We illustrate this point in Figure 7.8 by comparing the linear, 'classical' 2DFS, and EPP-2DFS spectra as a function of the angle between the monomer transition dipole moments θ_{sd} (see Figure 7.2B). As the relative dipole angle is increased from 20° – 80°, more intensity is partitioned into the otherwise weaker transition. The EPP-2DFS spectrum features a strong cross peak (below the diagonal) for all values of θ_{sd}. As θ_{sd} is increased, the intensity of a second peak (above the diagonal) gradually increases.

In our current calculations, we did not consider the effects of inhomogeneous broadening. Our results indicate that in the homogeneous limit, EPP-2DFS presents significant advantages by narrowing 2D spectral lines and thereby reducing the effects of spectral congestion. The EPP-2DFS method may also be useful in the regime where inhomogeneous broadening becomes significant, as is often the case for complex molecular systems. While each individual photon created by the PDC source has a large uncertainty in its energy, the sum of the frequencies of the photons in any entangled pair must add to that of the narrow-band cw pump laser. In principle, the pump laser frequency ω_p can be tuned to a specific frequency within the inhomogeneously broadened absorption spectrum to selectively excite a small sub-population of molecules, similar in practice to the techniques of persistent spectral hole-burning and fluorescence line narrowing.[39, 119] Only those electronically coupled dimers that match the TPA resonance condition will contribute to the signal. This apparently simultaneous high temporal and spectral resolution is possible due to the time-frequency entanglement of

the photon pairs, as discussed in Sec. 5 above. The approach would allow one to selectively monitor different species in a mixture, and to investigate the nature of the heterogeneity that gives rise to the static site energy disorder.

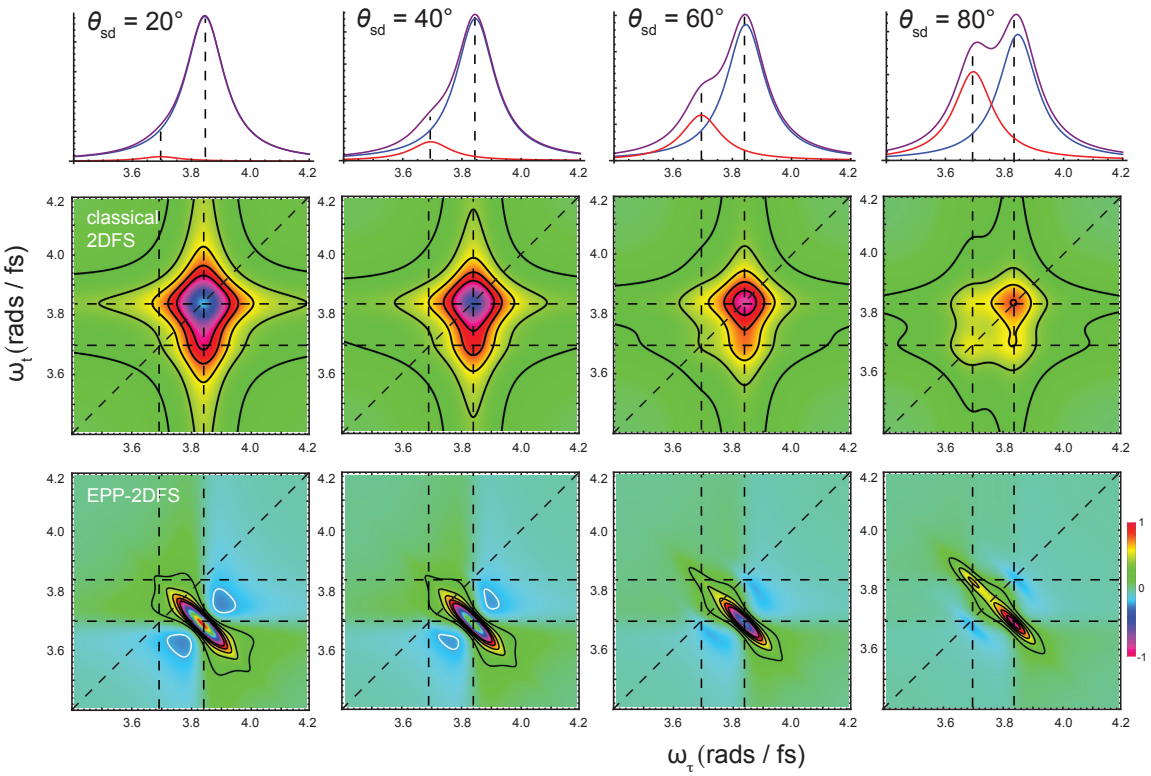

Figure 7.8. Simulated classical linear (top row), classical 2DFS total correlation spectra (middle row), and EPP-2DFS (bottom) for an electronically coupled molecular dimer using the same model parameters as for the spectra shown in Figures 7.6 and 7.7. The angle between the monomer transition dipole moments is varied from left to right, demonstrating the sensitivity of the EPP-2DFS observable to dimer conformation.

8. Conclusions

By incorporating a separated two-photon ('Franson') interferometer into the framework of a two-dimensional fluorescence spectroscopy experiment, we have proposed a new form of two-dimensional molecular spectroscopy with uniquely useful

capabilities. Entangled-photon pair two-dimensional fluorescence spectroscopy (EPP-2DFS) can extract the TPA signal from electronically coupled molecular systems, while simultaneously determining the couplings between distinct electronic states. TPA processes are important to a variety of material and biological applications, such as TPA fluorescence imaging.[120] Conventional methods to measure TPA require the use of relatively high-energy ultra-short light pulses, in addition to often-difficult experimentation to separate the weak nonlinear signal from linear 'background.' In EPP-2DFS, a cw pumped source of time-frequency-entangled photon pairs is used to excite the sample, and this leads to a number of important advantages over 'classical' ultrafast-pulse measurements. These include the enhancement of the TPA signal, which scales linearly with the excitation intensity of the entangled photons, and the suppression of the linear 'background.' Although the source is cw, the time-frequency entanglement of the photon pairs leads to the ability to probe the femtosecond Rabi oscillations associated with electronic coherences, while simultaneously selecting a narrow spectral sub-population of molecules within an inhomogeneously broadened distribution. Finally, the 2D line shapes are greatly narrowed (with width $\sim \tilde{\gamma}_{ee}^{-1} = \tilde{\gamma}_{e'e'}^{-1} = \Gamma^{-1}$) in comparison to 'classical' 2DFS, and this too is due to the energy conservation condition imposed by the time-frequency entanglement of the field.

Test calculations performed on an electronically coupled molecular dimer suggest that the EPP-2DFS method can be useful to elucidate dimer conformation. This is because the TPA signals, which contribute only to 2D cross-peaks, can be readily separated from the one-photon absorption processes that dominate 'classical' 2DFS signals, and which contribute to 2D diagonal peaks and off-diagonal cross-peaks. We see

that the greatly simplified 2D spectra are sensitive to dimer conformation. Hence, EPP-2DFS represents a promising strategy to isolate specific nonlinear signal terms, and thereby facilitate the extraction of model Hamiltonian parameters.

CHAPTER VIII

CONCLUDING REMARKS

1. Summary

Fully understanding the inner workings of the complex macromolecular machines of biology requires experimental techniques that are high in information content and tailored to the specific questions the researcher is trying to address. The work I presented in this dissertation took advantage of the high information content and high signal-to-noise of 2D FS in uncovering interesting details about the behavior of numerous biologically-relevant systems. Here, I summarize the results.

A. Porphyrin Dimers in Liposomes

Lipid bilayers are used extensively in biology to induce order and assembly in macromolecular complexes. As a model system for studying membrane-induced assembly, I studied the temperature-dependent conformations of a tethered ZnTPP dimer embedded in liposomes. It was found that the dimer adopted a mixture of folded and extended conformations, and that the folded structure was favored by higher temperatures, indicating an entropy-driven folding process. A key development in 2D FS that enabled these conclusions was the separation of signals from the two species by spectrally filtering the sample's fluorescence output. By dissecting the overall enthalpy and entropy of folding into terms reflecting porphyrin-porphyrin and porphyrin-lipid interactions, we found that folding was driven by an increase in entropy of lipid side chains that became liberated from contacts with the porphyrin surfaces – a lipid analogue of the hydrophobic effect. These results are consistent with earlier experiments performed

on self-assembled MgTPP dimers in liposomes, which found that the dimers adopted a relatively open 't-shaped' structure that did not maximize porphyrin-porphyrin contacts.

Further experiments on both the MgTPP and ZnTPP dimers investigated the population-time dependence of their 2D FS signals. For both systems, it was found that their population time-dependence could not be modeled by standard Redfield theory alone. An additional time constant, attributed to excited state electronic dephasing, caused a *T*-dependent change in the relative quantum yield of the doubly-excited state relative to the singly-excited state. The *T*-dependence of both systems could be modeled well by a combination of the population transfer predicted by Redfield theory and this electronic dephasing correction, with each showing sub-100 fs dynamics. In the ZnTPP system, spectral diffusion was observable as well in the form of a broadening of the rephasing spectra in the antidiagonal direction. This process had a time constant of about 60 fs and led to only a partial decorrelation between subsequent transition frequencies.

B. Nucleic Acids

Cyanine dyes were used to investigate the effects of bacteriophage T4 gp41 and gp61 on the conformations of forked DNA constructs. It was found that a Cy3 dimer placed in the duplex region exhibited strong exciton coupling, as evidenced by a large change in the absorption spectrum, quenching of fluorescence, and a strong CD signal. When the Cy3 dimer was placed at the fork, it exhibited similar effects, but to a smaller degree. In addition, the CD signal of the fork-labeled construct was inverted relative to the duplex-labeled construct. Addition of gp41 and gp61 had little effect on the duplex-labeled construct, while for the fork construct, addition of gp41 and gp61 caused the spectra to appear progressively more like the monomer spectra. In addition to

investigating the effects of gp41 and gp61, Cy3- and Cy5-labeled DNA constructs were used to demonstrate the filtering of 2D FS signals by FRET properties. It was shown that control samples exhibiting low or high FRET enabled the detection of 2D spectra selectively through the donor or acceptor channels, respectively.

Further experiments on DNA utilized the fluorescent base analogue 2-AP. These experiments required the 2D FS system to be modified to generate near-UV laser pulses. It was found that the dinucleotide of 2-AP adopts a fully stacked conformation with a smaller twist angle than that seen in B-form DNA. This suggests that in the absence of strain generated by an extended sugar-phosphate backbone, adjacent DNA bases are most stable in a fully stacked conformation.

2. Future Directions

The work presented in this dissertation suggests a number of future pathways. Further exploration into the *T*-dependence of the porphyrin signals could reveal more information about the electronic dephasing process that must be invoked in order to fit the data, as well as about the possibility of electronic excitation transport between different dimers. In addition, investigating the $(ZnTPP)_2$ sample at longer population times could uncover slow processes that lead to full decorrelation between transition frequencies, perhaps involving solvent rearrangement or dimer conformational changes (in contrast to the partial decorrelation seen by T=195 fs).

The work on Cy3- and Cy5-labeled DNA lays the foundation for studies investigating the interactions of DNA and any of the bacteriophage T4 replication proteins. The FRET-filtered 2D FS technique that is established through this work has the

potential to be a very powerful technique for the analysis of samples that exist in a mixture of different binding or conformational states. This technique would be especially powerful if a fluorescent base analogue dimer, such as two adjacent 2-aminopurine residues, was used as the donor. Using that type of sample, one could selectively probe the conformation of a specific site in the DNA using the dimer, while separating signals from different conformations by detecting donor or acceptor fluorescence.

The work on 2-AP dinucleotide suggests a large number of possible extensions. The dinucleotide studied had only one phosphate group between the two bases. By comparing its conformation to constructs with either one or two phosphate groups on the 'outside' of the dinucleotide, one could study how repulsion between negatively charged phosphate groups affects the conformation. In addition, by doing a temperature-dependent study, one could determine whether the extensive stacking observed in the dinucleotide is enthalpy- or entropy-driven, as was done for $(ZnTPP)_2$. We also intend to incorporate 2-AP dimers into oligonucleotides about eight bases in length, in order use 2D FS to study the effects of T4 single-stranded DNA binding protein gp32 on DNA conformation.

Finally, we are involved in ongoing collaborations in which we plan to test experimentally our theoretical predictions about EPP-2DFS. Our calculations predict that this should be a highly useful technique for the study of systems with broad spectral lineshapes.

APPENDIX A

SUPPORTING INFORMATION FOR CHAPTER II:

THEORY FOR THE SPECTROSCOPY OF

EXCITON-COUPLED MOLECULAR DIMERS

1. Calculations of the Transition Dipole Moment Magnitude and the Coupling Strength

We calculated linear absorbance, circular dichroism (CD), and 2D spectra of exciton-coupled dimers for various conformations. For our linear absorbance and CD calculations, we used established methods,[47] which we briefly outline below.

We define the coupling parameter V according to

$$V \equiv \frac{3}{8\pi^3 N_A} * \frac{10^{30}}{100} \int_{-\infty}^{\infty} \frac{\alpha(\bar{\nu})}{\bar{\nu}} d\bar{\nu} \tag{A.1}$$

Here, α is the absorption coefficient expressed in SI units, N_A is Avogadro's number, and $\bar{\nu}$ is the energy of the optical transition. We obtained the factor $\int_{-\infty}^{\infty} d\bar{\nu}\alpha(\bar{\nu})/\bar{\nu} =$ 44.3 M^{-1} cm^{-1} by numerical integration of the experimental absorption line shape of the MgTPP monomer in liposomes. We thus determined the value V = 8,890 $cm^{-1}Å^3$, and the magnitude of the transition dipole moment according to

$$|\mu|^2 = \frac{3\varepsilon_0 hc}{2\pi^2 N_A} \int_{-\infty}^{\infty} \frac{\alpha(\bar{\nu})}{\bar{\nu}} d\bar{\nu} = 4\pi\varepsilon_0 hc \frac{100}{10^{30}} * V \tag{A.2}$$

where ε_0 is the vacuum permittivity. The above procedure yielded a value for μ = 1.33 *D*. The coupling strength V_{12} was calculated in the point dipole approximation according to

$$V_{12} = \frac{V}{R^3}\left[\hat{\mu}_1 \cdot \hat{\mu}_2 - 3\left(\hat{R} \cdot \hat{\mu}_1\right)\left(\hat{\mu}_2 \cdot \hat{R}\right)\right]. \tag{A.3}$$

2. Calculation of the Linear Absorption Spectrum

We define the integrated area $A \equiv \int_{-\infty}^{\infty} \alpha(\bar{\nu}) d\bar{\nu}$ of the uncoupled monomer transition. This parameter was obtained using the first equality of eq A.2, and approximating the transition energy as constant across the absorption line shape. The height *h* of the line shape was then calculated according to

$$h = \frac{A}{\sigma_1 \sqrt{\pi}} \tag{A.4}$$

where σ_1 is related to the width of the Gaussian line shape. For all of our calculations, we used the same values for σ_1 in both linear absorbance and circular dichroism spectra. The relative intensity of a ground state accessible transition to the ± exciton was determined according to

$$a_{\pm} = 1 \pm \cos\delta \tag{A.5}$$

where δ is the relative angle between monomer transition dipoles.

The linear absorbance was calculated by summing over the ± exciton features, which were modeled as motionally narrowed Gaussian line shapes

$$\alpha(\bar{\nu}) = a_{bl} + \sum_{n=\pm} h\, a_n e^{-(\bar{\nu}-\varepsilon_n)^2/\sigma_1^2} \tag{A.6}$$

In eq A.6, a_{bl} is a baseline offset, h is the height given by eq A.4, a_n is the relative intensity of the nth exciton feature given by eq A.5, and ε_n is its transition energy (given by $\varepsilon_{\pm} = \varepsilon_1 \pm V_{12}$).

3. Calculation of the Circular Dichroism (CD) Spectrm

For a dimer with a given conformation, the rotational strength $RS^{\pm}$ associated with a ground state accessible transition to the ± exciton is given by

$$RS^{\pm} = \pm \frac{\varepsilon_1}{4\hbar}\left[\boldsymbol{\mu}_1 \times \boldsymbol{\mu}_2 \cdot \boldsymbol{R}\right] \tag{A.7}$$

where ε_1 is the transition energy of the uncoupled monomer. The values obtained for $RS^{\pm}$ were used to determine the integrated area $A^{\pm} \equiv \int_{-\infty}^{\infty}\left[\alpha_l^{\pm}(\bar{\nu}) - \alpha_r^{\pm}(\bar{\nu})\right]$ associated with the CD of each exciton feature, according to the relationships

$$RS^{\pm} = \frac{3\ln(10)c^2\varepsilon_0}{4\pi N_A}\int_{-\infty}^{\infty}\frac{\left[\alpha_l^{\pm}(\bar{\nu})-\alpha_r^{\pm}(\bar{\nu})\right]}{\bar{\nu}}d\bar{\nu} \cong \frac{3\ln(10)c^2\varepsilon_0}{4\pi N_A}\cdot\frac{A^{\pm}}{\bar{\nu}} \tag{A.8}$$

In eq A.8, we have defined the absorption coefficients for excitation using left (right) circular polarized light $\alpha_l^{\pm}$ ($\alpha_r^{\pm}$). Similar to the procedure we followed to calculate the linear spectra, we determined the height $h^{\pm}$ of an exciton feature contributing to the CD according to

$$h^{\pm} = \frac{A^{\pm}}{\sigma_1\sqrt{\pi}} \tag{A.9}$$

We note that the sign of the value obtained for $h^{\pm}$ corresponds to the sign of the rotational strength $RS^{\pm}$.

The CD was calculated by summing over the ± exciton features according to

$$\alpha_l(\bar{\nu})-\alpha_r(\bar{\nu}) = \sum_{n=\pm} h_n e^{-(\bar{\nu}-\varepsilon_n)^2/\sigma_1^2}\ , \tag{A.10}$$

where h_n is given by eq A.9, and ε_n is defined the same as in eq A.6.

APPENDIX B

SUPPORTING INFORMATION FOR CHAPTER VI:

EXCITED STATE DYNAMICS IN EXCITON-COUPLED DIMERS

1. Calculation of the Green's Function Matrix Elements

Green's functions were calculated using established procedures.[15, 95] This involved constructing the rate constant matrix $\underline{K}$:

$$\underline{K} = \begin{bmatrix} K_{22} & -K_{23} & -K_{24} & -K_{25} \\ -K_{32} & K_{33} & -K_{34} & -K_{35} \\ -K_{42} & -K_{43} & K_{44} & -K_{45} \\ -K_{52} & -K_{53} & -K_{54} & K_{55} \end{bmatrix} \tag{B.1}$$

where we have used the notation K_{ij} to mean the rate constant that couples the singly-excited state $|X_j\rangle$ to state $|X_i\rangle$, where $i, j \in \{2,3,4,5\}$. The matrix $\underline{V}$ that diagonalizes the matrix $\underline{K}$ was determined according to

$$\underline{V}^{-1}\underline{K}\underline{V} = \begin{bmatrix} \lambda_2 & & & \\ & \lambda_3 & & \\ & & \lambda_4 & \\ & & & \lambda_5 \end{bmatrix}. \tag{B.2}$$

$\underline{V}$ was then used to find the Green's function matrix $\underline{G}(T)$, whose elements describe the time evolution of population transfer between any two singly-excited states:

$$\underline{G}(T) = \underline{V}\begin{bmatrix} e^{-\lambda_2 T} & & & \\ & e^{-\lambda_3 T} & & \\ & & e^{-\lambda_4 T} & \\ & & & e^{-\lambda_5 T} \end{bmatrix}\underline{V}^{-1}. \qquad \text{(B.3)}$$

The Green's function matrix elements were used to calculate the 2D spectrum at each value of the population time *T*.

2. Estimation of Excitation Survival Probabilities in Multi-Donor/Acceptor Systems

In the work described in Chapter III, it was found that $(ZnTPP)_2$ adopts a mixture of J-type and H-type conformations in liposomes. Here we consider the possibility of electronic excitation transport (EET) among these different species. The Förster radii for EET among J- and H-dimers were estimated using eq 4.2. The parameters used were: $q = 0.033$ (J-dimer)[97] and $q = 0.033 * 0.0079$ (H-dimer), taking into account the relative quantum yields of J- and H-dimers determined in Chapter III. $\kappa^2 = 0.476$, assuming static (on the timescale of fluorescence) random orientation of adjacent dimers, and $n = 1.46$, using the refractive index of hydrogenated fats to approximate that of the hydrophobic region of the membrane. The overlap integral J was calculated according to eq B.4, using the entire absorption [$\varepsilon_A(\lambda)$] and normalized fluorescence [$F_D(\lambda)$] spectra of the mixture of J- and H-dimers in liposomes.

$$J = \int_0^\infty \varepsilon_A(\lambda)\lambda^4 F_D(\lambda)\, d\lambda \qquad \text{(B.4)}$$

In this equation, *A* stands for 'acceptor' and *D* stands for 'donor.' Because the overlap integral was calculated using the entire absorption and fluorescence spectra, it places an upper limit on the transfer probabilities from J- to H-dimers or any other combination, because any one species only contributes a portion of the absorption and emission spectra. The overlap integral calculated as above is equal to $1.52*10^{14}\,M^{-1}cm^{-1}$. Using these parameters, the Förster radius for each possible transfer scenario is shown in Table B.1.

Table B.1. Förster radii of J- and H-dimer pairs

D-A[a]	J-J	H-H	J-H	H-J
R_0 (nm)	1.89[b]	0.85[c]	<J-J[d]	>H-H[e]

[a]*D*onor-*A*cceptor pair. [b]Based on a quantum yield of 0.033 and the full overlap integral. [c]Based on a quantum yield of 0.033*0.0079 and the full overlap integral. [d]Inequality based on the smaller overlap integral of J-emission and H-absorption as compared to J-emission and J-absorption. [e]Inequality based on the larger overlap integral of H-emission and J-absorption as compared to H-emission and H-absorption.

The transfer probabilities were then estimated as described in [96]. Equation B.5 describes that the probability $\langle G^S(t)\rangle$ that an originally excited chromophore is still excited after a time t in a system with one donor and *N-1* traps.

$$\langle G^S(t)\rangle = \left[\mu^{1/3}\gamma(2/3,\mu) - \mu^{1/3}\Gamma(2/3) + \exp(-\mu)\right]^{N-1} \tag{B.5}$$

Here, $\mu = 2Q^6 t/\tau_F$, $Q = R_0^{DT}/2R_m$, and $\Gamma(2/3) = 1.25411794$. τ_F is the fluorescence lifetime, R_0^{DT} is the Förster radius for donor-trap EET, and R_m is the radius of the liposome. $\gamma(2/3,\mu)$ is given by eq B.6.

$$\gamma(a,x) = \int_0^x e^{-t} t^{a-1}\, dt \tag{B.6}$$

Equation B.7 describes the probability that the originally excited chromophore is still excited after t in a system with *N* donors.

$$\left\langle G^S(t)\right\rangle = \exp\left(\frac{(N-1)}{2}\left[\mu^{1/3}\gamma(2/3,\mu) - \mu^{1/3}\Gamma(2/3) + \exp(-\mu) - 1\right]\right) \tag{B.7}$$

These equations are accurate for short time and small Q,[96] which is the situation we are interested in here.

The number of lipid molecules in a liposome of radius R_m is given by eq B.8, which calculates the combined surface area of the outer and inner membrane monolayers (with radii R_m and $R_m - h$, respectively) and divides by the lipid head group area.

$$N_L = \frac{4\pi R_m^2 + 4\pi(R_m - h)^2}{a} \tag{B.8}$$

For DSPC, the lipid used in our experiments, $h \approx 4.05$ nm and $a \approx 0.66$ nm^2.[121] The number of porphyrins in a liposome is $N_p = N_L/30$. The average surface area per

porphyrin is nearly independent of R_m for values of R_m above about 50 nm. For these calculations, we assumed $R_m = 500$ nm .

Considering J-to-J transfer, $N_J = N_P / 10.8$ and $R_0 \approx 1.89$ nm as discussed above. Equation B.7 then predicts that within τ_F, about 8% of initially excited J-dimers will have transferred their energy to other J-dimers. Using $N_H = N_P * 9.8 / 10.8$ and $R_0 \approx 0.85$ nm for H-to-H transfer, eq B.7 predicts that within τ_F, 15% of initially excited H-dimers will have transferred their energy to other H-dimers. Equation B.7 likewise predicts that within τ_F, 55% of J-dimers will have transferred their energy to H-dimers, and 2% of H-dimers will have transferred their energy to J-dimers, while applying eq B.5 to these transfer processes predicts an 80% transfer rate for J-to-H and a 3% rate for H-to-J. Because the differences in energy between the excited states of these different species are on the order of $k_B T = 201$ cm^{-1} at 17°C, we expect that this system will behave in a manner intermediate between the one donor and $N-1$ traps system (eq B.5) and the N donors system (eq B.7). As discussed in the main text, the process of J-to-H transfer during the population time, which these calculations predict will be the most probable form of EET, could lead to a larger increase in the upper cross peak than that predicted by Redfield theory alone. The results of the calculations are summarized in Figure B.1.

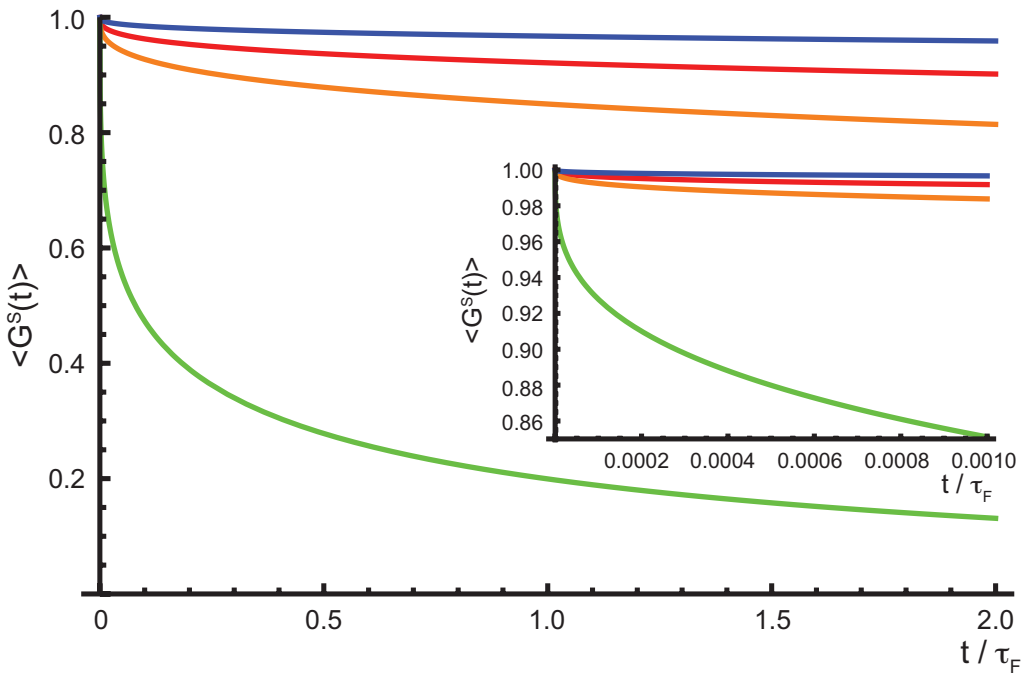

Figure B.1. Plots of initial excitation survival probability $\left\langle G^S(t)\right\rangle$ as a function of time relative to fluorescence lifetime τ_F. The traces represent decay of the initially excited population due to J-to-J transfer (red), H-to-H transfer (orange), J-to-H transfer (green) and H-to-J transfer (blue). J-to-H transfer is clearly faster than the other processes. The J-to-J and H-to-H traces were calculated using eq B.7 whereas the J-to-H and H-to-J traces were calculated using eq B.5. The large plot shows the behavior out to $t = 2\tau_F$, and the insert shows the early-time behavior.

REFERENCES CITED

1. Yang, M.; Szyc, L.; Elsaesser, T. Vibrational Dynamics of the Water Shell of DNA Studied by Femtosecond Two-Dimensional Infrared Spectroscopy. *J. Photochem. Photobiol., A* **2012,** *234*, 49-56.

2. Lin, Y.; Li, Y.; Crosson, S.; Dinner, A. R.; Scherer, N. F. Phase Resetting Reveals Network Dynamics Underlying a Bacterial Cell Cycle. *PLoS Biol.* **2012,** *8*, e1002778.

3. Mueser, T. C.; Hinerman, J. M.; Devos, J. M.; Boyer, R. A.; Williams, K. J. Structural Analysis of Bacteriophage T4 DNA Replication: A Review in the Virology Journal Series on *Bacteriophage T4 and Its Relatives*. *Virol. J.* **2010,** *7*, 1-17.

4. Tekavec, P. F.; Lott, G. A.; Marcus, A. H. Fluorescence-Detected Two-Dimensional Electronic Coherence Spectroscopy by Acousto-Optic Phase Modulation. *J. Chem. Phys.* **2007,** *127*, 214307.

5. Jonas, D. M. Two-Dimensional Femtosecond Spectroscopy. *Annu. Rev. Phys. Chem.* **2003,** *54*, 425-463.

6. Brixner, T.; Stenger, J.; Vaswani, H. M.; Cho, M.; Blankenship, R. E.; Fleming, G. R. Two-Dimensional Spectroscopy of Electronic Couplings in Photosynthesis. *Nature* **2005,** *434*, 625-628.

7. Tian, P.; Keusters, D.; Suzaki, Y.; Warren, W. S. Femtosecond Phase-Coherent Two-Dimensional Spectroscopy. *Science* **2003,** *300*, 1553-1555.

8. Lott, G. A.; Perdomo-Ortiz, A.; Utterback, J. K.; Widom, J. R.; Aspuru-Guzik, A.; Marcus, A. H. Conformation of Self-Assembled Porphyrin Dimers in Liposome Vesicles by Phase-Modulation 2D Fluorescence Spectroscopy. *Proc. Natl. Acad. Sci. U.S.A.* **2011,** *108*, 16521-16526.

9. Perdomo-Ortiz, A.; Widom, J. R.; Lott, G. A.; Aspuru-Guzik, A.; Marcus, A. H. Conformation and Electronic Population Transfer in Membrane-Supported Self-Assembled Porphyrin Dimers by 2D Fluorescence Spectroscopy. *J. Phys. Chem. B* **2012,** *116*, 10757-10770.

10. Widom, J. R.; Lee, W.; Perdomo-Ortiz, A.; Rappoport, D.; Molinski, T. F.; Aspuru-Guzik, A.; Marcus, A. H. Temperature-Dependent Conformations of a Membrane Supported Zinc Porphyrin Tweezer by 2D Fluorescence Spectroscopy. *J. Phys. Chem. A* **2013,** *117*, 6171-6184.

11. Jose, D.; Datta, K.; Johnson, N. P.; von Hippel, P. H. Spectroscopic Studies of Position-Specific DNA "Breathing" Fluctuations at Replication Forks and Primer-Template Junctions. *Proc. Natl. Acad. Sci. U.S.A.* **2009,** *106*, 4231-4236.

12. Datta, K.; Johnson, N. P.; von Hippel, P. H. DNA Conformational Changes at the Primer-Template Junction Regulate the Fidelity of Replication by DNA Polymerase. *Proc. Natl. Acad. Sci. U.S.A.* **2010,** *107*, 17980-17985.

13. Widom, J. R.; Johnson, N. P.; von Hippel, P. H.; Marcus, A. H. Solution Conformation of 2-Aminopurine Dinucleotide Determined by Ultraviolet Two-Dimensional Fluorescence Spectroscopy. *New J. Phys.* **2013,** *15*, 025028-1-16.

14. Raymer, M. G.; Marcus, A. H.; Widom, J. R.; Vitullo, D. L. P. Entangled Photon-Pair Two-Dimensional Fluorescence Spectroscopy (EPP-2DFS). *J. Phys. Chem. B* **2013**, DOI 10.1021/jp405829n.

15. Cho, M. *Two-Dimensional Optical Spectroscopy*. 1st ed.; CRC Press: Boca Raton, 2009.

16. Voet, D.; Voet, J. G. *Biochemistry*. John Wiley & Sons, Inc.: New Jersey, 2011.

17. Gouterman, M., Optical Spectra and Electronic Structure of Porphyrins and Related Rings In *The Porphyrins: Physical Chemistry, Part A*, Dolphin, D., Ed. Academic Press: New York, 1979; Vol. III, pp 1-156.

18. MacMillan, J. B.; Molinski, T. F. Long-Range Stereo-Relay: Relative and Absolute Configuration of 1,N-Glycols from Circular Dichroism of Liposomal Porphyrin Esters. *J. Am. Chem. Soc.* **2004,** *126*, 9944-9945.

19. Allen, T. M.; Cullis, P. R. Liposomal Drug Delivery Systems: From Concept to Clinical Applications. *Abs. Drug Deliv. Rev.* **2013,** *65*, 36-48.

20. Silvius, J. R. *Thermotropic Phase Transitions of Pure Lipids in Model Membranes and Their Modifications by Membrane Proteins*. John Wiley & Sons, Inc.: New York, 1982.

21. Lee, W.; Jose, D.; Phelps, C.; Marcus, A. H.; von Hippel, P. H. A Single-Molecule View of the Assembly Pathway, Subunit Stoichiometry, and Unwinding Activity of the Bacteriophage T4 Primosome (Helicase-Primase) Complex. *Biochemistry* **2013,** *51*, 3157-3170.

22. Mishra, A.; Behera, R. K.; Behera, P. K.; Bijaya, M. K.; Behera, G. P. Cyanines During the 1990s: A Review. *Chem. Rev.* **2000,** *100*, 1973-2011.

23. Johnson, N. P.; Baase, W. A.; von Hippel, P. H. Low-Energy Circular Dichroism of 2-Aminopurine Dinucleotide as a Probe of Local Conformation of DNA and RNA. *Proc. Natl. Acad. Sci. U.S.A.* **2004,** *101*, 3426-3431.

24. Jose, D.; Weitzel, S. E.; von Hippel, P. H. Breathing Fluctuations in Position-Specific DNA Base Pairs Are Involved in Regulating Helicase Movement into the Replication Fork. *Proc. Natl. Acad. Sci. U.S.A.* **2012,** *109*, 14428-14433.

25. Tanford, C. The Hydrophobic Effect and the Organization of Living Matter. *Science* **1978,** *200*, 1012-1018.

26. Schenning, A. P. H. J.; Hubert, D. H. W.; Feiters, M. C.; Nolte, R. J. M. Control of Aggregation and Tuning of the Location of Porphyrins in Synthetic Membranes as Mimics for Cytochrome P450. *Langmuir* **1996,** *12*, 1572-1577.

27. McGaughey, G. B.; Gagné, M.; Rappé, A. K. Π-Stacking Interactions. *J. Biol. Chem.* **1998,** *273*, 15458-15463.

28. Steinberg, I. Z.; Scheraga, H. A. Entropy Changes Accompanying Association Reactions of Proteins. *J. Biol. Chem.* **1963,** *238*, 172-181.

29. Finkelstein, A.; Janin, J. The Price of Lost Freedom: Entropy of Bimolecular Complex Formation. *Protein Engineering* **1989,** *3*, 1-3.

30. Balaban, T. S. Tailoring Porphyrins and Chlorins for Self-Assembly in Biomimetic Artificial Antenna Systems. *Acc. Chem. Res.* **2005,** *38*, 612-623.

31. Ganapathy, S.; Oostergetel, G. T.; Wawrzyniak, P. K.; Reus, M.; Chew, A. G. M.; Buda, F.; Boekema, E. J.; Brant, D. A.; Holzwarth, A. R.; de Groot, H. J. M. Alternating *Syn-Anti* Bacteriochlorophylls Form Concentric Helical Nanotubes in Chlorosomes. *Proc. Natl. Acad. Sci. U.S.A.* **2009,** *106*, 8525-8530.

32. Didraga, C.; Knoester, J. Absorption and Dichroism Spectra of Cylindrical J Aggregates and Chlorosomes of Green Bacteria. *J. Luminesc.* **2003,** *102-103*, 60-66.

33. Wasielewski, M. Self-Assembly Strategies for Integrating Light Harvesting and Charge Separation in Artificial Photosynthetic Systems. *Acc. Chem. Res.* **2009,** *42*, 1910-1921.

34. Wasielewski, M. Energy, Charge, and Spin Transport in Molecules and Self-Assembled Nanostructures Inspired by Photosynthesis. *J. Org. Chem.* **2006,** *71*, 5051-5066.

35. Moreira, L. M.; dos Santos, F. V.; Lyon, J. P.; Maftoum-Costa, M.; Pacheco-Soares, C.; Soares da Silva, N. Photodynamic Therapy: Porphyrins and Phthalocyanines and Photosensitizers. *Aust. J. Chem.* **2008,** *61*, 741-754.

36. Hidalgo, A. A.; Tabak, M.; Oliverira Jr., O. N. The Interaction of Meso-Tetraphenylporphyrin with Phospholipid Monolayers. *Chem. Phys. of Lipids* **2005,** *134*, 97-108.

37. Komatsu, T.; Moritake, M.; Tsuchida, E. Molecular Energy and Electron Transfer Assemblies Made of Self-Organized Lipid-Porphyrin Bilayer Vesicles. *Chem. Eur. J.* **2003,** *9*, 4626-4633.

38. Kasha, M.; Rawls, H. R.; El-Bayoumi, M. A. The Exciton Model in Molecular Spectroscopy. *Pure Appl. Chem.* **1965,** *11*, 371-392.

39. Mukamel, S. *Principles of Nonlinear Optical Spectroscopy*. Oxford University Press: Oxford, 1995.

40. Tekavec, P. F.; Dyke, T. R.; Lott, G. A.; Marcus, A. H. Wave Packet Interferometry and Quantum State Reconstruction by Acousto-Optic Phase Modulation. *J. Chem. Phys.* **2006,** *125*, 194303-1-19.

41. Stomphorst, R. G.; Koehorst, R. B. M.; van der Zwan, G.; Benthem, B.; Schaafsma, T. J. Excitonic Interactions in Covalently Linked Porphyrin Dimers with Rotational Freedom. *J. Porphyrins and Phthalocyanines* **1999,** *3*, 346-354.

42. Koolhaas, M. H. C.; van der Zwan, G.; van Mourik, F.; van Grondelle, R. Spectroscopy and Structure of Bacteriochlorophyll Dimers. I. Structural Consequences of Nonconservative Circular Dichroism Spectra. *Biophys. J.* **1997,** *72*, 1828-1841.

43. Won, Y.; Friesner, R. A.; Johnson, M. R.; Sessler, J. L. Exciton Interactions in Synthetic Porphyrin Dimers. *Photonsynthetic Research* **1989,** *22*, 201-210.

44. Golonzka, O.; Tokmakoff, A.; Polarization-Selective Third-Order Spectroscopy of Coupled Vibronic States. *J. Chem. Phys.* **2001,** *115*, 297-309.

45. Kim, J.; Mukamel, S.; Scholes, G. D. Two-Dimensional Electronic Double-Quantum Coherence Spectroscopy. *Acc. Chem. Res.* **2009,** *42*, 1375-1384.

46. Khalil, M.; Demirdoven, N.; Tokmakoff, A. Coherent 2D IR Spectroscopy: Molecular Structure and Dynamics in Solution. *J. Phys. Chem. A* **2003,** *107*, 5258-5279.

47. Nordén, B.; Rodger, A.; Dafforn, T. *Linear Dicrhoism and Circular Dichroism: A Textbook on Polarized-Light Spectroscopy*. RSC Publishing: Cambridge, UK, 2010.

48. Tanford, C. *The Hydrophobic Effect*. 2 ed.; John Wiley & Sons: New York, 1980; p 233.

49. von Hippel, P. H. From "Simple" DNA-Protein Interactions to the Macromolecular Machines of Gene Expression. *Annu. Rev. Biophys. Biomol. Struct.* **2007,** *36*, 79-105.

50. von Hippel, P. H. Protein-DNA Recognition: New Perspectives and Underlying Themes. *Science* **1994,** *263*, 769-770.

51. Spolar, R. S.; Record, M. T. Coupling of Local Folding to Site-Specific Binding of Proteins to DNA. *Science* **1994,** *263*, 777-784.

52. Molinski, T. F.; Makarieva, T. N.; Stonik, V. A. (-)-Rhizochalin Is a Dimeric Enantiomorphic (2R)-Sphingolipid. Analysis of Pseudo-C2 Symmetric Bis-2-Amino-3-Alkanols by CD. *Angew. Chem. Int. Ed.* **2000,** *39*, 4076-4079.

53. Dalisay, D. S.; Quach, T.; Molinski, T. F. Liposomal Circular Dichroism. Assignment of Remote Stereocenters in Plakinic Acids K and L from a Plakortis-Xestospongia Sponge Association. *Org. Lett.* **2010,** *12*, 1524-1527.

54. Dalisay, D. S.; Quach, T.; Nicholas, G. N.; Molinski, T. F. Amplification of Cotton Effects of a Single Chromophore through Liposomal Ordering. Stereochemical Assignment Plakinic Acids (I-J) from *Plakortis*. *Angew. Chem. Int. Ed.* **2009,** *48*, 4367-4371.

55. Collini, E.; Wong, C. Y.; Wilk, K. E.; Curmi, P. M. G.; Brumer, P.; Scholes, G. D. Coherently Wired Light-Harvesting in Photosynthetic Marine Algae at Ambient Temperature. *Nature* **2010,** *463*, 644-647.

56. Abramavicius, D.; Palmieri, B.; Voronine, D. V.; Šanda, F.; Mukamel, S. Coherent Multidimensional Optical Spectroscopy of Excitons in Molecular Aggregates; Quasiparticle Versus Supermolecule Perspectives. *Chem. Rev.* **2009,** *109*, 2350-2408.

57. Ginsberg, N. S.; Cheng, Y.-C.; Fleming, G. R. Two-Dimensional Electronic Spectroscopy of Molecular Aggregates. *Acc. Chem. Res.* **2009,** *42*, 1352-1363.

58. Collini, E.; Scholes, G. D. Coherent Intrachain Energy Migration in a Conjugated Polymer at Room Temperature. *Science* **2009,** *323*, 369-373.

59. Zhang, T.; Kuznetsova, I.; Meier, T.; Li, X.; Mirin, R. P.; Thomas, P.; Cundiff, S. T. Polarization-Dependent Optical 2D Fourier Transform Spectroscopy of Semiconductors. *Proc. Natl. Acad. Sci. U.S.A.* **2007,** *104*, 14227-14232.

60. Stone, K. W.; Gundogdu, K.; Turner, D. B.; Li, X.; Cundiff, S. T.; Nelson, K. A. Two-Quantum Two-Dimensional Fourier Transform Electronic Spectroscopy of Biexcitons in GaAs Quantum Wells. *Science* **2009,** *324*, 1169-1173.

61. Huang, X.; Rickman, B. H.; Borhan, B.; Berova, N.; Nakanishi, K. Zinc Porphyrin Tweezer in Host−Guest Complexation: Determination of Absolute Configurations of Diamines, Amino Acids, and Amino Alcohols by Circular Dichroism. *J. Am. Chem. Soc.* **1998,** *120*, 6185-6186.

62. Matile, S.; Berova, N.; Nakanishi, K.; Novkova, S.; Philipova, I.; Blagoev, B. Porphyrins: Power Chromophores for Structural Studies by Exciton-Coupled Circular Dichroism. *J. Am. Chem. Soc.* **1995,** *117*, 7021-7022.

63. Rappé, A. K.; Casewit, C. J.; Colwell, K. S.; Goddard III, W. A.; Skiff, W. M. UFF, a Full Periodic Table Force Field for Molecular Mechanics and Molecular Dynamics Simulations. *J. Am. Chem. Soc.* **1992,** *114*, 10024-10035.

64. Rappé, A. K.; Colwell, K. S.; Casewit, C. J. Application of a Universal Force Field to Metal Complexes. *Inorg. Chem.* **1993,** *32*, 3438-3450.

65. TURBOMOLE V6.3 2011, a Development of University of Karlsruhe and Forschungszentrum Karlsruhe GmbH (http://www.turbomole.com).

66. Byrd, R. H.; Nocedal, J.; Waltz, R. A., KNITRO: An Integrated Package for Nonlinear Optimization. In *Large-Scale Nonlinear Optimization*, G. di Pillo, M. R., Ed. Springer-Verlag: 2006; pp 35-59.

67. Zein, M.; Winter, R. Effect of Temperature, Pressure and Lipid Acyl Chain Length on the Structure and Phase Behaviour of Phospholipid–Gramicidin Bilayers. *Phys. Chem. Chem. Phys.* **2000,** *2*, 4545-4551.

68. Walrafen, G. E.; Fisher, M. R.; Hokmabadi, M. S.; Yang, W.-H. Temperature Dependence of the Low- and High-Frequency Raman Scattering from Liquid Water. *J. Chem. Phys.* **1986,** *85*, 6970-6982.

69. Doxastakis, M.; Sakai, V. G.; Ohtake, S.; Maranas, J. K.; de Pablo, J. J. A Molecular View of Melting in Anhydrous Phospholipidic Membranes. *Biophys. J.* **2007,** *92*, 147-161.

70. Sintes, T.; Baumgärtner, A. Protein Attraction in Membranes Induced by Lipid Fluctuations. *Biophys. J.* **1997,** *73*, 2251-2259.

71. Jose, D.; Weitzel, S. E.; Jing, D.; von Hippel, P. H. Assembly and Subunit Stoichiometry of the Functional Helicase-Primase (Primosome) Complex of Bacteriophage T4. *Proc. Natl. Acad. Sci. U.S.A.* **2012,** *109*, 13596-13601.

72. Selvin, P. R.; Ha, T., *Single-Molecule Techniques*. Cold Spring Harbor Laboratory Press: Cold Spring Harbor, New York, 2008.

73. West, W.; Pearce, S. The Dimeric State of Cyanine Dyes. *J. Phys. Chem.* **1965,** *69*, 1894-1903.

74. Ward, D. C.; Reich, E.; Stryer, L. Fluorescence Studies of Nucleotides and Polynucleotides. *J. Biol. Chem.* **1969,** *244*, 1228-1237.

75. Ernst, R. R.; Bodenhausen, G.; Wokaun, A. *Principles of Nuclear Magnetic Resonance in One and Two Dimensions*. Oxford University Press: Oxford, U.K., 1990.

76. Jonas, D. M. Optical Analogs of 2D NMR. *Science* **2003,** *300*, 1515-1517.

77. Woutersen, S.; Hamm, P. Nonlinear Two-Dimensional Vibrational Spectroscopy of Peptides. *J. Phys.: Condens. Matter* **2002,** *14*, R1035-R1062.

78. Chung, H. S.; Ganim, Z.; Jones, K. C.; Tokmakoff, A. Transient 2D IR Spectroscopy of Ubiquitin Unfolding Dynamics. *Proc. Natl. Acad. Sci. U.S.A.* **2007,** *104*, 14237-14242.

79. Szyc, L.; Yang, M.; Nibbering, E. T. J.; Elsaesser, T. Ultrafast Vibrational Dynamics and Local Interactions of Hydrated DNA. *Angew. Chem. Int. Ed.* **2010,** *49*, 3598-3610.

80. Mukamel, S.; Abramavicius, D.; Yang, L.; Zhuang, W.; Schweigert, I. V.; Voronine, D. V. Coherent Multidimensional Optical Probes for Electron Correlations and Exciton Dynamics: From NMR to X-Rays. *Acc. Chem. Res.* **2009,** *42*, 553-562.

81. Jiang, J.; Mukamel, S. Two-Dimensional Near-Ultraviolet Spectroscopy of Aromatic Residues in Amyloid Fibrils: A First Principles Study. *Phys. Chem. Chem. Phys.* **2011,** *13*, 2394-2400.

82. West, B. A.; Womick, J. M.; Moran, A. M. Probing Ultrafast Dynamics in Adenine with Mid-UV Four-Wave Mixing Spectroscopies. *J. Phys. Chem. A* **2011,** *115*, 8630-8637.

83. Selig, U.; Schleussner, C.-F.; Foerster, M.; Langhojer, F.; Nuernberger, P.; Brixner, T. Coherent Two-Dimensional Ultraviolet Spectroscopy in Fully Noncollinear Geometry. *Optics Letters* **2010,** *35*, 4178-4180.

84. West, B.; Moran, A. M. Two-Dimensional Electronic Spectroscopy in the Ultraviolet Wavelength Range. *J. Phys. Chem. Lett.* **2012,** *3*, 2575-2581.

85. Aeschlimann, M.; Brixner, T.; Fischer, A.; Kramer, C.; Melchior, P.; Pfeiffer, W.; Schneider, C.; Strüber, C.; Tuchscherer, P.; Voronine, D. V. Coherent Two-Dimensional Nanoscopy. *Science* **2011,** *333*, 1723-1726.

86. Jean, J. M.; Hall, K. B. 2-Aminopurine Fluorescence Quenching and Lifetimes: Role of Base Stacking. *Proc. Natl. Acad. Sci. U.S.A.* **2001,** *98*, 37-41.

87. Sowers, L.C.; Fazakerley, G. V.; Eritja, R.; Kaplan, B. E.; Goodman, M. F. Base Pairing and Mutagensis: Observation of a Protonated Base Pair between 2-Aminopurine and Cytosine in an Oligonucleotide by Proton NMR. *Proc. Natl. Acad. Sci. U.S.A.* **1986,** *83*, 5434-5438.

88. Holmén, A.; Nordén, B.; Albinsson, B. Electronic Transition Moments of 2-Aminopurine. *J. Am. Chem. Soc.* **1997,** *119*, 3114-3121.

89. Tian, P.; Warren, W. S. Ultrafast Measurement of Two-Photon Absorption by Loss Modulation. *Optics Letters* **2002,** *27*, 1634-1636.

90. Solie, T. N.; Schellman, J. A. The Interaction of Nucleosides in Aqueous Solution. *J. Mol. Biol.* **1968,** *14*, 61-77.

91. Cantor, C. R.; Schimmel, P. R. *Biophysical Chemistry: The Conformation of Biological Macromolecules*. W. H. Freeman: New York (pgs. 335-336), 1980; Vol. I.

92. Mukamel, S. Multidimensional Femtosecond Correlation Spectroscopies of Electonic and Vibrational Excitations. *Annu. Rev. Phys. Chem.* **2000,** *51*, 691-729.

93. Cho, M.; Fleming, G. R. The Integrated Photon Echo and Solvation Dynamics. II. Peak Shifts and Two-Dimensional Photon Echo of a Coupled Chromophore System. *J. Chem. Phys.* **2005,** *123*, 114506.

94. Milota, F.; Sperling, J.; Nemeth, A.; Mančal, T.; Kauffmann, H. F. Two-Dimensional Electronic Spectroscopy of Molecular Excitons. *Acc. Chem. Res.* **2009,** *42*, 1364-1374.

95. Milota, F.; Sperling, J.; Nemeth, A.; Abramavicius, D.; Mukamel, S.; Kauffmann, H. F. Excitonic Couplings and Interband Energy Transfer in a Double-Wall Molecular Aggregate Imaged by Coherent Two-Dimensional Electronic Spectroscopy. *J. Chem. Phys.* **2009,** *131*, 054510-054523.

96. Finger, K. U.; Marcus, A. H.; Fayer, M. D. Structure of Complex Systems Using Electronic Excitation Transport: Theory, Monte Carlo Simulations, and Experiments on Micelle Solutions. *J. Chem. Phys.* **1994,** *100*, 271-286.

97. Quimby, D. J.; Longo, F. R. Luminescence Studies on Several Tetraarylporphyrins and Their Zinc Derivatives. *J. Am. Chem. Soc.* **1975,** *97*, 5111-5117.

98. Hybl, J. D.; Yu, A.; Farrow, D. A.; Jonas, D. M. Polar Solvation Dynamics in the Femtosecond Evolution of Two-Dimensional Fourier Transform Spectra. *J. Phys. Chem. A* **2002,** *206*, 7651-7654.

99. West, B. A.; Molesky, B. P.; Montoni, N. P.; Moran, A. M. Nonlinear Optical Signatures of Ultraviolet Light-Induced Ring Opening in A-Terpinene. *New J. Phys.* **2013,** *15*, 025007-1 - 025007-21.

100. Horodecki, R.; Horodecki, P.; Horodecki, M.; Horodecki, K. Quantum Entanglement. *Rev. Mod. Phys.* **2009,** *81*, 865-942.

101. van Enk, S. J.; Lutkenhaus, N.; Kimble, H. J. Experimental Procedures for Entanglement Verification. *Phys. Rev. A* **2007,** *75*, 052318-1-14.

102. Chaves, R.; Davidovich, L. Robustness of Entanglement as a Resource. *Phys. Rev. A* **2010,** *82*, 052308-1-10.

103. Franson, J. D. Two-Photon Interferometry over Large Distances. *Phys. Rev. A* **1991,** *44*, 4552-4555.

104. Franson, J. D. Bell Inequalities for Position and Time. *Phys. Rev. Lett.* **1989,** *62*, 2205-2208.

105. Franson, J. D. Violations of a Simple Inequality for Classical Fields. *Phys. Rev. Lett.* **1991,** *67*, 290-293.

106. Gea-Banacloche, J. Two-Photon Absorption of Nonclassical Light. *Phys. Rev. Lett.* **1989,** *62*, 1603-1606.

107. Lee, D.-I.; Goodson, T. Entangled Photon Absorption in an Organic Porphyrin Dendrimer. *J. Phys. Chem. B* **2006,** *110*, 25582-25585.

108. Fei, H.-B.; Jost, B. M.; Popescu, S.; Saleh, B. E. A.; Teich, M. C. Entanglement-Induced Two-Photon Transparency. *Phys. Rev. Lett.* **1997,** *78*, 1679-1612.

109. Dayan, B. Theory of Two-Photon Interactions with Broadband Down-Converted Light and Entangled Photons. *Phys. Rev. A* **2007,** *76*, 043813-1-19.

110. Joobeur, A.; Saleh, B. E. A.; Teich, M. C. Spatiotemporal Coherence Properties of Entangled Light Beams Generated by Parametric Down-Conversion. *Phys. Rev. A* **1994,** *50*, 3349-3361.

111. Khan, I. A.; Howell, J. C. Experimental Demonstration of High Two-Photon Time-Energy Entanglement. *Phys. Rev. A* **2006,** *73*, 031801-1-4.

112. Mancini, S.; Giovannetti, V.; Vitali, D.; Tombesi, P. Entangling Macroscopic Oscillators Exploiting Radiation Pressure. *Phys. Rev. Lett.* **2002,** *88*, 120401-1-4.

113. Widom, J. R.; Rappoport, D.; Perdomo-Ortiz, A.; Thomsen, H.; Johnson, N. P.; von Hippel, P. H.; Aspuru-Guzik, A.; Marcus, A. H. Electronic Transition Moments of 6-Methyl Isoxanthopterin - a Fluorescent Analogue of the Nucleic Acid Base Guanine. *Nucl. Acids Res.* **2013,** *41*, 995-1004.

114. Datta, K.; Johnson, N. P.; Villani, G.; Marcus, A. H.; von Hippel, P. H. Characterization of the 6-Methyl Isoxanthopterin (6-MI) Base Analog Dimer, a Spectroscopic Probe for Monitoring Guanine Base Conformations at Specific Sites in Nucleic Acids. *Nucl. Acids Res.* **2011,** *40*, 1191-1202.

115. van Amerongen, H.; Valkunas, L.; van Grondelle, R. *Photosynthetic Excitons*. World Scientific: Singapore, 2000.

116. Read, E. L.; Engel, G. S.; Calhoun, T. R.; Mančal, T.; Ahn, T. K.; Blankenship, R. E.; Fleming, G. R. Cross-Peak-Specific Two-Dimensional Electronic Spectroscopy. *Proc. Natl. Acad. Sci. U.S.A.* **2007,** *104*, 14203-14208.

117. Zanni, M.; Ge, N.-H.; Kim, Y. S.; Hochstrasser, R. M. Two-Dimensional IR Spectroscopy Can Be Designed to Eliminate the Diagonal Peaks and Expose Only the Crosspeaks Needed for Structure Determination. *Proc. Natl. Acad. Sci. U.S.A.* **2001,** *98*, 11265-11270.

118. Golonska, O.; Tokmakoff, A. Polarization-Selective Third-Order Spectroscopy of Coupled Vibronic States. *J. Chem. Phys.* **2001,** *115*, 297-309.

119. Levenson, M. D.; Kano, S. S. *Introduction to Nonlinear Laser Spectroscopy*. Academic Press: London, 1988.

120. So, P. T. C.; Dong, C. Y.; Masters, B. R.; Berland, K. M. Two-Photon Excitation Fluorescence Microscopy. *Annu. Rev. Biomed. Eng.* **2000,** *2*, 399-429.

121. Lewis, B. A.; Engelman, D. M. Lipid Bilayer Thickness Varies Linearly with Acyl Chain Length in Fluid Photphatidylcholine Vesicles. *J. Mol. Biol.* **1983,** *166*, 211-217.